EVALUATION OF PERFORMANCE OF FRICTION STIR WELDED AA2519-T87 ALUMINIUM ALLOY JOINTS

A Thesis

Submitted by

S. SREE SABARI
Roll No. 1133050005

In partial fulfillment for the requirements of the award of the degree of

DOCTOR OF PHILOSOPHY
IN
MANUFACTURING ENGINEERING

**DEPARTMENT OF MANUFACTURING ENGINEERING
FACULTY OF ENGINEERING AND TECHNOLOGY
ANNAMALAI UNIVERSITY
ANNAMALAINAGAR – 608 002
TAMIL NADU, INDIA
2016**

ANNAMALAI UNIVERSITY

Dr. V. BALASUBRAMANIAN, M.E., Ph.D (IITM)
Professor
Department of Manufacturing Engineering
Faculty of Engineering & Technology
Annamalai University
Annamalainagar – 608 002
Tamil Nadu
India

CERTIFICATE

This is to certify that the thesis entitled **"EVALUATION OF PERFORMANCE OF FRICTION STIR WELDED AA2519-T87 ALUMINIUM ALLOY JOINTS"** is a bonafide work **Mr. S. Sree Sabari (Roll No. 1133050005),** Ph.D Scholar, Department of Manufacturing Engineering, Faculty of Engineering & Technology, Annamalai University who carried out research under my supervision. Certified further, that to the best of knowledge this thesis has not previously formed the basis for the award of any Degree, Diploma, Associateship, Fellowship or other similar title to the candidate.

Signature of the Research Supervisor

Station: Annamalainagar

Date: 01.09.2016

<div align="center">

DECLARATION BY THE CANDIDATE SUBMITTING THESIS

ANNAMALAI UNIVERSITY
Annamalainagar

DECLARATION

</div>

I, **Mr. S. Sree Sabari (Roll No. 1133050005)** Research Scholar in the Department of **Manufacturing Engineering** declare that the work embodied in this Ph.D thesis entitled **Evaluation of Performance of Friction Stir Welded AA2519-T87 aluminium alloy joints** is a result of my own **bonafide** work carried out with my personal effort and submitted by me under the **supervision of Dr. V. Balasubramanian at Annamalai University, Annamalainagar.** The contents of this thesis have not formed the basis for the award of any Degree/Diploma/Fellowship/Titles in this University or any other University or similar Institutions of Higher Learning.

I declare that I have faithfully acknowledge and given credit and referred to the researchers where their works have been cited in the body of the thesis. I further declare that I have not willfully copied some other's data/work/results etc. reported in the journals, magazines, books, reports, dissertations, theses, internet etc. and claimed as my own work.

<div align="right">

Signature of the Research Scholar

</div>

Station: Annamalainagar

Date: 01.09.2016

ABSTRACT

In recent days, armour grade steels in the military vehicle are replaced by the lighter materials for better mobility. Aluminium alloy AA2519-T87 is a potential candidate, to replace steel in few defence applications due to its high specific strength, high fracture toughness and ballistic immunity. Researchers confirmed that friction stir welding (FSW) can produce sound joints of heat-treatable aluminum alloys. However, the thermal cycles exerted during FSW, resulted in the reduction of mechanical properties of the joints due to coarsening and dissolution of strengthening precipitates in the thermo-mechanically affected zone (TMAZ) and heat affected zone (HAZ) of the joints. Hence, these regions attain lower hardness (softening) and so termed as the lowest hardness distribution region (LHDR). The deteriorated mechanical properties can be restored by employing the aging techniques namely artificial aging (AA), solution treatment + artificial aging (STA) techniques. To overcome the problems associated with FSW process in TMAZ and HAZ can be eliminated to some extent using underwater friction stir welding (UWFSW) technique. During UWFSW, the high heat dissipation capacity of water controls the conduction of heat to TMAZ and HAZ and thereby improves the joint strength.

Though the UWFSW process will yield joints with superior properties, the process parameters and tool geometry has to be selected in such a way to attain defect free, sound joints. The material flow behaviour and heat generation are the key factors decide the quality of the FSW and UWFSW joints, which is entirely different in both the processes. Hence in this investigation effect of process parameters namely, tool

rotational speed (1100 rpm - 1500 rpm), tool traverse speed (20 mm/min - 40 mm/min), tool tilt angle (0˚ - 4˚) and tool pin profiles (Straight cylindrical, straight threaded cylindrical, taper cylindrical and taper threaded cylindrical) on microstructure, tensile properties and microhardness characteristics of FSW and UWFSW joints were studied.

From the results, it was found that the UWFSW joint fabricated using taper threaded tool pin profile yielded higher tensile strength of 345 MPa. UWFSW joints showed 20 % enhancement in joint efficiency compared to FSW joints. The superior performance of UWFSW joints over FSW joints is attributed to the presence of relatively finer grains in the stir zone, marginally higher hardness of stir zone, high volume fraction of precipitates in lower hardness distributed region (LHDR), and appreciably lower width of LHDR. Moreover, the effect of on the properties of FSW and UWFSW joints were analyzed. An enhanced tensile strength of 395 MPa and maximum hardness of 151 HV was achieved in the STA joints. Both FSW and UWFSW joints undergone similar precipitation behaviour during STA treatment exhibit almost same properties. During STA treatment, homogenization and reprecipitation occurred in the entire joint unlike AA condition. The superior mechanical properties of STA joint are mainly attributed to the presence of finer precipitates with dense distribution in the stir zone region.

KEY WORDS: Friction stir welding, Underwater friction stir welding, Process parameters, Post weld heat treatment, Microstructure, Mechanical Properties

TABLE OF CONTENTS

LIST OF TABLES

LIST OF FIGURES

ABBREVIATIONS

AA	Aluminium Association
AA	Artificial Aging
APC	Armor Personnel Carriers
AS	Advancing Side
ASTM	American Society for Testing of Metals
AW	As Welded Condition
DAQ	Data Acquisition System
DPR	Defect Prone Region
EBW	Electron Beam Welding
EFV	Expeditionary Fighting Vehicle
FEM	Finite Element Method
FSP	Friction Stir Processed Zone
FSW	Friction Stir Welding
GMAW	Gas Metal Arc Welding
GPZ	Guinier-Preston zones
GTAW	Gas Tungsten Arc Welding
HAZ	Heat Affected Zone
LHDR	Low Hardness Distribution Region
MICV	Mechanized Infantry Combat Vehicles
MIG	Metal Inert Gas
Nd:YAG	Neodymium-Doped Yttrium Aluminium Garnet
OM	Optical Microscope
PAW	Plasma Arc Welding
PDF ICCD	Powder Diffraction Files from the International Centre for Diffraction
PFZ	Precipitates Free Zone
PIR	Pin Influenced Region

PM	Parent Metal
PWHT	Post Weld Heat Treatment
RS	Retreating Side
SAD	Selected Area Diffraction
SEM	Scanning Electron Microscopy
SIR	Shoulder Influenced Region
STA	Solution Treatment followed by Artificial Aging
STC	Straight Cylindrical
SZ	Stir Zone
TAC	Taper Cylindrical
TEM	Transmission Electron Microscope
THC	Straight Threaded Cylindrical
TMAZ	Thermo Mechanically Affected Zone
T_{PIR}	Thickness of Pin Influenced Region
TRS	Tool Rotational Speed
T_{SIR}	Thickness of Shoulder Influenced Region
TTA	Tool Tilt Angle
TTC	Taper Threaded Cylindrical
TTP	Taper Threaded Pin Profile
TTS	Tool Traverse Speed
UTS	Ultimate Tensile Strength
UWFSW	Underwater Friction Stir Welding
VOR	Lower Vortex Region
WEDM	Wire-cut Electric Discharge Machining
XRD	X Ray Diffraction

NOTATIONS

English Symbols

C	Celsius
A_s	Shoulder's Surface Area
f	Feed Rate
F	Force
F_n	Normal Force
h_{down}	Convection Coefficient of Bottom Surface
h_{up}	Convection Coefficient of Top Surface
K	Thermal Conductivity
Q	Heat Input
q_g	Heat Generation Per Unit Volume
q_{pin}	Heat Flux at Tool Pin
$q_{shoulder}$	Heat Flux at Tool Shoulder
R	Distance from the Center Axis of the Tool
r_p	Pin Radius
T	Torque
T_0	Reference Temperature
T_{amb}	Ambient Air Temperature
T_{amb}	Ambient Temperature
Ybar(T)	Average Shear Stress of the Material

Greek Symbols

°	Degree
μm	Micrometer
α	Thermal Diffusivity of the Material
β	Mg-Si Precipitates
ε	Surface Emissivity
η	Efficiency Factor
θ	Precipitate

μ	Friction Coefficient
ρ	Density of the Material
σ	Stefan-Boltzmann Constant
ω	Angular Velocity of the Tool

Units

cm	Centimeter
g	Gram
h	Hour
kN	Kilo Newton
kW	Kilo Watts
ml	Milliliter
mm	Millimeter
MPa	Mega Pascal
RPM	Revolutions Per Minute
s	Seconds
V	Volt
Wt	Weight

DEDICATION

This thesis work would have been impossible without the infinite love and unending support from my mother, **Mrs. L.Senbakom** to whom this thesis is dedicated.

ACKNOWLEDGEMENT

for their unconditional love and support. Thanks for excusing me for my absences during the difficult times incurred during last five and half years.

(S.SREE SABARI)

CHAPTER 1
INTRODUCTION

1.1 GENERAL CHARACTERISTICS OF ALUMINIUM AND ITS ALLOYS

The combination of beneficial properties like high strength to weight ratio and good ductility makes aluminium as one of the economical and most desired metallic materials for wide range of engineering applications (Totten 2003). Aluminium possesses high ductility and high malleability, so it can easily be rolled into very thin sheets (foils). It can be readily be die-forged or formed as well. Aluminium has a density of 2.7 g/cm^3, approximately one third as much as steel. Aluminium exhibits high reflective nature. It makes aluminium a very effective barrier against thermal radiation, suitable for applications like automotive heat shield. The high reflectivity gives aluminium a decorative appearance (Carroll *et al.* 2000).

Aluminium exhibits higher corrosion resistance. This is due to the dense, strong passivating film of aluminium oxide which forms immediately on its surface upon exposure to the atmosphere. The exposed surface of aluminium associate with oxygen to form an inert oxide layer. If the oxide layer of aluminium is removed or scratched, it will instantly form yet again. Aluminium is non-ferromagnetic and exhibit high electrical conductivity, so that it is desirable in electrical and electronics industries (Christian 2004). It is non-flammable, which is important in applications involving, handling of inflammable or explosive materials (Polmear 1995). One of the significant characteristics of aluminium is its high machinability and workability. It can be cast by any known method, rolled to any thickness, drawn, stamped,

hammered, forged, and extruded to any conceivable shape. Due to the range of beneficial properties of aluminium alloys, it is extensively used for wide range of industrial applications. Therefore, aluminium and its alloys are most usable materials next to steel, in terms of engineering applications (Kelkar *et al.* 2001).

	Characteristics	Application
1XXX Series 99% Al	Exceptional High formability, corrosion resistance and electrical conductivity	Packaging and foil, roofing, cladding, low-strength corrosion resistant vessels and tanks
2XXX Series Al-Cu	High strength, at room and elevated temperatures	Highly stressed parts, aerospace structural items, heavy duty forgings, heavy goods vehicle wheels, cylinder heads, pistons
3XXX Series Al-Mn	High formability and corrosion resistance with medium strenght	Packaging ,roofing and cladding, Chemical drums and tanks, process and food handling equipment
4XXX Series Al-Si	Good flow characteristics, medium strenght	Filler metal, cylinder heads, engine blocks, valve bodies, architectural purposes
5XXX Series Al-Mg	Excellent corrosion resistance, toughness, weldability and moderate strength	Cladding, vessel hull and superstructures, structural members, vessels and tanks, vehicles, rolling stock, architectural applications
6XXX Series Al-Mg-Si	High corrosion resistance, excelent extrudability, moderate strength	High-strenght structural members, vehicles, rolling stock, marine applications, architectural applications
7XXX Series Al-Mg-Zn	Very high strength, special high toughness versions	High stregth structural members, heavy section aircraft forgings, military bridging, armour plate, heavy goods vehicle and rolling stock extrusions
8XXX Series Al-other elements	High conductivity, strength, hardness	
9XXX Series Not used		

Wrought Aluminium Alloy Series

Fig. 1.1 Aluminium alloying elements and series name correspondence, and individual applicability (Avner 2000)

2

1.2 CLASSIFICATION OF ALUMINIUM ALLOYS

To improve the properties of pure aluminium, other materials Cu, Mg, Mn, Zn, Si are primarily alloyed to produce aluminium alloy with high mechanical properties. Based on the alloying system, the Aluminium Association designated the aluminium alloys (Fig. 1.1). The alloy designation system is as follows.

- First digit - Principle alloying element(s).

- Second digit - Variation of primary alloy

- Third and fourth digits - Distinct alloy variations

1.2.1 Aluminium-Copper Alloys (AA2xxx)

The 2xxx series represents the main class used in the aerospace transportation industry due to the high strength attained by precipitate strengthening. However, the corrosion resistance and weldability are the poorest among all Al-alloys. Copper is the principal alloying element in the 2xxx series alloys. Copper has a maximum solubility of 0.1 wt % at room temperature and 5.7 wt % at 548 ˚C (Fig. 1.2). In the Al-rich end of the Al-Cu system, a eutectic reaction takes place at a composition of 33.2 wt % Cu at 548 ˚C. The resulting eutectic contains both α-aluminium and the Al_2Cu intermetallic phase. The Cu-content in the θ-phase is within a range of 52.5 to 53.7 wt % at the eutectic temperature, with the range narrowing as the temperature drops (Hatch 1984). In commercial alloys, the Cu-concentration can reach up to 10-14 wt % in cast alloys, but for wrought alloys, the concentration is limited to 4-6 wt % (around the maximum solubility of Cu in α-aluminium).
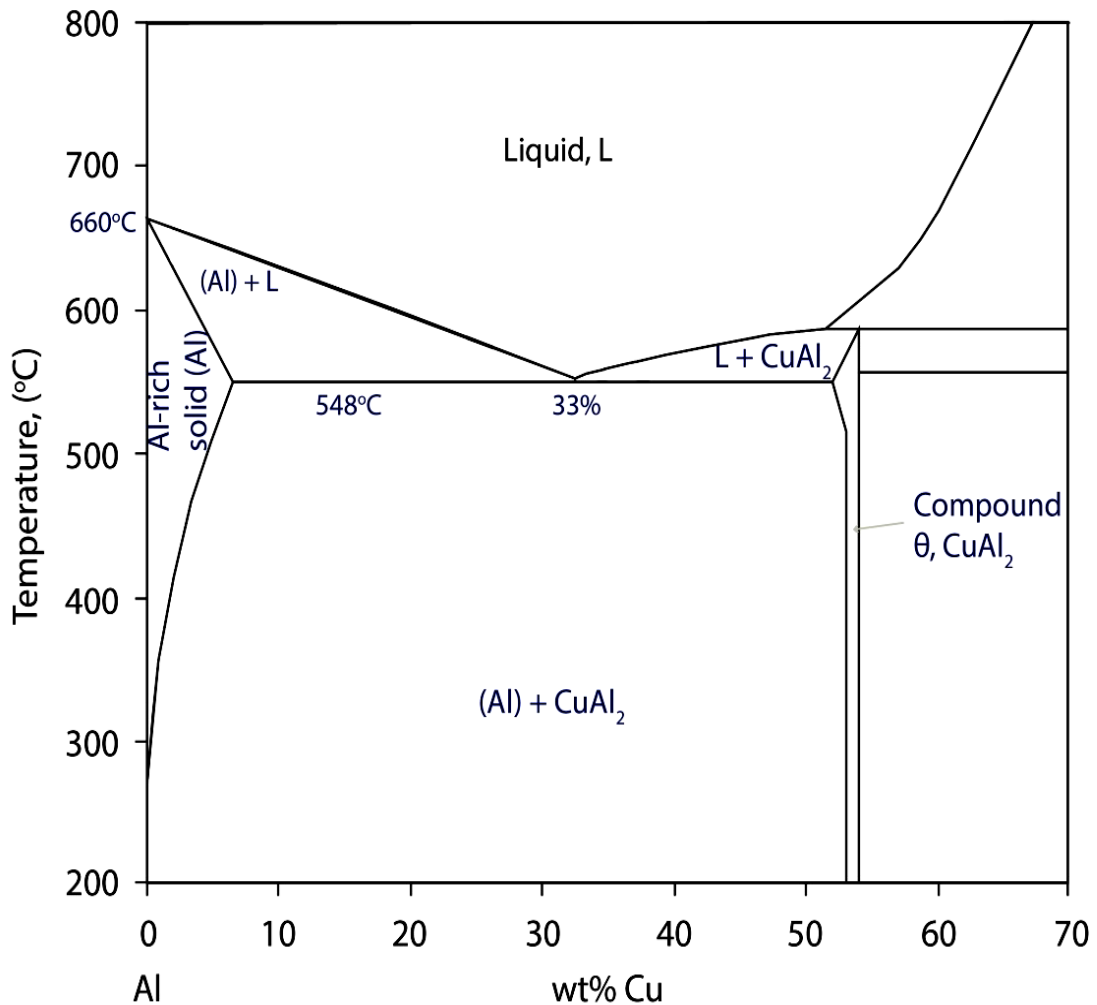
Fig. 1.2 The Al-rich corner in the Al-Cu system (Davis 1993)

1.2.2 Intermetallic phases in AA2xxx

Due to the many alloying elements and impurities in the 2xxx series, the intermetallic

particle structure can be considered as the most complex among all Al-alloys.

Additions of magnesium are often used to improve the strength. The addition of

lithium to Al-Cu (Mg) alloys has also been found to significantly enhance the

strength and weldability to levels higher than any other Al-alloy class. Other

elements may exist as impurities (e.g. silicon and iron), or as additives to improve the

strength, such as: manganese, titanium, zinc, and chromium (Mondolfo 1976).

Generally, the alloying elements in the 2xxx series alloys form two types of intermetallic particles in the aluminium matrix (Smith 1996):

i. Age hardening metastable and stable (soluble) precipitates: fine spherical or plate-like coherent precipitates (few nanometres thick) that form only during room or low temperature aging after solution heat treatment and quenching. They are the main strengthening mechanism due to their small size. On further aging, these phases coarsen until they transform to incoherent equilibrium phases (reaching 1-10 μm size) which contain Cu and/or Mg, such as: θ-Al_2Cu phases. They differ from primary precipitates in that they can be fully re-dissolved at around 515-550 ˚C. During recrystallisation, the concurrent dissolution/precipitation of these phases can influence the resulting grain structure depending on the starting material condition (e.g. solution-treated or aged) and the type of the precipitates (Majimel e*t al.* 2004).

ii. Constituent (*primary* insoluble) particles: which contain Si, Fe or Mn, in addition to Cu or Mg, such as $Al_{12}(Fe,Mn)_3Si$, Al_7Cu_2Fe or $Al_5Cu_2Mg_8Si_6$ (1-10 μm size) (Smith 2000).

1.2.3 Aging behaviour of Al-Cu system

The 2xxx series alloys are heat treatable alloys differ from the not heat treatable alloys in that they attain their strength through precipitation-hardening. Because of the nature of the Al-Cu system (Fig. 2.3), if an alloy of composition less than 5 wt % Cu is heated to the region (515-550 ˚C) to force all the copper to go into solution then quenched, a supersaturated solution will form. Since supersaturation is unstable,

a driving force exists to precipitate the excess copper to reach a metastable or equilibrium state (Wang *et al.* 2006).

The precipitation sequence in the Al-Cu system is as follows:

Supersaturated solid solution (SSSS) → GPZ II (θ'') → GPZ I (θ') → θ (stable)

where, SSSS is the supersaturated solid solution. On aging the alloy at room temperature, GPZ (Guinier-Preston zones) form, which are coherent disk-shaped regions of few atoms thick (0.4-0.6 nm) and 8-10 nm in diameter. If the alloy is heated to around 100 ˚C or higher, GPZ II (θ'') replace GPZ I (Shercliff *et al.* 2005). These are also coherent plate-like precipitates, which are 1-4 nm thick and 10-100 nm in diameter. On further heating, θ' forms, which are semi-coherent plate-like precipitates also parallel to 10-150 nm thick. If heating continues, the incoherent micron-sized equilibrium phase θ (Al$_2$Cu) forms. The material attains its strength through the interaction of the precipitates to dislocations (cutting or Orowan bowing) (Eskin *et al.* 2005; Wang *et al.* 2005).

1.3 ALUMINIUM ALLOYS CHOSEN FOR THIS INVESTIGATION

Lightweight military vehicles such as personnel carriers and combat vehicles are being increasingly used to improve mobility and deployability of armed forces (Jonathan and Montgomery 2004). High performance aluminum (Al) alloys are typically used in fabricating these vehicles to provide both structural strength and energy absorbing capacity against projectile and fragment impacts as well as blast loadings. AA 2519 is a new grade of Al-Cu alloy, which was developed mainly for armour applications (Fisher *et al.* 2002). It has excellent tensile and fracture

toughness properties. It has a unique combination of properties such as high strength to weight ratio and good ballistic properties. In the fabrication of light combat vehicles like Expeditionary Fighting Vehicle (EFV) (Fig. 1.3), Armor Personnel Carriers (APC) and Mechanized Infantry Combat Vehicles (MICV), this reduced weight leads to a desirable increase in efficiency. It has been found out that the new alloy had a better ballistic performance as compared to previous aluminum armor alloys; AA5083, AA7039 and AA2219. This superior ballistic performance of 2519 alloy is generally attributed to the formation of fine and uniform dispersion of θ' precipitates (Thomas and Wolfe 1987).

Though AA2519-T87, has got an edge over its 6xxx and 7xxx series counterpart strength and toughness. It also suffers from poor as-welded joint strength. This is true both in autogenous welds as well as those welded with the matching filler. The loss of strength is due to the melting and quick resolidification, which renders all the strengthening precipitates to dissolve and the material is as good as a cast material with solute segregation and large columnar grains (Senthil *et al.* 2007). The gap between strength values of the base metal and weld metal is significantly large forcing the design engineers to use thicker base metal plates, which in turn increase the total weight of the structure. This fact is of concern in military and aerospace application because, use of thicker plates due to low yield strength of the weld metal result in lowering of the pay load. If the yield strength of the weld metal can be increased by some means it will be of advantage (Xin-ming *et al.* 2007).

Fig. 1.3 Expeditionary Fighting Vehicle (EFV) having 2519 structure (Cho and Bes 2006)

1.4 FUSION WELDABILITY ISSUES OF ALUMINIUM ALLOY

Aluminium is one of the material which is difficult to join by fusion welding methods. This is due to the low melting point and low hardness of the material. Conventional fusion welding methods such as metal inert gas (MIG) and plasma arc welding (PAW) often produce unfavourable cast microstructures in aluminium. Large distortions are caused by shrinkage in weld metal and heat affected zones. In addition extensive softening will occur in the HAZ, lowering the mechanical properties (Hou and Baeslack 1996).

Most aluminium alloys can be welded by electron beam welding (EBW) process, but cracking may be experienced with some of the heat-treatable alloys. The addition of filler metal may prevent weld-cracking. Wire feeders have been developed for use in EBW chambers. Aluminium alloys can be welded with either low or high voltage EBW equipment. The important advantages of welding aluminium by EBW process include welding of thick plate with narrow bead width, narrow HAZ and high speed for welding thin sheets. Vaporization and loss of low boiling point alloying elements are some of the problems encountered in the EBW (Koteswara *et al.* 2005).

Laser welding has been widely used in the automotive, aerospace and heavy manufacturing industries to join a variety of materials including aluminium alloys. Porosity, loss of alloying elements and for some heat-treatable aluminium alloys, solidification cracking are the most common problems encountered in the laser welding of these alloys. Nd: YAG laser is, therefore, more attractive for the welding of aluminium alloys. The high reflectivity of the aluminium material limits the usage of laser beam welding (LBW) process (Paston *et al.* 1998).

Fusion welding of Al-alloys requires high heat input due to their good thermal conductivity, as well as shielding gas (as in metal inert gas or MIG welding) due to the high affinity of aluminium for oxygen (Ericsson and Sandstrom 2003). Regardless of the alloy type (e.g. heat treatable or non-heat treatable), or the starting temper (aged, work hardened, annealed), the chosen welding technique should have a relatively localized thermal field since temperatures as low as 150-250 °C can result in a heat-affected zone (HAZ) which can weaken the joint. Temperatures close to

550 °C and higher can cause various defects, such as: mechanical distortion, solidification cracks, and liquation cracking. Even if all these precautions are considered, the joint surface has to be meticulously cleaned mechanically or chemically to remove any hydrocarbon compounds (e.g. lubricants) since they can lead to the formation of porosity (Mitra 2001) The formation of oxide layer over the surface limits the usage of fusion welding processes. The high difference in melting point of the oxide layer and aluminium material creates problems in the weld region.

1.5 FRICTION STIR WELDING (FSW)

It is a solid-state joining technology which has been used to successfully weld aluminium and its alloys. FSW is performed with a non-consumable rotating tool consisting of a smaller diameter pin and larger diameter shoulder. The forces generated during FSW are significant; and a proper fixture design is critical to the success of the weld. The working principle of FSW process is schematically represented in the Fig. 1.4. The tool contacts and penetrates into the abutting edges of the sheets being joined and traverses along the faying interface of the joint. While the tool rotates, it generates a large amount of frictional heat on the work piece. This heat softens the material surrounding the pin and facilitates movement of material flow around the pin to displace material from the front of pin to the backside of the rotating pin. Since no melting occurs in this process, the process was patented as a solid-state joining technology.

The centre of the joint, the weld nugget, namely, stir zone (SZ), exhibits a size and morphology which depends on the size and geometry of the tool involved. In terms

10

of the weld nugget microstructure, it is grouped into three features of the adjacent space, consisting of the stir zone, thermo-mechanically affected zone (TMAZ), and heat affected zone (HAZ) (Piyush and Antony 2015).
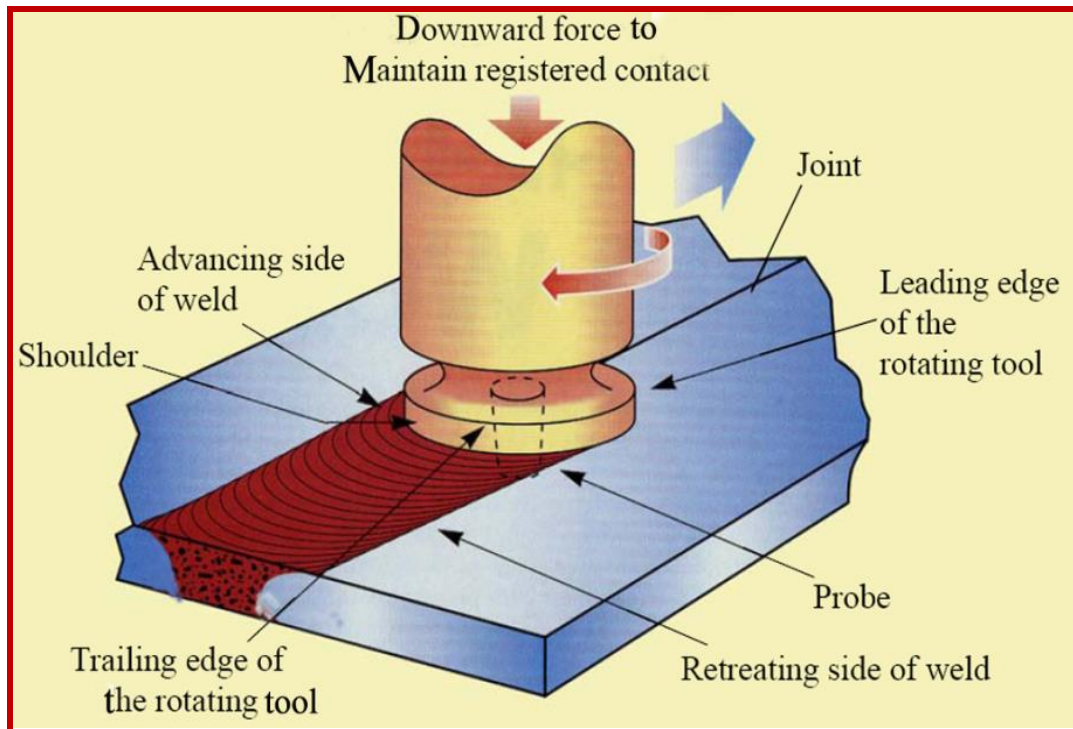
Fig. 1.4 FSW working principle

At present, the FSW process is found to be more efficient to join aluminium alloys. However the thermal cycles deteriorate the properties of age-hardenable aluminium alloys. So it is necessary to further reduce the temperature prevailed in the joints. Underwater friction stir welding (UWFSW) is a variant of FSW process which utilizes water to dissipate the heat. Fig. 1.5 shows the schematic demonstration of the UWFSW process. The workpiece was fixtured on the backing plate in the tank. The water is flowed into the tank through the inlet so that the tool shoulder should be fully in immersed condition. During welding, the inlet and outlet valves are adjusted

to control the flow to maintain the temperature of water below 60 ˚C near to the welding location.
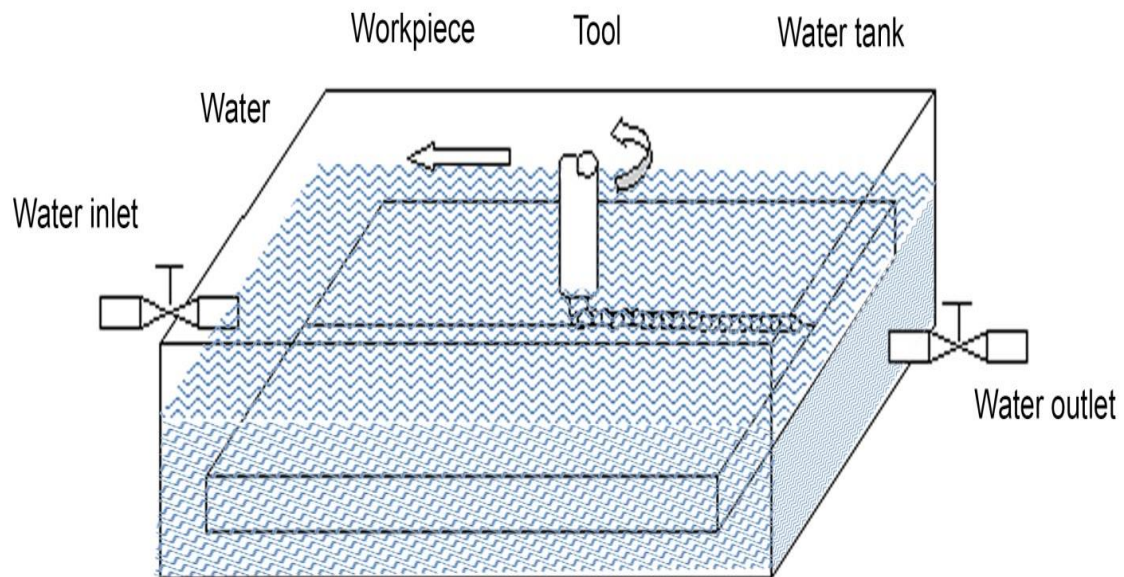
Fig. 1.5 Schematic representation of underwater friction stir welding

Figure 1.6a, 1.6b shows the photographs of conventional air cooled FSW process and water cooled FSW joints respectively (Huijie and Huijie 2012). In accordance with the current trend, the present investigation is carried out to derive the benefits of FSW process and UWFSW process for joining age hardenable AA2159-T87 aluminium alloy, which is not so easy, by fusion welding processes.
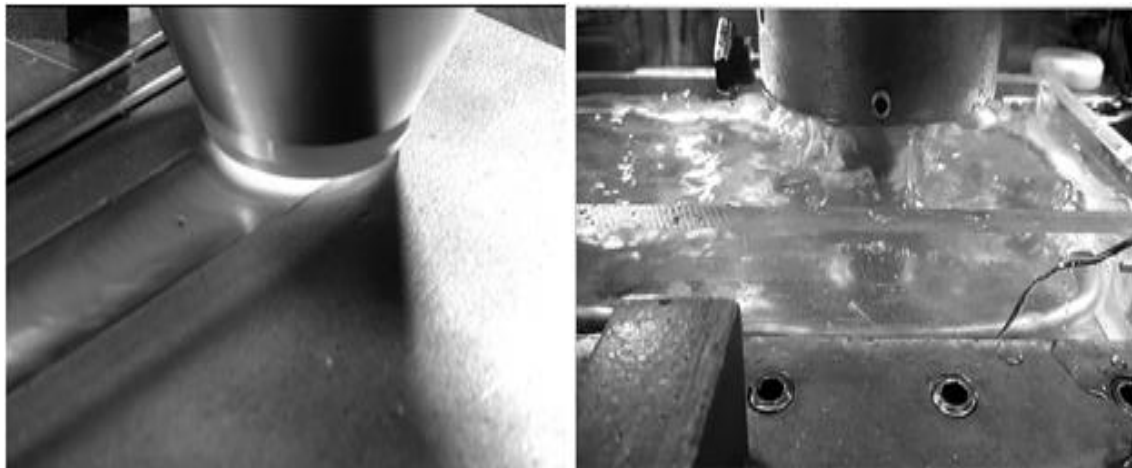
a. **Air cooled FSW process**   b. **Water cooled FSW process**

Fig. 1.6 Photographs of variants of FSW process

1.6 OUTLINE OF THE THESIS

Chapter 1 briefly explains the introduction about the aluminium alloys, weldability of Al alloys, working principle of FSW process. Chapter 2 presents the critical review of the literature focused on the effect of process parameters on the microstructural characteristic, tensile properties and hardness of FSW and UWFSW joints. The motivation to carry out this research work, scope and objectives of this investigation are also presented in Chapter 2. Chapter 3 describes the experimental procedures used in this research. This includes details about the tool designs, cooling medium and process parameters. The effect of tool pin profiles on tensile properties and microstructural characteristics of FSW and UWFSW joints are discussed in Chapter 4. Similarly the effect of process parameters namely tool rotational speed, tool traverse speed and tool tilt angle on tensile properties and microstructural characteristics of FSW and UWFSW joints are presented in the Chapter 5, Chapter 6 and Chapter 7 respectively. Chapter 8 provides the thermal analysis of FSW and

13

UWFSW processes. The effect of post weld heat treatment on mechanical and metallurgical properties of FSW and UWFSW joints are discussed in Chapter 9. The last chapter (Chapter 10) summarizes the work that has been done and the important conclusions derived from this work.

CHAPTER 2
LITERATURE REVIEW

2.1 EFFECT OF TOOL PIN PROFILE

2.1.1 Tensile properties

The influence of tool pin profile on the metallurgical and mechanical properties of friction stir welded metal matrix composite was investigated by Vijay and Murugan (2004). From the results (table 2.1) it is understood that the joint welded by square pin profiled tool exhibits high tensile strength when compared to the other joints. The joint fabricated by tapered square pin profiled tool has the least tensile strength. The tensile strength of the joints, welded using hexagon, tapered hexagon, octagon and tapered octagon pin profiled tools, do not change significantly. It is due to the difference in the dynamic orbit created by the eccentricity of the rotating tool of the FSW process.

Table 2.1 Mechanical properties of FSW joints for different pin profiles (Vijay and Murugan, 2004)

Types of tool Profile	Average tensile strength (MPa)	Average (%) Elongation	Joint efficiency (%)
Tapered square	223.33	5.32	78.92
Tapered hexagon	247.89	6.67	87.59
Tapered octagon	245.27	6.22	86.67
Square	281.51	6.37	99.47
Hexagon	262.29	5.83	92.68
Octagon	240.00	3.39	84.81

Palanivel *et al.* (2012) studied the effect of pin profile on joint properties of friction stir welded aluminum alloys. Pin profile considerably influenced the microstructure and tensile strength of the joints. The variation in tensile strength of the joints was attributed to material flow behavior, loss of cold work in the HAZ, dissolution and over aging of precipitates and formation of macroscopic defects in the weld zone.

2.1.2 Microhardness

Elangovan *et al.* (2008) studied the effect of tool pin profiles on mechanical properties of friction stir welded AA6061 aluminium alloy. Five different tool pin profiles namely, straight cylindrical, tapered cylindrical, threaded cylindrical, triangular, and square had chosen for the investigation. Of the five joints, the highest hardness value of 87 HV was recorded in the joint fabricated using square pin profiled tool and the lowest hardness value of 60 HV was recorded in the joint fabricated using straight cylindrical pin profiled tool (Fig. 2.1). This was attributed because, pins with flat faces like square pin produced the pulsating stirring action and caused reduction in grain size and homogenous redistribution of the second phase particles throughout the matrix.

In another study, Elangovan *et al.* (2007) studied the effect of pin profiles along with the effect of tool rotation speed. Of the five joints, the highest hardness value of 105 HV has been recorded in the joint fabricated using square pin profiled tool and the lowest hardness value of 85 HV has been recorded in the joint fabricated using straight cylindrical pin profiled tool. This is because, the higher number of pulsating action experienced in the stir zone of square pin profiled tool produces finer grained

microstructure with uniformly distributed precipitates (CuAl$_2$) and in turn yields higher strength and hardness.
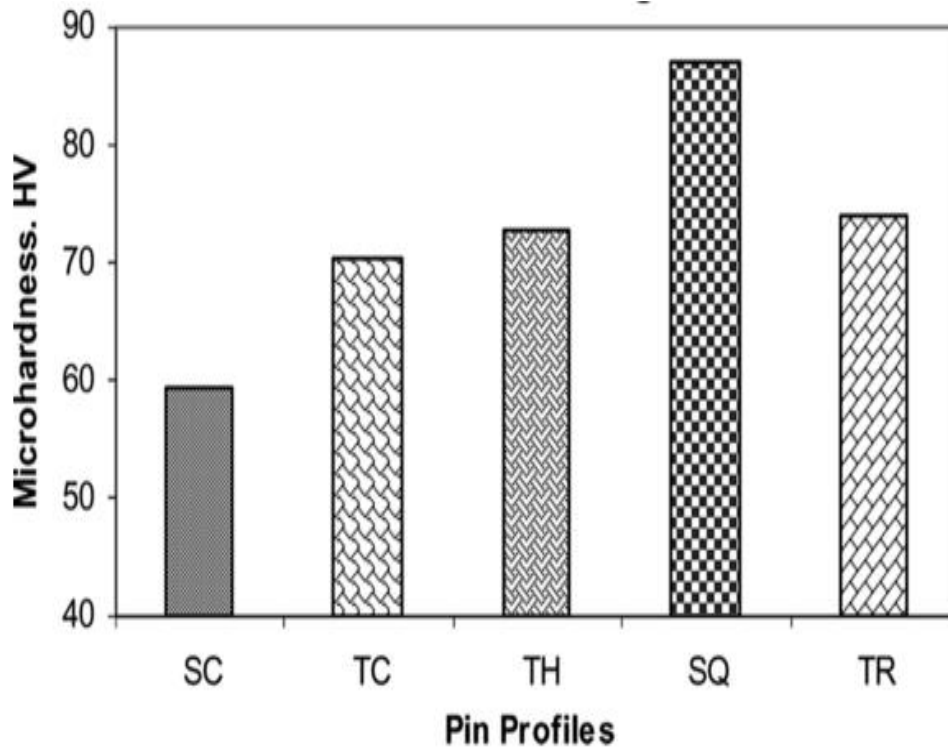
Fig. 2.1 Effect of tool pin profiles on stir zone hardness (Elangovan *et al.*, 2008)

2.1.3 Microstructure

The role of an FSW tool on material flow and weld formation was conducted by Kumar *et al.* (2008) in similar material joining of 7020 aluminium alloy. An attempt was made to understand the mechanism of material flow in friction stir welded plates. Their results showed that there are two different modes of material flow regimes involved in the friction stir weld formation, namely, pin driven flow and the shoulder driven flow, caused by the rotation of the pin and shoulder respectively. They concluded that it is important that the design of the pin be such that the

maximum amount of transferred material is retained in the weld cavity, and the shoulder-driven material flow can be described as the effectiveness of the shoulder in keeping the material in the weld cavity.

In FSW process, the role of the tool pin was to shear the material to its back during the translation of the tool and the inserted rotating pin brings the material towards both sides of the joint line to the plastic state, aided by the frictional heat input of the shoulder (Judy *et al.* 2016). Welds made with straight cylindrical pin tool typically show voids on the advancing side. There seems to be no vertical motion of the material, which was apparently necessary to stabilize the rotational zone and to provide sufficient deformation of the material to obtain a sound weld (Ravindra *et al.* 2014). In FSW process, the material that was stirred originates from the upper portion of the path of the welding tool pin. The stirred material was forced down in the weld by the threads on the pin and was deposited in the weld nugget. The other material in the weld zone simply extrudes around the retreating side of the welding tool pin, rising in the weld as it goes around the pin (Colligan 1999).

2.2 EFFECT OF TOOL ROTATIONAL SPEED

2.2.1 Tensile properties

Yong *et al.* (2004) investigated the tensile strength of the friction stir processed 1050 aluminum alloy. They observed that the hardness and tensile strength increased significantly with decreased tool rotation speed as shown in Fig. 2.2. The results showed that at 560 rpm, the hardness tensile strength increased as a result of grain refinement by up to 37 % and 46 % respectively compared to the as-received

material. The hardness was higher on the advancing side than that of the retreating side. The study concluded that the results demonstrate that the friction stir processing technique is highly effective for creating improved mechanical properties resulting from grain refinement.
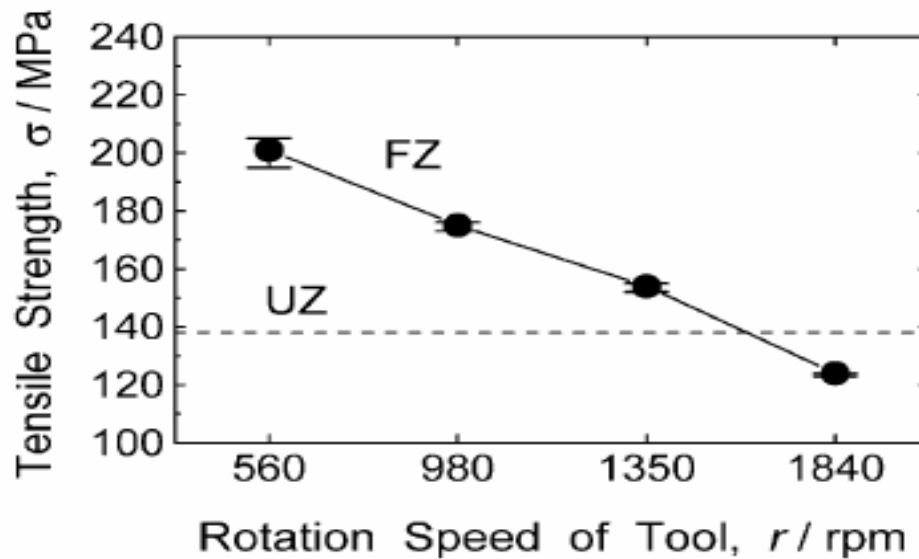
Fig. 2.2 Tensile strength for unprocessed zone and friction stir zone at different tool rotational speed (Yong *et al*., 2004)

2.2.2 Microhardness

Won *et al.* (2004) investigated the FSW joints of AA6061 aluminium alloy and they observed that the hardness of the stir zone increased with the tool rotation speed. A higher tool rotation speed resulted in lower cooling rate because stir zone reached a higher temperature. At low heat input, finer grain size leads to high strength and hardness. The rubbing of the tool shoulder on the work piece develops frictional heat. As the tool rotational speed increases the frictional heat also increases due to the increased residing time of tool.

The hardness of the friction stir welded AA5083 stir zone decreased with increasing rotation speed. The average grain size of the stir zones of the welded joints with a speed of 250, 320, 800 rpm was about 0.23, 0.35 and 1.28 µm, respectively, i.e., the grain size increased with the rotation speed. The increase in grain size led to the lower hardness value of the stir zone which was produced at the higher rotation speed (Yutaka *et al.* 2003).

Zhang *et al.* (2011) studied the microstructure and mechanical properties as a function of rotation speed in underwater friction stir welded aluminum alloy joints. A softening region having lower hardness than the parent metal (PM) (120-130 HV) is produced in all the joints welded at different rotation speeds, which is a typical characteristic for the FSW of heat treatable aluminum alloys. The width of the softening region increases with the increase of rotation speed. When the rotation speed is low (e.g. 600 rpm), the strain hardening of the low-density dislocations is insufficient to recover the strength loss induced by precipitate deterioration, and thus the lowest hardness is in the SZ. In the case of high rotation speeds, the hardness of the SZ is improved due to the increase in dislocation density, and then the lowest hardness location is shifted to the TMAZ or the HAZ. Although increasing the rotation speed widens the softening region of the underwater joints, the maximum detrimental effect of thermal cycles on joint properties is weakened from 600 to 800 rpm and reaches a plateau in the rotation speed range of 800-1200 rpm. The occurrence of the plateau is attributed to that the severe heat absorption capacity of water can effectively control the temperature level of the weakest location of the joints. Nevertheless, if the rotation speed increases up to a rather high value (e.g.

1400 rpm), the heat input plays the dominant role and lowers the hardness minimum markedly.

In friction stir welded AA 7010 aluminium alloy, when the spindle speed was increased, the hardness levels at the base of the weld increased more rapidly than at the top, so that the hardness values converge at high spindle speeds. This behaviour corresponds to the development of a more uniform temperature distribution within the nugget zone, as the heat input was increased (Hassan *et al.* 2002).

2.2.3 Microstructure

Tool rotation speed appears to be the most significant process variable as it tends to influence the translational velocity (Yutaka *et al.* 2002). Higher tool rotation speed resulted in a higher temperature and slower cooling rate in the (friction stir processing) FSP zone after welding. A higher tool rotation speed makes excessive release of stirred materials to the upper surface, which resultantly left voids in the FSP zone. But lower heat input condition caused by lower tool rotation speed resulted in lack of stirring. The area of the FSP zone decreased with the decrease in the tool rotation speed and influenced the temperature distribution in the FSP zone (Hassan *et al.* 2003).

Microstructure and mechanical properties as a function of rotation speed in underwater friction stir welded aluminum alloy joints were studied by Zhang *et al.* (2011). Fig. 2.3 shows the cross-sections of the underwater joints. In the figure (and throughout the paper), retreating and advancing sides of the joint are abbreviated as

21

RS and AS, respectively. Three microstructural zones, i.e. SZ, TMAZ and HAZ are identified in the joints, as denoted in Fig. 2.3c. With increasing rotation speed, the SZ presents a size increase in the lower part, implying the strengthening of tool pin effect on material plastic flow near the bottom surface. At the rotation speed of 600 rpm, the TMAZ is not evident from the cross-section owing to the small size. Above 600 rpm, the TMAZ becomes discernible and its size increases progressively with the rotation speed. No welding defects are detected in the joints under the rotation speed range of 600–1200 rpm. However, at the high rotation speed of 1400 rpm, a large amount of fine voids are formed in the SZ. The exact location of the void defect is marked by an arrow in Fig. 2.3e.

a. 600 rpm

b. 800 rpm

c. 1000 rpm

d. 1200 rpm

e. 1400 rpm
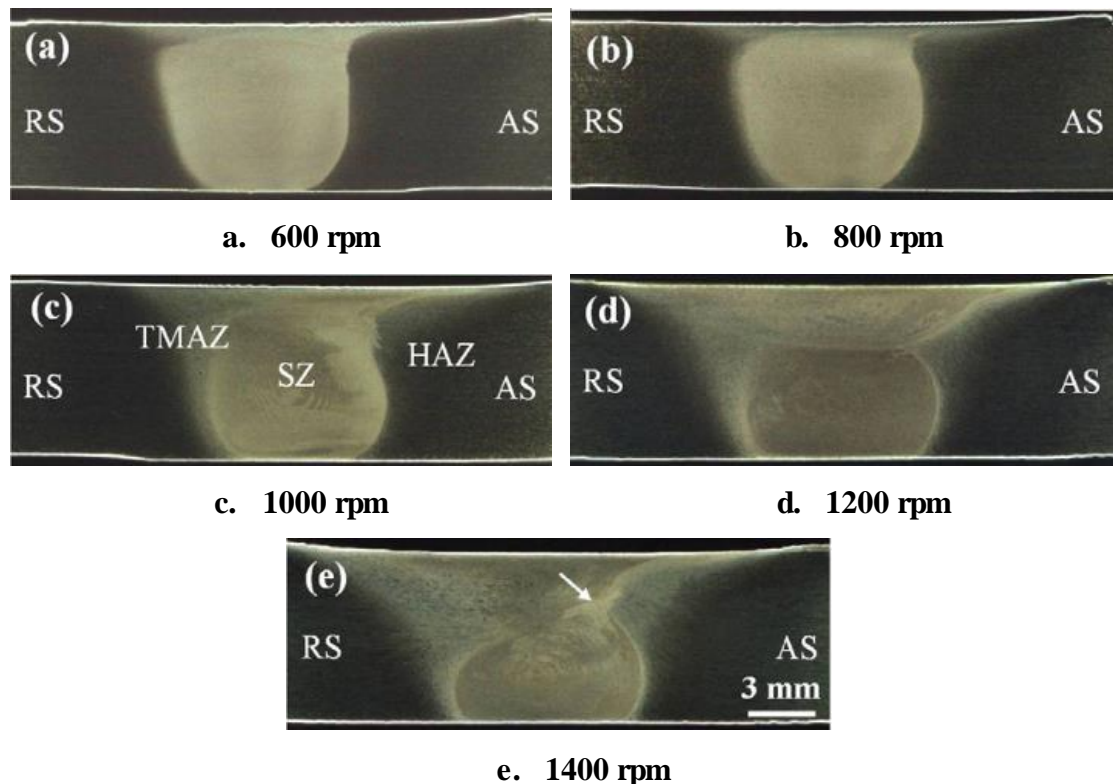
Fig. 2.3 Cross-sections of the joints welded at different rotation speeds

(Zhang *et al.*, 2011)

At the cross sectional level, it is obvious that all the weld nugget was formed by the mixing of deformed materials from both side of the plates. This is due to the abrasion, wear and shearing of dissimilar material by tool rotating action (Dehghani *et al.* 2013)**.** Thus, the tool rotational speed has greater effect on good surface morphology and material flow behaviour.

It is well established that the dynamic recrystallization during the FSW process results in the generation of fine and equi-axed grains in the nugget zone. It is reported that the grain size decreases from the parent material towards the nugget zone. FSW process parameters, tool design, forge force and active cooling, all exert significant influences on the size of the recrystallized grains in the FS welded material (Rajakumar *et al.* 2011). Sato *et al.* (2016) studied the effect of tool rotational speed on microstructure in FSW process, and reported that recrystallized grain size can be reduced by decreasing the tool rotation rate, as well as the overall heat input.

The variation in appearance and volume fraction of the second phase particles of AA7010 alloy with respect to tool rotational speed was investigated by Hassan *et al* (2002). As the rotational speed is increased, the temperature within the nugget became higher and more uniform, and there by the volume fraction of coarse second phase particles decreased at different positions within the nugget zone region. However, at very high spindle speeds the distribution of finer precipitates within the grains became significant and the overall volume fractions began to increase once again.

2.3 EFFECT OF TOOL TRAVEL SPEED

2.3.1 Tensile properties

Moataz *et al.* (2005) have reported that the tool travel speed has greater force on the grain growth of the friction stir welded AA 2095 aluminum alloy. It was also reported that the variation in both the strength and ductility was a part of the tool travel speed. Lakshminarayanan *et al.* (2008) evaluated the percentage of the contribution from the different FSW process parameters. The survey concluded that the tool travel speed contribution was 33 % towards the tensile force of the FSW joints.

The effect of welding speed on microstructure and mechanical properties of friction stir welded copper was investigated by Shen *et al.* (2010). FSW was conducted at a constant rotation rate of 600 rpm together with different welding speeds of 25, 50, 100, 150 and 200 mm/min. Fig. 2.4 shows the tensile properties of the joints welded at various welding speeds. It can be observed that the ultimate tensile strength (UTS) and elongation have a similar variation trends. Both increase at first and decrease finally with increasing welding speed. It is noted that the UTS and elongation of joints obtained at the welding speed range of 25−150 mm/min have little change, and their highest values are corresponding to the welding speeds of 50 mm/min and 100 mm/min, respectively
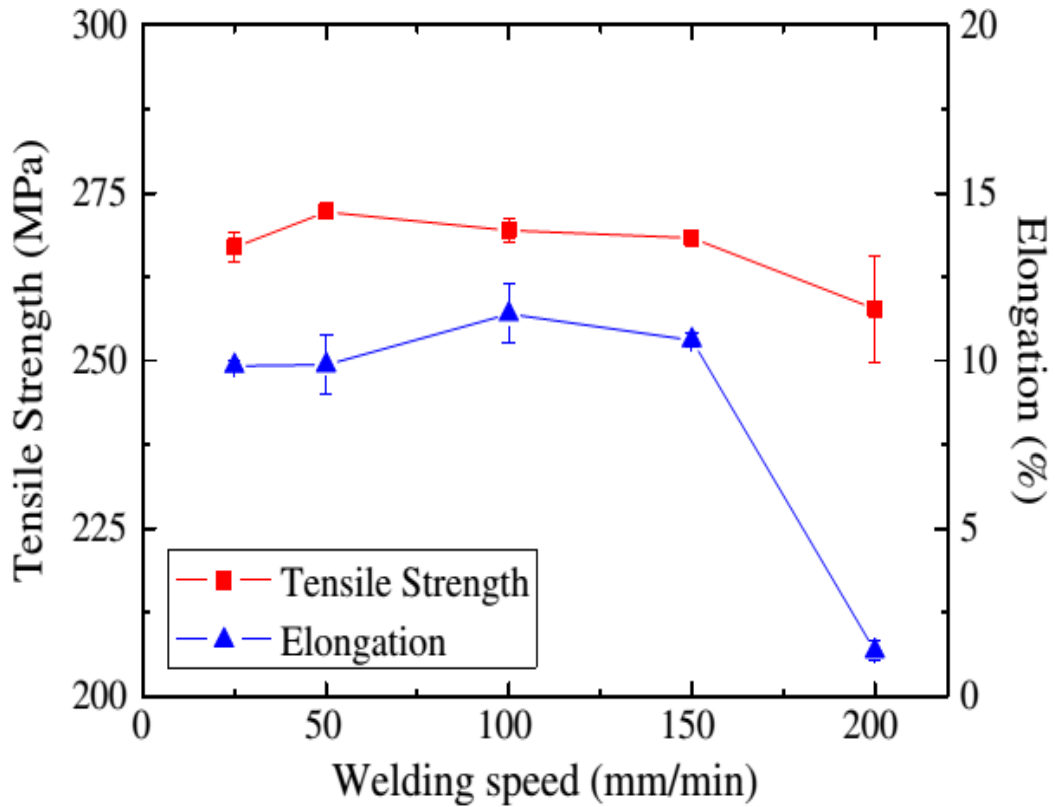
Fig. 2.4 Effect of welding speed on tensile properties (Shen *et al.*, 2010)

Sarvghad *et al.* (2011) determined the effect of high feed speed on the microstructure and mechanical properties of Cu–30Zn alloy. Therefore, it can also be concluded that the mechanical properties are definitely affected by the formation and morphology of the stir bands.

2.3.2 Microhardness

Al-Badrawy and Abo El-Nasr (2010) carried out experiments to understand the effect of tool rotational speed on FSWed Al 7075-T6 joints on hardness characteristics. The hardness profile indicates a decrease in the hardness compared to that of the base alloy. This behavior has been attributed to the dissolution of precipitates into solution and subsequently the weld cooling rates do not favor nucleation and growth of all the

precipitates. The main reason for this behavior may be attributed to grain refinement in the weld zone. The material that flows around the tool undergoes intense plastic deformation at elevated temperatures, normally leading to a very fine grain structure in the center of the weld region in addition to redistribution of the precipitates to creation in inhomogeneity on the microscopic scale.

a. **Air cooling**   b. **Water cooling**
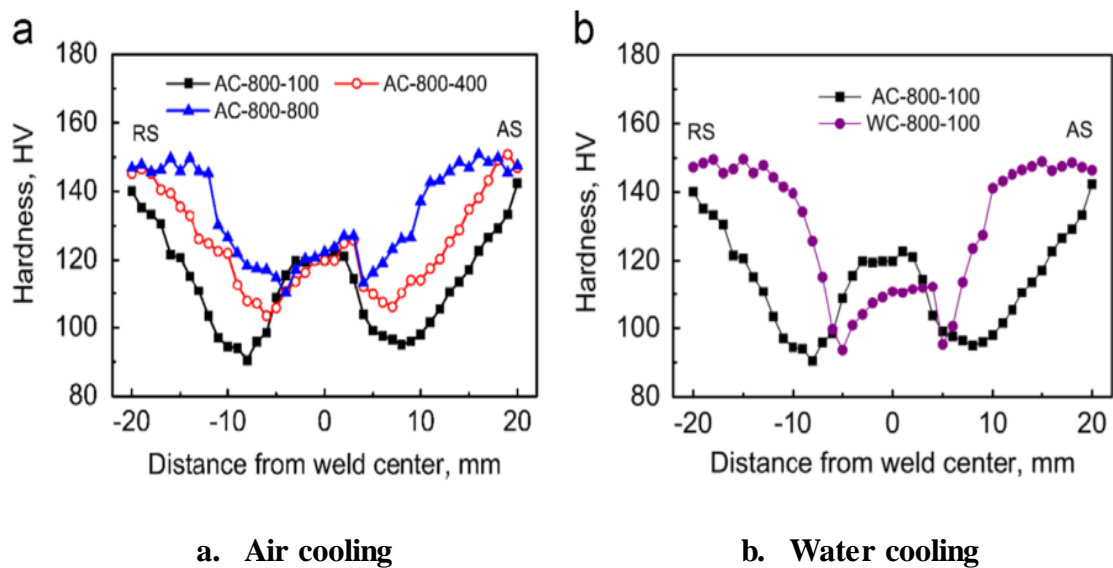
Fig. 2.5 Microhardness profiles of FSW 2014Al-T6 joints (Zhang *et al.*, 2014)

The effects of the welding speed and water cooling on the hardness profiles of the FSW 2014Al-T6 joints under air cooling and water cooling was studied by Zhang *et al.* (2014). All the hardness profiles exhibited a "W" shape with a low hardness distribution region (LHDR) on both AS and RS of the FSW joints and the hardness of the SZ was lower than that of the PM (Fig 2.5). At a constant rotational rate of 800 rpm, increasing the tool travel speed from 100 to 800 mm/min enhanced the hardness values of the LHDR and moved their position towards the weld center (Fig. 2.5a). The water cooling exerted no noticeable influence on the hardness values of the

LHDR but moved the position of the LHDR towards the weld center (Fig. 2.5b). Furthermore, the water cooling reduced the hardness of the SZ.

2.3.3 Microstructure

Few researchers revealed that wormholes are formed in welds, as a result of insufficient material flow towards the bottom of the weld, and also because of inadequate heat under the tool shoulder. According to Crawford et al. 2006, at a constant tool rotational speed, an increase in the tool travel speed leads to wormhole initiation near the bottom of the weld, and a high weld pitch ratio. This is the ratio of the traverse speed to the rotational speed; is also known to cause wormholes in welds.

Friction stir welded AA2095 at higher welding rates resulted in shorter exposure times at higher temperatures. Welding at the higher rates resulted in a structure with a higher dislocation density because of the limited time available for recovery process. The faster the welding rate the higher was the dislocation density generated which resulted in an angled dislocation structure, indicating an early stage of dynamic recovery (Hanadi *et al.* 2002)**.**

Yutaka *et al.* (2004) investigated the effect of tool traverse speed on microstructure and they inferred that the base material had an elongated coarse grain structure, while the stir zones consisted of equiaxed grain structures. Grain size in the stir zone increased with an increase in the heat input during FSW. Welds with lower welding

speeds proved that the grains contained many sub boundaries. The sub grain size increased with the increasing heat input during FSW. It is inferred that the greater heat input resulted in larger grains with a lower density of dislocations and sub-boundaries in the stir zone.

2.4 EFFECT OF TOOL TILT ANGLE

2.4.1 Tensile properties

Muhayat *et al.* (2014) studied the effect of tool tilt angle on mechanical properties of friction stir welded AA 5083 Joints. Transverse tensile strength of the FSW joints has been evaluated. From the study, it can be inferred that the tool tilt angle influenced on tensile properties of the FSW joint. The joint fabricated at the tool tilt angle of 1° has shown the lowest tensile strength of 233.5 MPa. The increase of the tool tilt angle lead to the increase of the tensile strength, and it reached a maximum value of 306 MPa at tool tilt angle of 4°. The tunnel defect occurred when the joint was produced at tool tilt angle of 1°, 2° and 3°. These tunnel defect generally occurred in advancing side of the weld nugget, thus seriously degrading the tensile properties of the joint and causing the joint fractures at the advancing side of weld nugget. On the other hand, when the joint produced at tool tilt angle of 4°, it was defect free joint, the tensile properties of the joint only depended on the hardness distribution.

Kumar *et al.* (2008) reported that the tensile strength increases with increase the tool tilt angle. It is due to surface contact between tool shoulder and work-pieces. At lower tool tilt angle, large surface contact between tool and workpiece causes excess

heat generated. Excessive heat in weld region results, pulling the plasticized material apart from welds line and produce defective joints. At higher tool tilt angle, the flow of plasticized material is sufficient due to good forging action. Good forging action leads to less porosity, fine and homogeneous grains. So, high tensile strength was achieved.

2.4.2 Microhardness

Increase in tool tilt angle can nominally raise the material forging force and undertake the material in a bit more severe plastic deformation, leading to more breaking down of the grains and finer grain structure and higher hardness. Although increase in the tool tilt angle first boosts the material forging force, by further increase, the plowing force of the tool pin outweighs and results in some defects and weakens the weld material (Parviz *et al.* 2015).

Kush and Vishvesh (2016) studied the effects of tilt angle on properties of dissimilar friction stir welding copper to aluminum. In this study, the tool tilt angle was varied from 0° to 4° with an interval of 1° while the other parameters such as rotational speed, welding speed, tool pin offset, and workpiece material position were kept constant. Results of macro hardness variations for different tilt angles are shown in Fig. 2.6. It was noted that the macro-hardness value in the nugget area was increasing as tilt angle increases from 0° to 4°. Maximum macro-hardness 186 HV was observed in the stir zone at tilt angle 4° while minimum macro-hardness 58 HV was observed in the stir zone at tilt angle 0°. Drastic increase in macro hardness at stir zone was noticed for all the samples as shown in Fig. 2.6. The increase in the macro-

hardness values in these regions can be attributed to dynamic recrystallization which has occurred during the welding process.
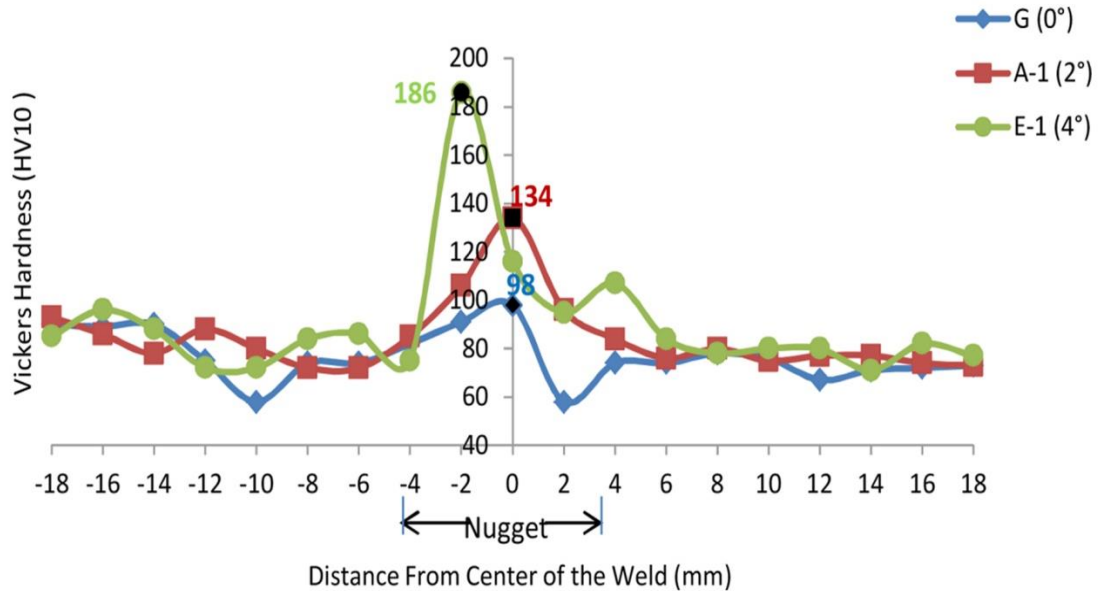
Fig. 2.6 Microhardness plot for varying tool tilt angles (Kush and Vishvesh, 2016)

Yucel *et al.* (2013) studied the effect of welding parameters on the microstructure and strength of friction stir weld joints in twin roll cast Al-Mn1Cu plates. The plates were butt welded with the friction stir welding process which employed a non-consumable tool, tilted by 1.5° and 3° with respect to the plate normal. The decrease in tilt angle improves the interaction of the tool with the butting plates and increases heat generation. Decreasing the tool tilt angle (TTA) to 1.5° also produced a favorable impact, yielding a UTS value of 137 ± 0.7 MPa, comparable to the UTS of the base plate, 145 MPa. This marked improvement in UTS is attributed to the increase in the heat input owing to an increased frictional heat generation. There

30

appears to be a perfect correlation between the UTS and the size of the weld zone. The increase in the latter is reflected by an improvement in the UTS.

2.4.3 Microstructure

In FSW, adequate axial force should exceed the flow stress of material to make defect-free joints. Axial force drives the plasticized material in the stir zone to complete the extrusion process. Axial force plays important role in deciding the plunge depth of the pin (Kumar and Kailash 2008).

At low axial force, tunnel defect was observed in the middle of the weld cross section in the retreating side because the insufficient downward force caused no vertical flow of the material. When the axial force was increased further, a large volume of flash and excessive thinning was observed due to higher heat input (Mohamadreza *et al.* 2011).

The heat generation in FSW was in direct proportion to the deformation and frictional energy generated in the welding. The latter depends on the friction coefficient and friction area between the tool shoulder and the workpiece surface as well as on the rotation speed of the welding head pin and the pressure applied to the welding head shoulder (Buffa *et al.* 2009).

The influence of the axial force on the formation of FSP zone in AA6061 aluminium alloy showed that the joint fabricated with 7 kN yielded higher tensile strength and

hardness due to fine equiaxed grains with uniform distribution of the fine strengthening precipitates throughout the matrix (Elangovan *et al.* 2008)
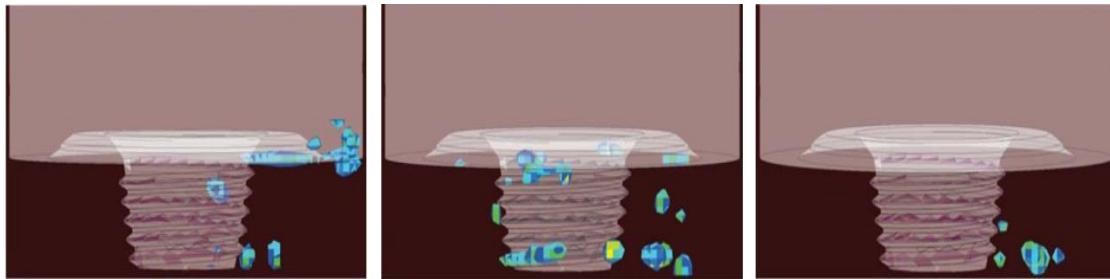
a. **Tool tilt angle - 2°**   b. **Tool tilt angle – 2.5°**   c. **Tool tilt angle - 3°**

Fig. 2.7 Spatial distribution of the marker-material (Grujicic *et al*., 2012)

Grujicic *et al*. (2012) analyze the effect of the tool tilt angle on the material flow (Fig. 2.7). Examination of the results displayed in these figures reveals that the highest extent of marker-material mixing/dispersion is attained in the baseline case and that this extent decreases with a deviation in the tilt-angle from its baseline value. In other words, a tilt-angle around the baseline value of 2.5° appears to be optimal (Fig. 2.7b). This finding is in accordance with the experimental observations in the FSW welding practice. The existence of an optimum tilt-angle is generally described as a trade-off between the maximization of the forging pressure (favors a large tilt-angle) and minimization of the workpiece weld ''ploughing'' (favors a smaller tilt-angle). The present results show that maximization of workpiece-material stirring/ mixing also favors an optimal value of the tilt-angle.

The gap between the tool and the work piece made from the tilt of the tool expands by increasing the tilt angle. Therefore, by increasing the tilt angle, the plasticized material escapes easily from the bottom of the tool shoulder. Consequently, a

discontinuity occurs in the weld, which leads to the formation of some voids at the surface. Increasing the tilt angle facilitates removal of the material away from the bottom of the tool. On the other hand, with decreasing tilt angle, forging of the material will not take place, thus the weld will not develop. Therefore, there is an optimum value of tilt angle in FSW (Reshad *et al.* 2010).

An attempt has been made by Gopala *et al.* (2014) to study the influence of tool tilt angle on Aluminium 2014-T6 welds. The tool tilt angles were varied from 0˚ to 3˚ degrees at an interval of 0.5˚. It was observed that the defect size reduces gradually from the lower tool tilt angle to higher tool tilt angle and vanishes at 3˚ tool tilt angle (Fig. 2.8). Increase in tool tilt results in sharp increase in Z-torque, X-load and Z-load with slight increase in temperature. High torque, load and temperature indicate that the material is heated up to a wider extent and stirred adequately to fill the cavities left unfilled at low tool tilt angle. Increase of tool tilt angle also results in increase of forging action on the trailing edge of the weld thereby filling the cavities which otherwise remains at lower tool tilt angle.
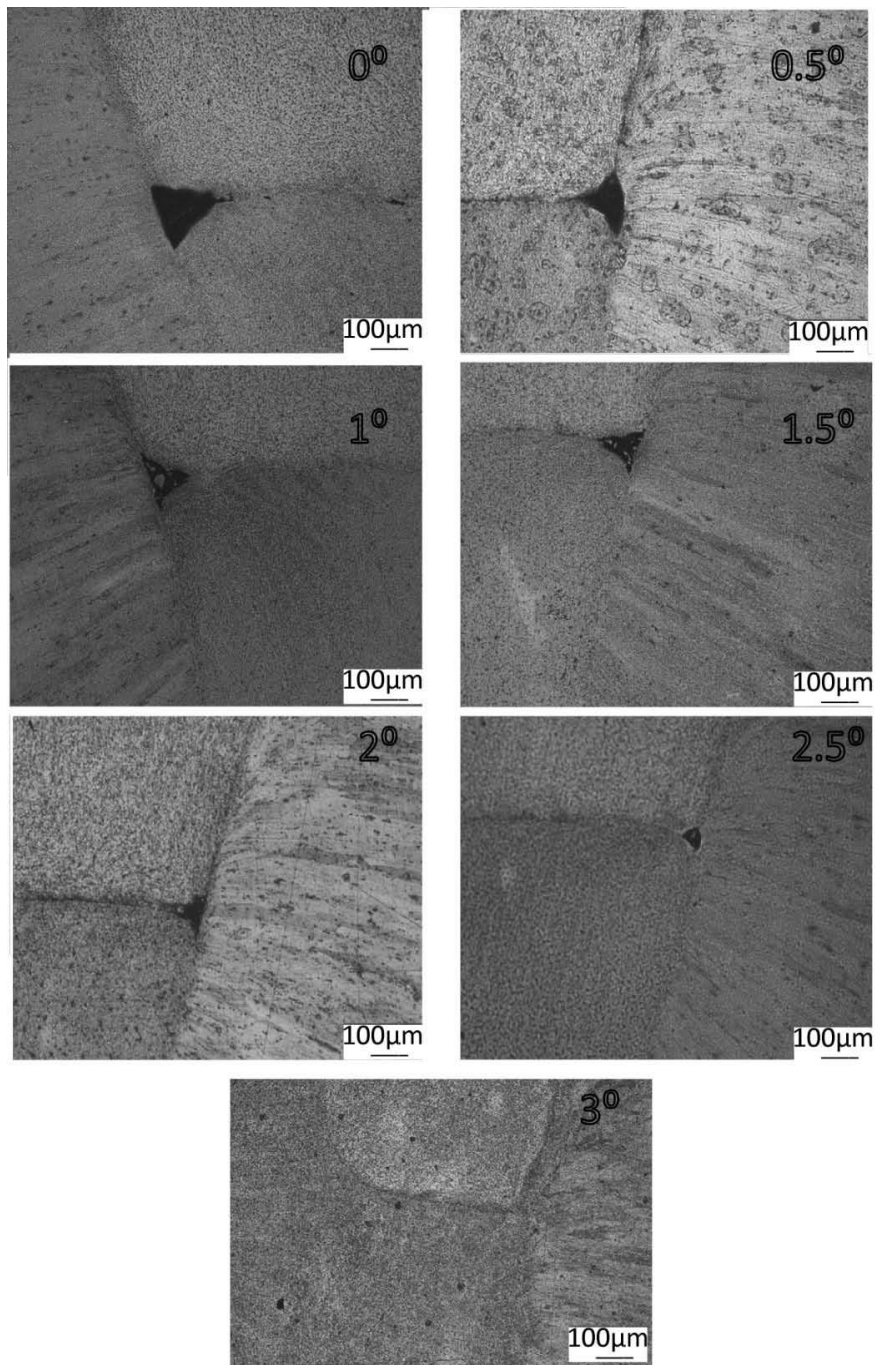
Fig. 2.8 Defect size at different tool tilt angle (Gopala *et al.*, 2014)

2.5 THERMAL ANALYSIS OF FSW AND UWFSW PROCESSES

The heat input into the weld in the FSW process is an important quantity, due to its influence on the resulting properties of the weld. Heat generation during FSW arises

from two sources: friction at the surface of the tool, and the deformation of the material around the tool. The heat generated is often assumed to occur predominantly under the shoulder, due to its greater surface, and to be equal to the power required to overcome the contact forces between the tool and the work piece (Colligan and Mishra 2008).

Average heat input in FSW has been proposed by many authors in the context of simple energy models (Cavaliere *et al*. 2009). Although, this is only an estimate of the heat input since there may be losses that depend on the input parameters. For example, the rate of heat loss through radiation or by conduction from the anvil and the tool, may change based on the weld parameters. Hence, the heat input (J/mm) from the shoulder of the tool in FSW is determined through the spindle torque measurements. These are constant, once the thermal equilibrium has been reached. This is given by (Lombard 2007)

$$Q= 2\pi\omega T\eta/f \qquad\qquad\qquad (2.1)$$

Where, Q is the heat input (J/mm), η is the efficiency factor, ω is the rotational speed (rpm), T is the torque (Nm), f is the feed rate (mm/min).

Study on governing parameters of thermal history during underwater friction stir welding was made by Hossein *et al*. (2015). The results reveal that upon comparison to FSW in air medium, both translational and axial forces considerably increase leading to greater heat generated by the underwater FSW tool. However, the peak temperature in each point during underwater welding declines dramatically (40 %) compared to the in-air welding, which can be attributed to the extreme boiling heat

transfer of water on both the workpiece and FSW tool. This behavior may be the main reason for the acquired mechanical properties of the underwater-welded AA7075-T6 plates as a precipitating hardening alloy. The mentioned heat transfer is non-uniform over the workpiece and comprises different types including nucleation and transition boiling as well as free convection. Furthermore, the study of the mechanical characteristics revealed that underwater welding leads to joints with more strength and lower ductility compared to those obtained by in-air welding.

Zhang *et al.* (2013) done the thermal modeling of underwater friction stir welding of high strength aluminum alloy. From the analysis it was found that notably, the temperature distributions at the leading and trailing edges of the tool are asymmetrical with respect to the tool axis for normal FSW (Fig. 2.9). The temperature at trailing edge is relatively high and exhibits low gradient. This should be attributed to the gradual accumulation of heat input behind the tool during the welding. In contrast, the isothermals of underwater FSW severely move towards the tool axis, and the moving extent at the trailing edge is larger than that at the leading edge. For this reason, the underwater FSW presents higher temperature gradient at both tool trailing and leading edges than the normal FSW; furthermore, the temperature distributions are more symmetrical with respect to the tool axis between the both edges.
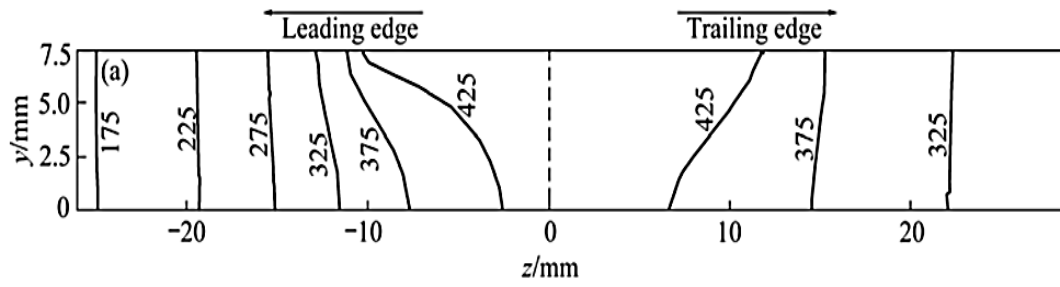
a. Normal joint
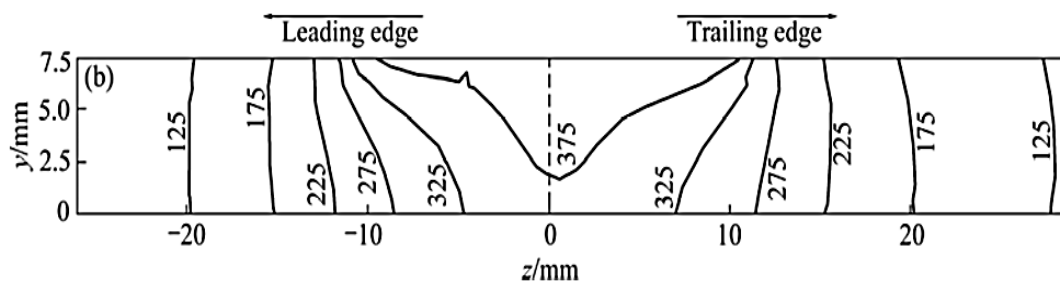
b. Underwater joint

Fig. 2.9 Temperature distributions on longitudinal section of joints

(Zhang _et al.,_ 2013)

2.6 EFFECT OF POST WELD HEAT TREATMENT (PWHT)

2.6.1 Tensile properties

Heat treatable aluminum alloys acquired their strength from hardening precipitates. After solution heat treating, the distribution of these precipitates is optimized through aging processes, i.e. controlled heating and cooling. The strengthening precipitates in heat treatable aluminium alloys are needle-like or plate-like phase structures that are finely and uniformly distributed. These precipitates hinder dislocation movement and the strength is improved. On disruption of precipitation distribution, lead to decrement in the strength (Adeosun _et al._ 2010).

37

Zhili *et al.* (2011) studied the effect of post-weld heat treatment on the plastic deformation behavior of friction stir welded 2024 - O aluminum alloy at annealing temperatures from 250 °C to 450 °C with an interval of 50 °C for 2 hours, followed by cooling to 200 °C in the furnace. The plastic deformation of as-welded joint is very heterogeneous. In contrast, the plastic deformation of PWHT joint is relatively homogeneous by both the nugget and the base material showing large deformation. The decrease in elongation of as-welded joints is completely recovered by PWHT. The high ductility of the joint is mainly attributed to the retention of the fine-equiaxed grains in the nugget during PWHT.

Bayazid *et al.* (2016) systematically investigated the effect of cyclic solution treatment on microstructure and mechanical properties of friction stir welded 7075 Al alloy. The results showed that precipitate particles of the welding area before and after heat treatment are $MgZn_2$ and $MgAlCu/A_{17}Cu_2Fe$, respectively. CST (cyclic solution treatment) improves tensile strength and elongation while homogenizes the hardness distribution of the FSWed joint. A noteworthy enhancement in the hardness (~ 45%) and tensile strength (~33%) of the FSWed sample is achieved after CST and aging at 130 ˚C for 24 h. The tensile fracture surface of the Al alloy joint demonstrates fine dimples after CST while less developed dimples are detected after aging.

Chaitanya *et al.* (2013) observed all the applied post weld heat treatments increased the size of aluminum grains in all zones of friction stir weld joints. Abnormal grain growth was observed in entire zone modified by friction stir welding in case of

solution treated joints with and without artificial aging. The naturally aged joints offered the highest mechanical properties while solution treated joints offered lowest mechanical properties of the joints. Naturally aged joints yielded highest tensile strength (94.9%) and elongation (174.2%) efficiencies while artificially aged joints yielded highest yield strength efficiency (96.7%). Further, post weld heat treatment also affected fracture location and mode of fracture.

Guven *et al.* (2014) studied the effects of initial temper condition and post weld heat treatment on the properties of dissimilar friction-stir-welded joints between AA7075 and AA6061 aluminum alloys. The authors concluded from their investigation PWHT generally resulted in an increase in the strength values of both O and T6 joints; thus, very high joint performance values in terms of tensile strength were obtained, i.e., higher than 85 %.

2.6.2 Microhardness

Izabela *et al.* (2014) reported that natural aging notably influences the mechanical properties of friction stir welded 7136 aluminum alloy and cannot be neglected in practical applications of the alloy in the friction stir welded condition. The hardening effect resulting from the natural aging is associated with the nucleation of the large volume fraction of GP(I) rather than GP(II) precipitates.

Hakan *et al.* (2010) investigated the effect of post-weld heat treatment on the mechanical properties of 2024-T4 friction stir-welded joints. Solution heat treatment

and various ageing treatments were carried out to the welded joints. The PWHT procedures caused abnormal coarsening of the grains in the weld zone, which resulted in a drop in micro-hardness at the weld zone compared to the base material of the joints. T6 (190°C − 10 h) ageing treatment after welding was found to be more beneficial than the other heat treatments in enhancing the mechanical properties of the 2024- T4 joints. However, the T6 (190°C − 10 h) heat treatment led to significant ductility deterioration in the joint.

Peng *et al.* (2013) found that hardening in stir zone in as welded condition was seen to be predominantly coming from grain refinement and formation of dislocation cells, while subsequent hardening during PWNA (post weld natural aging) was seen to be from formation of Mg-Si co-clusters. On the other hand, softening in HAZs in as welded condition, occurring for high stir zone temperatures, was found to be from formation of overaged β" precipitates, while subsequent hardening during PWNA was from formation of fine precipitates, Orowan strengthening, and dislocation cells.

Rui-dong *et al.* (2011) studied the hardness of stir zone (SZ) at as-weld state and post-welding natural aging (PWNA) state under different heat input conditions were investigated for friction stir-welded joints of 2024 aluminum alloy thin-sheets. Examination of tested results reveals that welding heat input has obvious effect on the hardness of the SZ. Under the high welding heat input condition, the hardness of the SZ is lower than that of the parent metal (PM). However, under low welding heat input condition, the hardness of the SZ exhibits strong dependency on the rotational speed of the stirring tool. With increasing the rotational speed of the stirring tool, the

hardness of the SZ increases. The average hardness in the SZ of the joint welded at 1500 rpm and 1000 mm/min achieves the PM level. In comparison, the effect of the PWNA on the improvement of the hardness in the SZ is limited. The variation in the strengthening-phase particles plays a more important role than does grain size in the SZ for the improvement of hardness.

2.6.3 Microstructure

Wanchuck *et al.* (2007) reported that the microstructural softening and the natural aging observed in the dynamic recrystallized zone and thermo mechanically affected zone are mainly caused by the frictional heating from the tool shoulder, resulting in dissolution and reprecipitation of strengthening precipitates.

Chen *et al.* (2009) studied the Precipitate evolution in friction stir welding of 2219-T6 aluminum alloys. From the study, it was found that the strengthening precipitates morphology in the WNZ is significantly different from that in the PM. The precipitates distribute on the fine grains (Fig. 2.10a). The precipitate is characterized by selected area diffraction (SAED). The SAED result shows that the diffraction spots are from θ phase, which indicates the presence of a high volume fraction of θ phase in this region. It implies that some metastable precipitates, present in the PM, have been transformed to stable precipitates. In order to verify the presence of solution during welding, post-weld ageing heat treatment (PWHT) was performed. After ageing heat treatment the stable precipitates still distribute on the equiaxed grains (Fig. 2.10c), while a large number of plate shaped precipitates re-precipitate

(Fig. 2.10d). This implies that a great deal of metastable precipitates solutionize into the α(Al) solid solution during welding.

Sivaraj *et al.* (2014) reports the effects of post weld heat treatments, namely artificial ageing and solution treatment followed by artificial ageing on microstructure of friction stir welded AA7075-T651 aluminium alloy. The solutionizing process during the STA treatment caused the dissolution of precipitates in the matrix. The artificial ageing process in the STA treatment caused the re-precipitation of finer θ' (Mg(Zn,Al,Cu)$_2$) in the stir zone. This is the reason for the higher hardness and tensile strength.

The as-welded weld had a softened region, which was characterized by dissolution and growth of precipitates. The precipitate-dissolved region contained a minimum hardness in the as-welded condition. Postweld aging significantly increased the density of strengthening precipitates and led to a high hardness in the precipitate-dissolved region. The density of strengthening precipitates was hardly increased in the precipitate-coarsened region, which showed a slight increase in hardness during postweld aging. Subsequent aging after solution treatment led to a high density of strengthening precipitates and brought, homogeneously, a high hardness in the overall weld (Chen *et al.* 2009).
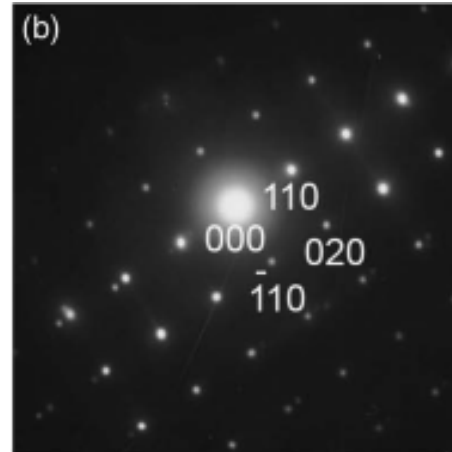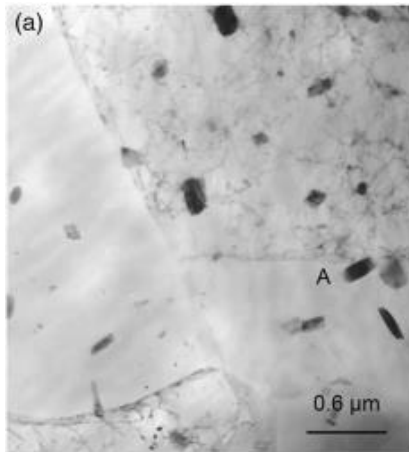
(a) Precipitates and grains structure in
the as-welded condition

(b) The SAD pattern
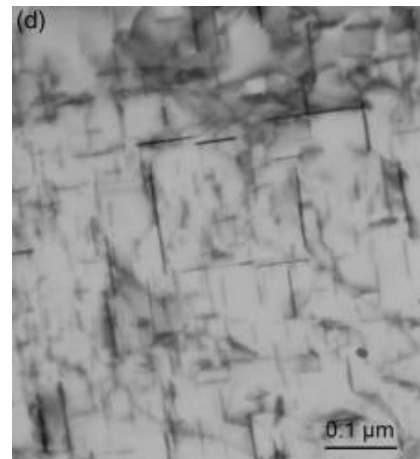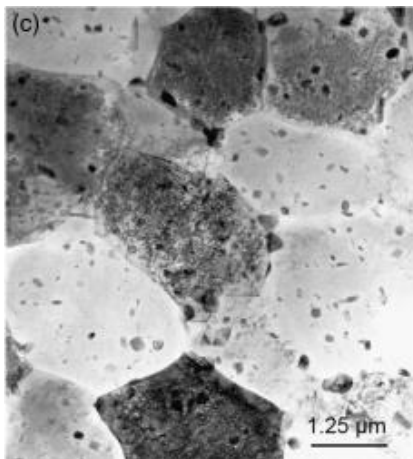
(c) Low magnification TEM image
showing θ precipitates and grains
structure in the PWHT condition

(d) High magnification TEM image
showing the re-precipitated metastable
precipitates in the PWHT condition.

Fig. 2.10 Microstructure in the weld nugget zone (Chen *et al.* 2009)

2.7 SUMMARY OF THE LITERATURE REVIEW

From the above literature review, it is understood that the process parameters namely
tool rotational speed, tool traverse speed, tool tilt angle and tool pin profile have
significant effect on the mechanical properties of the FSW and UWFSW joints. The

previous studies demonstrated the feasibility of joining of Al alloys using UWFSW process for enhancing the strength of the joints. However the relationship between the process parameters and the joint performance is not yet systematically investigated. Moreover, the comparative study on FSW and UWFSW joints focussing on aging behaviour, thermal behaviour and mechanical properties are scanty in the open literature. Hence to explore the advantages of water cooling, an attempt was made in this investigation to study the effect of process parameters on mechanical properties and aging behaviour of UWFSW joints and compare with air cooled FSW joints.

2.8 MOTIVATION TO THE PRESENT WORK

It is presently well demonstrated that friction stir welding (FSW) process can join aluminium alloys with superior joint properties compared to other welding processes. However, the heat generated during FSW can alter the precipitation behaviour of the aluminium alloys. The strength and hardness of the age hardenable aluminium alloys mainly rely on the precipitate type, size and its distribution. During FSW, the thermal condition prevails in the thermo-mechanical affected zone (TMAZ) and heat affected zone (HAZ) causes precipitate coarsening and dissolution of precipitates. In addition, the grain coarsening is also occurred in the above said zones. Hence, these regions attain lower hardness (softening) and so termed as the lowest hardness distribution region (LHDR).

The hardness values reported in the LHDR were nearly 50 % lower than the hardness of the parent metal. Moreover, the tensile fracture occurred exactly in the LHDR.

44

Hence enhancing the hardness of the LHDR is mandatary to improve the joint properties of the FSW joints. During UWFSW, the high heat dissipation capacity of water controls the conduction of heat to TMAZ and HAZ. The low heat prevailing in the TMAZ and HAZ will not be sufficient to coarsen or dissolute the precipitates. In addition, the width of the TMAZ and HAZ can also be minimized by limiting the heat and plastic deformation by UWFSW. In order to take the full advantage of water cooling, tool pin profiles and the process parameters namely tool rotational speed, tool traverse speed and tool tilt angle are to be properly selected to achieve the sound UWFSW joints. The heat generation and material flow in UWFSW process is entirely different from FSW process. So it is necessary to study the material flow behaviour and resultant tensile properties due to the difference in the cooling medium and process parameters. On the other hand, the loss in hardness due to undesirable precipitate transformation can be significantly improved by postweld heat treatment methods. Hence in this investigation, an attempt was made to study the effect of process parameters and PWHT methods on tensile properties and microhardness of FSW and UWFSW joints.

2.9 SCOPE AND OBJECTIVES

From the above literature review, it is understood that the UWFSW process has shown advantages over conventional FSW process but the process parameters are to be optimally selected to achieve sound joints. Therefore it is necessary to understand the effect of process parameters on the joint quality and the correlation with the microstructure and resultant mechanical properties. It is also important to understand the influence of post-weld artificial ageing treatment on the microstructure and

mechanical properties of FSW and UWFSW joints to explore the optimal path for improving the mechanical properties. Based on the above discussion, following objectives are framed for this investigation.

i. Study the effect of process parameters namely, tool pin profile, tool rotation speed, tool travel speed and tool tilt angle on the microstructure and mechanical properties of UWFSW joints of AA2519-T87 alloy and compare with conventional air cooled FSW joints.

ii. Analyzing the heat generation and heat dissipation of FSW and UWFSW processes using experimental and numerical method

iii. Study the effect of PWHT on the microstructural features and mechanical properties of FSW and UWFSW joints of AA2519-T87 alloy.

CHAPTER 3
EXPERIMENTAL WORK

3.1 INTRODUCTION

The aim of the this research work is to evaluate the performance of friction stir welded AA2519-T87 joints. In order to accomplish the main objectives following sequence of experimental work was planned: The experimental plan of the present investigation is shown in the form of a flowchart (Fig. 3.1).

(i)   Evaluation of chemical composition and mechanical properties of parent metal (AA2519-T87)

(ii)   Fabrication of friction stir welded AA2219-T87 aluminium alloy joints using different process parameters namely tool pin profile, tool tilt angle, tool rotational speed and tool travel speed under two cooling mediums namely air cooling and water cooling

(iii)   Thermal analysis of FSW and UWFSW processes

(iv)   Carrying out post weld heat treatment (PWHT) on the joints using two treatments namely, artificial aging (AA) and solution treatment + aging (STA)

(v)   Characterization of FSW and UWFSW joints using light optical microscope to reveal the joint quality, grain size, grain orientation and material flow behaviour

(vi)   Evaluation of transverse tensile properties of the joints and fracture surface was characterized by scanning electron microscope

(vii)   Recording the microhardness of various regions of the joint and identifying lower hardness distribution region (LHDR)
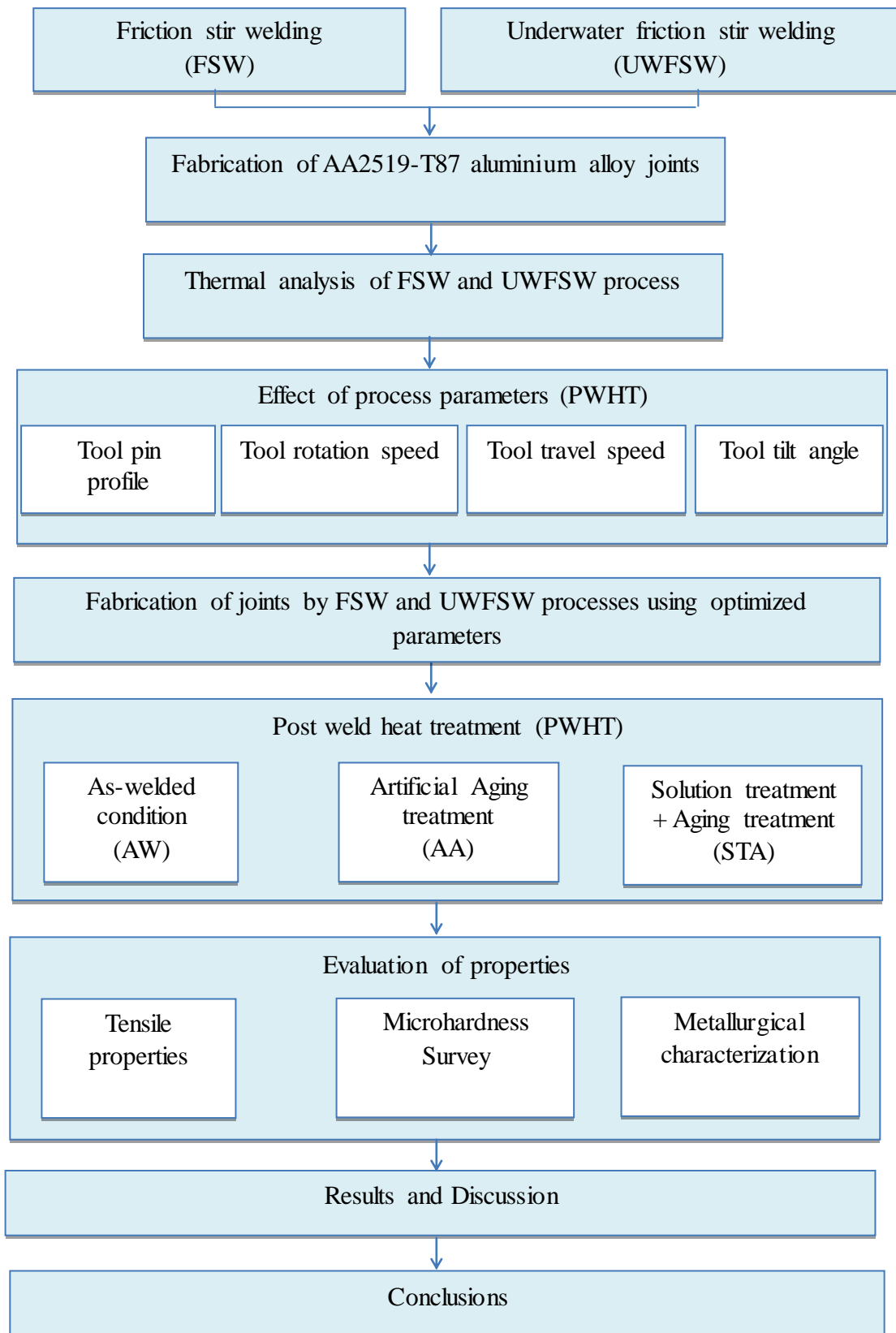
47

Fig. 3.1 Work Plan

48

3.2 BASE METAL PROPERTIES EVALUATION

In this investigation, rolled plates of AA 2519-T87 aluminium alloy were used as the parent metal (PM). The vacuum spectrometer (ARL, model 3460) was employed to estimate the wt % of the individual alloying elements present in the parent metal. The spectrums were acquired by igniting sparks at various locations, and their compositions were estimated (Table 3.1). The tensile properties and microhardness of the parent metal were evaluated and presented in Table 3.2. The parent metal exhibited yield strength of 427 MPa, tensile strength of 452 MPa and elongation of 11.2 %. The parent metal recorded a hardness of 160 HV.

Table 3.1 Chemical composition (wt %) of AA 2519-T87 aluminium alloy

Cu	Mn	Mg	V	Fe	Si	Ti	Al
5.71	0.27	0.47	0.05	0.1	0.04	0.02	Balance

Table 3.2 Mechanical properties of AA 2519-T87 aluminium alloy

0.2 % Yield strength, (MPa)	Ultimate tensile strength, (MPa)	Elongation in 50 mm gauge length, (%)	Hardness, $HV_{0.05}$
427	452	11.2	160

The light optical micrograph (Fig 3.2a) of parent metal is characterized by the presence of coarse elongated grains of 49 μm. The TEM image of parent metal (Fig. 3.2b) is characterized by the presence of dense fine θ'(CuAl$_2$) precipitates in the Al matrix. The precipitates is 3 nm thick and 43 nm diameter.
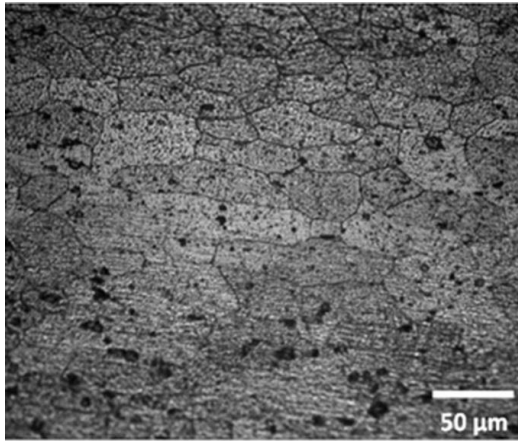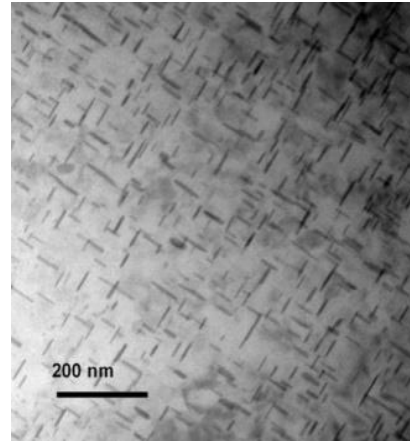
a. Light optical micrograph   b. TEM

Fig. 3.2 Micrographs of parent metal

3.3 FABRICATION OF JOINTS

In this investigation, an indigenously designed computer numerical controlled FSW (22 kW; 4000 rpm; 60 kN) was used to fabricate the joints. The butting faces of the plates to be joined were milled and polished to make them flat. The surface undergone friction with the shoulder was polished by using emery papers and rubbed with acetone to remove the oxide layer. The plates were rigidly clamped to ensure that the plates should not abut during welding. The rotating tool was slowly plunged into the interface of two materials at a rate of 1 mm/sec until the shoulder surface touched the workpiece surface. A dwell period of 30 s was maintained for all the joints in order to preheat and soften the preheat zone. The rotating tool was traversed along the weld line at a constant welding speed and finally the tool was pulled out. In this investigation, the welding was done perpendicular to the rolling direction of the parent metal. Welding process parameters, pin profile and tool offset exert significant effect on the material flow pattern and temperature distribution, thereby influencing the microstructural evolution of material. In this investigation, process parameters

50

such as tool rotation speed of 1100 -1500 rpm, tool travel speeds of 20-40 mm/min and tool tilt angles of 0˚-4˚ were used to fabricate the FSW and UWFSW joints. The details of the process parameters used in this investigation are presented in Table 3.3. In addition, the four different pin profiles namely straight cylindrical pin (STC), straight threaded cylindrical pin (THC), taper cylindrical pin (TAC) and taper threaded cylindrical pin (TTC) were used to fabricate the joints. The tool dimensions and the photograph of the fabricated tools are shown in the Fig 3.3 and Fig 3.4 respectively.

Table 3.3 Welding parameters and tool dimensions used in this investigation

Process Parameters	Values
Tool traverse speed (mm/min)	20, 25, 30, 35, 40
Tool rotational speed (rpm)	1100, 1200, 1300, 1400, 1500
Tool shoulder diameter (mm)	18
Pin length (mm)	5.7
Pin diameter (mm)	5-6
Tool tilt angle, degree	0°, 1°, 2°, 3°, 4°
Pin Profile	Straight cylindrical (STC), straight threaded cylindrical (THC), taper cylindrical (TAC) and taper threaded cylindrical (TTC).
Tool material	Hardened super high speed steel

The joints were fabricated using two processes namely FSW and UWFSW. In FSW process, the joints were fabricated in the air medium (open atmosphere) whereas in UWFSW process, the joints were made in the water medium (submerged in water). During UWFSW process, a stainless steel water tank was mounted on the backing plate of standard FSW machine. The dimension of the water tank was 400 mm $\times$ 400

mm × 100 mm. The joints were rigidly clamped in the water tank. The water was allowed to flow into the tank through the inlet valve to the level over the tool shoulder. The inlet and the outlet of the tank were adjusted so that the water remains cold near to the welding location. The water flow was adjusted to maintain the water level just below the tool shank. The welding setups used for fabricating the FSW and UWFSW joints are shown in Fig. 3.5. Square butt joint configuration of 300 mm × 300 mm × 6 mm was used in this investigation. Fig. 3.6 and Fig. 3.7 show the photographs of the FSW and UWFSW joints respectively.
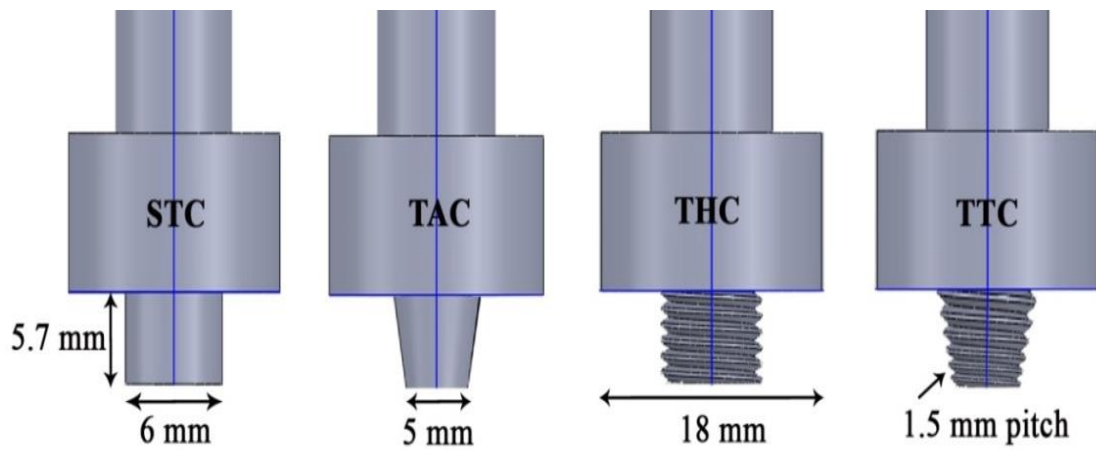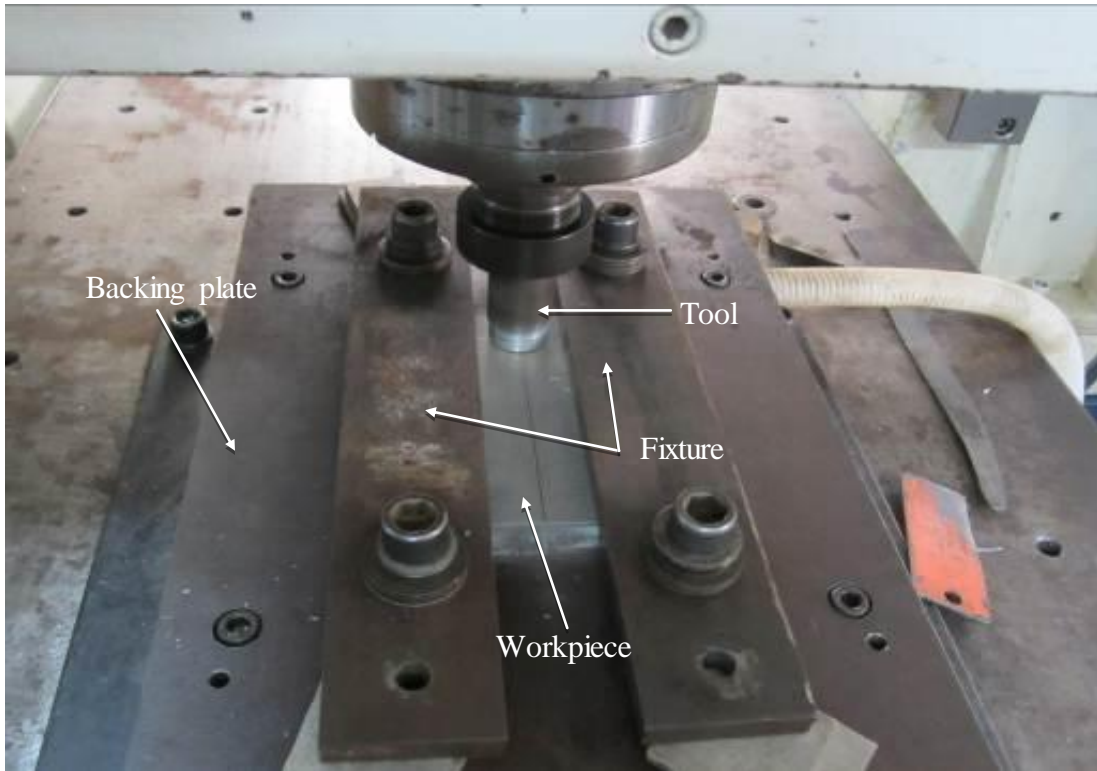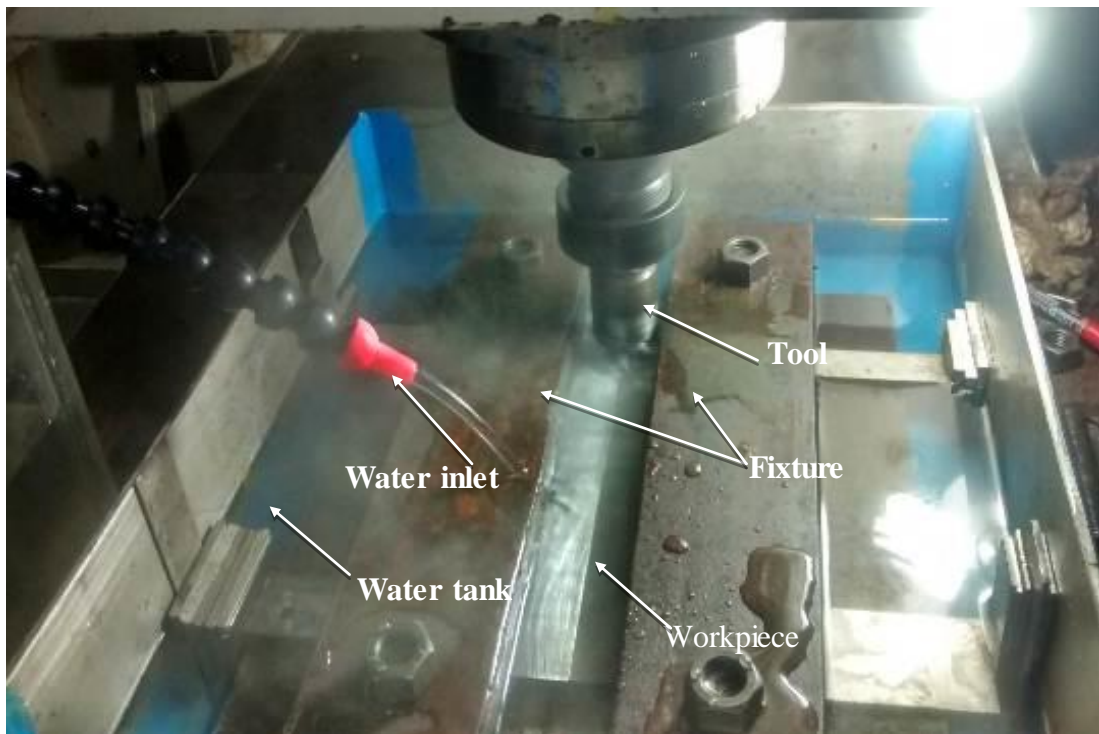

Fig. 3.3 Dimensions of the various tool pin profiles

Fig. 3.4 Photographs of different pin profiles

a. FSW setup

b. UWFSW setup

Fig. 3.5 Photograph of welding setup used in this investigation

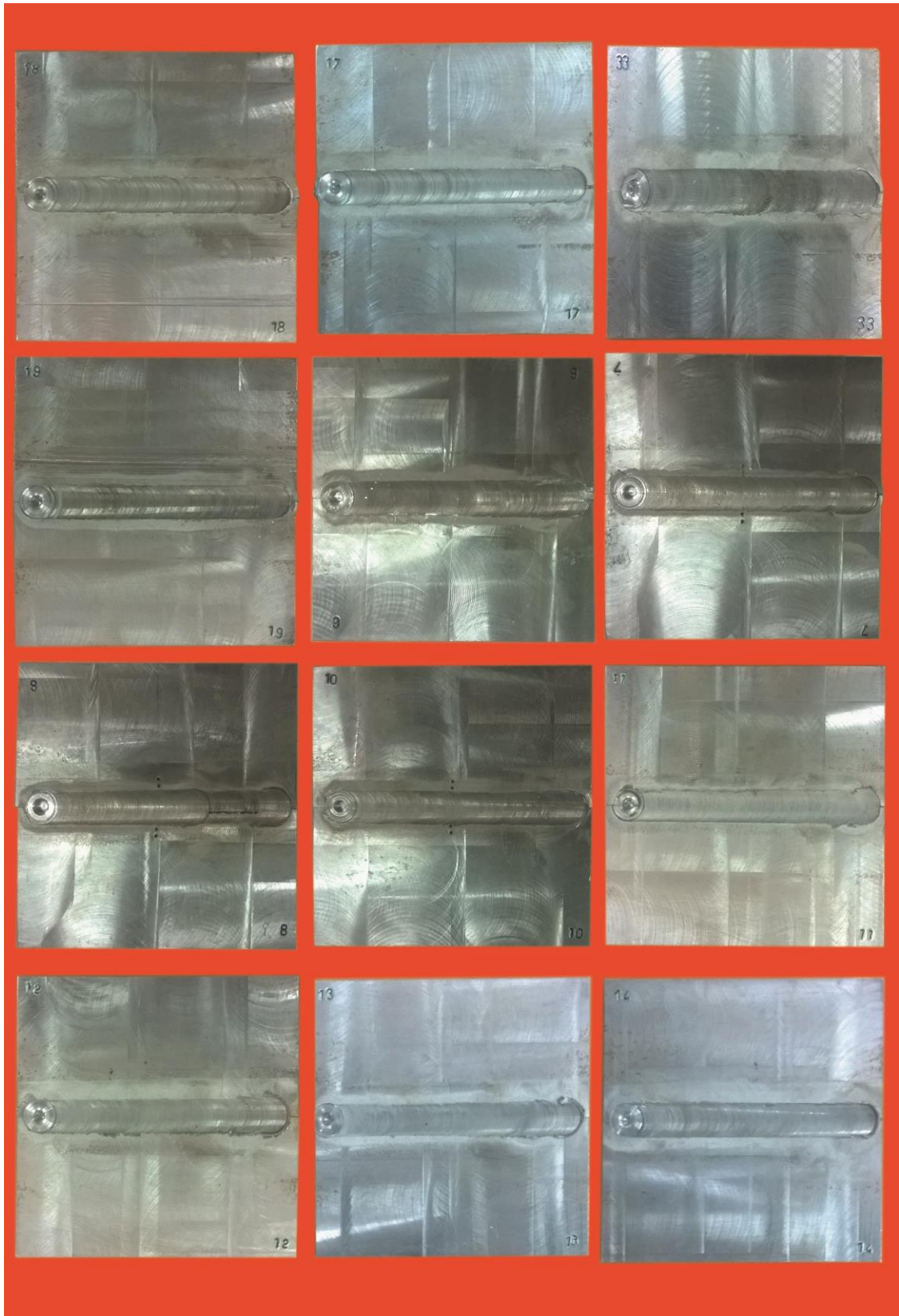**Fig. 3.6 Photograph of fabricated FSW joints**

Fig. 3.7 Photograph of fabricated UWFSW joints

3.4 TEMPERATURE MEASUREMENT

K-type thermocouple was employed to measure the thermal cycles prevailed during welding at mid length (i.e 75 mm). The hole size of 1 mm diameter and 3 mm depth was drilled at the backside of the plates which was 19 mm from the weld center in the retreating side (RS). The thermocouples were embedded at the hole. The K type thermocouples which exhibit higher sensitivity of 41 µV/°C were employed for temperature measurement. The LabView software was used to record the temperature with the help of computer integrated data acquisition system. Moreover, during UWFSW process, the K-type thermocouple was employed to monitor the temperature of the water near the welding location not to exceed above 60 °C.

3.5 POST WELD HEAT TREATMENT

The FSW joints were subjected to two post weld heat treatments (PWHT) namely artificial aging (AA) and solution treated + artificial aging (STA). Solution treatment (ST) was carried out at the 535 °C for a soaking period of 90 minutes. During ST, the joints were induction heated from room temperature to 535 °C at a rate of 100 °C per hour. After completion of the soaking period, the joints were quenched in the cold water bath. Artificial aging treatment was carried out at 175 °C for a soaking period of 12 hours. FSW joints were placed into the induction furnace and heated to the soaking temperature at a rate of 100 °C per hour. After completion of the soaking period, the joints were allowed to cool down to the room temperature, in the furnace itself. For the solution treated and aged (STA) joint, both the AA and ST were followed one after the other to get the collective effect of the treatments.

3.6 SPECIMEN PREPARATION

In this investigation, the mechanical properties like tensile properties and microhardness were evaluated and light optical microscopy is used majorly to characterize the weld joint. The specimens required for testing and characterization were machined from the joints by employing wire-cut electric discharge machining (WEDM) process. The scheme of extraction of tensile test specimen, microhardness testing specimen and metallographic specimens are shown in Fig. 3.8
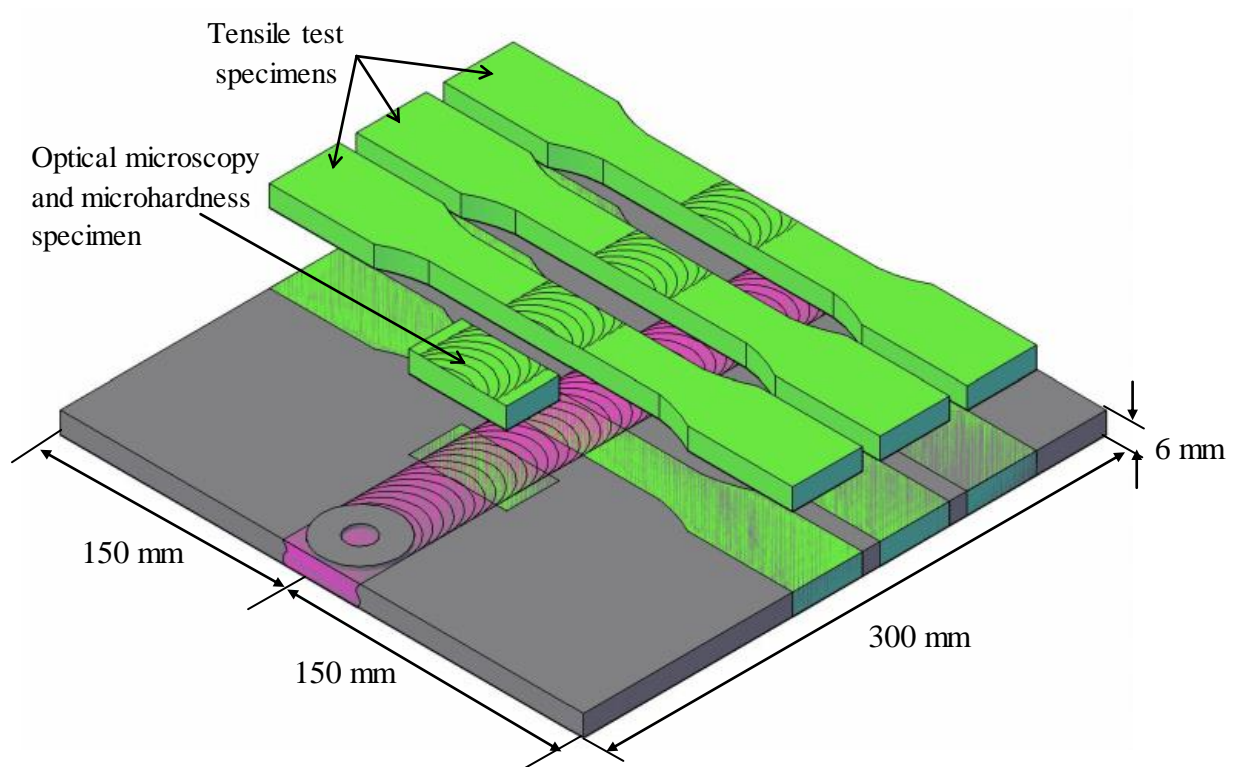

Fig. 3.8 Scheme of specimen extraction diagram

3.7 MECHANICAL PROPERTIES EVALUATION

3.7.1 Tensile testing

The tensile test samples were extracted from the weld joints and then the samples were flattened by polishing to ensure that the entire specimen has equal cross

57

sectional area. The sample preparation (Fig. 3.9) and testing procedures for tensile test were followed as per the ASTM E8M-15a guidelines. The samples were tested using servo controlled universal testing machine (Make: FIE Blue Star, India; Model: UNITEK 94100). The tensile specimens were loaded at the rate of 1.5 kN/min. The tensile properties like 0.2% offset yield strength, ultimate tensile strength and percentage of elongation were evaluated from the tensile test.
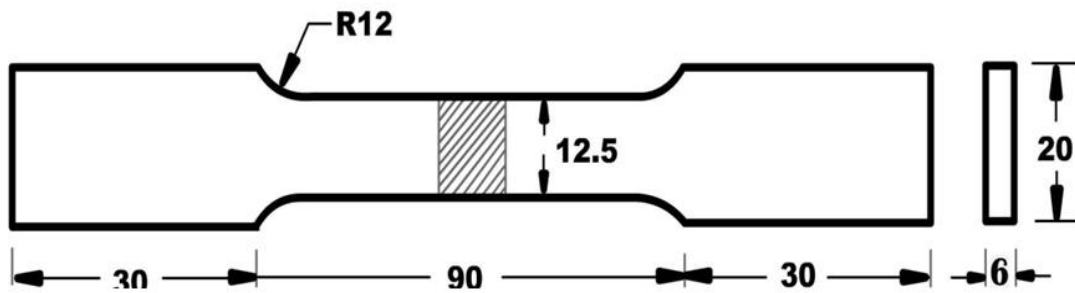

Fig. 3.9 Dimensions (mm) of tensile test specimen

Fig. 3.10 Photographs of tensile test specimens (before testing)

Fig. 3.11 Photographs of tensile test specimens (after testing)

3.7.2 Microhardness survey

The sample preparations and the testing procedures for the microhardness measurements were followed as per the guidelines from ASTM E 384-99 (Standard test method for microindentation hardness of materials). The microhardness were measured at the mid thickness region in the cross section of the various zones of the joints. The samples prepared for light optical microscopy were used for the microhardness survey. Vickers micro hardness tester (Make: SHIMADZU, Japan; Model: HMV-2T) was used to measure the microhardness by using indenting load of 0.05 kg for a dwell time of 15 seconds using.

3.8 METALLURGICAL CHARACTERISTICS EVALUATION

In this investigation, several characterization procedures were undergone to analyze the microstructure of the welded joints. The techniques used to examine the microstructure include light optical microscopy (OM), scanning electron microscopy (SEM) and transmission electron microscopy (TEM).

3.8.1 Light optical microscopy (OM)

Microstructural examination was carried out using an light optical microscope (Make: MEJI, Japan; Model: MIL 7100) interfaced with image analyzing software (Metal vision). The specimens were extracted from the welded joints so as to comprise stir zone, TMAZ, HAZ and parent metal regions. All the sides of the samples were polished to ensure the flatness of the sample. The specimens for metallographic examination were roughly polished by the emery sheets with large grit size and subsequently polished using different grades of water emery papers to get fine polish. Final polishing was done using alumina powder in the disc polishing machine. The specimens were etched as per the ASTM standard E407 (Standard practice for microetching of metals and alloys) with standard Keller's reagent made of 190 ml of distilled water, 5 ml of HNO_3, 3 ml of HCl and 3 ml of HF. The chemical etchants were swabbed and washed thoroughly in running water. After etching, the specimens were placed in the optical microscope to reveal the macrograph and micrograph of FSW and UWFSW joints. The average grain size in the PM, SZ, TMAZ and HAZ was measured by the line intercept method as per the ASTM E112-13 standard guideline.

To analyze the entire fracture path, the cross sectional macrograph of the fractured specimens were characterized using light optical microscope. The fracture macrograph specimens were extracted from the tensile tested specimens and polished at the cross section. Kellers reagent was applied to reveal the various regions which make ease for the precise identification of fracture path.

3.8.2 Scanning electron microscopy (SEM)

Scanning Electron Microscope (Make: JEOL, Japan; Model: 4802) was employed to characterize the fractured surface of the tensile test specimens. The high magnified SEM images enabled to analyze and study the fracture morphology and nature of the fracture.

3.8.3 Transmission electron microscopy (TEM)

The size, shape and distribution of precipitates in the LHDR were analyzed using a transmission electron microscope (TEM). The sample size of 3 mm diameter was extracted and polished to 10 μm thick using ion milling process. The size, approximate inter-particle spacing and area fraction of precipitates were measured as per the ASTM B276 guidelines using metal vision image analyzing software. Image resolution of 2048×2048 pixels was used for analysis. The image is normalized and the intensity is adjusted in such a way to differentiate the matrix and precipitates.

3.9 SUMMARY

The chemical composition, mechanical properties and microstructural features of parent metal provided the history of starting materials. Nearly 75 joints were fabricated in total and tensile test, hardness survey, microstructure analysis were carried out to evaluate performance of the FSW and UWFSW joints. The results obtained from the experimental work are presented in detail in the following chapters.

CHAPTER 4
EFFECT OF TOOL PIN PROFILE

4.1 INTRODUCTION

Though the FSW process will yield joints with superior properties, the process parameters and tool geometry has to be selected in such a way to attain defect free, sound joints. The material flow behaviour mainly decides the quality of the FSW joints. The material flow behavior in FSW depends on the process parameters such as tool rotation speed, tool traverse speed, axial force, tool tilt angle, tool shoulder diameter, tool shoulder profile and tool pin profile (Rajakumar *et al.* 2011). Among the parameters, tool pin profile plays an important role in stirring and extruding the material around the tool pin. Pin profile is a noteworthy part in deciding material flow path and therefore controls the tool travel speed of the welding process. The pin profile plays a primary role in controlling the rotary and transverse material flow, though the other parameters are supplementing the material flow by supplying the sufficient heat and force. The essential capacity of the non-consumable pivoting instrument pin is to blend the plasticized metal and move the same behind it to create sound weld joint. Chionopoulos *et al.* (2008) reported that the shape of the weld nugget and the TMAZ zone is solely based on the shape and the geometry of welding tool and not on the processing parameters. Vijay and Kumar (2013) proposed an analytical model to predict the heat generation by the taper pin profile. The study explained that the profile angle have greater effect in the material flow and heat generation.

The flow behavior of materials in FSW and UWFSW processes is entirely different, because of the difference in heat dissipation capacity of the cooling mediums. Hence, the thermal softening in the preheat zone, stir zone and TMAZ differs which in turn causes the difference in material flow behaviour. Many research works were previously carried out to understand the flow behavior of materials in FSW process, but limited research works have been reported so far related to the material flow behaviour of UWFSW process (Kumar and Suvarna 2012; Fujii *et al.* 2006; Woo *et al.* 2007; Hamilton *et al.* 2008). Hence, in this investigation, an attempt has been made to study the effect of pin profiles on stir zone characteristics and the resultant tensile properties of the joints made by FSW and UWFSW processes.

4.2 MACROGRAPHS

Table 4.1 shows the appearance of the top surface and the cross sectional macrograph of the FSW and UWFSW joints fabricated using different pin profiles. The surfaces of all the joints are free from surface defects. The weld surface is smooth and composed of closely spaced ripples in all the joints. However, a distinct band of white region is observed next to the weld region on both sides of the UWFSW joints. The macro features of the stir zone exhibit different material flow behavior. From the macrograph, the stir zone can be divided into upper shoulder influenced region (SIR), middle pin influenced region (PIR) and lower vortex region (VOR). In both air and water cooling medium, the tunnel defects are observed in the advancing side-PIR of the joints fabricated using STC and TAC profiled tools. But, the joints fabricated using THC and TTC profiled tools yielded defect free stir zones in both air and water

cooling medium. The defective joints are not considered for further analysis and the defect free THC and TTC joints alone are considered.

Table 4.1 Effect of tool pin profile on top surface and cross sectional macrographs
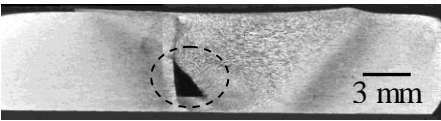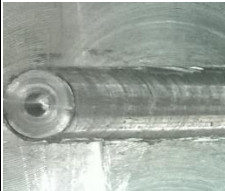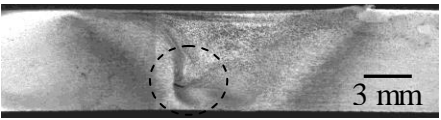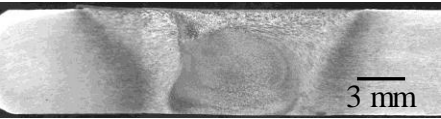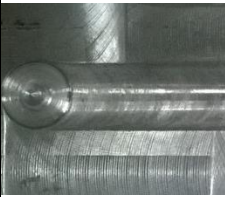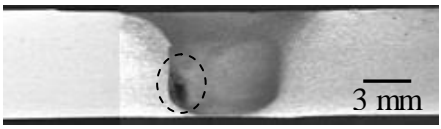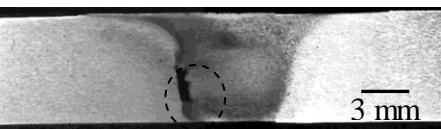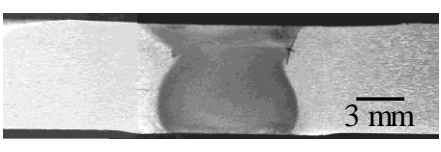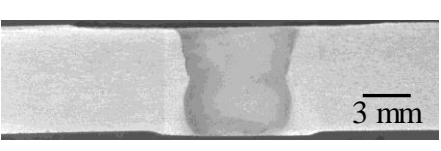
Name of the joint	Top surface	Cross sectional macrograph		Observation
		AS	RS	
FSW-STC				Defect free top surface but tunnel defect is observed at the advancing side
FSW-TAC				Defect free top surface but tunnel defect is observed at the advancing side
FSW-THC				Defect free stir zone at both top surface and cross section
FSW-TTC				Defect free stir zone at both top surface and cross section

Table 4.1 (contd.)

Name of the joint	Top surface	Cross section		Observation
		AS	**RS**	
UWFSW-STC				Defect free top surface but tunnel defect is observed at the advancing side
UWFSW-TAC				Defect free top surface but tunnel defect is observed at the advancing side
UWFSW-THC				Defect free stir zone at both top surface and cross section
UWFSW-TTC				Defect free stir zone at both top surface and cross section

4.3 TENSILE PROPERTIES

Fig. 4.1 shows the stress strain curves of the FSW and UWFSW joints fabricated using THC and TTC tools. The transverse tensile properties like yield strength, ultimate tensile strength and elongation were derived from the 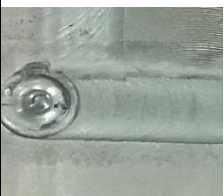stress strain curves and presented in the Table 4.2. The unwelded parent metal (PM) showed tensile strength of 452 MPa with an elongation of 11.2 %. The UWFSW-THC joint exhibited tensile strength of 327 MPa which is 30 % lower than PM and it showed an

66

elongation of 7.94 % which is also 30 % lower than PM. The UWFSW-TTC joint yielded tensile strength of 345 MPa which is 25 % lower than PM and it showed an elongation of 9.17 % which is 20 % lower than PM.   FSW-TTC joint exhibited tensile strength of 267 MPa and joint efficiency of 59 % which is 9 % higher than the FSW-THC joint. Of the four joints, UWFSW-TTC joint showed higher joint efficiency of 76 % which is 5 % higher than UWFSW-THC joint, 29 % higher than FSW-THC joint and 22 % higher than FSW-TTC joint.
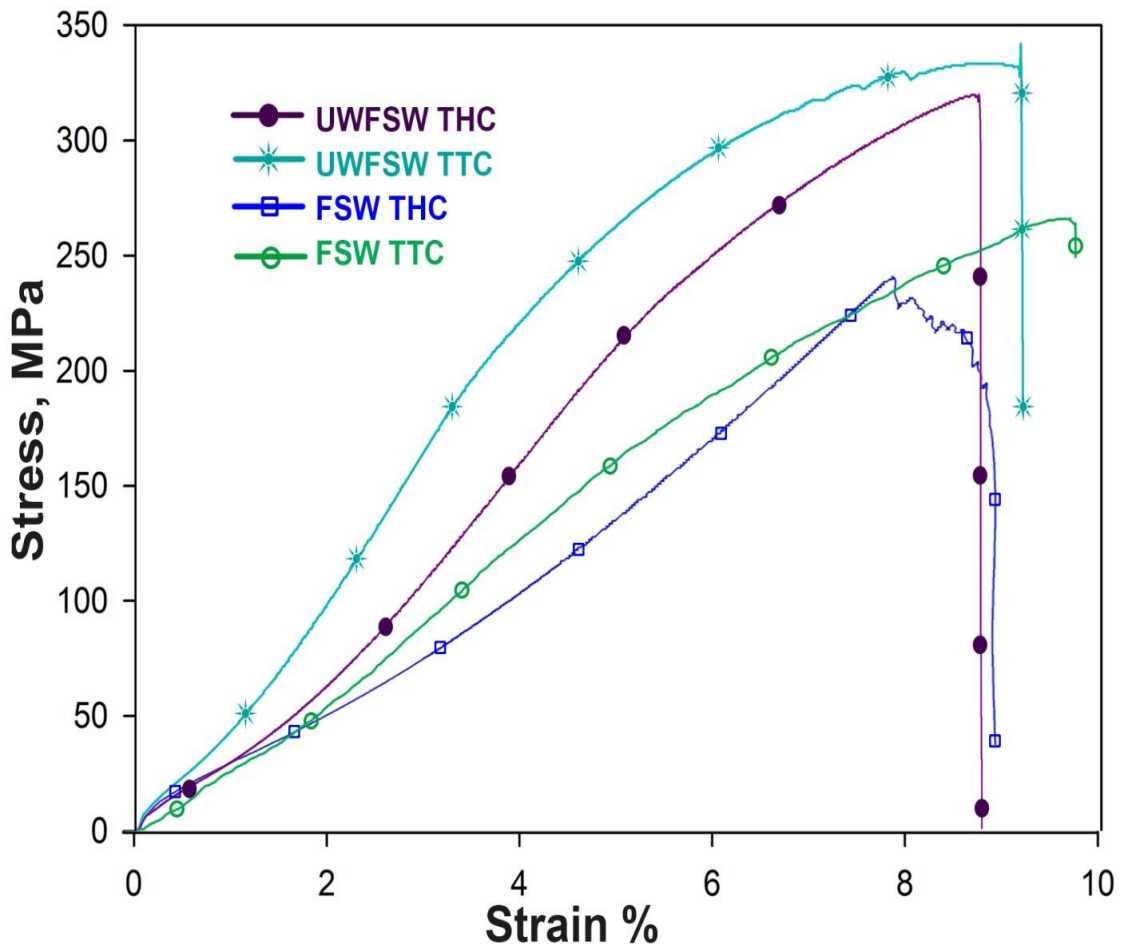
Fig. 4.1 Stress strain curves
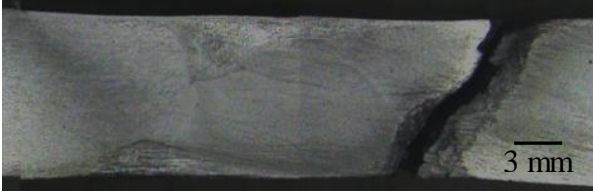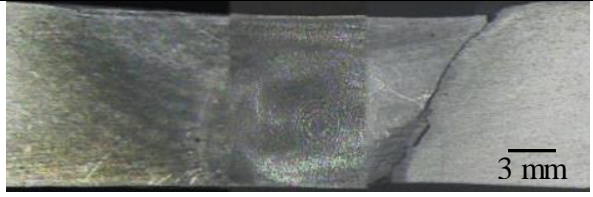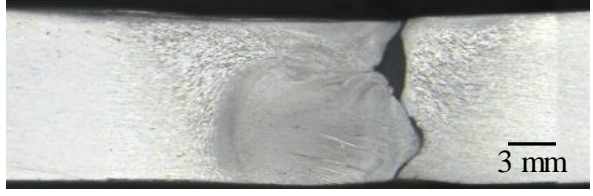
Table 4.2 Transverse tensile properties of the joints

	0.2 % Yield strength (MPa)	Tensile strength (MPa)	Elongation in 50 mm gauge length (%)	Joint efficiency (%)
Parent metal	427	452	11.2	-
UWFSW-THC	301	327	7.94	72
UWFSW-TTC	322	345	9.17	76
FSW-THC	218	244	9.2	54
FSW-TTC	230	267	9.85	59

Fig. 4.2 show the typical fracture surface at macro and micro level magnifications. The joints fabricated using THC and TTC pin profile in water cooling medium, shows two different patterns on fracture surface, one at the SIR and another at PIR. But the entire fracture region of FSW-THC and FSW-TTC joints exhibit only one fracture pattern. At higher magnification, all the joints show fine populated dimples in the fracture surface, irrespective of the pin profiles and cooling medium. The dimples are oriented towards the loading direction and the presence of dimples suggests that the joints are failed predominantly in the ductile mode.

Table 4.3 show the fracture location of the tensile tested specimen. The cross sectional macrograph of the fractured specimen reveals the entire fracture path. It can be clearly seen that the fracture is observed in the TMAZ in all the joints. The FSW joints show the regular fracture path which is 45° inclined to the tensile loading direction. But the UWFSW joints show an irregular fracture path along the outer periphery of the stir zone.

Table 4.3 Effect of tool pin profile on fracture path

Name of the joint	Fracture path		Observation
	AS	RS	
FSW-THC			Fracture is occurred in the RS-TMAZ which is 45° inclined to the loading direction
FSW-TTC			Fracture is occurred in the RS-TMAZ which is 45° inclined to the loading direction
UWFSW-THC			Fracture is occurred in the TMAZ in which the fracture is irregular
UWFSW-TTC			Fracture is occurred in the TMAZ in which the fracture is irregular

Tool pin profiles	Macro level fracture surface	SEM fracture surface
FSW-THC		
FSW-TTC		
UWFSW-THC		
UWFSW-TTC		
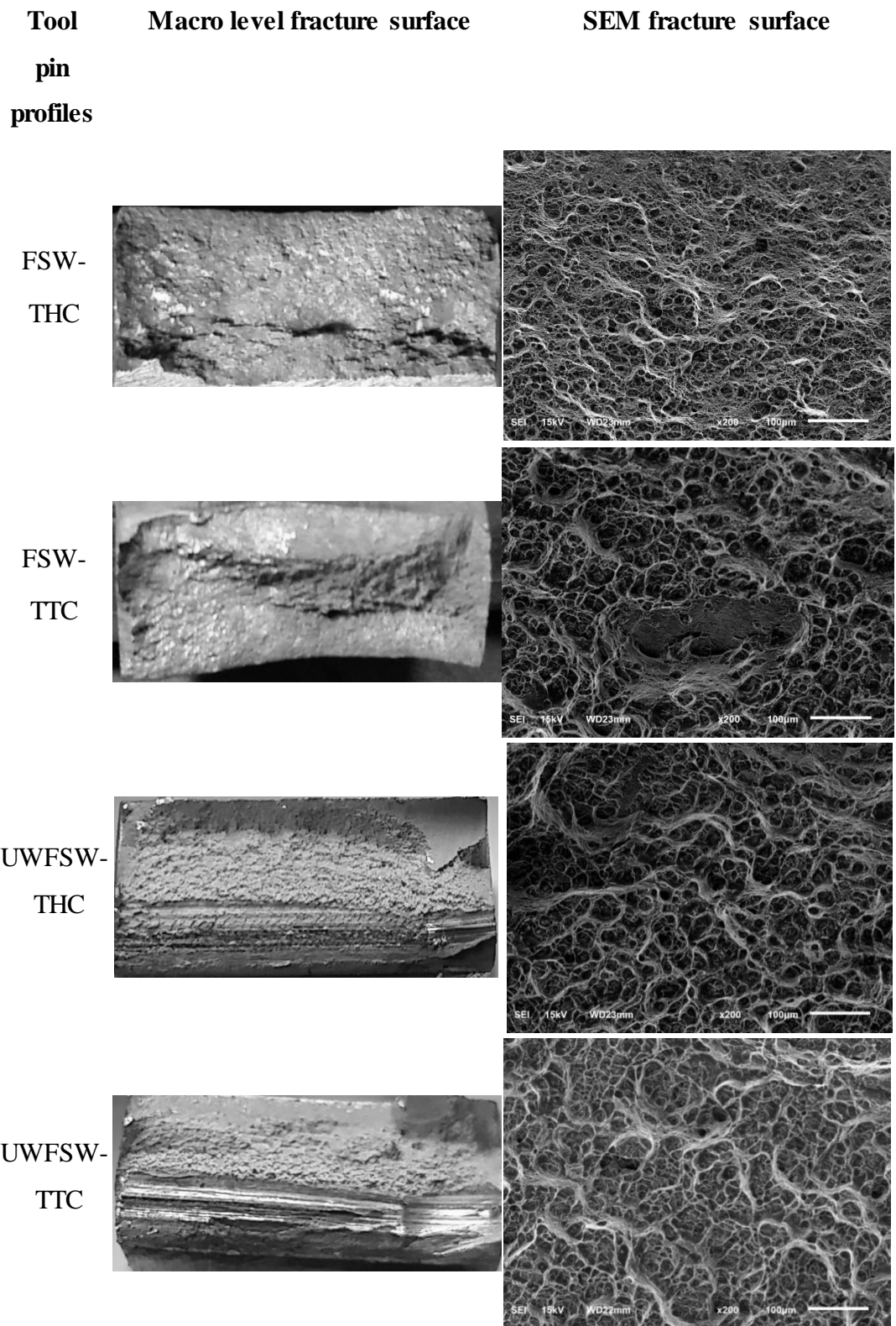
Fig. 4.2 Fracture surface analysis

4.4 MICROHARDNESS

Fig. 4.3 shows the microhardness measurement across the mid thickness region of the joints. In all the joints, typical W shaped hardness plots were recorded. Among the various regions, the TMAZ on both the AS and RS of the joints recorded lower hardness. In air cooling condition, FSW-THC joint recorded lowest hardness of 78 HV whereas FSW-TTC joint recorded 80 HV in the RS. In the water cooling condition, UWFSW-THC joint recorded lowest hardness of 82 HV whereas UWFSW-TTC joint recorded 93 HV in the RS. It is observed that the location of the LHDR is closer to the weld center in UWFSW joints but it is marginally away from weld center in FSW joints. It is also observed that the LHDR is wider in FSW joints and narrower in the UWFSW joints.
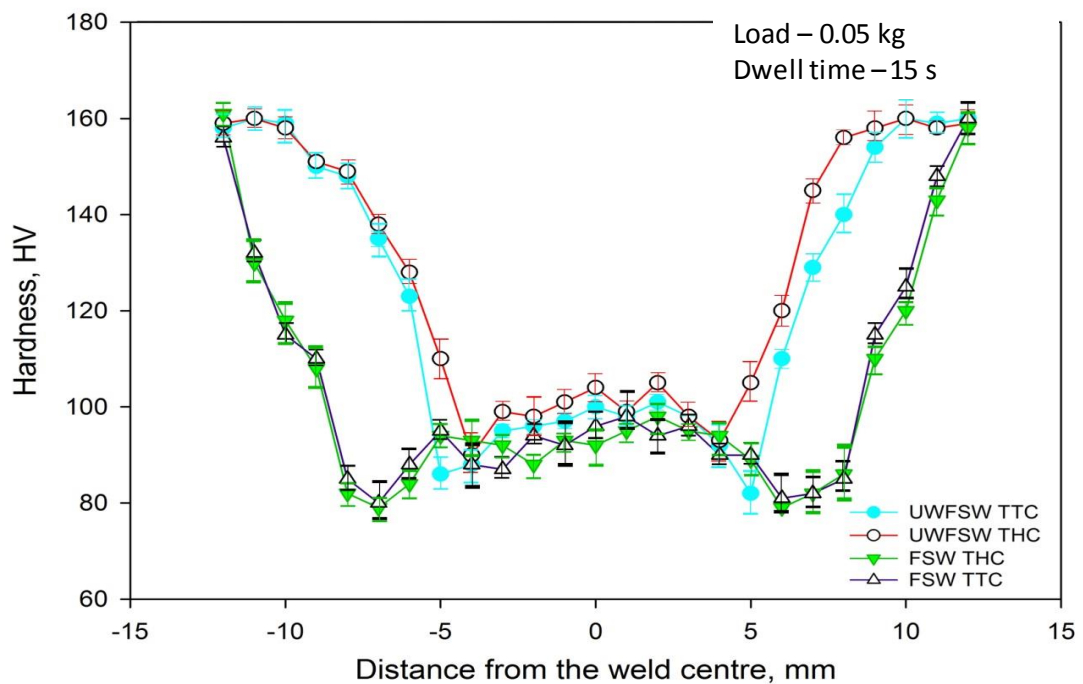
Fig. 4.3 Microhardness plot

In all the joints, the hardness of the SZ are higher than the TMAZ. SZ of UWFSW-TTC joint recorded higher hardness of 105 HV whereas lower hardness of 86 HV was recorded in FSW-THC joint. The hardness of the HAZ are lower however it is higher than the TMAZ. It is observed that there is an increase in hardness from TMAZ to PM region. The joint fabricated using water cooling medium recorded marginally higher hardness in all the regions than the joint fabricated under air cooling medium. Among the pin profiles, the joint fabricated using TTC pin profiled tool in water cooling medium recorded higher hardness than its counterparts.

4.5 MICROSTRUCTURE

Figs. 4.4a, 4.4b, 4.5a, and 4.5b show the stir zone micrographs of the joints fabricated using THC and TTC tools in both air and water cooling medium. It can be observed that dynamic recrystallization has occurred during the FSW and UWFSW process. It can also be noticed that grains are fine and equi-axially oriented in the SZ irrespective of the cooling medium. The average grain diameter at various regions were quantified and presented in table 4.4. In stir zone, the grain diameter of FSW joints is higher than the UWFSW joints. The joint made using TTC tool shows lower grain size than THC tool under both the cooling mediums and the average grain diameter is 15 μm and 3.3 μm for FSW and UWFSW joints respectively. The average grain diameter of the stir zone of the joint made by THC tool is measured as 17.5 μm and 5.2 μm for FSW and UWFSW joints respectively.

FSW UWFSW

Stir
zone

AS-
TMAZ

RS-
TMAZ

RS-
HAZ

Fig. 4.4 Optical micrograph of the various regions of THC joint

73
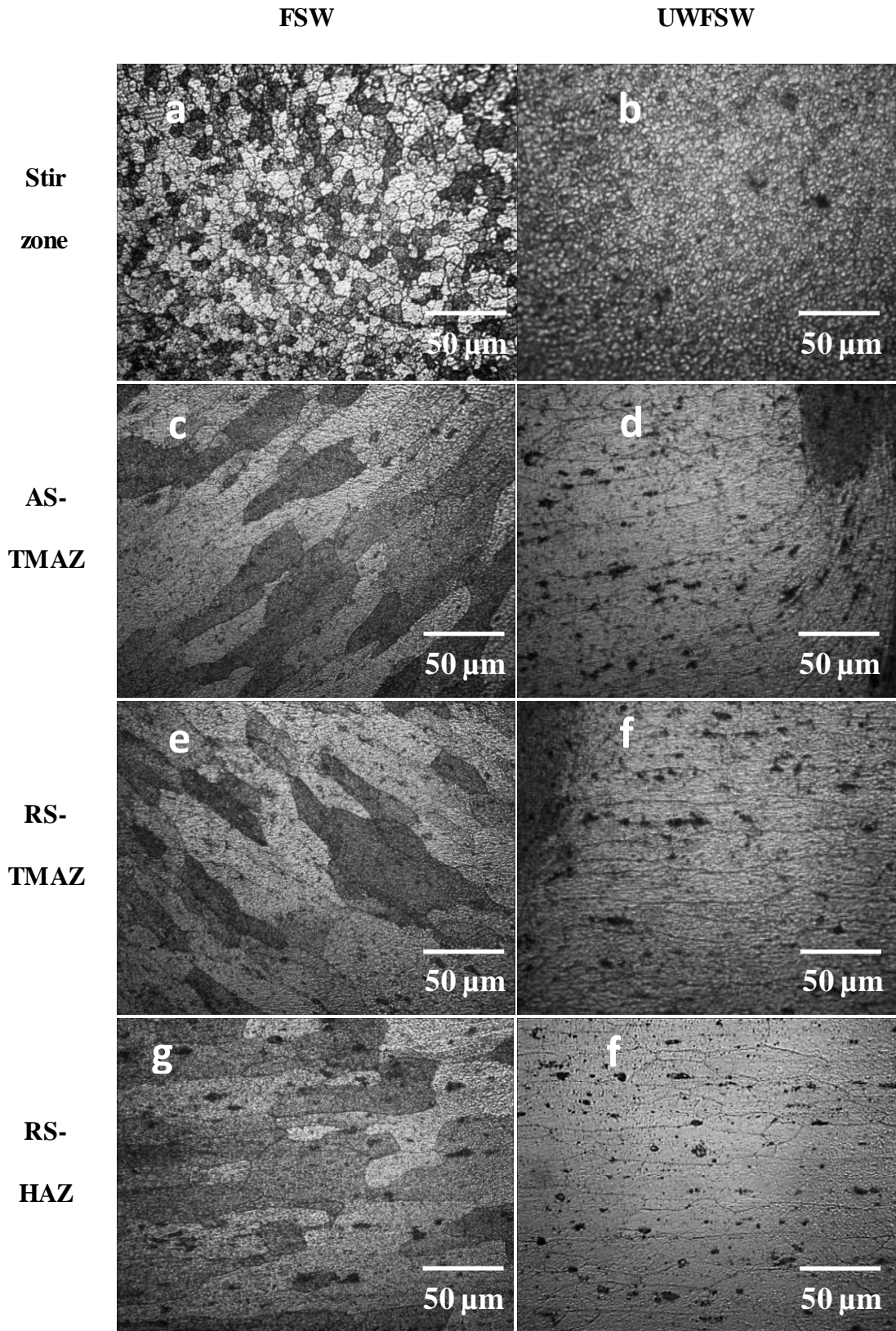
Fig. 4.5 Optical micrograph of the various regions of TTC joint
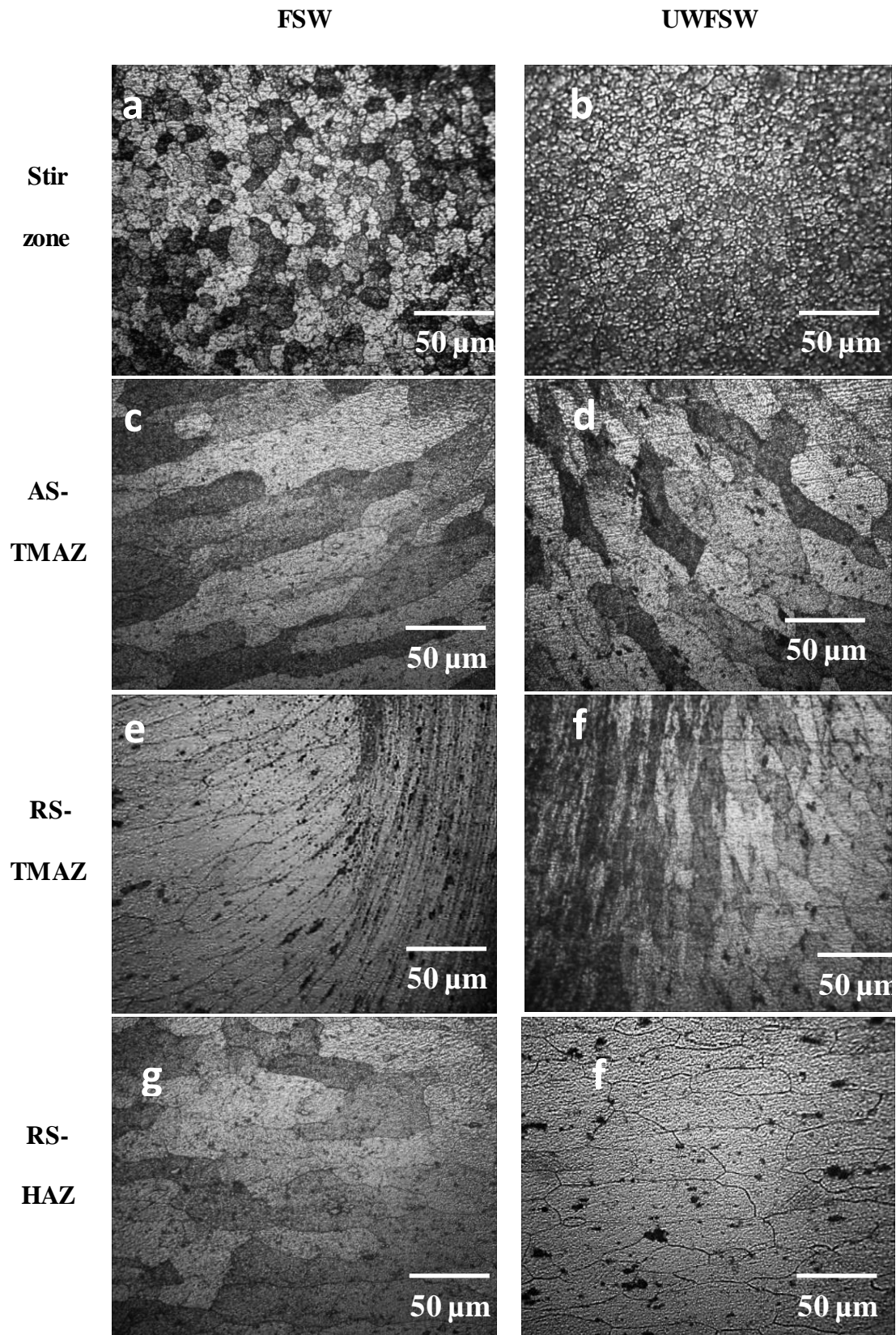
Figs. 4.4c, 4.4d, 4.4e and 4.4f shows the TMAZ micrographs of the joints fabricated using THC in both air and water cooling medium. The AS-TMAZ (advancing side - thermo mechanically affected zone) of joint made by THC profiled tool shows coarse and severely deformed elongated grains at the interface. The RS-TMAZ (retreating side-thermo mechanically affected zone) micrograph is characterized by elongated and upward oriented grains whereas the deformation is gradually reduced from the interface. Figs. 4.5c, 4.5d, 4.5e and 4.5f show the TMAZ micrographs of the joints fabricated using TTC in both air and water cooling medium. The joint fabricated using TTC tool exhibit symmetric material flow in both the AS-TMAZ and RS-TMAZ in both the air cooling and water cooling conditions. The grain size and extent of deformation is more or less similar in both the sides.

Table 4.4 Average grain diameter of various regions

Pin profile	SZ (µm)	AS-TMAZ (µm)	RS-TMAZ (µm)	RS-HAZ (µm)	PM (µm)
FSW-THC	17.5	85	85	64	
FSW-TTC	15	82	82	60	49
UWFSW-THC	5.2	54	54	52	
UWFSW-TTC	3.3	50	50	49	

The average grain diameter of AS-TMAZ and RS-TMAZ are equal and measured as 54 µm and 50 µm for the THC and TTC joint respectively for FSW joints. Similarly, the average grain diameter of AS-TMAZ and RS-TMAZ are equal and measured as 85 µm and 82 µm for the THC and TTC joint respectively for FSW joints. In

comparison, the grain diameter of TMAZ of UWFSW joint is 40 % higher than the FSW joints is respective of pin profiles. It is noticed that the TMAZ micrograph of UWFSW joints shows the interface microstructure from SZ to TMAZ. But at the same magnification level, only a part of TMAZ is seen for the FSW joints. This suggests that the width of the TMAZ region is much wider in FSW joints.

Figs. 4.4g, 4.4f, 4.5g and 4.5f show the HAZ micrographs of the joints It is observed that no mechanically induced deformation took place but grain coarsening occurred in all the joints. The HAZ micrograph of the joint made by THC profiled tool reveals larger grains of 52 μm but TTC joint shows grains of 49 μm in water cooling condition. The HAZ grain size of UWFSW-THC joint is higher than the grain size of PM (of 49 μm) whereas it is equal to the HAZ grain size of UWFSW-TTC joint. In air cooling condition, the HAZ micrograph of the joint made by THC profiled tool reveals larger size of 64 μm but TTC joint shows grains of 60 μm. The FSW joints contain coarser grains in HAZ than the UWFSW joints.

a. **FSW-THC**   b. **UWFSW-THC**

c. **FSW-TTC**   d. **UWFSW-TTC**
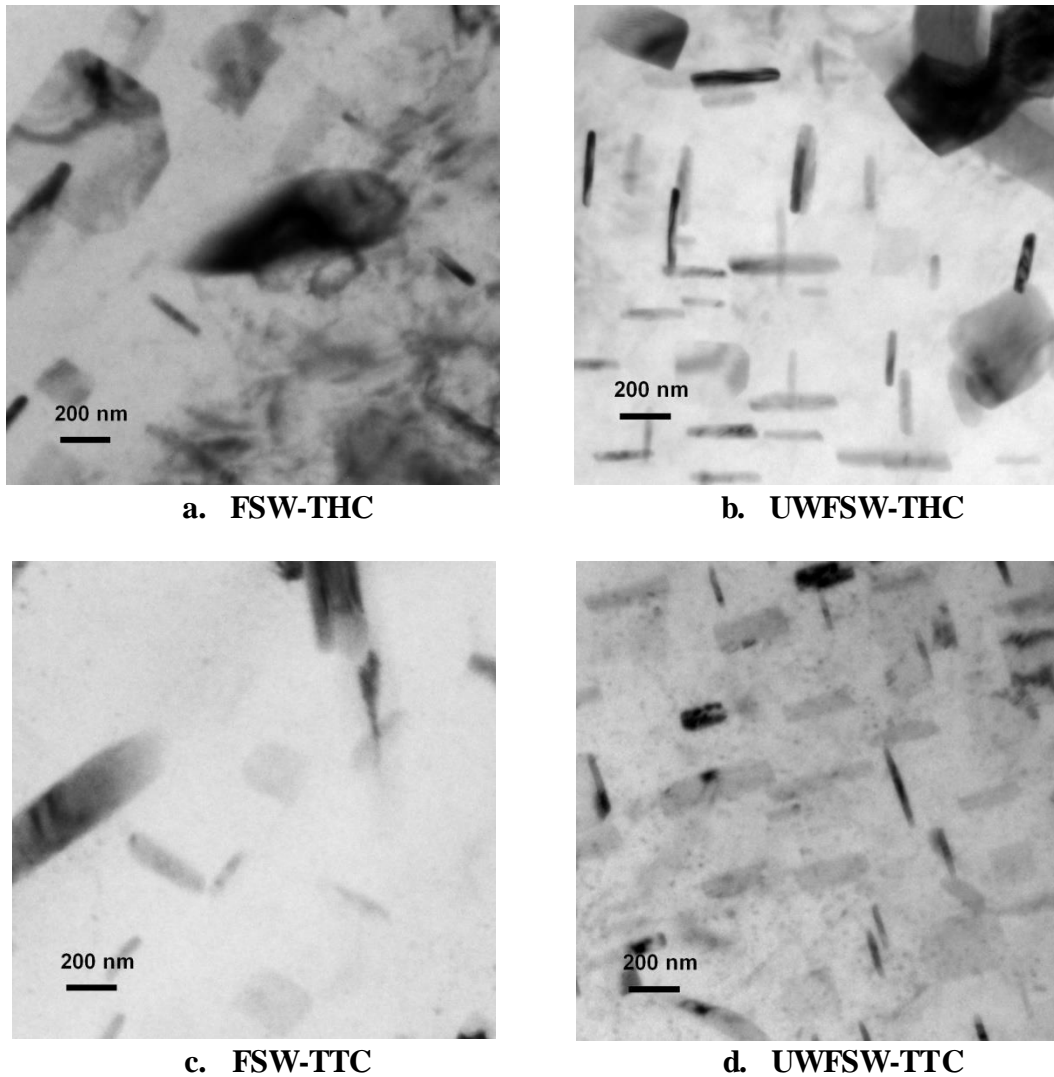
Fig. 4.6 TEM images of LHDR

Fig. 4.6 shows the TEM micrographs of LHDR of all the joints. The LHDR is characterized by the presence of precipitate free zone (PFZ) and coarsened precipitates. LHDR of the joints contain lower volume fraction of precipitates than the parent metal. The FSW joints fabricated using THC and TTC profiled pins show more or less identical precipitation behaviour, however the size of the precipitates of TTC joint is appreciably lower than the THC joints. The LHDR of FSW joints are characterized by the presence of few coarse θ (CuAl$_2$) precipitates and larger PFZ. The dissolution of precipitate is relatively lower in LHDR of UWFSW joints and it is

composed of dense coarse stable θ precipitates. From the TEM micrographs, it is evident that the volume fraction of precipitates is higher in UWFSW joints than in FSW joints.

4.6 DISCUSSION

4.6.1 Effect of tool pin profiles on the joint quality

In UWFSW process, the soundness of joint is decided by the heat generation and the material flow behavior (Mishra and Ma 2005). The heat generation and material flow are classified into three states, namely, insufficient state, balance state and excess state. The tool pin profile is one of the predominant parameters controlling these states. The defect free joints can be made, if the proper tool pin profile is used for making FSW joints (Zhang *et al.* 2011a; Zhang *et al.* 2011b).

In this investigation, the defect free joints were achieved while using THC and TTC pin profiled tools in both air and water cooling medium (Table 4.1). During each rotation of the tool, the threaded profile extrudes cylindrical sheets of material around the tool pin from AS to RS and from RS to AS. The peaks and valleys of threaded pin profile offer more friction over the plasticized material which promotes sticking condition. Thus the extent of heat generation and plasticization is sufficient to attain the balance state of heat and material flow. In general, the defect is formed in the weld periphery i.e the transformed layers around the tool pin. So the pin profile should capable of forming sufficient transforming layers. By creating enough transforming layers by plasticization and shearing of materials, the threaded pin profiles (THC and TTC) are capable of resulting sound joints.

78

The joints fabricated using STC and TAC pin profile, using both cooling medium, resulted in defects at the stir zone. The plain, featureless surface area offers lower friction over the plasticized material which promotes slipping condition. In addition, the featureless surface cannot direct the material flow intensively. Palanivel *et al.* 2012 reported that the plain taper surface results drop in frictional heat because of lower heat generation during sliding over sticking condition. Thus an insufficient heat state is prevailing in the SZ while using the above two pin profiles.

The STC pin profile is plain and straight and thus it exhibits a regular material flow during welding. The material transport from AS to RS and from RS to AS is uniform from SIR to PIR i.e) top to bottom of the joint. Usually it is not preferable because, the heat generation is varied from SIR to PIR. Thus the optimum combination of heat input and material flow is not met throughout the stir zone. The material flow should vary as like heat input to attain the balance state of heat and material flow. The size of the defect is larger in air cooling condition than the water cooling condition. The size of the defect should be reduced as approaching from insufficient heat state to balance state. Thus, it is inferred that, the STC pin profile cannot create defect free stir zone, since the plain and straight profile cannot able to support and direct the material to flow. Thus, in STC joints, the defects are formed primarily due to the attainment of insufficient material flow state rather due to the heat state.

In TAC pin profile, the taper surface is beneficial for aiding upward and downward flow, however the plain, featureless surface area creates lower friction which promotes slipping condition. In under water condition, the heat generated is low and thus insufficient heat state is attained. But, during the air cooling condition, the heat

generated is high and it is approaching the balance heat state. As the heat generated increases, the size of the defect is decreased. Thus, in TAC joints, the defects are formed due to the insufficient heat and material flow state.

Because of the insufficient heat generation and poor material flow, the plastic deformation around the pin is limited and thus the formation of transforming layer is limited. Thus the joints fabricated using STC and TAC tool exhibited defects in the stir zone. The wider transforming layer created around the tool pin with the help of threads is the prime reason for the defect free stir zone formation. By this way, the threaded pin profile tools create the balance state of heat and material flow to form the defect free stir zone.

It is also inferred that the change of cooling medium does not significantly influence the mechanism of defect formation. This is because the FSW process is carried out by localize application of frictional heat and pressure. The heat and pressure experienced is almost similar in FSW and UWFSW joints. The effect of cooling is higher in the TMAZ and HAZ region and minimal in the SZ. However the extent of heat loss from SZ is different which varies the defect size, grain size and resultant mechanical properties.

4.6.2 Effect of tool pin profiles on the mechanical properties of the joints

The age hardenable materials are mainly strengthened due to the presence of fine θ' precipitates. During loading these precipitates act as the obstacle for the dislocation

motion. The coarse stable θ precipitates cannot provide the hindrance effect due to low coherency. From the Hall Petch relation, it was understood that the hardness or strength decreases with an increase in the grain size (Xu *et al.* 2012). The TMAZ micrographs exhibit coarser grains and so reduced grain boundary strengthening is observed in this region. Thus the lower hardness of LHDR is attributed to the low grain boundary strengthening and precipitate hardening.

The heat input governs the above said strengthening mechanism. Decrease in heat input will increase the strengthening effects. Thus the UWFSW joint recorded higher hardness in the entire region than the FSW joint and therefor the UWFSW joint exhibited higher tensile strength than the FSW joint. The higher tensile strength is attributed to the presence of relatively fine grains, high volume fraction of precipitates and appreciably narrow LHDR. On comparing the four joint conditions (FSW-THC, FSW-TTC, UWFSW-THC and UWFSW-TTC), the UWFSW-TTC joint shows enhanced tensile and hardness properties because, this joint experience the lowest temperature compared to its counterparts. So the pin profile capable of formation of the defect free stir zone at the minimum heat input is appreciable.

During tensile loading, the load will concentrate on the weakest zone in the joint. The TMAZ is identified as the LHDR and thus the load is concentrated on it and the failure occurred in this region. This is consistent with the microhardness plot and the fracture locations of both the joints (Fig. 4.3 and Table 4.3). Thus the fracture is occurring in the weakest region, i.e., at TMAZ. The FSW joints exhibit wider LHDR and the UWFSW joints exhibit narrow LHDR near to the weld periphery. Because of wider LHDR, the fracture path is 45˚ to the loading direction and the failure is

occurred by simple shearing. But in UWFSW joints, due to narrowed LHDR, the fracture path is restricted near to the weld periphery and thus the shape of the fracture path is similar to the shape of the weld periphery. In addition the grain orientation difference at the interface offers resistance to the tensile fracture and thus the fracture surface is not smooth.

From the tensile test results, it was observed that the weld joint undergone reduction in the ductility property (Table 4.1). The measures of ductility i.e elongation of the joints were lower than the parent metal. The poor precipitation strengthening and grain boundary strengthening of TMAZ offers less resistance to tensile load. Therefore the load was accommodated in TMAZ which cause yielding of TMAZ. The load concentration phenomenon is called strain localization (Fu *et al.* 2011). Because of strain localization, the TMAZ alone contributes to elongate during tensile loading. Therefore a reduced elongation value was observed in the joints compare to the parent metal. The elongation of joints are almost similar, however the UWFSW joints exhibit lower elongation than the FSW joints. This was attributed to the narrow TMAZ of UWFSW joints which undergone high extent of strain localization than the FSW joints.

4.6.3 Effect of tool pin profiles on microstructure

The heat generation and the plastic deformation during FSW and UWFSW process drive the recrystallization process in the stir zone (Liu *et al.* 2010). Thus a new set of fine grains are observed in the stir zones of the joints fabricated using THC and TTC tools in both the cooling conditions. In the TMAZ, the heat input and the deformation

is not sufficient to recrystallize the grains (Yoon *et al.* 2015). Thus elongated coarse grains are observed in both the joints. The HAZ only experiences the heat and no deformation is occurred, hence this region exhibit undeformed coarse grains. The high heat dissipation capacity of water, readily convect the heat from the SZ, TMAZ and HAZ. Thus the heat availability in UWFSW in various regions is lower than the FSW joints. During the FSW process, the loss of heat due to air cooling is minimal. Because of high heat input and slow cooling rate, the joint fabricated using air cooling medium reveals marginally larger grains and wider stir zone than the joint fabricated using water cooling medium. In FSW joint, the width of TMAZ is wider and it is located away from the weld centerline. This is attributed to the presence of wider stir zone and occurrence of extensive deformation in the TMAZ. In addition to the change of the cooling medium, the change of pin profile has effect in heat generation. The THC profiled tool exhibit larger frictional contact area to create higher frictional heat than TTC profiled tool pin. Thus the THC joint exhibit high heat input and slow cooling rate than the TTC joint.

Zhang *et al.* (2013) referred SZ as the reprecipitation zone, SZ-TMAZ interface as the dissolution zone and TMAZ to HAZ as the overaging zone. During FSW and UWFSW process, the heat generated is high to solutionize the precipitates in the SZ. On cooling cycle, the heat is utilized to reprecipitate in the SZ. In the SZ-TMAZ interface, the heat is sufficient to solutionize the precipitates, but unable to reprecipitate because of the high cooling rate. The heat prevails in the regions from TMAZ to HAZ is not sufficient to solutionize and so coarsening of precipitate is happening in the above said regions. Thus, these regions are termed as overaged

zone. Because of this reason, TMAZ undergone overaging during FSW and UWFSW and coarse precipitates are observed. However, both coarsening and the dissolution of precipitates are observed in the LHDR because of the heterogeneous precipitation. Increase in heat input increases the precipitate size and dissolution of precipitates. Hence the high input FSW-THC joint exhibit low volume fraction of coarse precipitates in the LHDR.

4.7 SUMMARY

The effect of tool pin profiles on the stir zone characteristics and tensile properties of friction stir welded and under water friction stir welded AA2519-T87 aluminium alloy joints was investigated and the following important observations were made:

i. Of the four tool pin profiles used in this investigation, straight threaded cylindrical pin profile (THC) and taper threaded cylindrical pin profile (TTC) yielded defect free weld surface and stir zone formation in both air cooling and water cooling medium. It is attributed to the attainment of optimum level of heat generation and proper material flow during stirring.

ii. The joint fabricated using taper threaded pin profile with water cooling exhibited tensile strength of 345 MPa and joint efficiency of 76 % (29 % higher than FSW-THC joint and 22 % higher than FSW-TTC joint).

CHAPTER 5
EFFECT OF TOOL ROTATIONAL SPEED

5.1 INTRODUCTION

The tool rotational speed is a significant parameter of FSW process which govern the heat generation, microstructure, mechanical properties, etc (Zhang *et al.* 2011; Kim *et al.* 2006). The tool rotational speed also influences the other parameters like translational velocity. Higher tool rotational speed achieved a higher temperature and slower cooling rate in the stir zone in the wake of welding. Higher tool rotational speed causes irrational landing of mixed materials to the upper surface, which resultantly leaves voids in the stir zone. Lower plasticization and poor stirring followed lower tool rotational speed. Higher tool rotational speed results in large sized stir zone and effects higher temperature distribution during welding (Raza *et al.* 2015). The joint property varies with the diverse welding conditions. As the tool rotational speed is increased, both the strength and elongation are increased, reaching a maximum before falling again at high rotational speeds. It is distinct that in FSW, as the rotational speeds increase, the heat input also increases (Li and Liu 2013). At the optimum spindle speed, for a given rotational speed, the strength of the stir zone material is more noteworthy than the parent alloy. Liu 2010; Zhang & Yu (2012) studied the effect of the process parameters on the tensile strength of UWFSW of aluminium alloy joints. They opined that the process parameters had greater effect on the tensile strength of the UWFSW joint. Liu *et al.* (2011) made an investigation to study the effect of tool rotational speed (TRS) on microstructural changes in UWFSW joints of AA2219-T6 alloy. TRS of 600-1400 rpm were accounted for the

85

investigation and found that the void defects were observed at the higher TRS from 1200 to 1400 rpm.

From the above studies, it is understood that the process parameters have significant effect on the joint quality and mechanical properties of the FSW and UWFSW joints. The previous studies demonstrated the feasibility of joining of Al alloys using UWFSW process for enhancing the strength of the joints. However the relationship between the process parameters and the joint performance is not yet systematically investigated. Hence in the present investigation, an attempt has been made to study the effect of tool rotational speed on tensile properties of UWFSW joints and compared with the tensile properties of conventional FSW joints.

5.2 JOINT QUALITY

The close up view of top surface of the FSW and UWFSW joints are shown in Table 5.1. It is observed that defect free top surfaces are (stir zone) resulted irrespective of the cooling condition and tool rotation speed. The stir zone surface is characterized by the presence of smooth, closely spaced ripple formation. It is interesting to observe a white region next to the stir zone in UWFSW joints. The joint quality was further examined by the cross sectional macrograph. The increase in tool rotation speeds from 1100 rpm to 1500 rpm shows variations in the material flow behaviour in both FSW and UWFSW joints. The defect free stir zone formation is observed in the joints fabricated using tool rotation speeds from 1100 rpm to 1400 rpm under air cooling condition. However, defective stir zone is formed in the joint fabricated using tool rotation speed of 1500 rpm. The UWFSW joints fabricated using tool

rotation speeds of 1100 rpm and 1500 rpm contains defects in the SZ whereas the joints fabricated using tool rotation speeds of 1200 rpm to 1400 rpm are free from defects. In this investigation, the defect free joints are considered for further testing and characterization.

Table 5.1 Effect of tool rotation speed on top surface and cross sectional macrographs
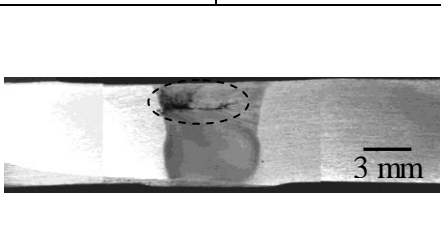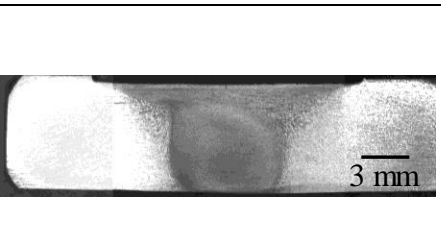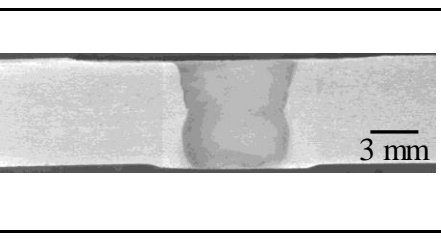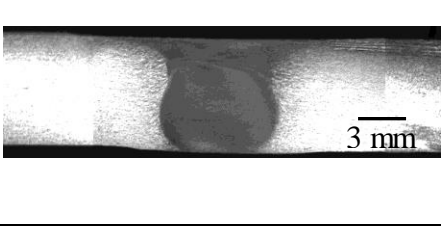
Name of the joint	Top surface	Cross sectional macrograph		Observation
		AS	RS	
UWFSW-1100 rpm		3 mm		Defect free top surface but defect is observed at the advancing side
UWFSW-1200 rpm		3 mm		Defect free stir zone at both top surface and cross section
UWFSW-1300 rpm		3 mm		Defect free stir zone at both top surface and cross section
UWFSW-1400 rpm		3 mm		Defect free stir zone at both top surface and cross section

Table 5.1 (contd.)

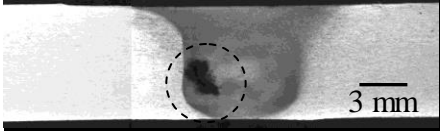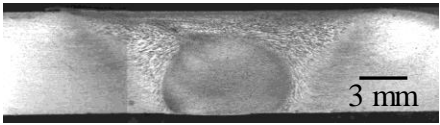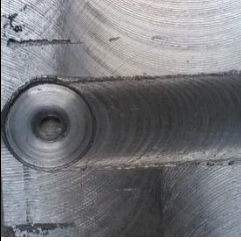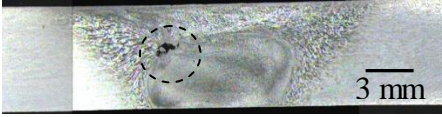| Name of the joint	Top surface	Cross sectional macrograph		Observation
		AS	**RS**	
UWFSW-1500 rpm		3 mm		Defect free top surface but tunnel defect is observed at the advancing side
FSW-1000 rpm		3 mm		Defect free stir zone at both top surface and cross section
FSW-1200 rpm				Defect free stir zone at both top surface and cross section
FSW-1300 rpm				Defect free stir zone at both top surface and cross section
FSW-1400 rpm		3 mm		Defect free stir zone at both top surface and cross section

Table 5.1 (contd.)

Name of the joint	Top surface	Cross sectional macrograph		Observation
		AS	RS	
FSW-1500 rpm			3 mm	Defect free top surface but defect is observed at the advancing side

5.3 TENSILE PROPERTIES

The stress strain curves of FSW and UWFSW joints are shown in Fig. 5.1. From the stress-strain curves, the tensile properties like yield strength, ultimate tensile strength and elongations of the joints were derived and presented in table 5.2. Of the welded joints, the UWFSW joint fabricated using tool rotation speed of 1200 rpm yielded higher tensile strength of 372 MPa which is 21 % lower than the parent metal strength. The FSW joint fabricated using 1100 rpm yielded highest tensile strength of 282 MPa under air cooling condition, which is 38 % lower than the parent metal. The joint efficiency of the UWFSW joint is higher than the FSW joints. The UWFSW joint fabricated using tool rotation speed of 1200 rpm showed highest joint efficiency of 82 %, which is higher than the joint fabricated using same tool rotation speed under air cooling. It is clearly evident that all the joints exhibited lower ductility (percentage of elongation) than the PM. But there is no appreciable variation in ductility of the joints irrespective of the tool rotation speed and the cooling medium.
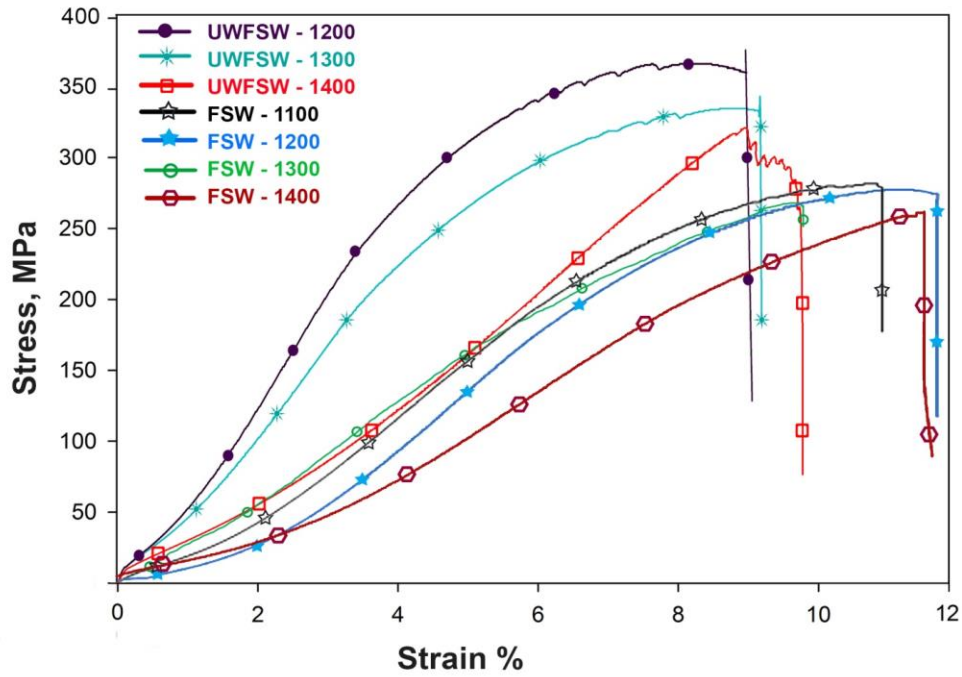
Fig. 5.1 Stress strain curves

Table 5.2 Transverse tensile properties of the joints

	0.2 % Yield strength (MPa)	Tensile strength (MPa)	Elongation in 50 mm gauge length (%)	Joint efficiency (%)
UWFSW-1200	344	372	9.01	82
UWFSW-1300	322	345	9.17	76
UWFSW-1400	295	319	9.85	70
FSW-1100	260	282	10.4	62
FSW-1200	255	275	10.5	60
FSW-1300	230	267	9.85	59
FSW-1400	245	260	10.82	57

The entire fracture path can be revealed from the cross sectional macrographs of the tensile tested samples (Table 5.3). The fracture path can be correlated with the microhardness plot. It is interesting to observe that the fracture is occurred in the

90

LHDR of the microhardness plot. It shows a good agreement between the LHDR and fracture location. In the FSW joints fabricated using tool rotation speed of 1200 to 1400 rpm, the fracture path is 45° inclined to the tensile loading direction. But in the UWFSW joints, an irregular fracture path along the outer periphery of the stir zone was observed. The similar irregular fracture path is observed in the FSW joint fabricated using lower tool rotation speed of 1100 rpm. Fig. 5.2 shows the fracture surface at macro and micro level magnification. At the macro level, the FSW joint exhibits more or less flat feature surface. But, the UWFSW joints exhibits two types of patterns in the fracture surface one at SIR and another at PIR. At higher magnification, all the joint exhibit fine dimples in the fracture surface. However the fracture surfaces of FSW joints exhibit a less number of dimples than the UWFSW joints. The presence of dimples resembles that all the joints undergone ductile mode of failure during the tensile test.

Table 5.3 Effect of tool rotational speed on fracture path
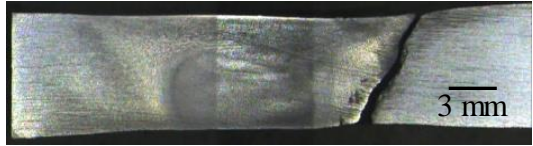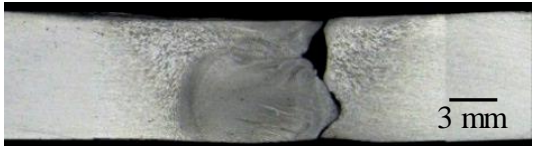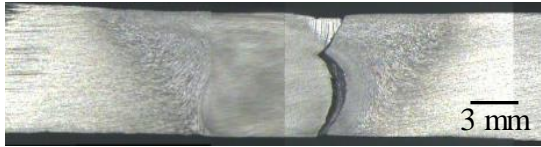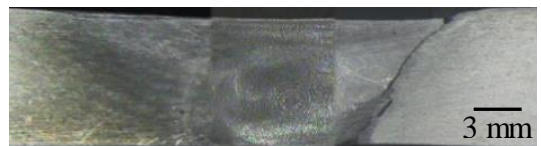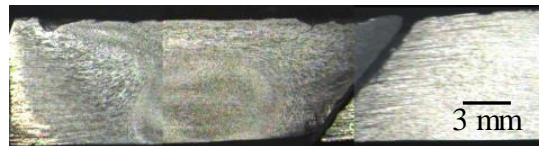
Name of the joint	Fracture path		Observation
	AS	RS	
UWFSW-1200	3 mm		Fracture is occurred in the RS-TMAZ which is 45° inclined to the loading direction
UWFSW-1300	3 mm		Fracture is occurred in the TMAZ in which the fracture is irregular
UWFSW-1400	3 mm		Fracture is occurred in the TMAZ in which the fracture is irregular

91

Table 5.3 (contd.)

Name of the joint	Fracture path		Observation
	AS	RS	
FSW-1100			Fracture is occurred in the TMAZ in which the fracture is irregular
FSW-1200			Fracture is occurred in the RS-TMAZ which is 45° inclined to the loading direction
FSW-1300			Fracture is occurred in the RS-TMAZ which is 45° inclined to the loading direction
FSW-1400			Fracture is occurred in the RS-TMAZ which is 45° inclined to the loading direction

Tool rotational speed	Macro level fracture surface	SEM fracture surface
UWFSW-1200		
UWFSW-1300		
UWFSW-1400		
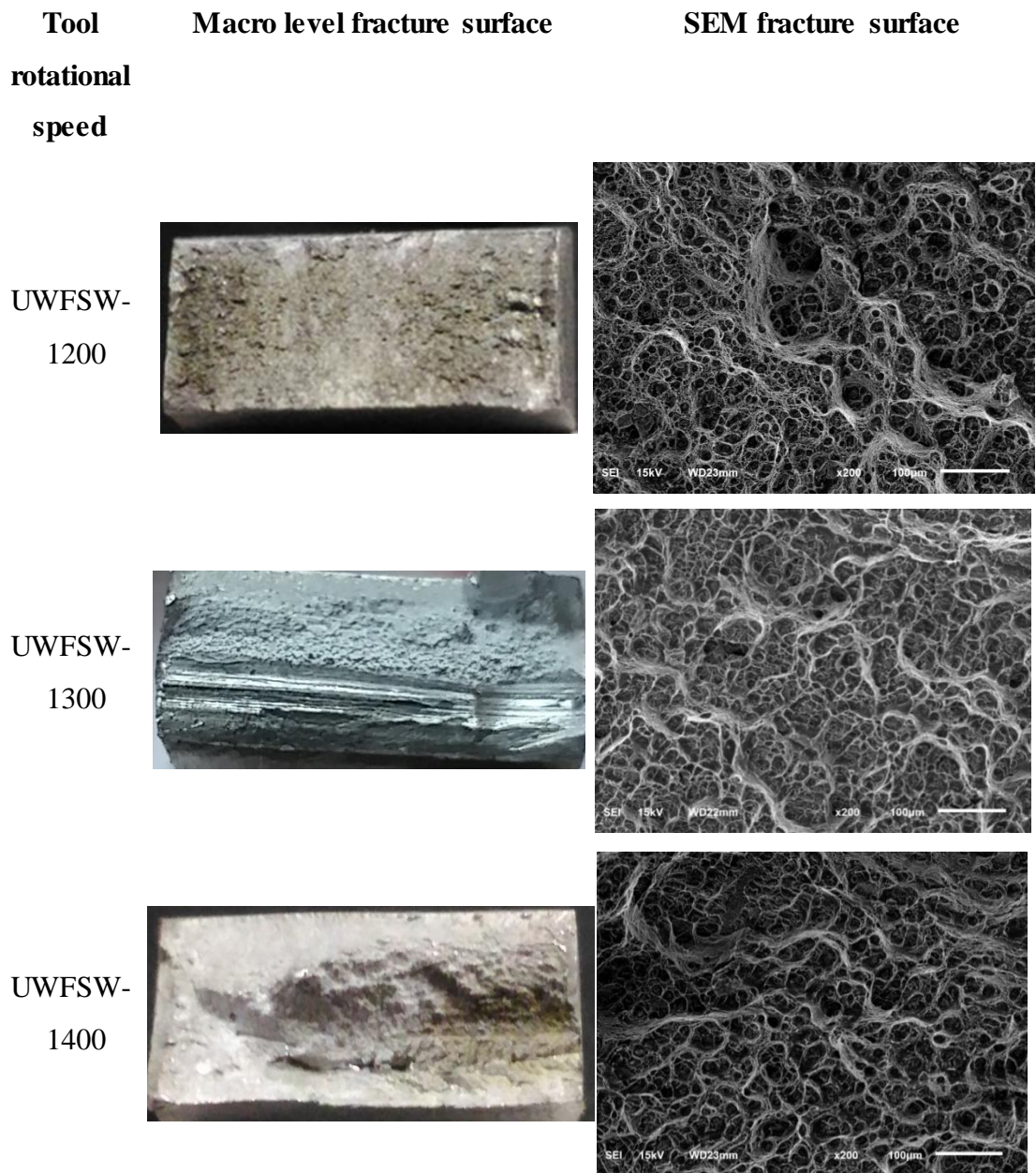
Fig. 5.2 Fracture surface analysis

FSW-1100
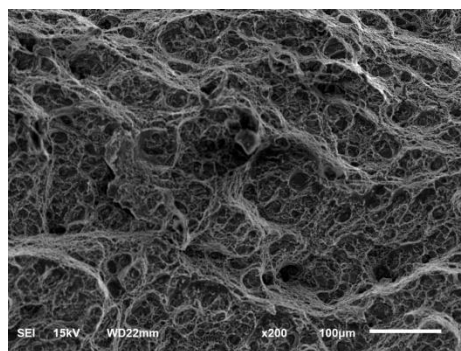
FSW-1200
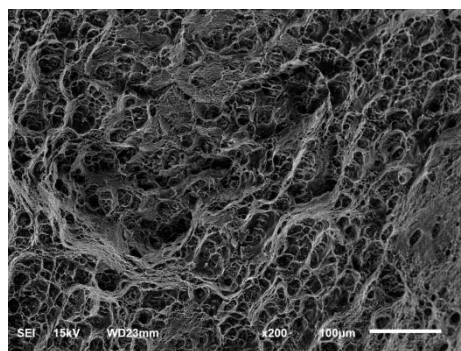
FSW-1300
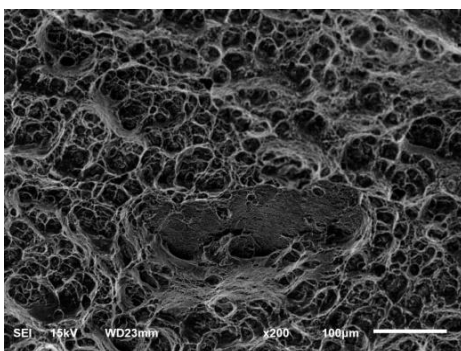
FSW-1400
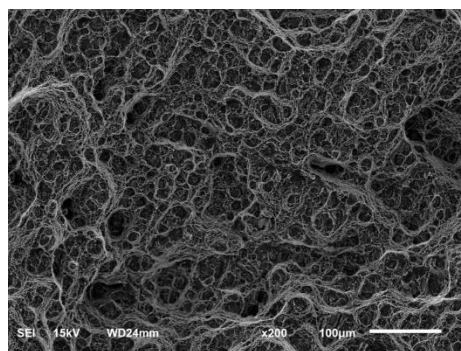
Fig. 5.2 (contd.)

5.4 MICROHARDNESS

Fig. 5.3 shows the microhardness plots of the various joints. It is observed that, typical 'W' shaped hardness plots are observed in all the joints. Among the various regions, the TMAZ on both the AS and RS exhibits lower hardness which can correlated with the macrostructure placed with. The FSW joint fabricated using tool rotation speed of 1400 rpm exhibit lowest hardness of 78 HV whereas the joint fabricated using same tool rotation speed under water cooling exhibit hardness value of 88 HV. It is observed that the UWFSW joints exhibit higher hardness than the FSW joints in all regions. Yet the hardness in the stir zone of all the joints does not exhibit significant variations. The scattered values in the SZ show a zigzag trend plot. The hardness in the SZ is higher than the TMAZ. The SZ of UWFSW joint fabricated using tool rotation speed of 1200 rpm exhibit higher hardness of 107 HV whereas lower hardness of 101 HV was recorded in the UWFSW joint fabricated using tool rotation speed of 1400 rpm. There observed abrupt increment in the hardness from HAZ to PM in the UWFSW joint whereas a gradual increment is observed in FSW joints. The hardness in the HAZ is remarkably higher than the TMAZ region. It is necessary to note that the LHDR of FSW far away from the weld center of the UWFSW joints.
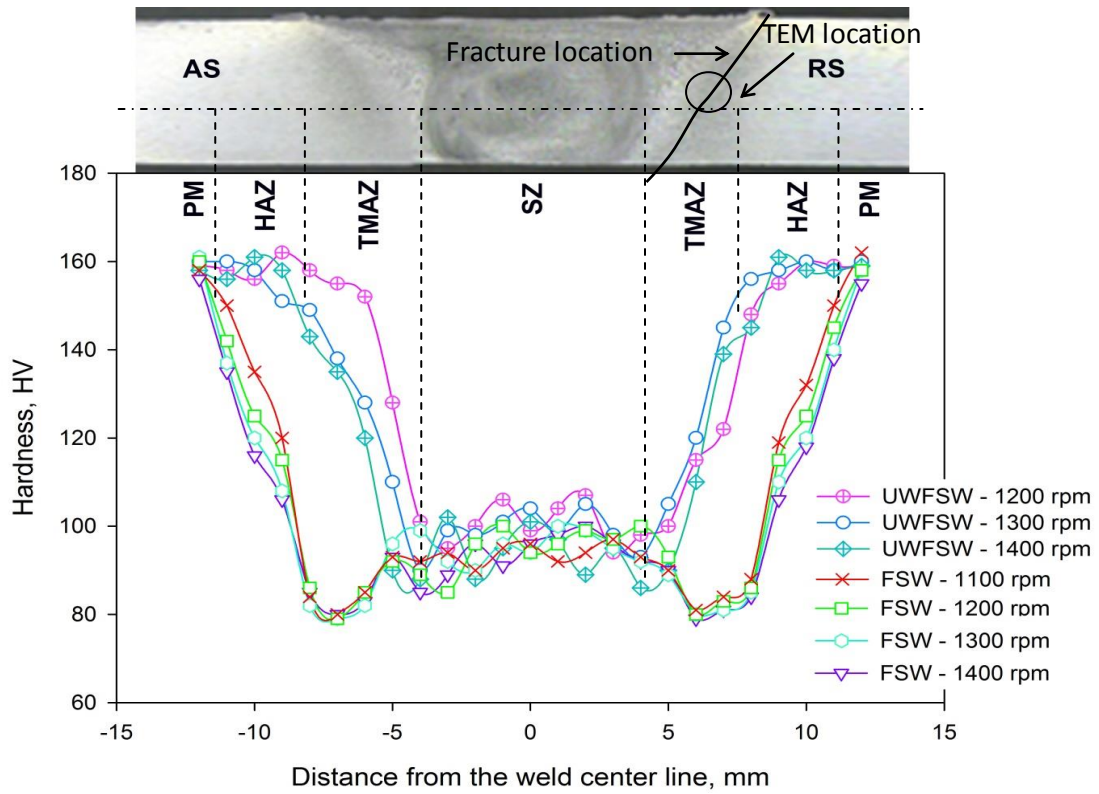
Fig. 5.3 Microhardness plot

5.5 MICROSTRUCTURE

Figure 5.4 and 5.5 shows the optical micrographs of the various regions of UWFSW and FSW joints. The stir zone is characterized by the presence of fine equi-axed recrystallized grains irrespective of the change in tool rotation speed and the cooling medium. The average grain size of each joint was measured and presented in table 5.4. It can be observed that the grain size of the SZ increases with increase of tool rotation speed under both the cooling medium. As the tool rotation speed increases from 1200 rpm to 1400 rpm, the grain size respectively, increases from 2.5 μm to 4.2 μm under water cooling condition. Similarly, as the tool rotation speed increases from 1100 rpm to 1400 rpm, the grain size respectively, increases from 11 μm to 17 μm under air cooling condition. The UWFSW results in finer grains than the FSW

96

joints in all the joints fabricated under varying tool rotation speed. The smaller grain size of 4.2 μm is obtained in the SZ of the joint fabricated using 1400 rpm under water cooling condition. But, higher grain size of 17 μm is observed in the joint fabricated using 1400 rpm under air cooling condition.

The recrystallization of grains are not observed in the TMAZ, whereas severely deformed grains are observed. The severity of deformation of grains is higher in the UWFSW joints whereas gradual deformations of grains are observed in the FSW joints. In UWFSW joints, more or less symmetrical material flow is observed, so that there is no obvious variation in the grain size of AS-TMAZ and RS-TMAZ. The average grain size is found to be to be 50 μm and 54 μm in the joint made using tool rotation speeds of 1300 rpm and 1400 rpm respectively. But in FSW joint, no symmetrical material flow is observed in the AS-TMAZ and RS-TMAZ. The grains deformed abruptly in the AS, whereas the grains deformed gradually in the RS. The average grain diameter of the RS-TMAZ is higher than the AS-TMAZ. It is noted that the TMAZ micrograph of UWFSW shows the interface microstructure which composes of partial HAZ, TMAZ and partial SZ. But at the same magnification level, just a part of TMAZ is seen in the FSW joints. From this it can be inferred that the TMAZ in FSW joints is wider than the UWFSW joints. The HAZ micrographs are composed of coarse elongated grains oriented towards the rolling direction. The grains are not undergoing mechanically induced deformation but only grain coarsening is observed in all the joints. The average grain size of HAZ of UWFSW joints is more or less equal to the parent metal grain size. But the average grain size of HAZ of FSW joints is higher than the parent metal.

	1200 rpm	1300 rpm	1400 rpm
SZ	a	b	c
AS-TMAZ	d	e	—
RS-TMAZ	g	h	i
AS-HAZ	j	—	l
RS-HAZ	m	n	o
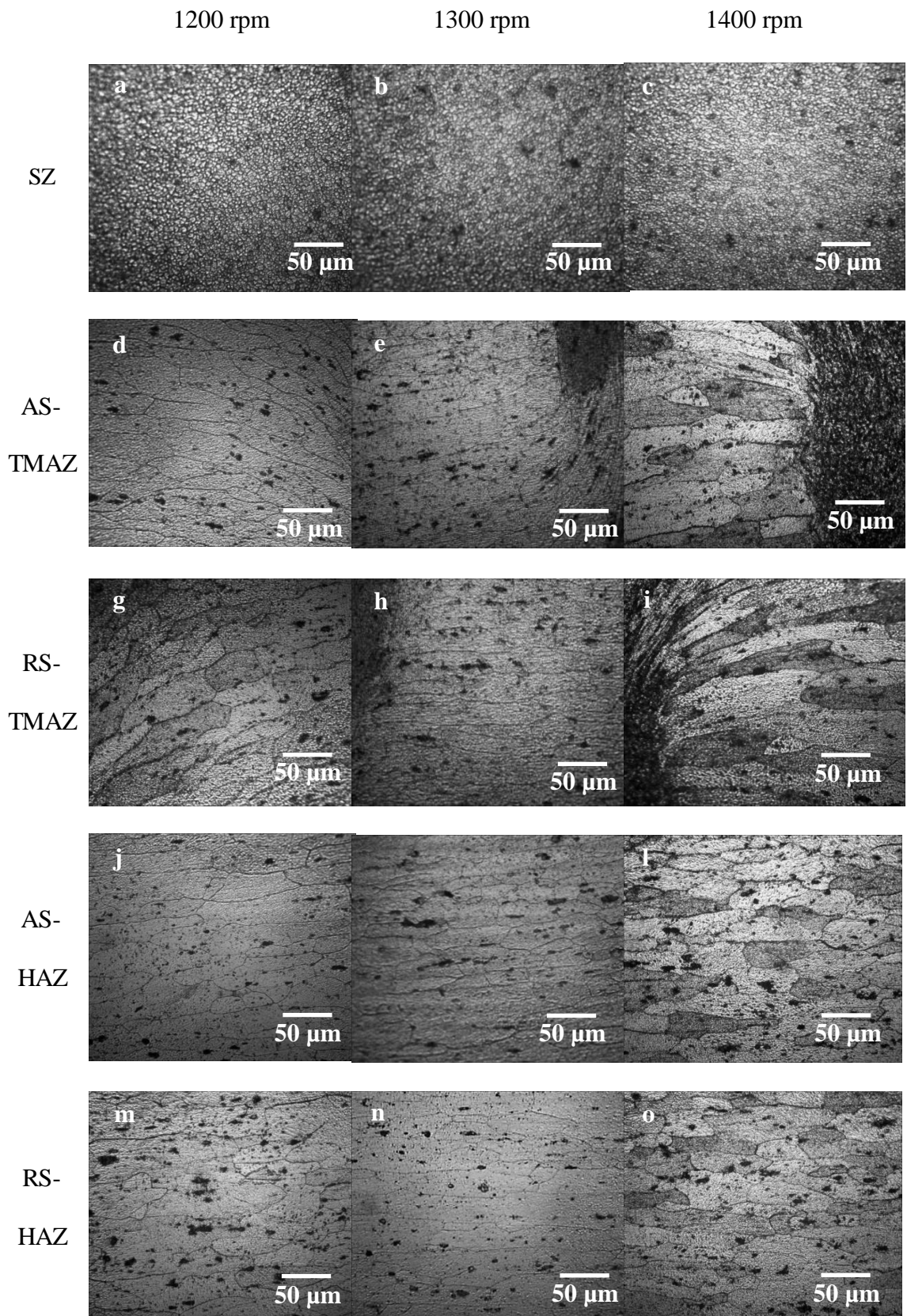
Fig. 5.4 Optical micrographs of various regions of UWFSW joints
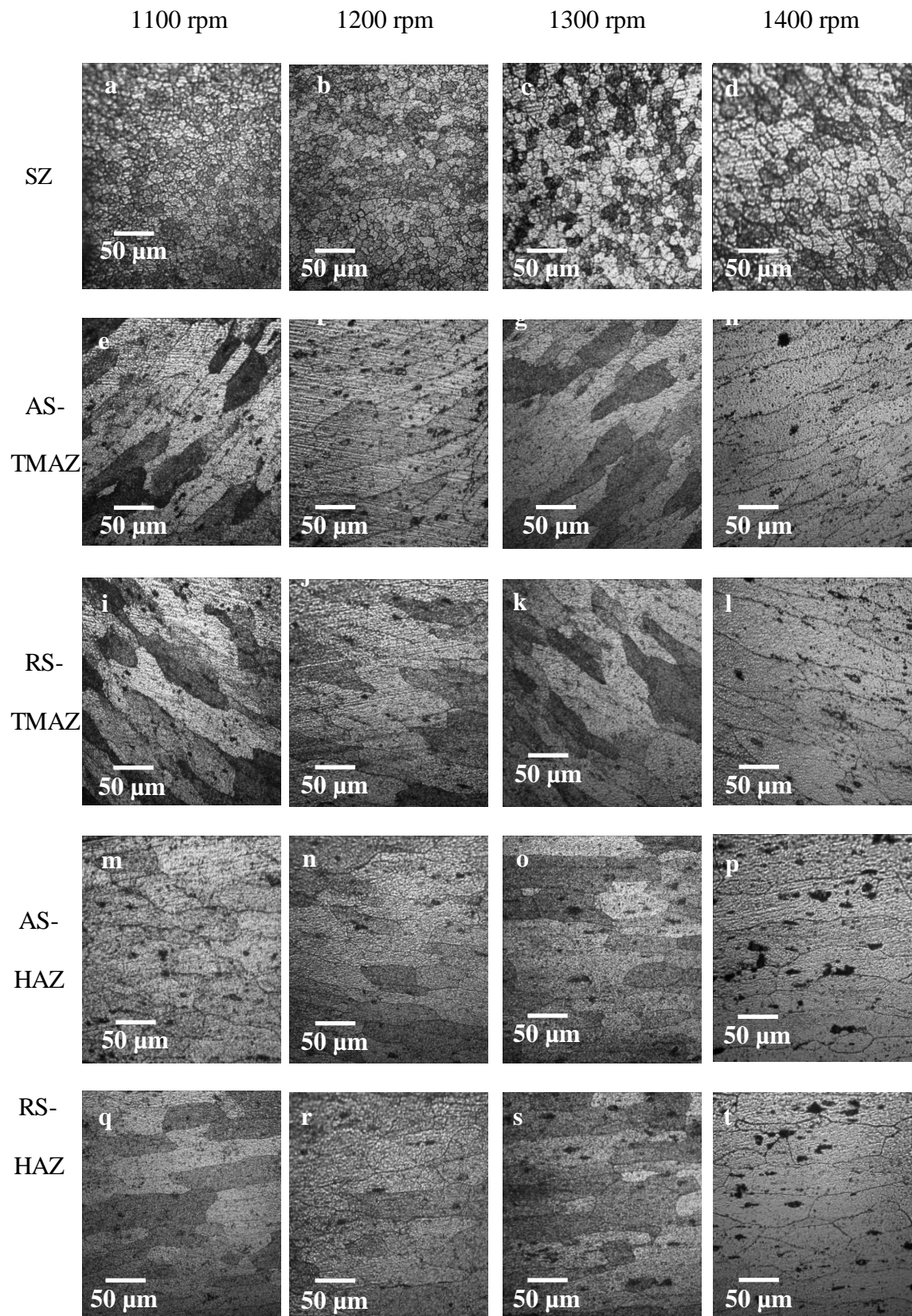
Fig. 5.5 Optical micrographs of various regions of FSW joints
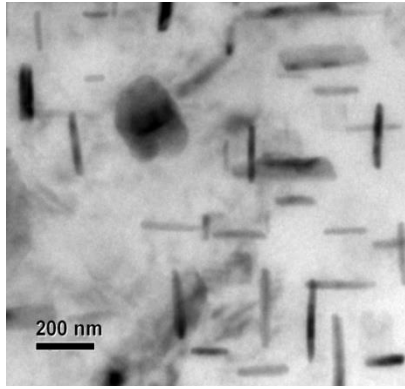
a. UWFSW-1200 rpm
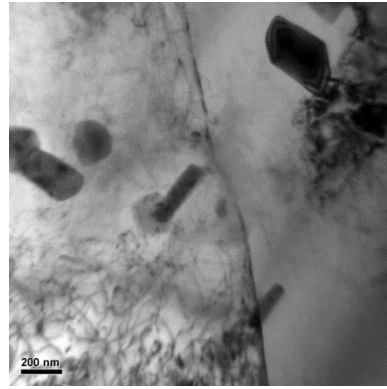
b. FSW-1200 rpm
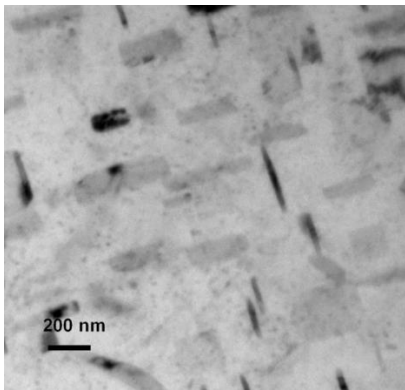
c. UWFSW-1300 rpm
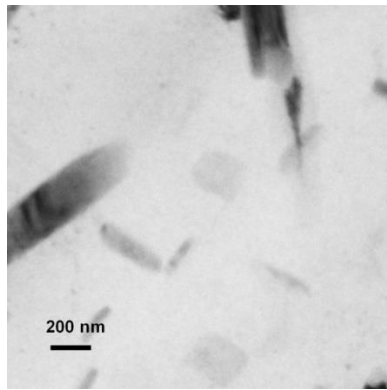
d. FSW-1300 rpm
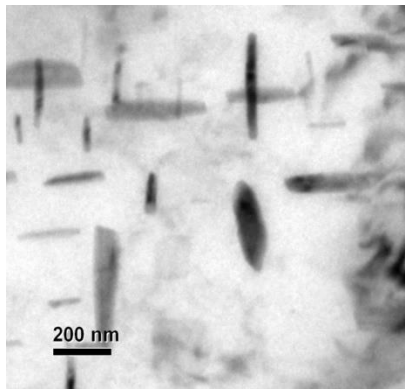
e. UWFSW-1400 rpm
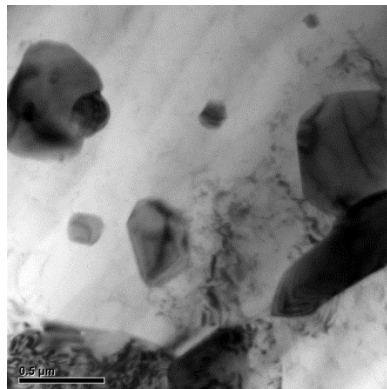
f. FSW-1400 rpm

Fig. 5.6 TEM micrographs

Table 5.4 Average grain diameter at various regions of the joints

Tool rotational speed	SZ (µm)	AS-TMAZ (µm)	RS-TMAZ (µm)	RS-HAZ (µm)	PM (µm)
UWFSW-1200	2.5	49	50	49	
UWFSW-1300	3.3	50	50	49	
UWFSW-1400	4.2	54	54	51	
FSW-1100	11	78	81	59	49
FSW-1200	12.5	80	82	60	
FSW-1300	15	82	82	60	
FSW-1400	17	85	86	62	

The LHDR i.e. the TMAZ is further characterized using TEM (Figure 5.6). From the micrographs of the LHDR, it can observe that coarsening and dissolution of precipitates occurred in all the joints. Nevertheless, the volume fraction of the precipitates varies in each LHDR. The TEM micrograph of the LHDR is characterized by the presence of coarse stable θ precipitates and the precipitates free zone (PFZ).

5.6 DISCUSSION

5.6.1 Effect of tool rotation speed on the joint quality

The quality of the FSW process is mainly depends on the heat generation and the material flow behaviour. The process parameters, tool dimensions and tool profiles are varied to attain the temperature and the material flow required for the defect free quality joint. An optimum combination of balance state of heat generation and balance state of material flow yields sound joints (Zhang *et al.* 2011). Tool rotation speed is an important process parameters of the FSW process which have greater

influence in the amount of heat generation and rate of heat generation and thereby it influence the material flow (Zhang *et al*. 2011). The rate of heat generation is one of the important aspects in the UWFSW process. Due to the water cooling, the material at the leading edge remains cold i.e the preheat zone is very confined and limited plasticization prevails. If the rate of heat generation is lower as the tool forwards due to poor thermal softening of ahead material, it will end up with defect formation.

At lower tool rotation speed, due to poor rubbing of the tool, the amount of heat generation and the rate of heat generation are in insufficient state. This is the reason for the defect formation in the joint fabricated using tool rotation speed of 1100 rpm under water cooling condition. But, the FSW joint results in defect free SZ formation at tool rotation speed of 1100 rpm. The poor heat absorption capability of air is not capable of dispersing the heat readily from the junction. Hence the heat gets buildup and thereby balance state of heat is attained in the FSW joint even at the lower tool rotation speed. The rate of heat generation is not so important in FSW, because it has a wider preheat zone. The material in the preheat zone was softened. On stirring the material flow more easily and so the defect free SZ was formed in the joint fabricated at the lower tool rotation speed of 1200 rpm.

The joint fabricated using higher tool rotation speed of 1500 rpm results in formation defects in the SZ in both FSW and UWFSW joints. Due high rubbing force, excess state of heat is attained which results in turbulent flow of materials. Moreover, due to the excess plasticization, the material get soft and therefore exhibit poor friction over the tool. This will promote the slipping of material and thereby resulted in defect

formation (Palanivel *et al.* 2012). This is the reason for the defect formation in the higher tool rotation speed of 1500 rpm. The joint fabricated using the tool rotation speeds of 1200 rpm to 1400 rpm results in defect free stir zone formation in both air and water cooling condition. This is attributed to attainment of balance state of heat and material flow.

5.6.2 Effect of tool rotation speed on the mechanical properties of the joints

Grain boundary strengthening and the precipitation hardening are the two main strengthening mechanisms decide the joint performance. The microstructural features in the various regions, especially in the LHDR significantly vary with respect to the tool rotation speed and thereby varies the mechanical properties. The extent of grain boundary strengthening can be expressed using Hall-Petch relation (Genevois *et al.* 2004). It states that the strength or the hardness is inversely proportional to the average grain size of the region. From the grain size measurements, it was inferred that the stir zone exhibit fine grains. The fine grains composed of numerous grain boundaries which offered resistance to the motion of dislocations during indentation or loading (Xu *et al.* 2012). Therefore the stir zone exhibits higher hardness than the TMAZ. The grains in the TMAZ underwent coarsening of grains, especially the joints fabricated using higher tool rotation speeds exhibits higher grain size. Because of the coarse boundary, the availability of the grain boundaries is very low and so it offers less resistance to dislocation motion Dieter DE (1986). Thus the grain boundary strengthening in the TMAZ is low.

It is obvious to note that the tensile fracture is exactly observed in the LHDR i.e., TMAZ region. From this, it can infer that the tensile strength and elongation are depending on the hardness in the LHDR of the joint. (Liu *et al.* 2003). The strength contribution by precipitation hardening is significant in the age hardenable alloys. The presence of fine precipitates offers more resistance to the dislocation motion and thereby it results in high strength or hardness (Sree *et al.* 2015). From the TEM microstructures of LHDR, it can evident that the change in cooling medium and tool rotation speed varies the precipitation behaviour. The higher volume fraction of the precipitates in the LHDR of UWFSW joints offers more hindering force than the FSW joints. Consequently, the hardness in the LHDR of UWFSW joints shows significant improvement than the FSW joints. The adjacent HAZ region of UWFSW joints shows a sharp increase in the hardness were as a relatively gradual increase in hardness was observed. Zhang *et al* referred SZ as the reprecipitation zone, SZ-TMAZ interface as the dissolution zone and TMAZ to HAZ as the overaging zone (Liu *et al.* 2011). The heat conducted to the HAZ of UWFSW was lower and it experience higher cooling rate due to the water cooling. By this way the overaging of HAZ is controlled greatly in the UWFSW joints than the FSW joints. This is the cause for the higher hardness in the HAZ of UWFSW joints than the FSW joints. On the other hand, the hardness in the HAZ of the UWFSW joints varies significantly with respect to the tool rotation speed. The low heat input created at low tool rotation speed exhibit high extent of control of overaging in TMAZ and HAZ. This is the primary cause for the higher hardness of the joint fabricated using tool rotation speed of 1200 rpm under water cooling condition.

During tensile loading, the load will concentrate in the softer zone of the joint which is called as strain localization. From the microhardness plot, TMAZ was identified as the softer region. Therefore the LHDR accommodate the load and so the tensile fracture was occurred exactly in the LHDR. The marginal improvement in the hardness of LHDR will increase the tensile strength by offering resistance to strain localization (Fonda and Bingert 2014). It is also noted that the weld joint exhibits lower elongation than the parent metal. This is because, the weakest region alone contributes to elongate by strain localization (Liu *et al.* 2010). Despite of the reduction in elongation, the inherent ductility property of parent metal is not significantly varied by the tool rotation speed or cooling medium. This is more evident from the fractographs in which all the joints show dimples on the fracture surface.

5.6.3 Effect of tool rotation speed on microstructure

The intense plastic deformation enabled by tool stirring and the heat generation enabled by tool rubbing promotes the recrystallization process in the SZ. (Fonda *et al.* 2006). This is the reason for the formation of a new set of fine grains in the SZ of all the joints. The heat and the plastic deformation are insufficient to recrystallize the grain in the TMAZ of all the joints. The adjacent region HAZ experience only the thermal cycles and no deformation take place over there. Hence undeformed coarse elongated grains are observed in the HAZ of all the joints.

Though the deformation and grain refinement or coarsening aspects are similar in all the joints, the grain size and the extent of deformation are varies based on the thermal

105

cycles experienced. In UWFSW process, the water dissipates the heat readily from the joint. Hence, less degree of heat and higher cooling rates were prevailed in the joint. This limits the grain growth remarkably and so the UWFSW joints exhibit lower grain size than the FSW joints. It also limits the precipitate coarsening and dissolution in the LHDR (Marceau *et al.* 2010). Among the UWFSW joints, the joint fabricated using lower tool rotation speed results in lower most grain size because of lower frictional heat input.

The high heat input increases the extent of deformation of thermal softening of materials and so the extent of plastic deformation is higher in the FSW joints. Therefore the width of the SZ and the TMAZ were larger than the UWFSW joints. The high heat dissipation capacity of water limits the plastic deformation in the SZ and TMAZ. Thus a narrowed dynamic volume of SZ and TMAZ were observed in the UWFSW joints.

In summary, the tool rotation speed must be lower, but enough to produce sufficient (optimum) state of frictional heat and resultant material flow to yield defect free joints with high. The present investigation demonstrates that the lower tool rotation speed results in insufficient state and the higher tool rotation speed results in excess state of heat generation which leads to defect formation. The poor joint quality is attributed to the inadequate tool stirring and the poor joint properties are owing to the high heat input.

5.7 SUMMARY

The effect of tool rotation speed on the stir zone characteristics and tensile properties of friction stir welded (FSW) and under water friction stir welded (UWFSW) AA2519-T87 aluminium alloy joints was investigated and the following important observations were made:

i.   UWFSW joints fabricated using tool rotation speed in the range of 1200-1400 rpm and FSW joints fabricated using tool rotation speed in the range of 1100-1400 rpm yielded defect free joints. It is attributed to the attainment of adequate heat generation and proper material mixing during stirring.

ii.   UWFSW joint fabricated using tool rotation speed of 1200 rpm exhibited maximum tensile strength of 372 MPa and joint efficiency of 82 %. On the other hand, tool rotation speed of 1200 rpm yielded maximum tensile strength of 282 MPa in conventional FSW joints. UWFSW joint showed 24 % higher joint efficiency compared to FSW joints.

CHAPTER 6
EFFECT OF TOOL TRAVERSE SPEED

6.1 INTRODUCTION

The tool travel speed determines the extent of time for which the pre-welded material is subjected to the hotness and deformity. An optimum selection of the process parameters is the key factor to create sound joints. This distinction in speeds decides the degree of asymmetric in the weld piece (Reza 2015). Ulysse et al (2002) found that pin forces increase with increasing welding speeds. It has been observed that presence of voids in the stir zone is related to the tool traverse speed (Ramachandran *et al.* 2015). Savolainen *et al.* (2012) demonstrates the impact of welding speed on the defect formation in the stir zone. The amount and severity of welding defect grows as a function of the deviation from the welding parameter window. Tool traverse speeds have greater influence on the formation of welding defects in the welds. Around the area where defect-free welds are formed, the amount and severity of welding defects grows as a function of the deviation from the values of the welding parameter window (Lakshminarayanan *et al.* 2011). Hidetoshi *et al.* (2006) investigated the temperature observations by experiment and numerical methods. The results showed that the temperature distribution is affected by the welding speed and also concluded that the lower welding speed is corresponds to a higher peak temperature. Of the many process parameters, tool travel speed is a significant parameter which has greater effect on heat generation. Moataz and Hanadi (2005) have reported that the tool travel speed had greater effect on the grain growth of friction stir welded AA2095 aluminium alloy.

From the above reviews, it is understood that the tool traverse speed is an important process parameter, which decides the heat generation and subsequent joint characteristics. Though the previous studies on UWFSW demonstrated the enhancement in strength and hardness properties, the relationship between the process parameters on the joint quality, microhardness and the tensile properties were not yet systematically investigated. Hence in this investigation, an effort has been made to understand the effect of tool traverse speed (TTS) on the stir zone formation and the resultant tensile properties of the UWFSW of AA2519 T87 aluminium alloy joints.

6.2 JOINT QUALITY

The joint quality of FSW and UWFSW joints were inspected on the top surface and cross section by macrographs (Table 6.1). The top surface of all the joints were free from defects. The top surface of the weld was characterized by the presence of closely consolidated ripples. The joint quality was further examined from the cross sectional macrographs. The change in tool traverse speed caused notable variations in the stir zone formation. The UWFSW joint fabricated using TTS of 20 mm/min to 30 mm/min resulted in defect free stir zone. However, UWFSW joints fabricated at the higher TTS of 35 mm/ min and 40 mm/ min are resulted with defects in the stir zone. Similarly the FSW joints fabricated using TTS of 25 mm/min to 40 mm/min resulted defect free stir zone, whereas TTS of 20 mm/ min resulted with a defect in SZ. In this investigation, the defect free joints are considered for further microstructural examination, microhardness measurements and tensile testing.

Table 6.1 Effect of tool traverse speed on top surface and cross sectional macrographs
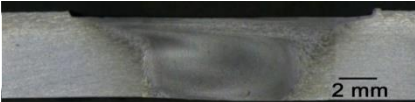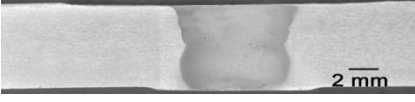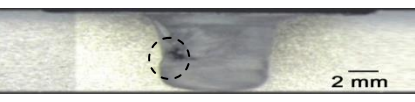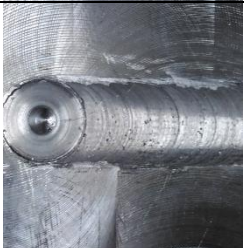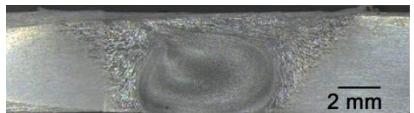
TTS, mm/min	Top surface	Cross sectional macrograph		Observation
		AS	RS	
UWFSW-20				Defect free stir zone (top surface and cross-section)
UWFSW-25				Defect free stir zone (top surface and cross section)
UWFSW-30				Defect free stir zone (top surface and cross section)
UWFSW-35				Defect free top surface but defect in the mid-thickness region
UWFSW-40				Defect free top surface but tunnel defect at the advancing side

Table 6.1 (contd.)

TTS, mm/min	Top surface	Cross sectional macrograph		Observation
		AS	RS	
FSW-20				Defect free top surface but pinhole defect at the mid-thickness region of AS
FSW-25				Defect free stir zone (top surface and cross-section)
FSW-30				Defect free stir zone (top surface and cross-section)
FSW-35				Defect free stir zone (top surface and cross-section)
FSW-40				Defect free stir zone (top surface and cross-section)

6.3 TENSILE PROPERTIES

Fig. 6.1 shows the stress strain curves of the joints fabricated using different TTS. The tensile properties like tensile strength, yield strength, percentage of elongation and joint efficiency were derived from the stress strain diagram and presented in the

table 6.2. The UWFSW joint fabricated using TTS of 30 mm/min yielded higher tensile strength of 345 MPa and joint efficiency of 76 %. The FSW joint fabricated using tool traverse speed of 25 mm/min showed lower tensile strength of 258 MPa and joint efficiency of 57 %. It is noted that, the increase in tool traverse speed increases the tensile properties. The tensile strength is higher in UWFSW joints than the FSW joints. It is observed that the joint efficiency is enhanced by 25 % and 28 % in the UWFSW joints fabricated using TTS of 25 mm/min and 30 mm/min than the respective FSW joints.   However, the percentage of elongation does not show any significant variation with respect to the welding process and TTS but the percentage of elongation of the joints is lower than the parent metal.

Table 6.3 reveals the tensile fracture path of the various joints. The tensile fractures invariably occurred exactly at the TMAZ of all the joints. While correlating the fracture path of the joints with the respective micro hardness plots, TMAZ could be identified as the weakest region (i.e LHDR). Two shapes of fracture paths are observed one is smooth straight fracture which is 45˚ inclined to the loading direction and the second is similar to the shape of weld periphery.
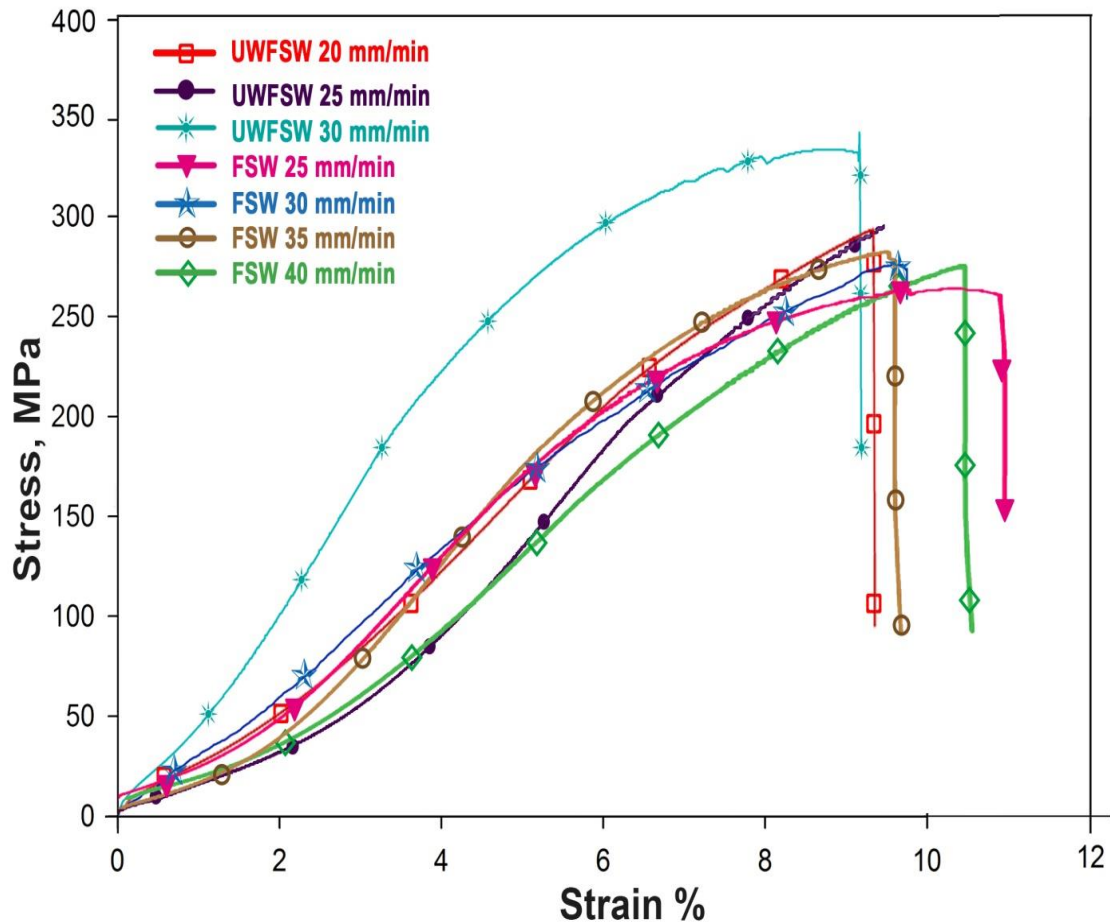
Fig. 6.1 Stress strain curves
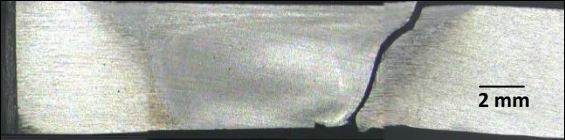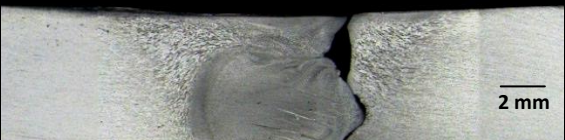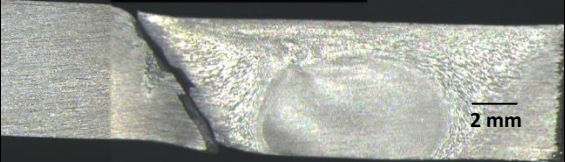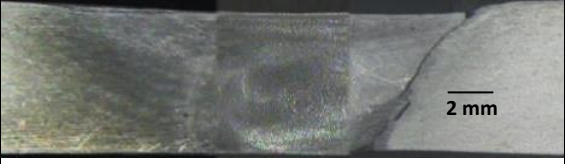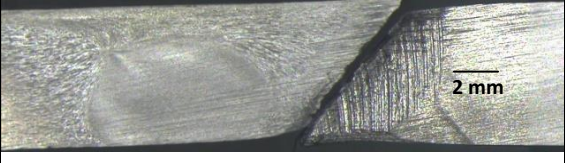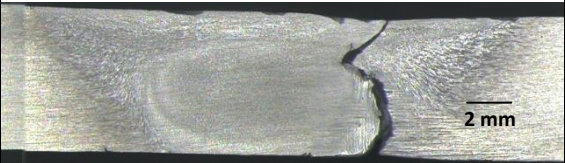
The fracture occurred in two locations, namely TMAZ-SZ interface and TMAZ. In all the UWFSW joints, the fracture occurred exactly in the retreating side TMAZ-stir zone interface. But in FSW joints, the location and fracture shapes are varying with respect to the TTS. At lower TTS of 20 mm/min, the fracture has occurred in the AS-TMAZ whereas the fractures occurred in the retreating side of the other FSW joints. The FSW joints fabricated using TTS of 25 mm/min, 30 mm/min and 35 mm/min exhibit 45˚ inclined fracture path but the fracture path is irregular for the joint fabricated using TTS of 40 mm/min.

113

Table 6.2 Effect of tool traverse speed on transverse tensile properties of the joints

Process	Tool traverse speed, mm/min	0.2 % Yield strength, MPa	Tensile strength, MPa	Elongation in 50 mm gauge length, %	Joint efficiency, %
UWFSW	20	260	294	9.8	65
	25	263	322	9.4	71
	30	322	345	9.17	76
FSW	25	232	258	11.0	57
	30	230	267	9.85	59
	35	250	260	9.8	58
	40	260	278	10.5	62

Fig. 6.2 shows the SEM fractographs of the various joints. The joints which have 45° inclined fracture path (simple shearing) showed flat macro level fracture surface whereas, the joints exhibiting zig zag fracture path showed uneven macro level fracture surface. The micro level fracture surfaces reveals fine populated dimples oriented towards the loading directions. All the joints exhibited fine dimples however the size and volume fraction of dimples slightly differs with respect to tool traverse speed and welding process.

114

Table 6.3 Effect of tool traverse speed on fracture path

TTS, mm/min	Fracture path		Observation
	AS	**RS**	
UWFSW-20			Fracture is occurred in the retreating side stir zone-TMAZ interface
UWFSW-25			Fracture is occurred in the retreating side stir zone-TMAZ interface
UWFSW-30			Fracture is occurred in the retreating side stir zone-TMAZ interface
FSW-25			Fracture is occurred in the AS-TMAZ which is 45° inclined to the loading direction
FSW-30			Fracture is occurred in the RS-TMAZ which is 45° inclined to the loading direction
FSW-35			Fracture is occurred in the retreating side stir zone-TMAZ interface
FSW-40			Fracture is occurred in the RS-TMAZ which is 45° inclined to the loading direction

115

TTS, mm/min	Macro level fracture surface	SEM fracture surface
UWFSW-20		
UWFSW-25		
UWFSW-30		
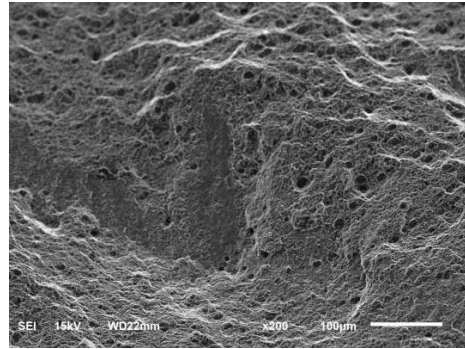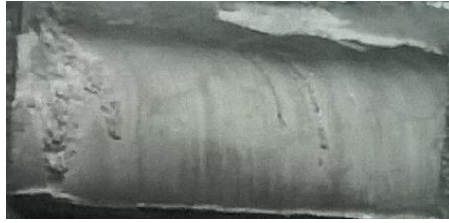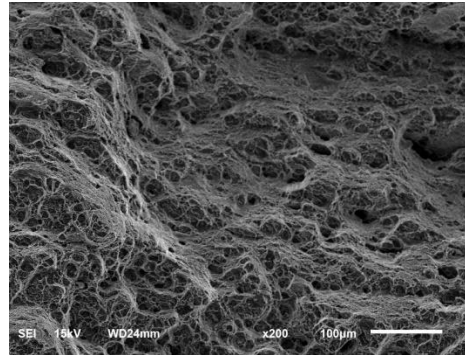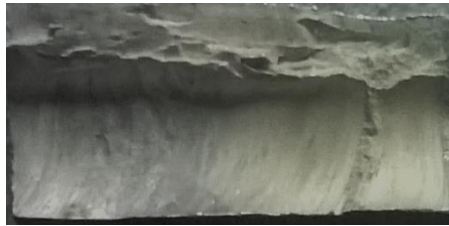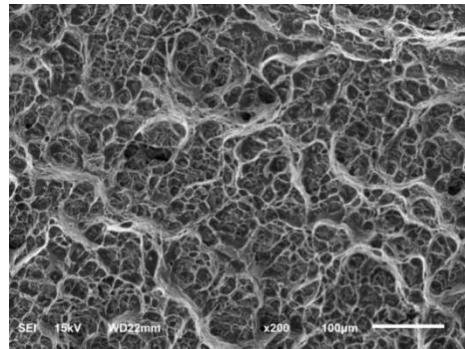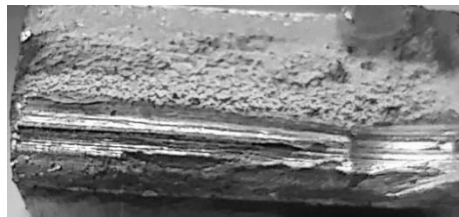
Fig. 6.2 Fracture analysis
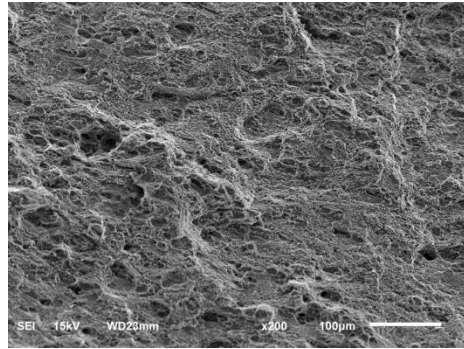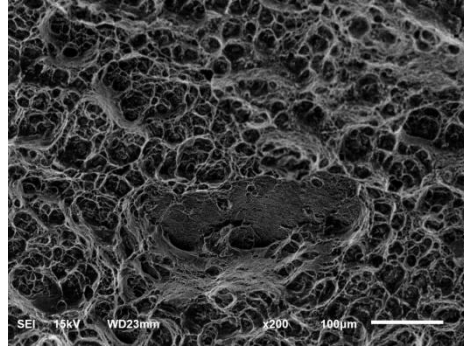
FSW-25	
FSW-30 mm/min	
FSW-35 mm/min	
FSW-40 mm/min	
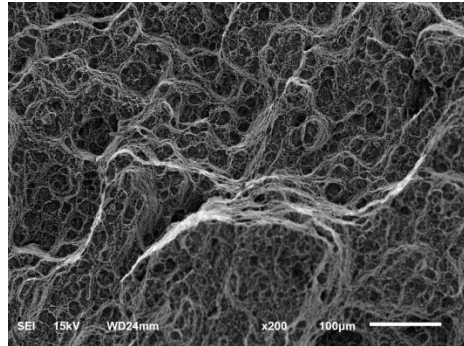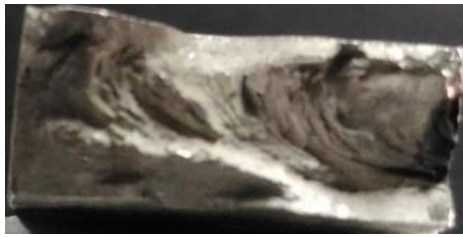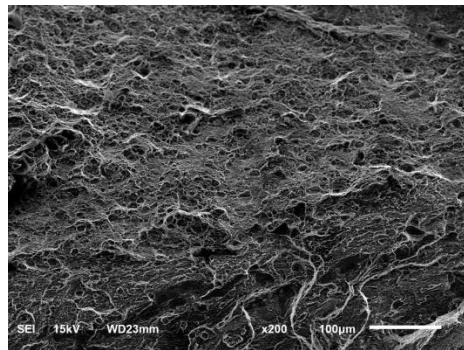
Fig. 6.2 (contd.)

6.4 MICROHARDNESS

Fig. 6.3 shows the microhardness plots of the FSW and UWFSW joints. A typical "W" shaped microhardness plots was observed in all the joints. Among the various regions, the hardness in the TMAZ at AS and RS are lower. The lower hardness of 76 HV is recorded in the RS-TMAZ of the FSW joint fabricated using TTS of 25 mm/min. It is also noted that the LHDR of the FSW joints are wider than the UWFSW joints.
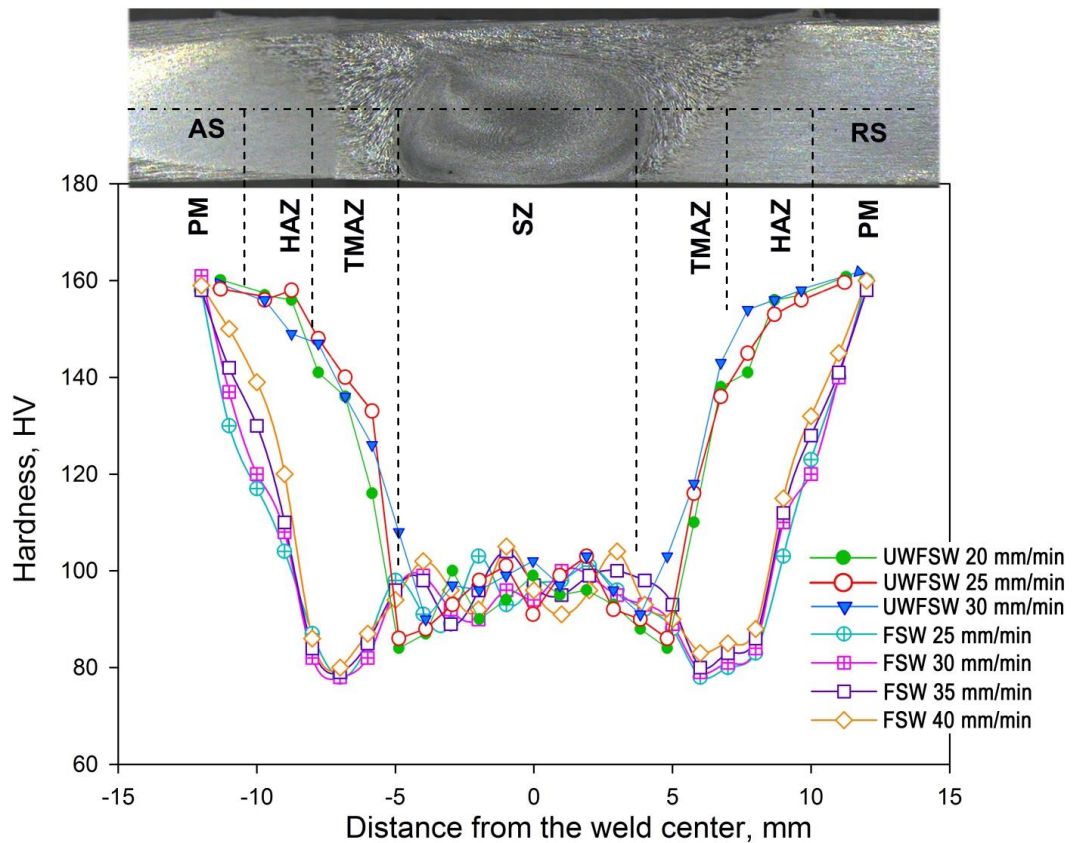
Fig. 6.3 Microhardness plot

The hardness values increased towards HAZ from TMAZ. It is obvious to note that the hardness increment towards HAZ is gradual in the retreating side where as it is sudden increase in the AS. The hardness value in the stir zones were measured to be 85-105 HV which is higher than the TMAZ. The microhardness plots in the stir zone showed a zig zag trend in all the joints. Irrespective of the TTS and process, there was no significant variation in hardness of the stir zone. However, the hardness of other zones like TMAZ and HAZ show increase in hardness with increase in TTS. The UWFSW joint fabricated using TTS of 30 mm/min exhibited relatively higher hardness in all the regions.

6.5 MICROSTRUCTURE

Figure 6.4 and 6.5 show the light micrographs of the defect free joints of FSW and UWFSW process. The stir zone micrographs were characterized by the presence of the fine equi-axed recrystallized grains. The average grain size of the FSW joints are higher than the UWFSW joints. The FSW joint fabricated using lower TTS of 25 mm/min exhibits stir zone with grain size of 17 μm. Similarly the UWFSW joint fabricated using lower TTS of 20 mm/min resulted in larger grain size of 5.4 μm, but finer than the FSW joints.

The TMAZ micrographs are composed of severely deformed grains extruded towards the stir zone. The extent of deformation of grains is gradual in the retreating side whereas deformation is abrupt in the AS of the FSW joints. However, in UWFSW joints, the extent of deformation is almost same in both AS and RS. The FSW joint fabricated using TTS of 25 mm/min resulted in larger grain size of 83 μm in the

TMAZ. The UWFSW joint fabricated using same TTS resulted in fine grain size of 55 μm.

Table 6.4 Effect of tool traverse speed on average grain diameter at various regions of the joints

Process	Tool traverse speed, mm/min	SZ, μm	AS-TMAZ, μm	RS-TMAZ, μm	AS-HAZ, μm	RS-HAZ, μm	PM, μm
UWFSW	20	5.4	56	57	50	50	
	25	4.2	55	55	49	49	
	30	3.3	50	50	49	49	
FSW	25	17	83	84	61	61	49
	30	15	82	82	60	60	
	35	12	80	82	60	60	
	40	11	77	81	59	59	

The grains in the HAZ experienced only thermal cycles and no deformation takes place. The average grain size of the HAZ in the AS and RS are measured to be same, irrespective of the change in cooling medium and TTS. The FSW joint fabricated using TTS of 25 mm/min resulted in larger grain size of 61 μm whereas lower grain size is observed in the UWFSW joints fabricated using TTS of 25 mm/min and 30 mm/min. From the microstructural examination, it is observed that the grain size of SZ and TMAZ increases with decrease in TTS.
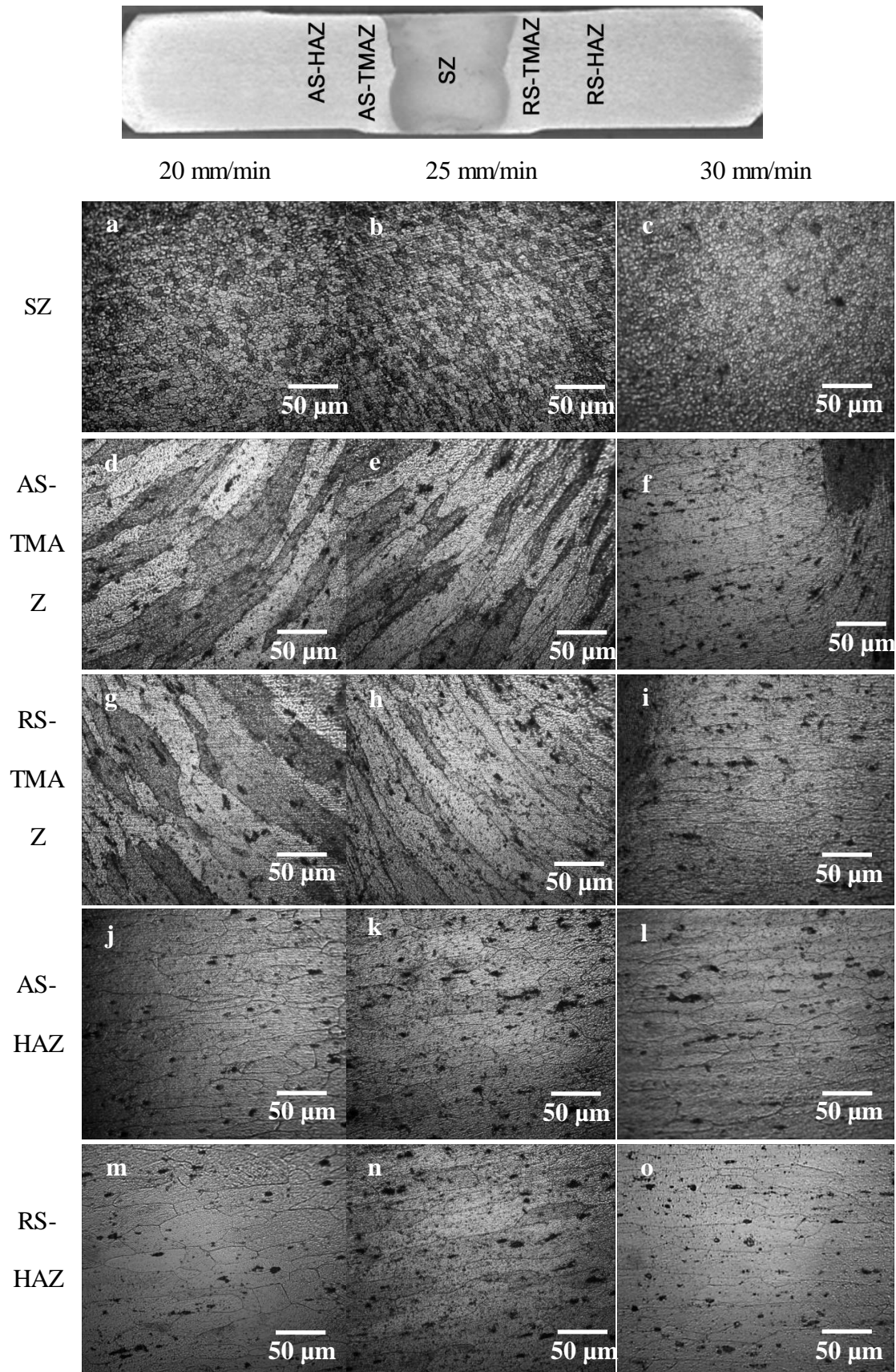
Fig. 6.4 Light optical micrographs of various regions of UWFSW joints
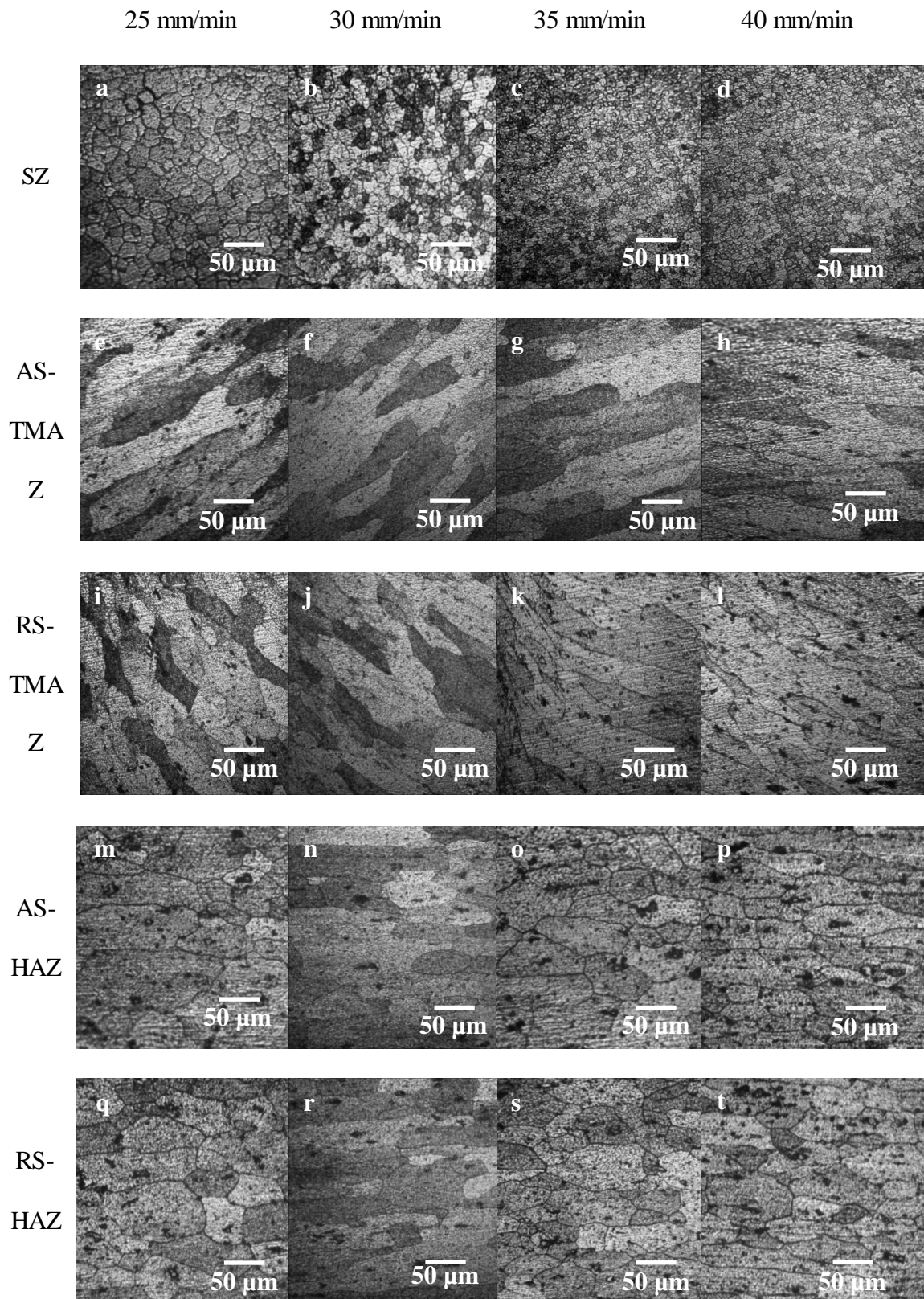
Fig. 6.5 Light optical micrographs of various regions of FSW joints
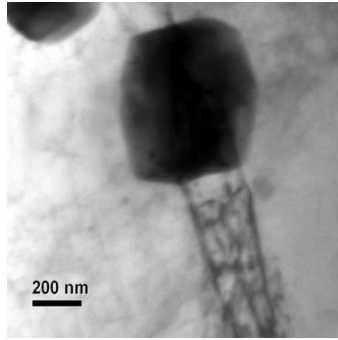
a. FSW - 25 mm/min
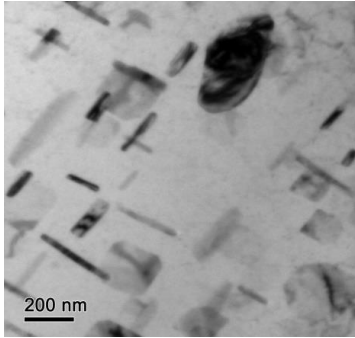
b. UWFSW-20 mm/min
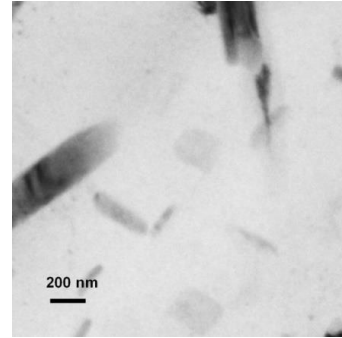
c. FSW- 30 mm/min
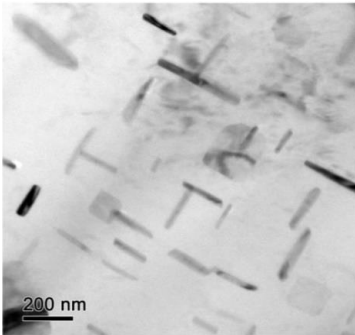
d. UWFSW-25 mm/min
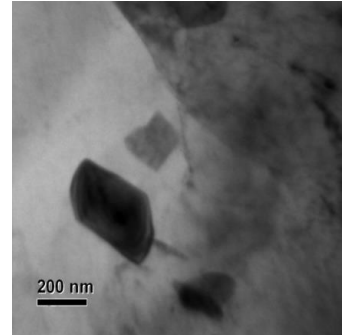
e. FSW- 35 mm/min
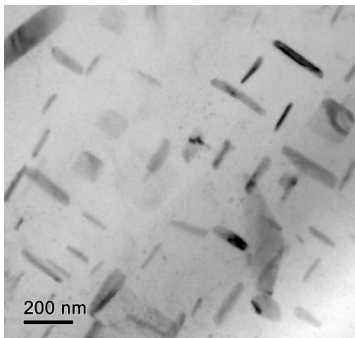
f. UWFSW-30 mm/min
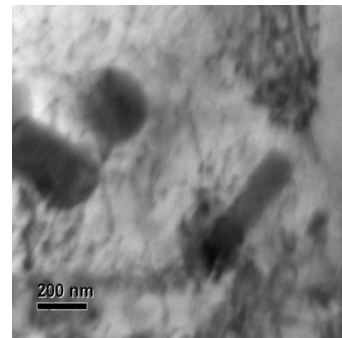
g. FSW- 40 mm/min

Fig. 6.6 TEM micrographs of LHDR

123

Fig. 6.6 shows the TEM micrographs of the LHDR of various joints. From the micrograph of the LHDR, it could be observed that the coarsening and dissolution of precipitates occurred invariably in all the joints, but the volume fraction of the precipitates is varies appreciably. The TEM micrograph of the LHDR is characterized by the presence of coarse stable θ precipitates and the precipitates free zone (PFZ). In UWFSW joints, the volume fractions of the precipitates are high compared to the FSW joints. The FSW joints fabricated using lower TTS of 25 mm/min and 30 mm/min composed of less number of precipitates. In UWFSW joints, the precipitation behaviour at the LHDR is more or less similar, however the volume fraction of precipitates is marginally lower in the joint fabricated using lower TTS of 20 mm/min.

Fig. 6.7 shows the temperature values recorded during the heating cycles and cooling cycles of the FSW and UWFSW joints fabricated using TTS of 30 mm/min. From the thermal plots, it is observed that the UWFSW joint experiences a lower temperature than the FSW joints. The UWFSW exhibits higher heating rate and higher cooling rates than the FSW joints.
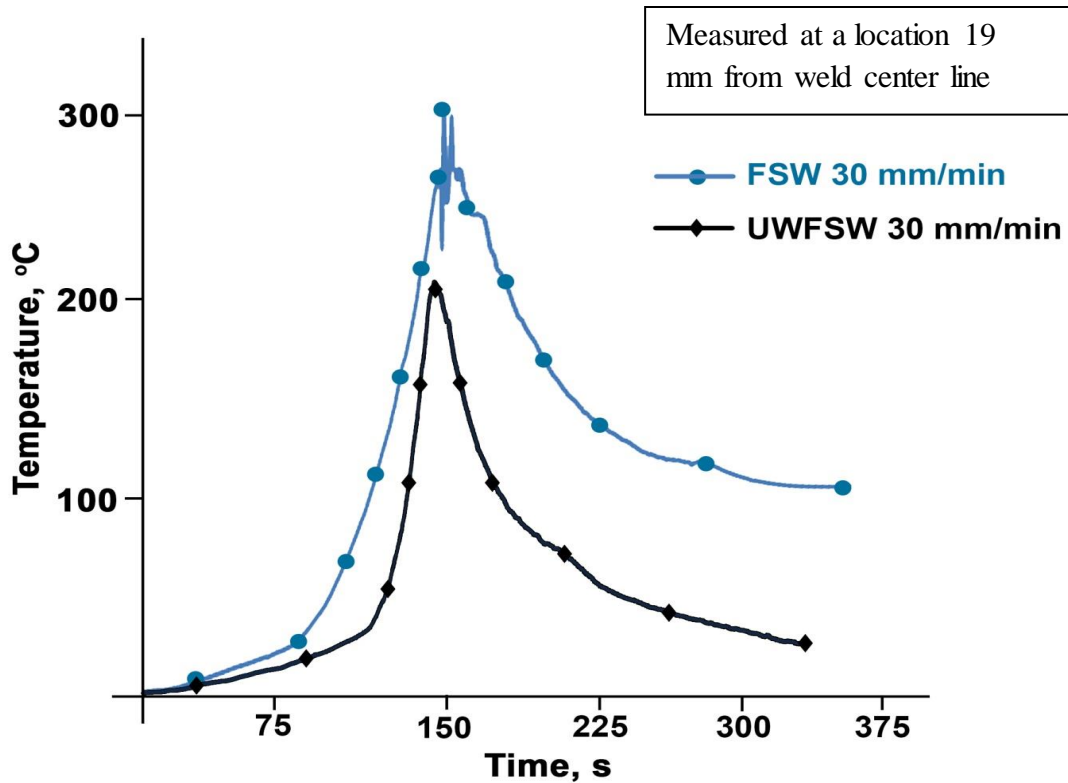
Fig. 6.7 Thermal histories

6.6 DISCUSSION

6.6.1 Effect of tool traverse speed on the joint quality

Zhang *et al.* (2012) reported that quality of FSW joints can be fabricated at wide range of process parameters whereas the possibility of fabricating defect free UWFSW joints was difficult. The present study showed good agreement with the previous studies, in which higher number of defect free joint were produced under air cooling than the water cooling conditions within the selected levels of tool traverse speed. The effect of cooling medium on the sound joint formation can be explained as follows. The balanced or sufficient state can be attained by selecting proper combination of tool rotational speed and welding speed. Improper selection of process parameters like low tool rotational speed or high welding speed resulted in

125

insufficient state where as high tool rotational speed or low welding speed resulted in excess state.

In water cooling condition, the joint fabricated using high TTS of 40 mm/min resulted defects in the stir zone. This was attributed to the attainment of insufficient heat and material flow state. Because of the short stirring time, the extent of thermal softening and plasticization was restricted which resulted in defective stir zone. During usage of lower TTS of 20 mm/min, the FSW and UWFSW joint also resulted in defective stir zone. The long stirring time results in high heat input and thereby greater extent of thermal softening occurs around the tool. The excess plasticization of material experiences drop in friction between the tool and the material. This promotes slipping condition which resulted in the formation of defects in the stir zone. The UWFSW joints fabricated using TTS of 20-30 mm/min and the FSW joint fabricated using TTS of 25-40 mm/min resulted in defects free stir zones. The above TTS lies between the insufficient state and excess state where the balance state of heat and material flow was attained resulted in defect free joints.

6.6.2 Effect of tool traverse speed on the mechanical properties of the joints

Weld joint properties are decided by various strengthening mechanism like, grain boundary strengthening, solid solution strengthening and precipitation hardening (De *et al.* 2011). According to the Hall-Petch relationship, the grain size is inversely propositional to the yield strength of the joints (Genevois *et al.* 2004). Increasing the TTS and the cooling medium, the grain size varied and thereby strength contribution due to grain boundary also varied. Again increasing the TTS from 20 mm/min to 40

126

mm/ min, the grain sizes also increases. Hence, increasing the TTS, the hardness of the various regions also increased. As the hardness increases, the tensile properties also increases with increase in TTS. This is because, the water cooling restricted the grain growth and therefore UWFSW joints have undergoes high degree of grain boundary strengthening. The area of the precipitate free zone increases with decrease in TTS. In PFZ, the $CuAl_2$ precipitates dissolved to form solid solution, which contributed to solid solution strengthening (Liu *et al.* 2010). However, the LHDR having wider PFZ resulted in lower hardness which resembles the effect of solid solution strengthening in the age hardenable aluminum alloy was relatively low.

According to the Ashby-Orowan expression the strength is inversely proportional to precipitate size and directly proportional to volume fraction of the precipitates (Dieter, 1986). The LHDR of UWFSW joints exhibited high volume fraction and the size of precipitates was relatively lower than the FSW joints. Therefore the hardness and the tensile properties were higher for the UWFSW joints. Increasing the TTS, the heat input also increased and so the coarsening and dissolution of precipitates increased. Because of the lower volume fraction and higher precipitate size, the joint fabricated using lower TTS end up with poor tensile properties. The tensile fracture behavior mainly depended on the hardness in the LHDR. During tensile test the load was concentrated in the weakest region (lower hardness distribution region). This phenomenon is called as strain localization. Higher the hardness in the LHDR offers more resistant to strain localization. The UWFSW joint fabricated using TTS of 35 mm min results in higher tensile strength of 345 MPa and joint efficiency of 76 %. From the elongation values and the SEM fracture analysis, it was inferred that all the

joints exhibit the same ductile behaviour. This is because the LHDR alone contributes to elongation and fractured in all the joints. The strain localization was also the reason for the lower elongation values of the joints than the parent metal. However, in bending, the elongation of FSW joint is higher than the parent metal. The weaker stir zone and TMAZ jointly contributed in total bending and therefore the elongation is higher in FSW joints. It is also noted from the bend test that the bending strength is higher than the tensile strength. This is because, in tensile test the entire cross sectional region undergoes tension load, but in bend test the convex part of sample undergoes tension and the concave part undergoes compression.

6.6.3 Effect of tool traverse speed on microstructure

In air cooling and water cooling conditions, the stir zone has undergone severe plastic deformation and experiences higher temperature, which resulted in alteration of precipitation behavior and grain morphologies. Deformation and the heat input prevailed in the stir zone was high enough for the recrystallization process. So a new set of fine recrystallized grains were resulted in the stir zones. But, the deformation and the heat in the TMAZ was not sufficient to recrystallize the grains. Therefore the TMAZ resulted in deformed grains with higher grain size. The HAZ region experienced only the thermal cycles whereas stirring force does not have any influence on the HAZ. The heat prevailing in the HAZ region coarsens the grains and so it exhibited higher grains size than parent metal.

Compared to the air cooling joints, the water cooled FSW joints experienced lower heat input (Fig. 6.7). The high heat dissipation capacity of water controls the

temperature level in the UWFSW joints. Hence, the grain coarsening and precipitate coarsening were limited. The heat prevailed in the FSW joints were utilized for the grain growth. And so the grain sizes in the various zones of the FSW joints are higher than the UWFSW joints. The water readily dissipated the heat from the HAZ region of the UWFSW joints, the intensity of the heat was insufficient for the grain growth. Hence, the grain sizes of HAZ in the UWFSW joints were almost equal to the parent metal. In addition, because of the low heat input, the extent of thermal softening was also restricted and thereby the plastic deformation was restricted. These were the reasons for the formation of narrowed TMAZ and HAZ in the UWFSW joints.

TMAZ in the UWFSW joints undergoes higher deformation than the FSW joints. Because of low heat input, the extent of plasticization was limited in the UWFSW joints and so less volume of material undergone stirring whereas large volume of material undergone stirring in FSW joints. Under the same magnitude of stirring force, the less plasticized volume of material in the UWFSW joints had undergone higher strain. Therefore the grains in the TMAZ have undergoes severe deformation in UWFSW joints. Similar to the cooling conditions, the variations in the TTS also have greater effect in change of grain morphology and precipitation behavior. As discussed above, due to long stirring time the joint fabricated using lower tool traverse speed resulted in high heat input. Therefore the grain size of the joints fabricated using lower TTS resulted in larger grain size than the higher TTS

AA2519 is a heat treatable aluminum alloy which is highly sensitive to temperature and strain rate. The temperature and the deformation in the TMAZ coarsen or

dissolute the precipitates. The tensile properties and the tensile fracture behavior of the joints were mainly dependent on the microhardness of the joint. From the TEM analysis, it was inferred that the precipitation behavior varies in the LHDR with respect to the TTS and cooling medium (Fig. 6.6). The extent of softening in the LHDR region depends on the volume fraction, degree of coarsening and presence of PFZ. The heat conducted from the stir zone and the heat generated due to plastic deformation in the TMAZ resulted in overaging. In overaging, the fine precipitates coarsens and the degree of coarsening of the precipitates depended mainly on the heating and cooling cycles during welding (Zhang *et al.* 2014). Lower TTS resulted higher heat input, low cooling rate which prevailed in the FSW joints. Because of the longer duration of over aging, the sizes of precipitates were larger. These were the reason for increase in precipitate size with decrease in TTS. But in water cooling, the duration of over aging of TMAZ was greatly reduced. Therefore the LHDR of UWFSW joints exhibits lower size precipitate size than the FSW joints. Moreover, the temperature attained in the TMAZ of UWFSW joints is very low and so the dissolution of precipitates was significantly limited.

6.7 SUMMARY

The influences of tool traverse speed (TTS) on the stir zone characteristics and tensile properties of friction stir welded (air cooled) and under water friction stir welded (water cooled) AA2519-T87 aluminium alloy joints were investigated and the following observations were made:

    i.   In the air cooled condition, TTS in the range of 25-40 mm/min and in the water cooled condition TTS in the range of 20-30 mm/min yielded defect

free joints. It is attributed to the attainment of adequate heat generation, sufficient plasticization and proper material mixing during stirring.

ii. The UWFSW joint fabricated using TTS of 30 mm/min exhibited maximum tensile strength of 345 MPa with a joint efficiency of 76 %. On the other hand, TTS of 40 mm/min yielded maximum tensile strength of 278 MPa in air cooled FSW joint. UWFSW joints showed 25 % higher joint efficiency than FSW joints.

CHAPTER 7

EFFECT OF TOOL TILT ANGLE

7.1 INTRODUCTION

In addition to the tool rotation speed and tool traverse speed, another parameter having significance in FSW process is the angle of the spindle or tool tilt angle with respect to the work piece surface. Tool tilt angle is characterized as the angle at which the tool is situated with respect to the workpiece surface, i.e. no or 0° tilted tool is situated perpendicular to the workpiece surface (Majid *et al.* 2016). A suitable tilt of the spindle towards the trailing direction enables the tool shoulder to hold the stirred material and so the material moves efficiently from the front to the back of the pin. Tilting the tool so that the rear of the tool is lower than the front, has been found to assist the forging process and the material flow during FSW. Tool tilt angle primarily influences the material consolidation and heat generation during welding. Shinoda *et al.* (2001) reported that the angle of stir tool affects the metal flow patterns in two directions: bottom flow and surface flow. Arici and Selale 2007 also studied the effect of tool tilt angle on the tensile strength and fracture locations of friction stir welding of polyethylene. It was observed that the tensile strength of the material decreased with increasing tool tilt angles and that the thickness of the welding zone decreased with increasing tool tilt angle. This affects the tensile strength of the joint. Muhayat et al (2007) reported that the increase of tool tilt angle resulted the increase of the welding temperature in advancing side and retreating side. It was also observed that increasing the tool tilt angle, increases the peak temperature.

Exploring the relationship between the tool tilt angle on the joint quality, mechanical properties and microstructural characteristic and defect formation mechanisms are of critical importance for obtaining high-quality FSW and UWFSW joints. Though tool tilt angle is a prominent process parameter but its effect on the joint quality and joint performance is still not clearly revealed by researchers in UWFSW process. Hence an investigation is made to study the effect of tool tilt angle on the microstructures and mechanical properties of UWFSW of AA2519-T87 aluminium alloy joints.

7.2 JOINT QUALITY

The photograph of the top surfaces and cross sectional macrographs reveals the joint quality (Table 7.1). The top surfaces of all the joints are free from surface defects. It is characterized by the presence of smooth and closely consolidated ripples. But, the cross sectional macrostructure shows significant variations with respect to the tool tilt angle. On increasing the tool tilt angle, three notable observations are seen, they are, the stir zone get thinning, the thickness of the shoulder influenced region (SIR) increases and the thickness of the PIR decreases (Fig. 7.1). The FSW and UWFSW joints fabricated using tool tilt angles of 0° and 1° resulted in defects in the stir zone. As the tool tilt angle increases from 0° to 1°, the size of the defect decreases in both air cooling and water cooling condition. In all the defective cases, the defects are occurred in the SIR-PIR interface of advancing side which is termed as defect prone region (DPR). Fig. 7.2 shows the magnified view of DPR which shows flow patterns around the defect region. It is clearly observed that, on increasing the tool tilt angle the material is pushed to fill the defects. On further increase of tool tilt angle from 2° to 4°, the defect is totally filled to form defect free joints.
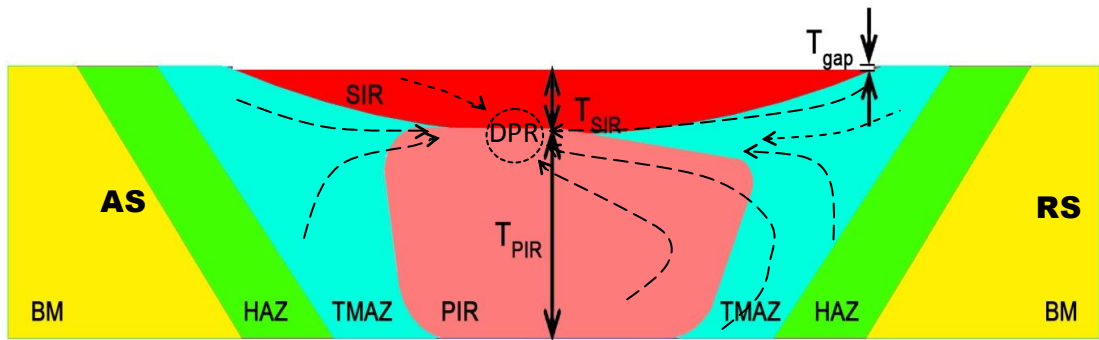
a. Typical material flow patterns in various regions of FSW joints

$$T_{gap} - 0° < 2° < 4° \qquad T_{SIR} - 0° < 2° < 3° \qquad T_{PIR} - 0° > 2° > 4°$$
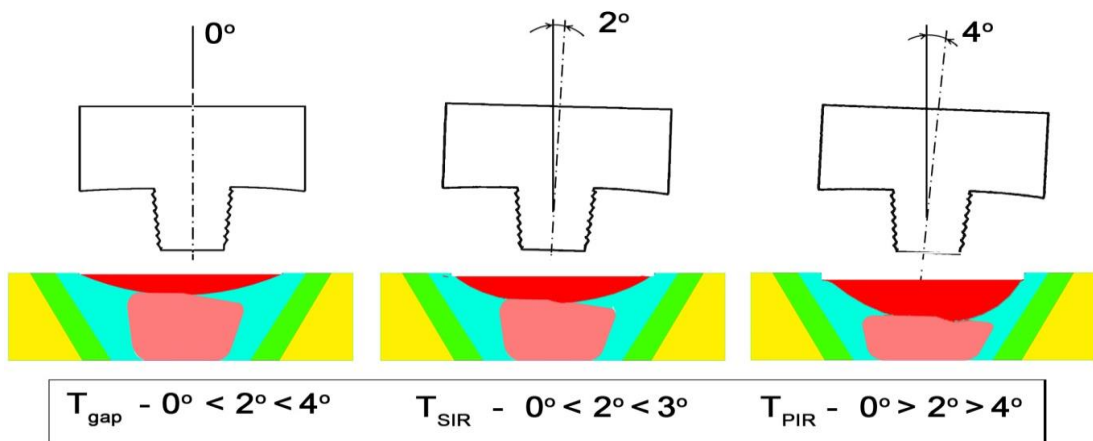
b. Effect of tool tilt angle on various thickness

Fig. 7.1 Schematic representation of effect of tool tilt angle
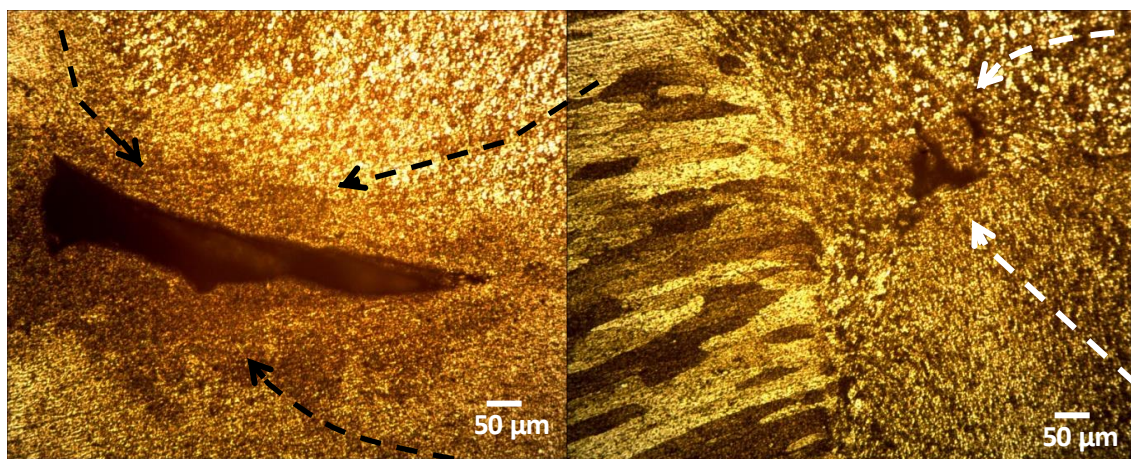
a. 0° - UWFSW joint   b. 1° - UWFSW joint

Fig. 7.2 Magnified view of defect prone region (DPR)

134

Table 7.1 Effect of tool tilt angle on cross sectional macrographs
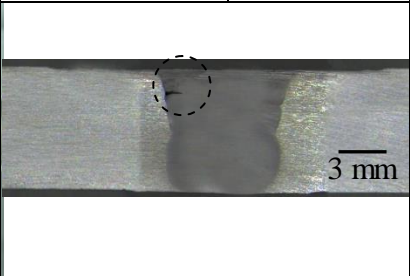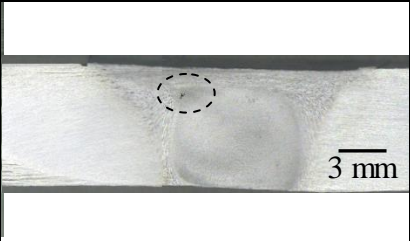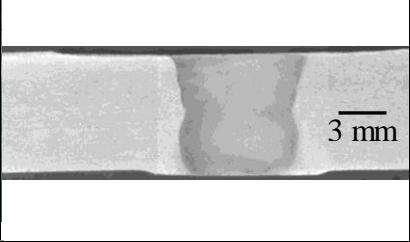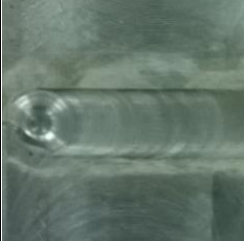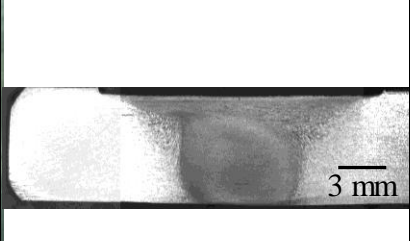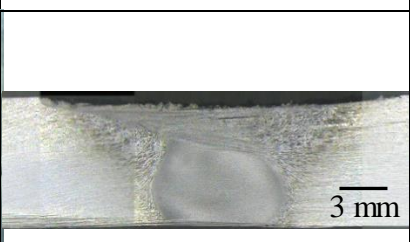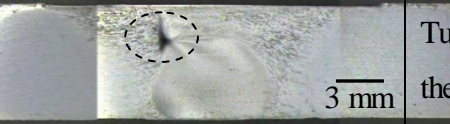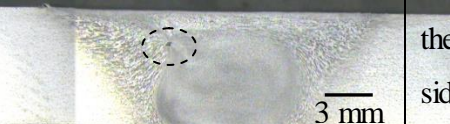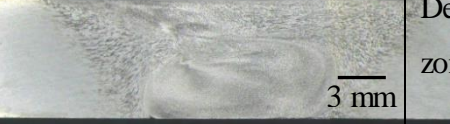
Joint type	TTA	Photograph of the top surface	Cross sectional macrograph		Observation
			AS	RS	
UWFSW	0°				Tunnel defect in the advancing side
	1°				Tunnel defect in the advancing side
	2°				Defect free stir zone
	3°				Defect free stir zone
	4°				Defect free stir zone

135

Table 7.1 (contd.)

Joint type	TTA	Photograph of the top surface	Cross sectional macrograph		Observation
			AS	RS	
FSW	0°		3 mm		Tunnel defect in the advancing side
	1°		3 mm		Tunnel defect in the advancing side
	2°		3 mm		Defect free stir zone
	3°		3 mm		Defect free stir zone
	4°		3 mm		Defect free stir zone

7.3 TENSILE PROPERTIES

The tensile properties of the joints were interpreted from the stress-strain diagram (Fig. 7.3) and presented in Table 7.2. The UWFSW joint fabricated using tool tilt angle of 2° resulted higher tensile strength of 345 MPa. The change in cooling medium has significant effect on the tensile strength. The tensile strength of UWFSW joint fabricated tool tilt angle of 2° is 34 % higher than the FSW joint. The joint efficiency of the UWFSW joint fabricate using lower tool tilt angle 2° yield high joint efficiency of 76 % whereas the FSW joint fabricated using higher tool tilt angle of 4° results lower joint efficiency of 51 %. It is clearly evident that all the joints exhibited lower ductility (percentage of elongation) ranges of 9-10.4 % than the PM of 11.2 %. But there is no appreciable variation in ductility of the joints irrespective of the tool tilt angle and the cooling medium.
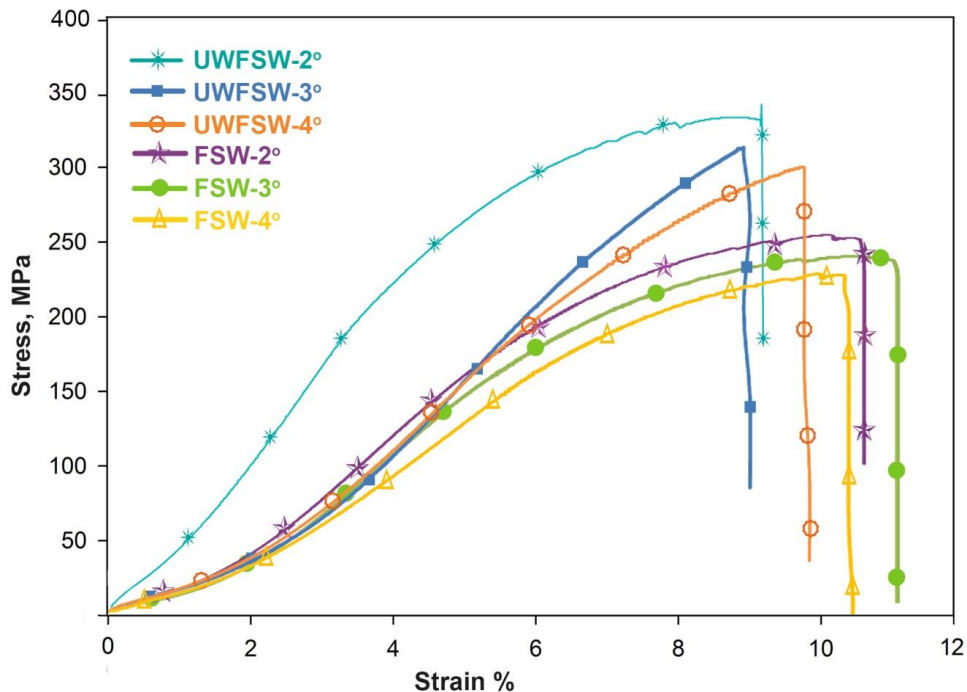
Fig. 7.3 Stress strain curves

Table 7.2 Transverse tensile properties of FSW and UWFSW joints

Joint type	Tool tilt angle	0.2 % Yield strength (MPa)	Tensile strength (MPa)	Elongation in 50 mm gauge length (%)	Joint efficiency (%)
UWFSW	2°	300	345	9.2	76
	3°	243	313	9.0	69
	4°	240	299	9.8	66
FSW	2°	234	256	10.5	56
	3°	230	244	11.0	54
	4°	220	229	10.4	51

Table 7.3 Effect of tool tilt angle on fracture path
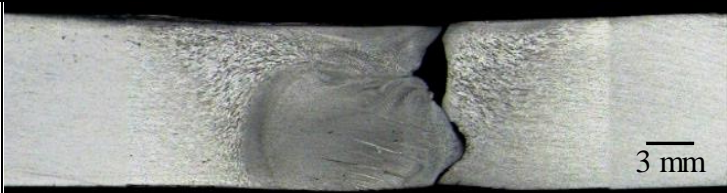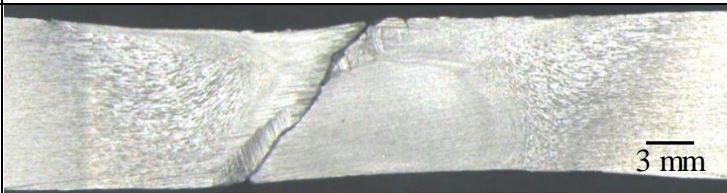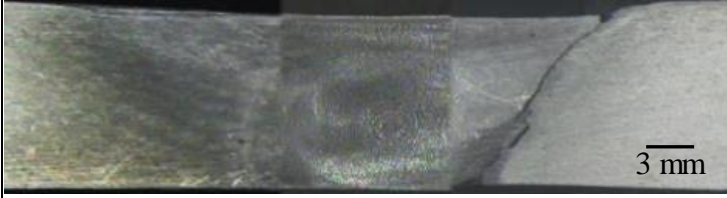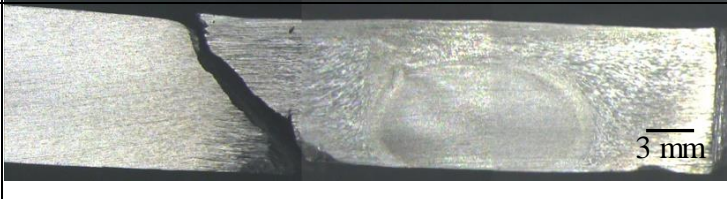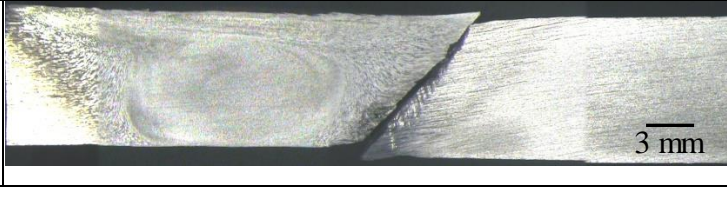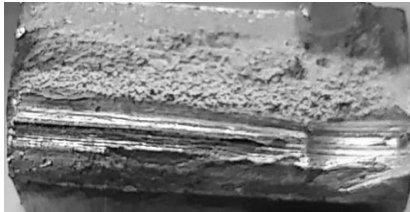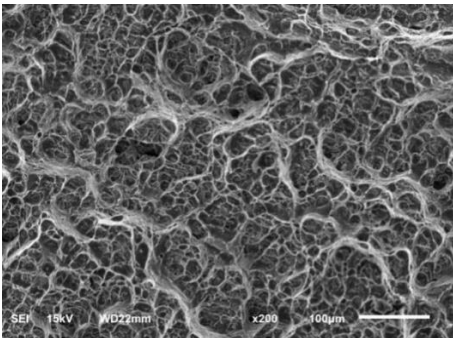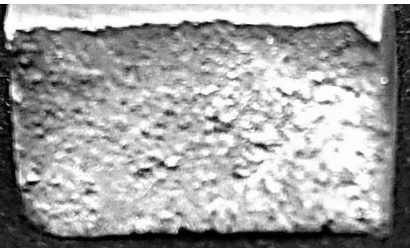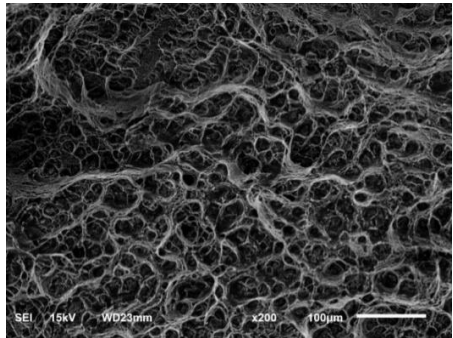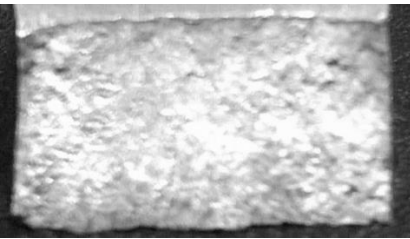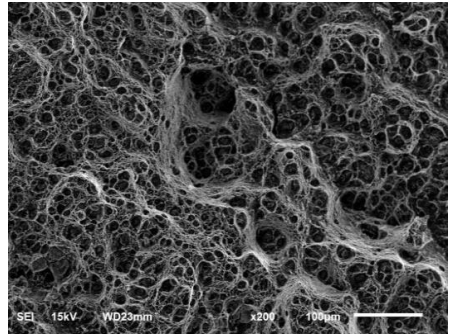
Tool tilt angle	Fracture path		Observation
	AS	RS	
UWFSW-2°			Fractured along the RS-TMAZ
UWFSW-3°			Fractured along the AS-TMAZ
UWFSW-4°			Fractured in AS-TMAZ and stir zone

Table 7.3 (contd.)

Tool tilt angle	Fracture path		Observation
	AS	RS	
FSW-2°			Fractured along the RS-TMAZ
FSW-3°			Fractured along the AS-TMAZ
FSW-4°			Fractured along the RS-TMAZ

The entire tensile fracture path can be clearly revealed from the macrographs shown in table 7.3. The entire fracture path is occurred in the TMAZ of all the joints except the UWFSW joint fabricated using tool tilt angle of 4° where, the fracture path is partially occurred in the stir zone and partly in the TMAZ. The fracture was occurred in the RS-TMAZ in the UWFSW joint fabricated using tool tilt angle of 2° whereas AS-TMAZ in 3° tilt angle. Similarly, The fracture was occurred in the RS-TMAZ in the FSW joint fabricated using tool tilt angles of 2° and 4° whereas AS-TMAZ in 3° tilt angle. It was notable that fracture path is straight and 45° inclined to the loading direction in all the joints except the UWFSW joint fabricated at the tool tilt angles of 2° and 3°.

Further the fracture surfaces were analyzed at the macro and micro level magnifications (Fig. 7.4). In macro level, all the joints exhibit flat fracture surface whereas the UWFSW-2˚ is not flat. The micro level fracture surfaces were characterized using SEM. All the joints exhibit similar fracture morphologies of fine populated dimples.

Joint Type	Tool tilt angle	Macro level fracture surface	SEM fracture surface
	2˚		
UWFSW	3˚		
	4˚		

2°

FSW   3°

4°
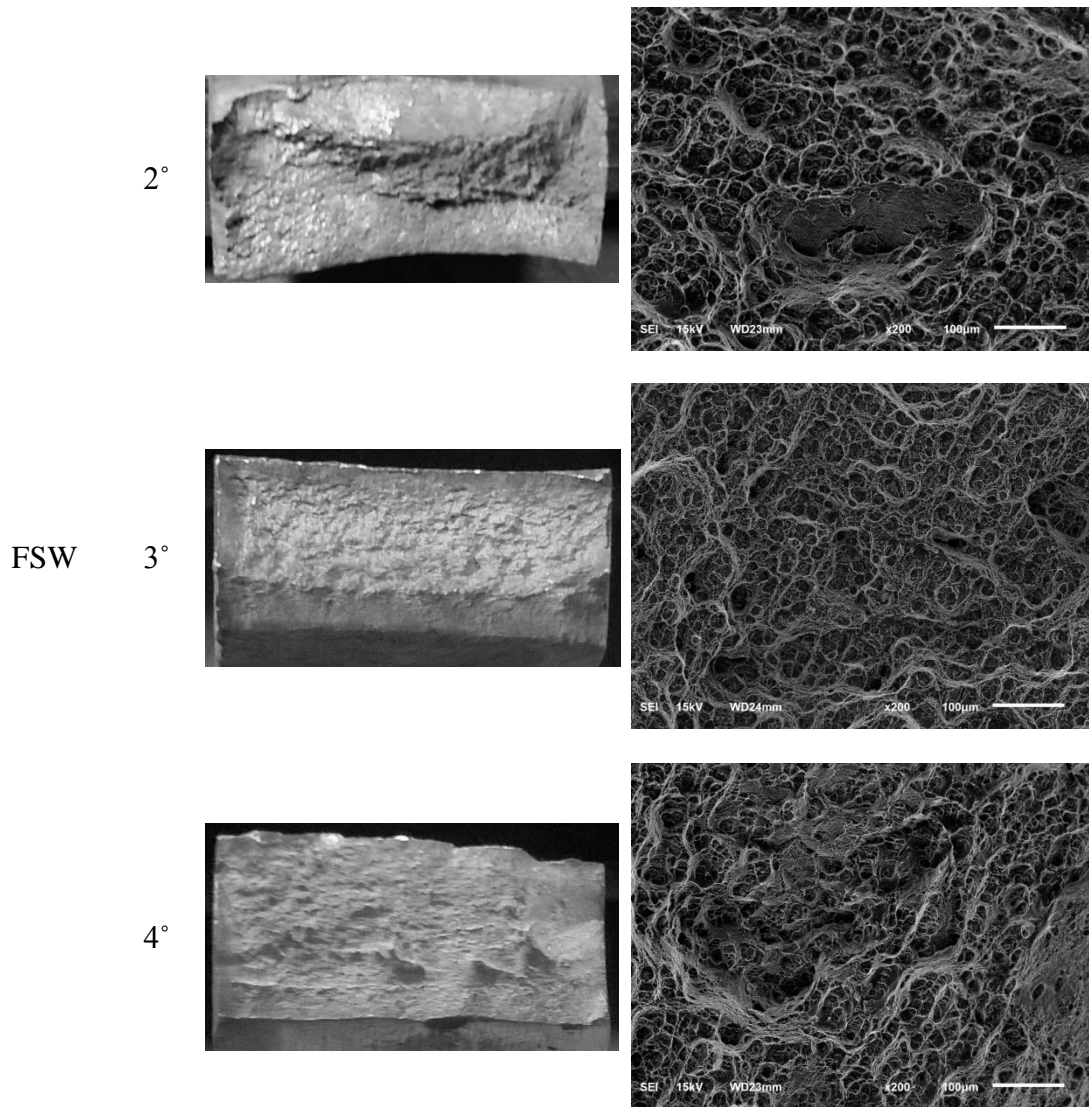
Fig. 7.4 (contd.)

7.4 MICROHARDNESS

Fig. 7.5 shows the microhardness plot of the different joints fabricated under varying tool tilt angle and cooling medium. The lower hardness is recorded in the TMAZ regions in all the joints. Among the various joints, the FSW joint fabricated using tool tilt angle of 4° resulted in lower hardness of 77 HV. It was observed that the lower hardness distribution region was wider in FSW joints whereas in UWFSW joint it is narrowed. The SZ exhibit higher hardness than the TMAZ region. The microhardness plot at SZ show scattered values from 89 HV to 110 HV. There

141

observed abrupt increment in the hardness from HAZ to PM for the UWFSW joint whereas a gradual increment is observed in FSW joints. The hardness in the HAZ is remarkably higher than the TMAZ region. It is necessary to note that the LHDR of FSW far away from the weld center of the UWFSW joints.
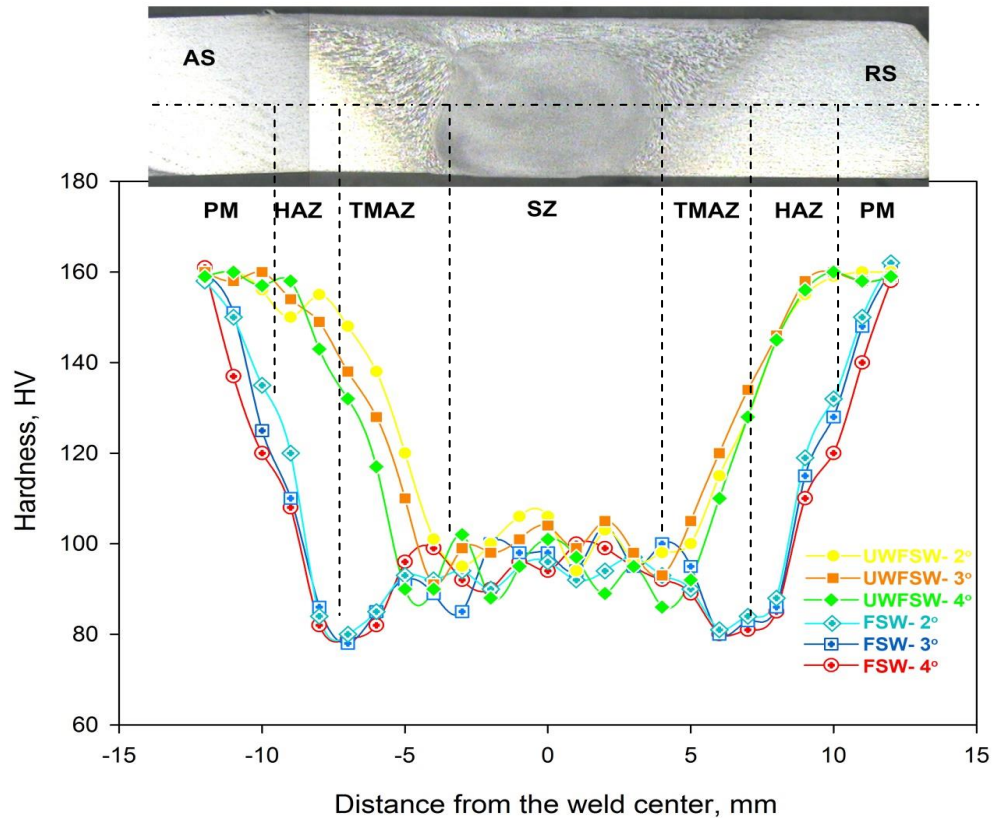
Fig. 7.5 Microhardness plot

7.5 MICROSTRUCTURE

The optical micrographs of UWFSW and FSW joints were shown in Fig. 7.6 and Fig. 7.7 respectively. The stir zone composed of fine equi- axis oriented grains in both FSW and UWFSW joints. However, the grain size in SZ of FSW joints exhibit comparatively larger size than the UWFSW joints. The FSW joint fabricated using tool tilt angle of 4˚ resulted larger grain size of 15 μm in SZ   whereas the UWFSW joint fabricated using tool tilt angle of 2˚ resulted   lower grain size of 2.5 μm in SZ (Table 7.4).

142

Fig. 7.6 Light optical micrographs of various regions of UWFSW joint
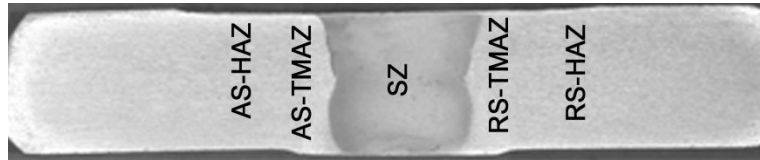
TTA	ASHAZ	ASTMAZ	SZ	RSTMAZ	RSHAZ
2°					
3°					
4°					
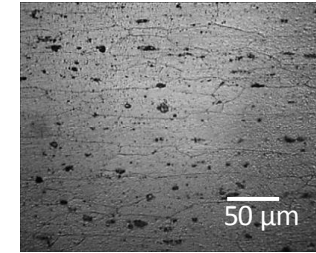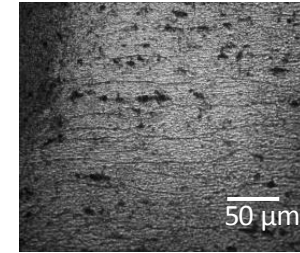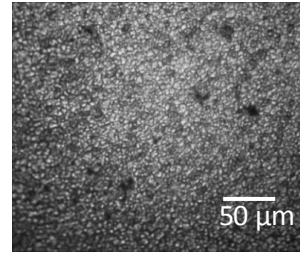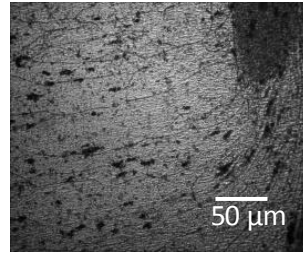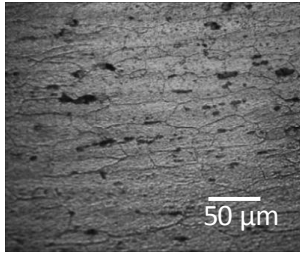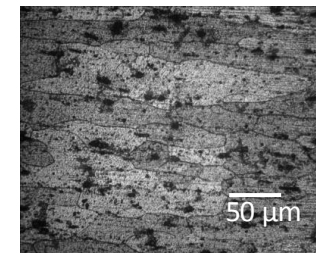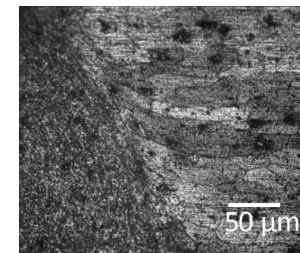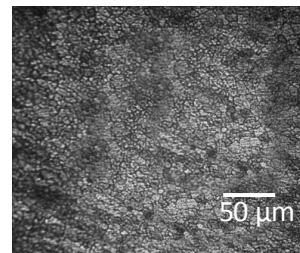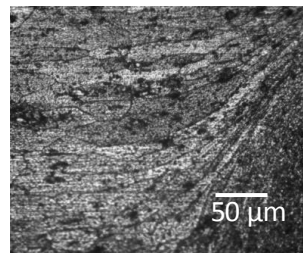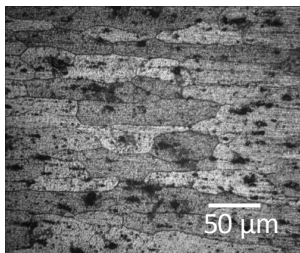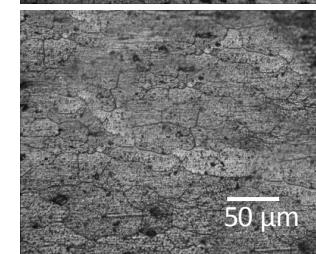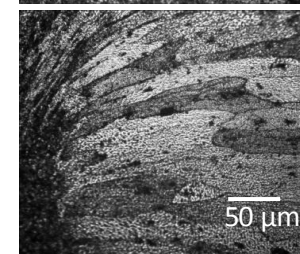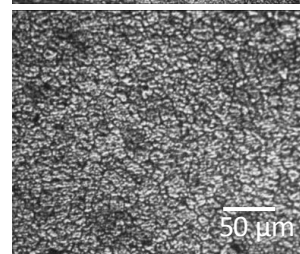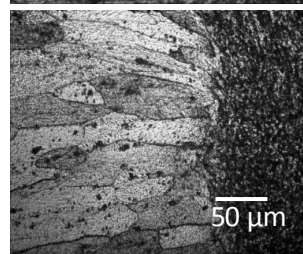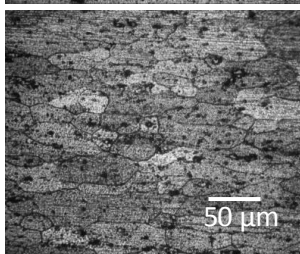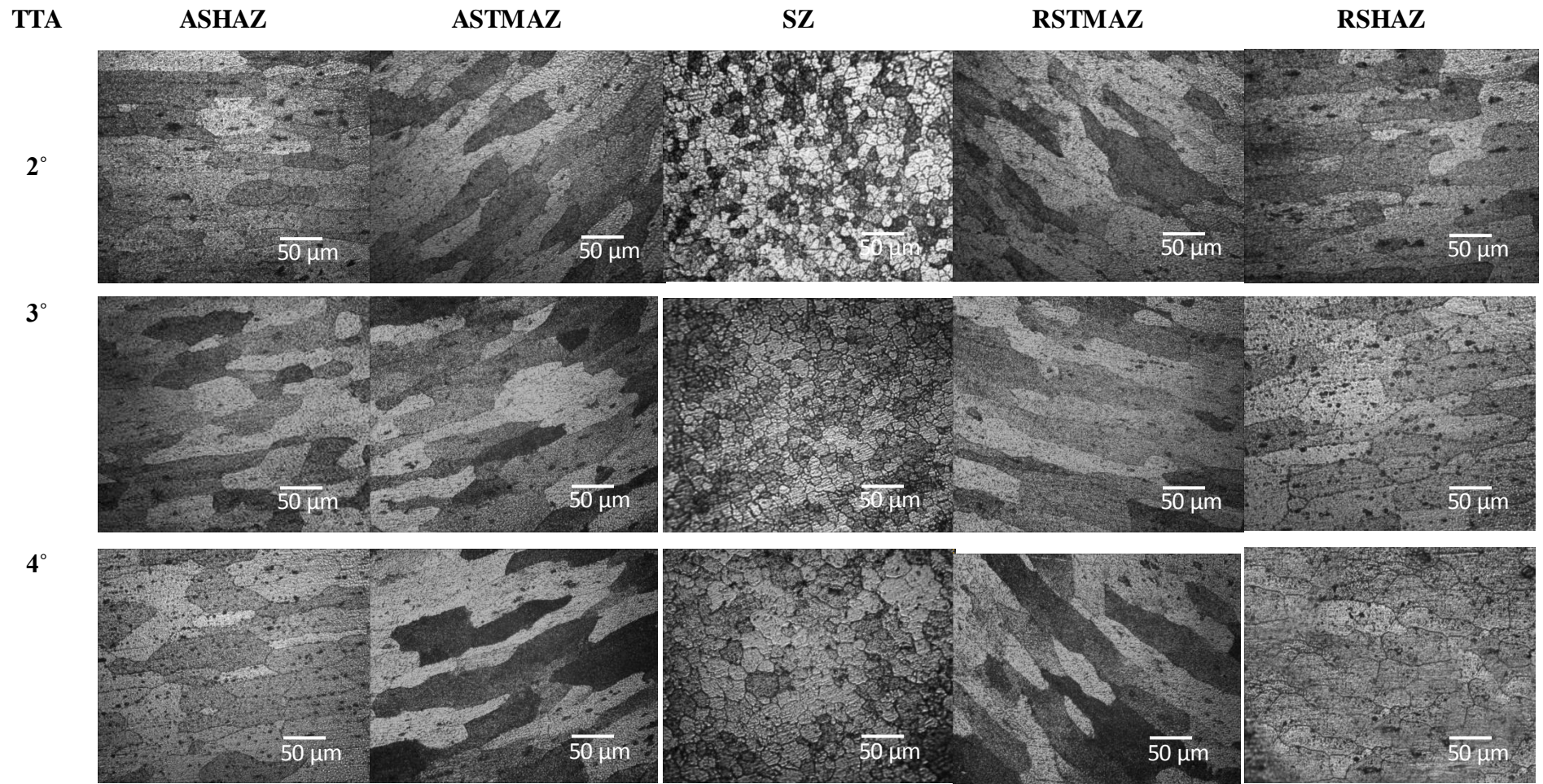
Fig. 7.7 Light optical micrographs of various regions of FSW joint

Table 7.4 Average grain diameter

Joint type	Tool tilt angle	SZ (μm)	AS-TMAZ (μm)	RS-TMAZ (μm)	AS-HAZ (μm)	RS-HAZ (μm)	PM (μm)
UWFSW	2°	2.5	49	50	49	49	
	3°	3.3	50	50	49	49	
	4°	4.2	54	54	51	51	49
FSW	2°	11	81	81	59	59	
	3°	12	81	82	60	60	
	4°	15	82	82	60	60	

The optical micrograph of TMAZ is characterized by the presence of highly deformed elongated grains. It is notable that the UWFSW joints undergone high degree of deformation in the TMAZ than the FSW joints. The change in tool tilt angle does not show significant variations in the grains sizes of FSW joints. The average grain size of UWFSW joints ranges from 81-82 μm. But, the change in tool tilt angle varies the grains sizes from 49-54 μm in the UWFSW joints.

The HAZ experiences only the thermal cycles whereas no deformation takes place. The micrograph is characterized by the coarse elongated grain oriented towards the rolling direction. The average grain size of HAZ of FSW joints exhibited higher grain size than the UWFSW joints. The joint fabricated using tool tilt angles of 3° and 4° resulted higher grain size of 60 μm. The UWFSW joints does not undergone grain coarsening and therefore the average grain size of UWFSW joints exhibits equal to parent metal grain size of 49 μm.
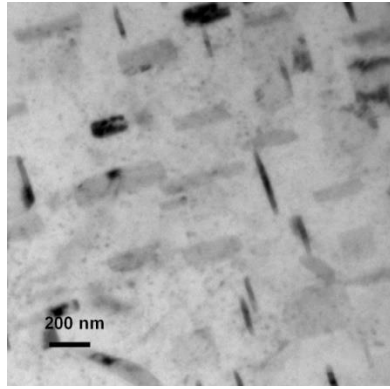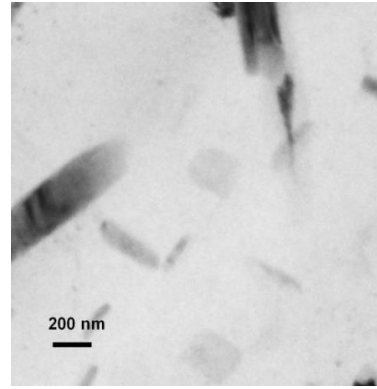
a. UWFSW - 2˚   b. FSW - 2˚
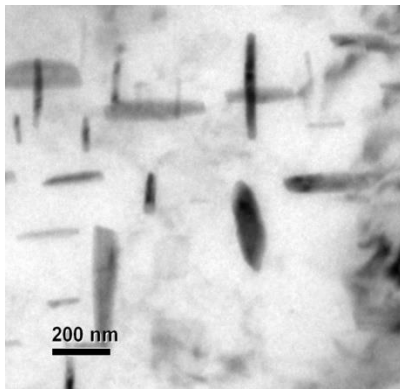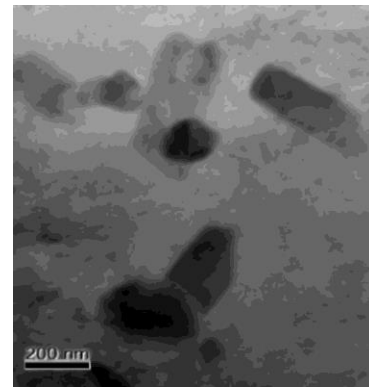
c. UWFSW - 3˚   d. FSW - 3˚
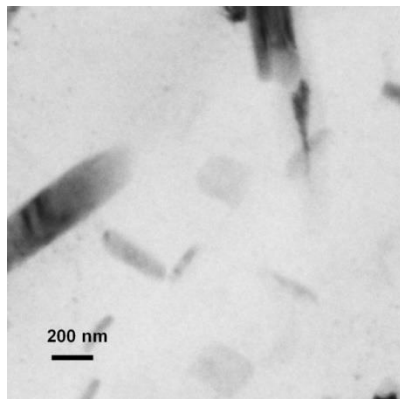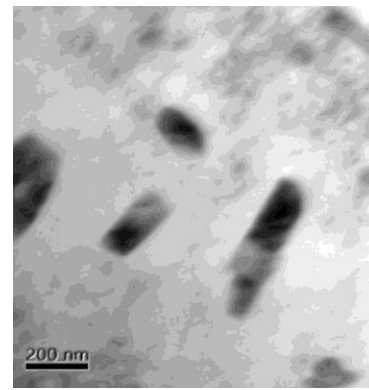
e. UWFSW - 4˚   f. FSW - 4˚

Fig. 7.8 TEM micrographs of LHDR

Fig. 7.8 revealed the TEM micrographs of parent metal and LHDR of FSW and UWFSW joints. The parent metal is characterized by the presence of fine needle like

146

precipitates densely distributed   in the Al matrix. The LHDR of FSW and UWFSW joints are characterized by presence of coarsened precipitates and PFZ. It is notable that the extent of precipitate coarsening and dissolutions are lower in UWFSW joints than FSW joints. The UWFSW joint fabricated using tool tilt angle of 2° show relatively lower precipitate size than the other joints

7.6 DISCUSSION

7.6.1 Effect of tool tilt angle on the joint quality

From the macrostructural analysis, it was evident that the tool tilt angle has significant effect on the governing of above said states. On increasing the tool tilt angle, the defect formation in the SZ is eliminated. The SZ was formed as a result of two process namely extrusion and forging, which is the key factor to attain the balance state of material flow. The extrusion process is mainly governed by the tool rotation speed and tool traverse speed, whereas the forging action is governed by the tool tilt angle (Mishra and Ma 2005). Due to tool inclination, the tool front end is lift upward and the tool rear end is lowered downwards. The lift of tool front end acts as the reservoir which accommodates the material flow and reduces the wastage of material as flash. However, at higher tool tilt angle the materials expelled out and formed as flash. This is the reason for the decrement in the stir zone thickness (increment in the T_{gap}).

The material flow is classified into shoulder driven material flow and pin driven material flow. The upper part of stir zone mainly experiences the stirring action of tool shoulder, while the lower part of stir zone mainly experiences the stirring action

of tool pin (Huijie and Huijie 2012). Therefore two regular patterns of material flow were observed at the upper and lower part of the stir zone. In SIR, the material experiences the circular flow and downward flow and in PIR, the material experiences the circular flow and upward flow. The shoulder driven flow and pin driven flow get junction at the advancing side of tool rear end. Due to mix up of two regular flow a turbulent flow is prevailed at the junction area. During stirring, the material was excavated from advancing side and flow around the tool to refill the vacant in the advancing side of tool rear end. The improper flow at this area results in defect formation.

Due to tool tilt angle, the lowered edge offers compressive force over the materials. On increasing the tool tilt angle, the forging pressure at the tool rear end increases. From the macrostructure examination, it was identified that the FSW and UWFSW joints fabricated using lower tool tilt angles of $0°$ and $1°$, the defects were formed because of the attainment of insufficient state of heat and material flow. The attainment of insufficient state is attributed to the poor forging pressure and low plasticization due to low heat input exerted during use of low tool tilt angles. On increasing the tool tilt angle from $0°$ and $1°$, the downward forging force and material fluidity is higher and so the thickness of SIR (T_{SIR}) increases. Therefore the material pushes towards the defect and partially filled it. On further increases the tool tilt angle from $2°$ to $4°$, the heat input and the forging force increases which fill the defects formed in the SZ. At the tool tilt angle of $4°$, balance state of heat input and material flow exist and thereby defect free stir zone was observed. However, the high extent of forging pressure reduces the weld thickness than the plate thickness.

The mechanism of joint formation and the resultant joint quality were almost same in the joints fabricated in air and water cooling medium. But it is noteworthy that TMAZ region of UWFSW joints were narrow than the FSW joint. The high heat dissipation capacity of water readily convect the heat from the weld adjacent region (Yong *et al.* 2015). Because of low heat, the plasticization of material around the stir zone was highly limited and thereby the TMAZ was narrow in UWFSW joints.

7.6.2 Effect of tool tilt angle on the mechanical properties of the joints

The absence of fine strengthening precipitates was the prime reason for the softening and exhibiting lower hardness values in the TMAZ (Huijie and Huijie 2013). The extent of strength contribution due to age hardening was poor in the LHDR. Moreover, the presence of elongated large grains offers low grain boundary strengthening in LHDR. During tensile loading, the load was concentrated in the weaker region and thereby the fracture was occurred in it. This is the reason for the occurrence of tensile fracture in the softer LHDR in all the joints. From this, it can infer that the lower LHDR has significant effect on the joint performance. By regulating the precipitation and grain growth in the LHDR, the joint performance can be greatly increased. The FSW joint fabricated using higher tool tilt angle of 4° resulted lower tensile strength. This was attributed to the large extent of precipitate coarsening in the LHDR compare to other joints. The maximum tensile strength was observed in the UWFSW joints fabricated using tool tilt angle of 2°. This was attributed to the lowered precipitate coarsening, high volume fraction of precipitates and higher hardness in the LHDR. The UWFSW joints exhibit higher tensile strength than the FSW joints. The water cooling controlled the precipitate coarsening and

149

reduces the width of softer LHDR. By this way, the hardness was marginally improved and thereby the joint efficiency was increased in the UWFSW joints.

7.6.3 Effect of tool tilt angle on microstructure

From the microstructural examination, it can infer that change in tool tilt angle alters the grain size and precipitation behaviour in the joints. The intense plasticization and high heat input created by tool stirring drives the recrystallization process in the stir zone (Radaj 1992). Therefore fine recrystallized equi-axis grains were formed in all the joints. The tool tilt angle has less significance in the recrystallization process; however the grain size increases with increase in tool tilt angle under both air and water cooling medium. The increase in axial load increases the friction force between the tool shoulder and the workpiece which increases the heat input prevailed in the SZ. The high heat input drives the grain growth. This is the prime reason for the increase of grain size in SZ with respect to increase in tool tilt angle. The grain boundaries contribute for strengthening and so lower hardness was not observed in the stir zone (Wang *et al.* 2016).

The adjacent TMAZ is influenced by both the thermal and deformation effect. However the extent of temperature and deformation is lower than the SZ and therefore no recrystallization occurred in the TMAZ (Zhu and Cha 2004). During stirring the materials in the TMAZ is pulled towards the SZ from both AS and RS. Therefore elongated grains were seen in the TMAZ. In underwater cooling condition, the TMAZ underwent severe deformation and exhibit lower width than the air cooling condition. In UWFSW joints, the materials around the SZ underwent lower thermal

softening and so less amount of material get deformed. Under the same process parameters, the stirring force generated by tool in UWFSW and FSW conditions is almost same. Because of limited thermal softening, less amount of material experience the stirring force and so the deformation was severe in UWFSW joints. On, increasing the tool tilt angle no significant grain growth was observed in the TMAZ.

The HAZ experiences only the thermal cycles and no deformation takes place. Therefore, coarse undeformed grains were present in the HAZ. Due to low heat input at UWFSW joints, the grain coarsening is avoided and the grain size was almost equal to the PM. In contrary, the grain coarsening is notable in the FSW joints. The grain sizes increases with increase in tool tilt angle due to increase in heat input.

The precipitation behaviour of LHDR are also varies with respect to the cooling medium and tool tilt angle. The thermal cycles exerted in the TMAZ coarsen or dissolute the precipitates during welding under both cooling medium. Hence LHDR was characterized by precipitate zone and coarse precipitates. In UWFSW joints, the LHDR experience controlled thermal cycles than FSW joint. This is the reason for reduced coarsening and dissolution of precipitates in the UWFSW joints. Therefore the UWFSW joints exhibit higher joint efficiency than the FSW joints.

7.7 SUMMARY

The effect of tool tilt angle on the joint characteristics of friction stir welded (air cooled and water cooled) AA2519-T87 aluminium alloy joints was investigated and the following important observations were made:

i. Of the various tool tilt angles (0˚ to 4˚) used, the joint fabricated using tool tilt angles of 2˚ to 4˚ resulted in defect free joints. The attainment of adequate heat generation and proper material flow with the aid of sufficient forging force caused by the higher tool tilt angle may be one of the reasons for the fabrication of defect free joints.

ii. The UWFSW joint fabricated using tool tilt angle of 2˚ exhibited maximum tensile strength of 345 MPa and joint efficiency of 76 %. Whereas, tool tilt angle of 2˚ yielded maximum tensile strength of 278 MPa in conventional FSW joints. UWFSW joints showed 25 % enhancement in joint efficiency compared to FSW joints.

CHAPTER 8
THERMAL ANALYSIS OF FSW AND UWFSW PROCESSES

8.1 INTRODUCTION

There are two objectives for the simulation of the friction stir welding, one is to understand the physics and other is to develop the predictive tool permitting to reduce the number of trial experiments. Various models exist which predict the heat generation during FSW. In the model by Yuh *et al.* (2003), the heat generation comes from the sliding friction, where Coulomb's law is used to estimate the shear or friction force at the interface. Russell *et al.* (2001) reported that the heat generation due to constant friction stress at the interface is equal to the shear yield stress at elevated temperature. Schmidt and Hattel (2008) estimated the heat generation based on assumptions for different contact conditions at the tool/material interface in FSW joints. The material flow and heat generation are defined by the contact conditions at the interface of tool and workpiece surface. Based on the contact condition three states namely sliding, sticking and partial sliding/sticking prevails during FSW.

Studying the thermal histories of the weld joints is useful to explore the fundamental aspects of UWFSW and FSW joints. In order to map the temperature distribution and to predict the thermal histories of welding processes, finite element method (FEM) was used by many researchers (Saad *et al.* 2016; Dialami et al. 2016; Kumaraswami *et al.* 2015). However, very few researchers have carried out experimental investigation and finite element analysis of UWFSW of aluminium alloys. Moreover, the previous investigations were focused on the microstructural characterization,

153

mechanical properties evaluation and FE analysis of the conventional FSW process. Very few publications are available on the comparison of experimental and numerical investigations of FSW and UWFSW of aluminium alloys. Hence, this investigation was carried out to evaluate the mechanical properties of FSW and UWFSW joints of high strength, armour grade AA2519-T87 aluminium alloy. Finite element analysis was also used to estimate temperature distribution during FSW and UWFSW of AA2519-T87 aluminium alloy. Further, width of the TMAZ region was estimated for both the joints (FSW and UWFSW) by FE analysis and compared with the experimental results.

8.2 TENSILE PROPERTIES

The tensile properties of FSW and UWFSW joints are compared in the Table 8.1. The maximum tensile strength of 372 MPa and 282 MPa were obtained for the optimized UWFSW and FSW conditions, respectively. The joint efficiency of UWFSW joint is 24 % higher than the FSW joint. However, the percentage of elongation of UWFSW joint is marginally lower than the FSW joints.

Table 8.1 Transverse tensile properties of optimized joints

	0.2 % Yield strength (MPa)	Tensile strength (MPa)	Elongation in 50 mm gauge length (%)	Joint efficiency (%)
FSW	260	282	10.4	62
UWFSW	344	372	9.01	82

154

8.3 FINITE ELEMENT ANALYSIS

This paper presents three-dimensional thermal analysis using the finite element code COMSOL. Dissimilar meshed model of varying size and element types were used in the FE analysis (Fig. 8.1). The meshed model composed of quadrilateral, triangular and square elements. The model is meshed into 6821 finite elements. In order to reduce the computational time and achieve accurate results, finer mesh was carried out near the tool and coarser mesh was carried out for the region away from the tool. The input parameters used for FE analysis is tabulated in Table 8.2.

8.3.1. Thermal boundary conditions

The heat generated during welding is lost due to three modes of heat transfer which greatly reduce the availability of heat required to weld the work piece. In welding, the heat is transferred by conduction, convection and radiation modes. The governing differential equation for three dimensional heat conduction equations for a solid in Cartesian coordinate system is given by (Radaj 1992)

$$\frac{\delta^2 T}{\delta x^2} + \frac{\delta^2 T}{\delta y^2} + \frac{\delta^2 T}{\delta z^2} + \frac{q_g}{k} = \frac{1}{\alpha}\left(\frac{\delta T}{\delta t}\right) \qquad (8.1)$$

Where, $\alpha = \frac{k}{\rho C_p}$ thermal diffusivity of the material, q_g is the heat generation per unit volume in W/m^3, ρ is density of the material in kg/m^3, C_p is specific heat in J/kgK and k are thermal conductivity W/mK.

Heat transfer from the work piece due to convection was applied in the free surface. The corresponding heat flux expression for free surface is (Zhu and Chao 2004)

$$q_{up,down} = h_{up,\ down} - (T_0 - T) + \varepsilon\sigma\left(T_{amb}^4 - T^4\right) \qquad (8.2)$$

155

Where, h_{up} and h_{down} are the convection coefficient of top and bottom surface respectively, T_0 is the reference temperature, T_{amb} is the ambient temperature, σ is the Stefan - Boltzmann constant and ε is the surface emissivity.

q_p, Heat flux applied in the surface area of the pin

q_s, Heat flux applied in the shoulder surface
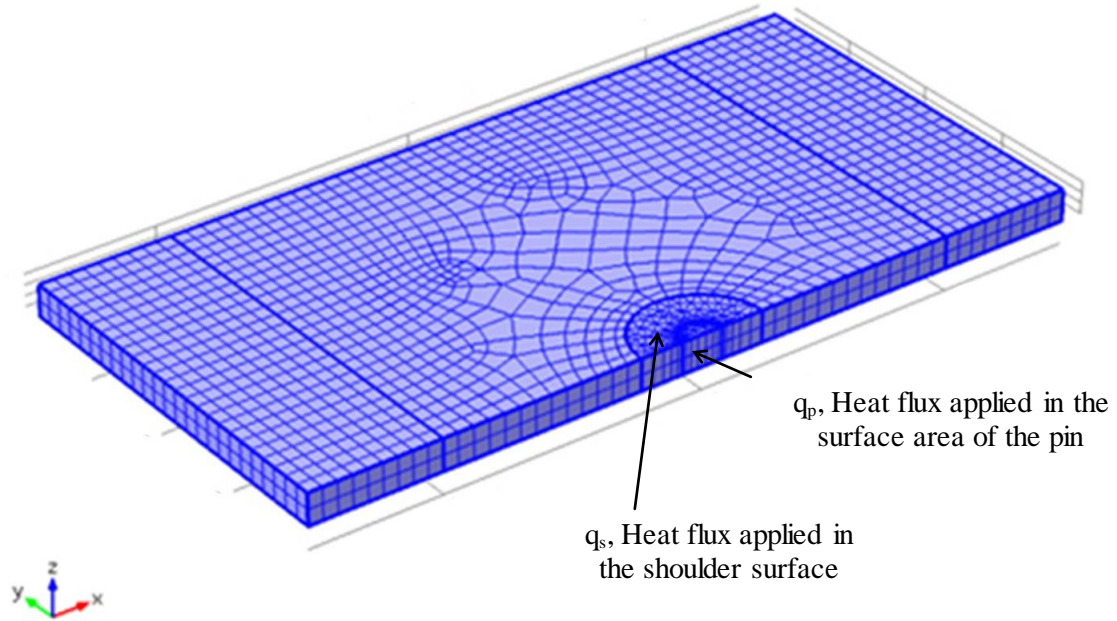
Fig. 8.1 3-Dimensional meshed model

The natural convection between aluminium and air was experimentally found by Choa et al as 15 W/(m^2°C) for FSW (Chao et al. 2003). Similarly Hui et al. 2013 found the heat transfer coefficient of UWFSW at top and bottom as 2000 W/(m^2°C) and 1000 W/(m^2°C) respectively. Temperature based material properties were considered for the finite element analysis. In this investigation, the thermal model was considered for the analysis and the material flow behavior was not accounted. The degree of heterogeneity between the advancing side (AS) and retreating side (RS) mainly depends on the material flow and the microstructure rather on the temperature distribution and hence symmetric model was considered for the analysis. The mid-plane of the butt joint was assumed to be a plane of symmetry in the

analysis. Zero displacement conditions were used for constraining the butt joint which resembling the complete fixed fixture.

Table 8.2 Input parameters used in FE analysis

Parameter	Notations	FSW	UWFSW
Ambient temperature ($^{\circ}$C)	T_0	30	30
Melting temperature ($^{\circ}$C)	T_{melt}	660	660
Heat transfer coefficient W/(m^2 $^{\circ}$C) (Liu et al. 2011)	h_{upside}	15	2000
Heat transfer coefficient W/(m^2 $^{\circ}$C) (Grujicic et al. 2010)	$h_{downside}$	200	1000
Welding speed (mm/min)	u_{weld}	30	30
Friction coefficient	μ	0.3	0.3
Rotation speed (rpm)	Ω	1100	1200
Normal force (kN)	F_n	12	12
Pin radius (mm)	r_{pin}	12-6	12-6
Shoulder radius (mm)	$r_{shoulder}$	30	30

8.3.2. Heat source modeling

The heat generated is concentrated locally and propagates rapidly into subsequent regions of the plates by heat conduction according to (Eq.8.1) as well as convection and radiation through the boundary. Constant heat fluxes were applied as the heat source in the tool shoulder- workpiece interface and tool pin- workpiece interface.

Heat generation in shoulder-work piece interface is the function of major element such as axial load, area subjected to friction, coefficient of friction and angular velocity. The heat flux can be mathematically expressed by Song and Kovacevic (2003).

157

$$q_{shoulder} = 2 \times \pi \times \mu \times F_n \times R \times \omega \qquad (8.3)$$

Where, F_n is the normal force (kN), A_s is the shoulder's surface area (mm^2), μ is the friction coefficient, R is the distance from the center axis of the tool (mm) and ω is the tool rotation speed (rpm).

The mathematical expression of heat generated at the interface of pin and work piece is adapted from Colegrove (2000).

$$q_p = \frac{\mu}{\sqrt{3 \times (1 + \mu^2)}} (r_p \times \omega) \times Y(T) \qquad (8.4)$$

Where, μ is the friction coefficient, r_p is the pin radius (mm), ω is to the angular velocity (rad/s), and Y(T) is the average shear stress of the material (N/mm^2). The input parameter used for the FEM simulation of FSW and UWFSW are presented in table 8.2.

8.3.3 Thermal analysis

Fig. 8.2 illustrates the top surface temperature contours for FSW and UWFSW joints. In FSW joint, the temperature distributed to the leading and trailing edge of the tool along the longitudinal direction seemed to be asymmetry. Symmetric temperature distribution is observed along the longitudinal direction for the UWFSW joint. Fig. 8.3 illustrates the thermal contours in the cross-section of the weld. In FSW joint, the temperature experienced by SIR, MTR and PIR are almost same around 550 ^{o}C (Fig. 8.3a). But in UWFSW joint, there exists a variation in SIR, MTR and PIR. Maximum temperature of 525 ^{o}C is witnessed in the SIR and gradually reduced towards PIR of

512 ^{o}C (Fig. 8.3b). This is clearly evident from the color contours which show intense blue color in the SIR and dull blue color in the PIR.

Similar to the longitudinal temperature contour map, the isothermals of UWFSW joint also remarkably move towards the tool axis in contrast to the FSW joint. The entire stir zone of FSW experienced same amount of heat. In UWFSW joint, the maximum temperature is at the SIR and the temperature is decreasing towards the PIR. TMAZ, the region next to stir zone exhibits band of temperature values fluctuating around 400 ^{o}C as shown in light blue color contour. The material experienced heat in this region is softened and deformed by the stirring action of tool. The FSW joint have wider range of temperature values than the UWFSW. Fig. 8.3c shows the temperature plot along the transverse direction. The higher range of temperature was recorded at the stir zone so that similar color was observed up to the weld periphery.
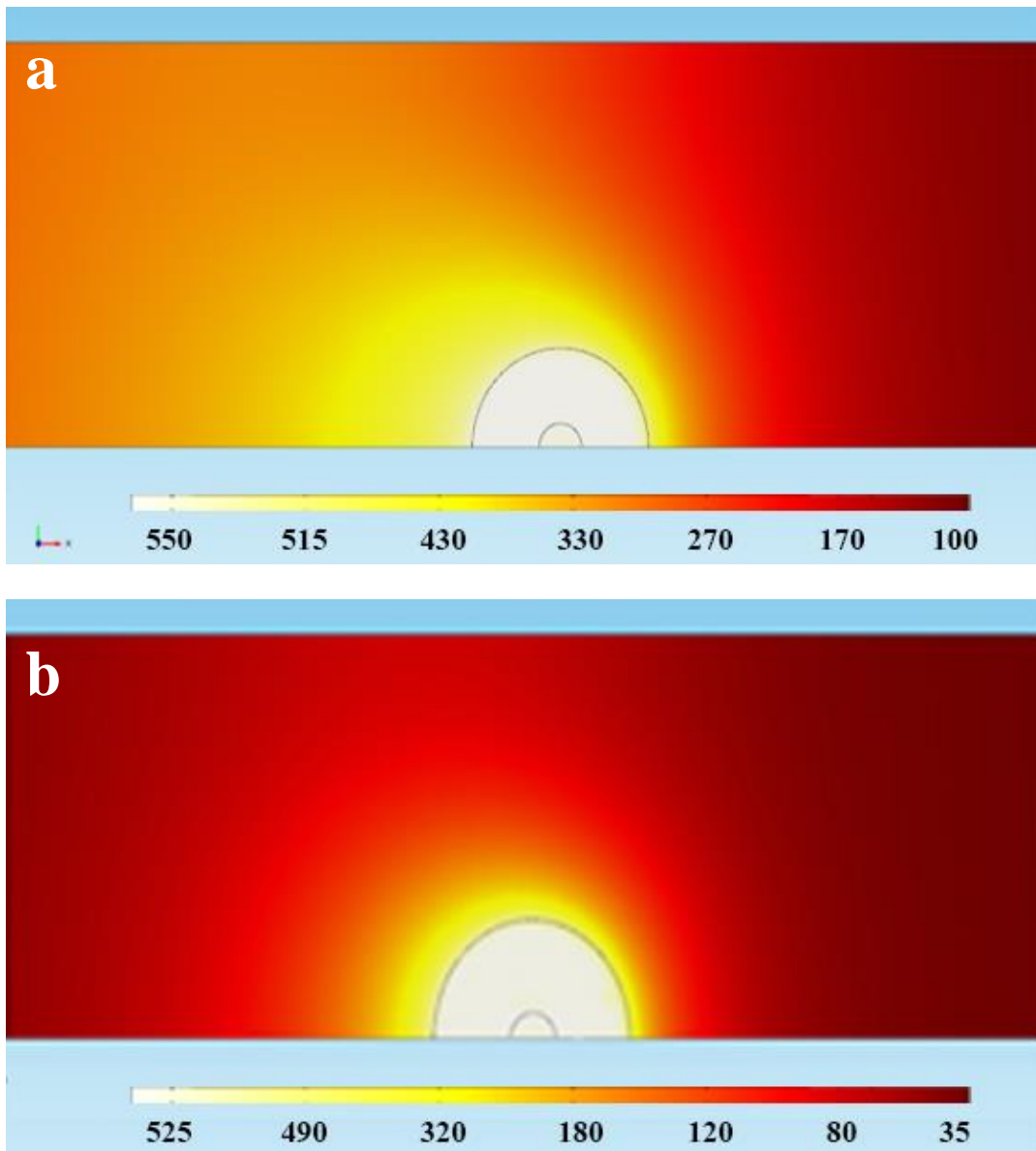
Fig. 8.2 Simulated temperature contour at top surface of the joints (a) FSW joint (b) UWFSW joint
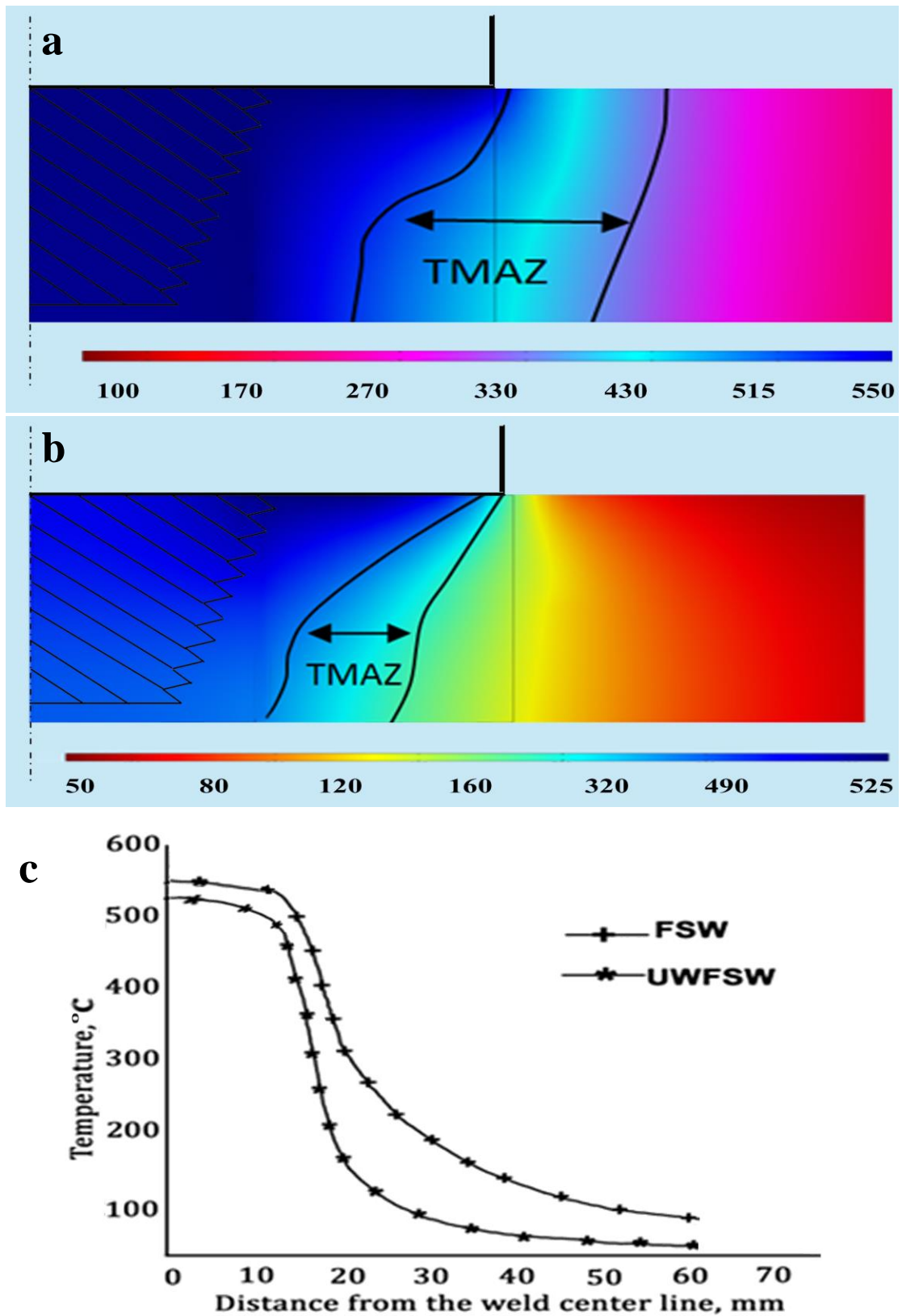
Fig. 8.11 Temperature profiles (a) Cross sectional temperature contour of FSW joint (b) Cross sectional temperature contour of UWFSW joint (c) Thermal plots

8.4 DISCUSSION

8.4.1 Effect of cooling medium on the mechanical properties

The region of fracture can be correlated with the LHDR of microhardness plot. In both the joints, the location of failure was found to be exactly in the TMAZ-stir zone interface. From this, it can infer that the extent of softening in LHDR of the joint was a vital factor deciding the tensile properties. From the TEM analysis, it can understand that the softening of TMAZ is attributed to the presence of coarsened precipitates and precipitate free zone (Fig. 5.6). However, the hardness of the LHDR of UWFSW is higher because of the high extent of precipitate hardening and strain hardening than the FSW joint. A similar strengthening effect was previously reported by Liu et al. (2010). The lower hardness of HAZ of FSW joint was attributed to the presence of high volume fraction of coarse θ' precipitates. The overaging of HAZ was greatly reduced in the UWFSW which results in higher hardness than FSW joint. This was attributed to the high cooling rate and the attainment of lower temperature in the HAZ. During hardness indentation, the hardening precipitates were not available in the TMAZ to limit the plastic deformation. During tensile loading, the strain gets localized at the softer TMAZ among the various regions of weld joint. Because of the strain localization, both FSW and UWFSW joints exhibit lower elongation than the parent metal. Moreover, absence of necking formation was seen due to the severe strain localization. The SEM characterization of fracture surfaces revealed dimples in both the UWFSW and FSW joints which indicates that both the joints undergone ductile mode of failure. However UWFSW joint exhibits fine dimples than FSW joint. During tensile loading, the second phase precipitates act as the nucleation sites for the voids formation. The voids were coalescence to form the final fracture. Relatively less coarse and high volume fraction of precipitates in the

162

UWFSW joints provides more nucleation sites than FSW joints and thereby fine populated dimples were found.

8.4.2 Effect of cooling medium on the thermal behaviour

During tool traverse, the leading edge of the tool get contacted with the cold zone which was generally referred as preheat zone. The high yield strength of the cold zone offers high resistance against the material flow. Due to tool rotation, intense frictional heat was generated in the tool-work piece contact area (Fig. 8.2). The cold zone or preheat zone conducts the heat from the interface. In UWFSW process, the heat conducted to preheat zone was readily dissipated by the convective heat transfer of water. The temperature attained in the preheat zone was too low for UWFSW joint than FSW joint. Therefore, high yield stress was created which in turn results high heat flux in the shoulder-work piece contact area. This was one of the reasons for the higher heat flux created in the shoulder-work piece contact area of UWFSW.

The material in the trailing edge of the tool experienced gradual drop in the temperature. Because of thermal softening, the material in the leading edge got drop in yield strength and got easily transported to the rear end. The plasticized material offer poor friction between the tool and work piece and therefore relatively low temperature is observed in the rear end. As the tool traverses, cooling cycle takes place in the welded region. Hence, low thermal gradient was observed at the rear side of the tool in FSW joint. The isothermal was larger at the rear and smaller at front of the tool. This was because of the heat buildup behind the tool during tool traversing. But in UWFSW process, the heat was readily dissipation by the water and hence high

thermal gradient was observed at the rear end. Moreover, similar isothermals were observed at both the front and rear end of the tool during UWFSW.

The temperature of isothermals can be correlated with the degree of thermal softening of the material. High temperature isothermal results in high degree of thermal softening and vice-versa. The isothermal was confined around the tool in UWFSW joint but for FSW joint, widespread isothermal was noted. Consequently thermal softening was also confined near the tool in UWFSW joint and the extent of thermal softening is higher for FSW joint. The softened band of material around the tool gets deformed to form stir zone and TMAZ. Because of the narrowed softening, the extent of region undergoing plastic deformation was limited in UWFSW joint. So a narrow TMAZ was formed in the UWFSW. All these facts are even more clearly evident from the cross sectional temperature mapping.

From the literature it was identified that the TMAZ of aluminium alloys experiences the temperature range of around 400 ^{o}C (Chen and Kovacevic 2003). The cross sectional thermal contour map shows the peak temperature attained in the various region (Fig. 8.3a and 8.3b). FSW joint shows a wider TMAZ region and the temperature range was around 400 ^{o}C. At this temperature, the material get soften and plasticized to form wider TMAZ. But in UWFSW joint, only a narrowed region experiences the same temperature. This was the main reason for achieving constricted TMAZ in the water cooled-FSW joint. The adjacent region was identified as HAZ region, which has peak temperature of around 300 ^{o}C. The temperature value was enough to alter the grain size and precipitates in the material. In FSW joint, a

164

wider region experienced this temperature. But, the same range of temperature values cannot be observed in the contour map of UWFSW joint. Hence from the FEM results, it could inferred that, the temperature range affecting the microstructure in HAZ was controlled significantly due to the high convection heat transfer nature of water.

8.5 SUMMARY

The experimental and numerical investigation on underwater friction stir welding (UWFSW) and friction stir welding (FSW) of armour grade, high strength AA2519-T87 aluminium alloy were conducted and following important observations were made:

i.   The peak temperature experienced by the FSW joint is 550 ^{o}C which is higher compared to the peak temperature experienced by UWFSW joint. UWFSW joint resulted in higher cooling rate and higher temperature gradient than FSW joint due to superior heat absorption capacity of the water cooling system.

ii. The coarsening and dissolution of precipitates resulted in TMAZ as the weaker zone. The thermal gradient along the transverse and longitudinal axis of the joint is controlled by the water cooling and thereby the weaker TMAZ and HAZ are appreciably narrowed. Ultimately reduction of width of weaker zone and reduction of overaging of HAZ are the reasons for the marginal increase in tensile properties.

CHAPTER 9
EFFECT OF POST WELD HEAT TREATMENT

9.1 INTRODUCTION

In FSW, the stir zone reaches solutionizing temperature due to frictional heating. AA2519 alloy is an age hardenable alloy, in which at the solutionizing temperature, it undergoes dissolution of precipitates (Yutaka *et al.* 1999). The strength of the age hardenable alloys are mainly depends on the presence of the semi coherent θ' precipitates. From literature, it is found that the loss of precipitates and coarsening of precipitates results in lowering the tensile properties (Hakan *et al.* 2009; Lee *et al.* 2003). So the PWHT is needed to regain deteriorated tensile properties of FSW joints.

During aging treatment, the precipitates will undergo transformation in size, shape and coherency. Balasubramanian *et al.* (2008) reported that the microstructure of the weld joint could be greatly altered by the PWHT. The aging time and aging temperature have a significant effect on the tensile strength and hardness of FSW joints of AA7075 alloy (Christian *et al.* 2010). Narasayya *et al.* 2014 and Izabela *et al.* 2014 reported that the aging of Al-Cu alloy improved the mechanical properties like hardness, tensile strength, strain hardening exponent and fracture toughness. Liu *et al.* (2004) opined that the hardening effect due to aging was mainly attributed to nucleation of precipitates in high volume fraction. The dislocations accelerated the heterogeneous nucleation and kinetics of precipitation. It altered the size and distribution of the precipitates and consequently influenced the yield strength (Guven

166

et al. 2014). Hence it is important to reveal the nature of dislocation and its effect on precipitation. The influences of FSW process parameters on the microstructure and mechanical properties of various grades of aluminium like AA1050, AA2024, AA5251, AA6061 and AA7075 were previously studied Maeda and Nogi (2003); Sonne *et al.* (2013) Etter *et al.* (2007); Madhusudhan *et al.* (2009); Sivaraj *et al.* (2014). The aging behavior of friction stir welded aluminium alloys like AA2219, AA7039 and AA6066 were also studied by few researchers Malarvizhi *et al.* (2008); Singh *et al.* (2011); Evren *et al.* (2007). However, the published information on response of friction stir welded AA2519-T87 aluminium alloy joints to PWHT is scant and hence this investigation is carried out.

9.2 TENSILE PROPERTIES

The super imposed stress strain diagram of AW, AA and STA joints are shown in the Fig. 9.1. The tensile properties like yield strength, ultimate tensile strength and elongation are derived from the stress-strain diagram and presented in the Table 9.1. The tensile strength is recorded as 248 MPa for AW-FSW, 342 MPa for AW-UWFSW, 326 MPa for AA-FSW, 395 MPa for STA-FSW and 395 MPa for STA-UWFSW joints. The AW joint exhibits lower tensile strength than the parent metal. The STA treatment improves the tensile strength of FSW joints. It was observed that the STA joints under air cooing and water cooling conditions exhibit same tensile strength. Thus a maximum joint efficiency of 85 % is observed in the STA joints under air cooling and water cooling conditions. Elongation of 9.02 % was observed in AW joint which is lower than the parent metal but higher than AA and STA joints.

167
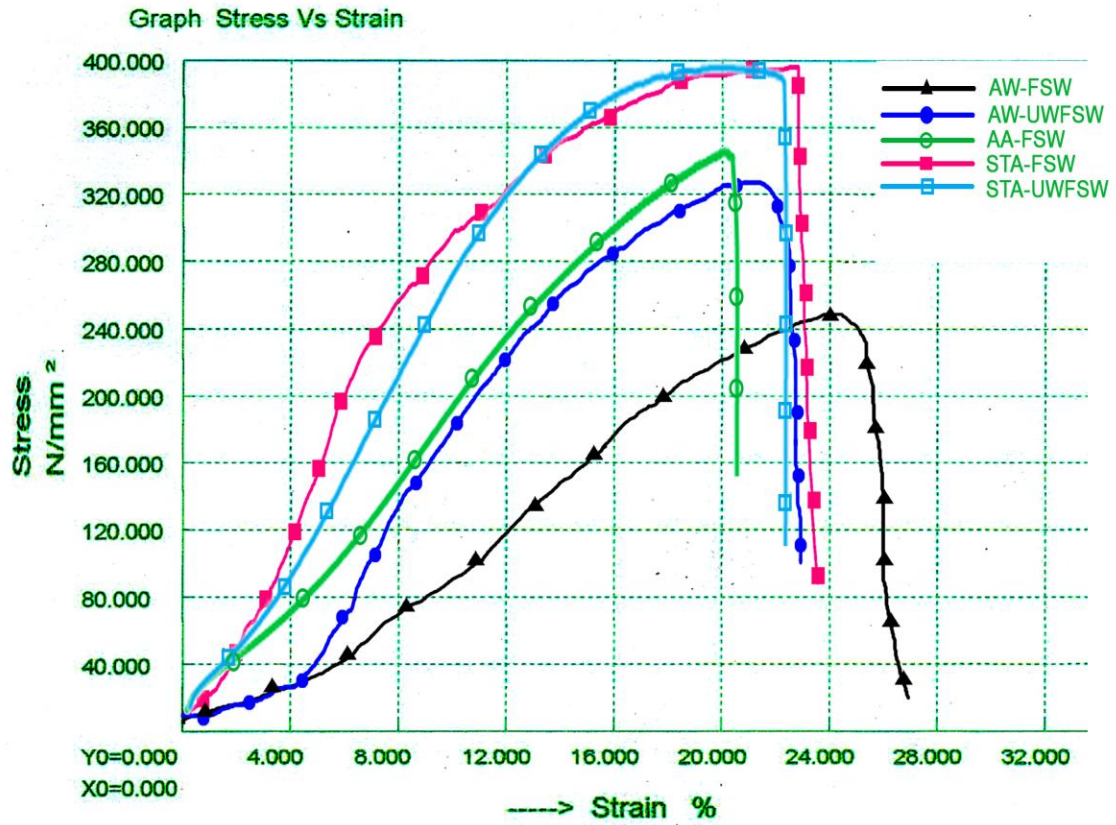
Fig. 9.1 Stress-strain curves

Table 9.1 Transverse tensile properties of parent metal and FSW joints

Joint	0.2 % Yield strength (MPa)	Ultimate tensile strength (MPa)	Elongation in 50 mm gauge length (%)	Joint efficiency (%)
PM	427	452	11.2	-
AW-FSW	198	248	9.02	55
AW-UWFSW	287	342	6.5	75
AA-FSW	283	326	7.1	72
STA-FSW	323	395	8.6	85
STA-UWFSW	360	395	8.4	85

Table 9.2 Effect of aging on fracture path
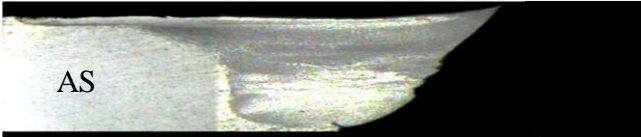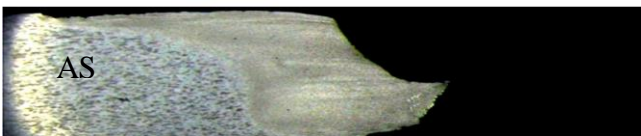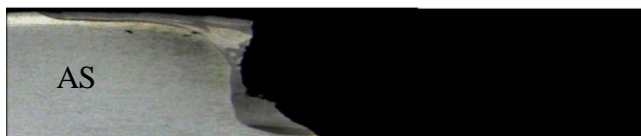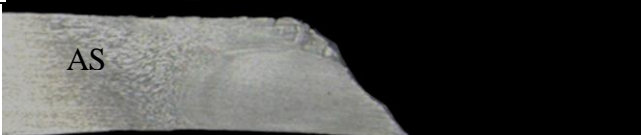
Name of the joint	Cross sectional macrograph	Observation
AW	AS	Fractured along the RS-TMAZ
AW-UWFSW	AS	Fractured along the RS-TMAZ
AA-FSW	AS	Fractured along the stir zone
STA-FSW	AS	Fractured along the stir zone
STA-UWFSW	AS	Fractured along the stir zone

Fig. 9.2 shows the fractographs of the weld joints. The SEM fractographs of AW-FSW joint fractographs show fine populated dimples than the parent metal (Fig. 9.2a). The AW-UWFSW joints exhibits larger voids than the air cooled conditions (Fig. 9.2b). The fractographs of AA-FSW joints shows populated dimples and a few flat featureless faces (Fig. 9.2c). The fractographs are characterized by the presence of fine dimples along with a few tear ridges in the STA-FSW and STA-UWFSW joints (Fig. 9.2d and 9.2e). Populated dimples are observed in all the joint conditions, but the sizes of dimples are comparatively higher than the parent metal.

Table 9.2 shows the cross sectional fracture path of the various joints. The AW joints under air cooled and water cooled exhibit fracture along the retreating side weld

periphery of the joint. But in both the aging conditions, the tensile fracture was shifted to the stir zone of the joints.
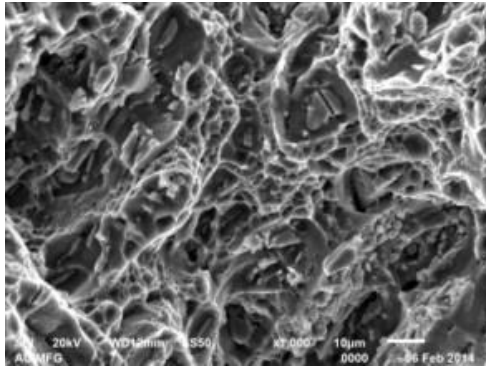
a. AW-FSW
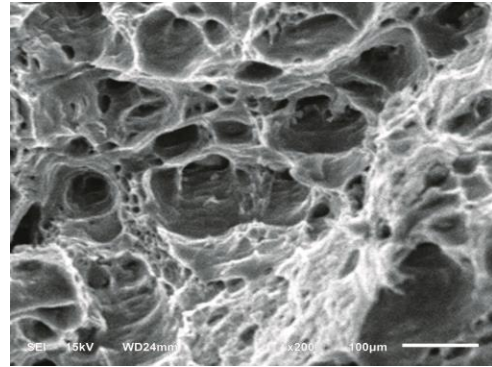
b. AW-UWFSW
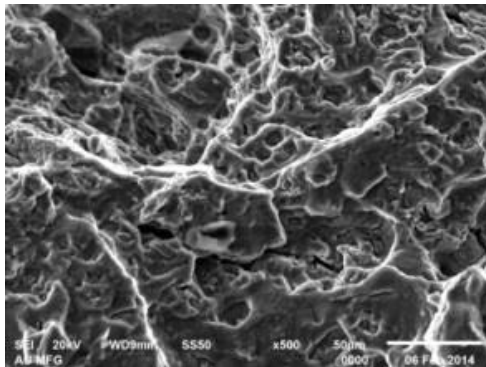
c. AA-FSW
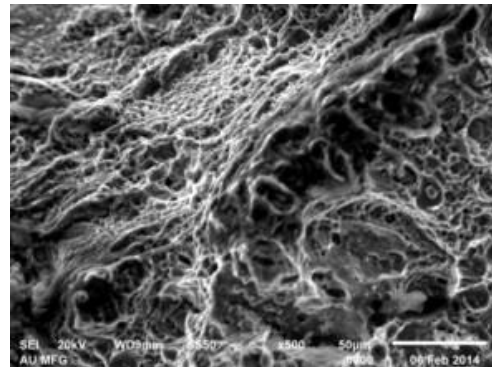
d. STA-FSW
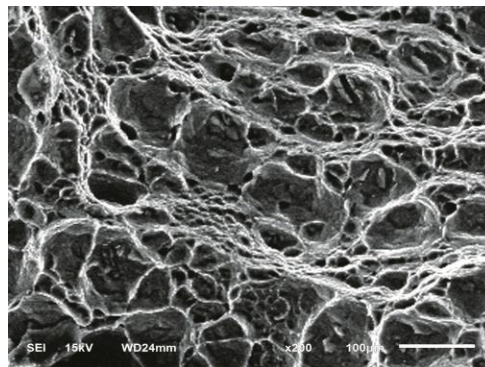
e. STA-UWFSW

Fig. 9.2 Fracture surface analysis

9.3 MICROHARDNESS

The microhardness measured across the welded joint at mid-thickness region is shown in Fig. 9.3. The AW-FSW joint shows lower hardness values in the TMAZ and the stir zone exhibits hardness of 116 HV. The hardness values decreased towards the TMAZ and then increased towards the parent metal. AW-UWFSW joints exhibit 108 HV in the stir zone and 80 HV in the TMAZ region. The stir zone hardness of the AA-FSW joint is 148 HV, but the other regions show a similar trend as seen in the AW-FSW joint. Maximum hardness of 151 HV and 152 HV was attained in the stir zone of STA-FSW and STA-UWFSW joints respectively, which is marginally lower than parent metal hardness of 161 HV. In both the STA joints, the hardness along the entire joint is almost same with little fluctuating values.
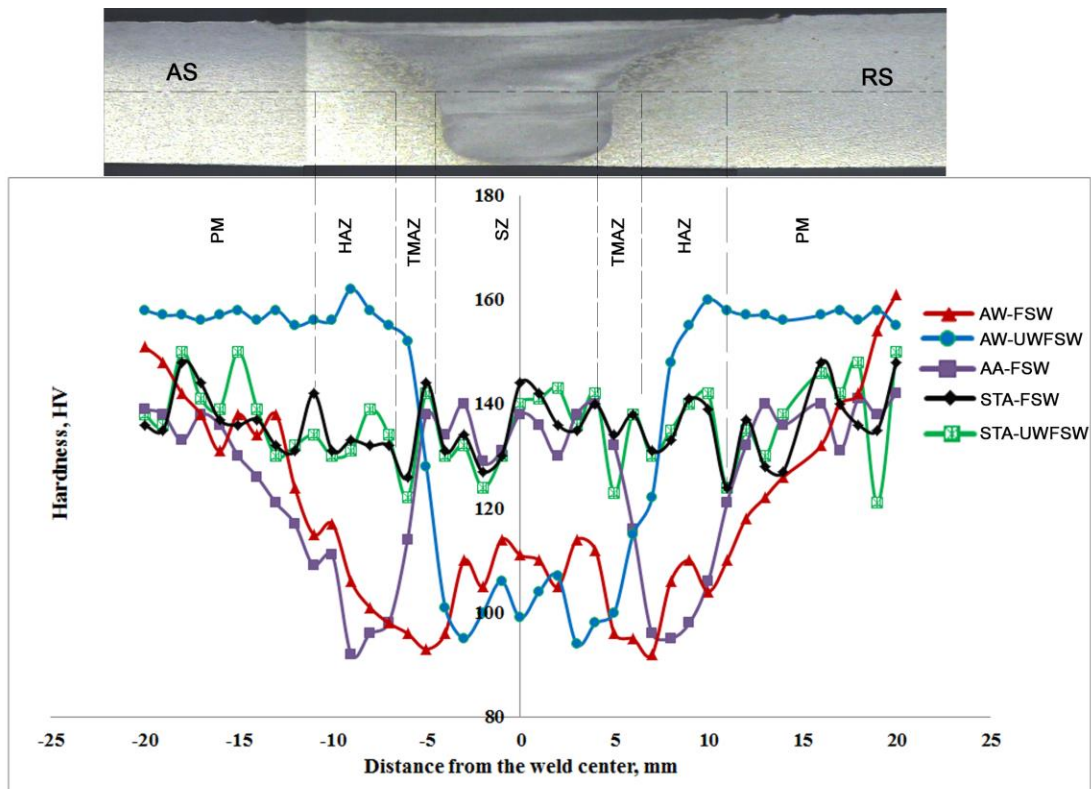
Fig. 9.3 Microhardness distribution

9.4 MICROSTRUCTURE

Fig. 9 4 shows the optical micrograph of stir zones of various joints. The stir zone of AW joints shows recrystallized grains of finer size than the parent metal. Fine grains are observed in the stir zone of AA and STA joints. Even later the aging treatment, no considerable grain growth is noticed in the stir zone of AA and STA joints. Fig. 9.5 shows the optical micrograph of TMAZ of all the joints. The interface microstructure shows transition grain size towards the stir zone. In the TMAZ of the RS, the coarse deformed grains are pulled towards the stir region. The AS TMAZ shows the abrupt transformation in the grain size and orientation towards stir zone. There is no significant changes are observed in the AW and PWHT joints under optical microscope.

Fig. 9.6 shows the TEM images of stir zone of AW, AA and STA joints. AA 2519-T87 is an age hardenable aluminum alloy strengthened by θ'- $CuAl_2$ phase, which is semi-coherent with Al matrix (Felix and Jayabalan 2015). Fig. 9.6a and 9.6b shows the TEM image of AW-FSW and AW-UWFSW joints respectively. This microstructure is characterized by the presence of precipitate free zones (PFZ), GP zone and dense dislocations. In the AA-FSW joint, the reprecipitation along the grain boundary is observed. The region adjacent to the grain boundary is identified as PFZ or Cu depleted. However, fine θ' precipitates with denser distribution are seen in the other region of the Al matrix (Fig. 9. 6c). Fig. 9.6d shows the TEM image of STA-FSW joint where dense distribution of θ' precipitates are observed in the Al matrix. Fig. 9.6e shows the TEM image of STA-UWFSW joint where dense distribution of

θ' precipitates along with dislocations are observed in the Al matrix. In all the PWHT conditions, the lost precipitates are recoverved.

a. AW-FSW joint   b. AW-UWFSW joint

c. AA-FSW joint   d. STA-FSW joint

e. STA-UWFSW joint

Fig. 9.4 Optical micrograph of the stir zone

	AS – TMAZ	RS – TMAZ
AW- FSW joint		
AW- UWFSW joint		
AA-FSW joint		
STA-FSW joint		
STA- UWFSW joint		
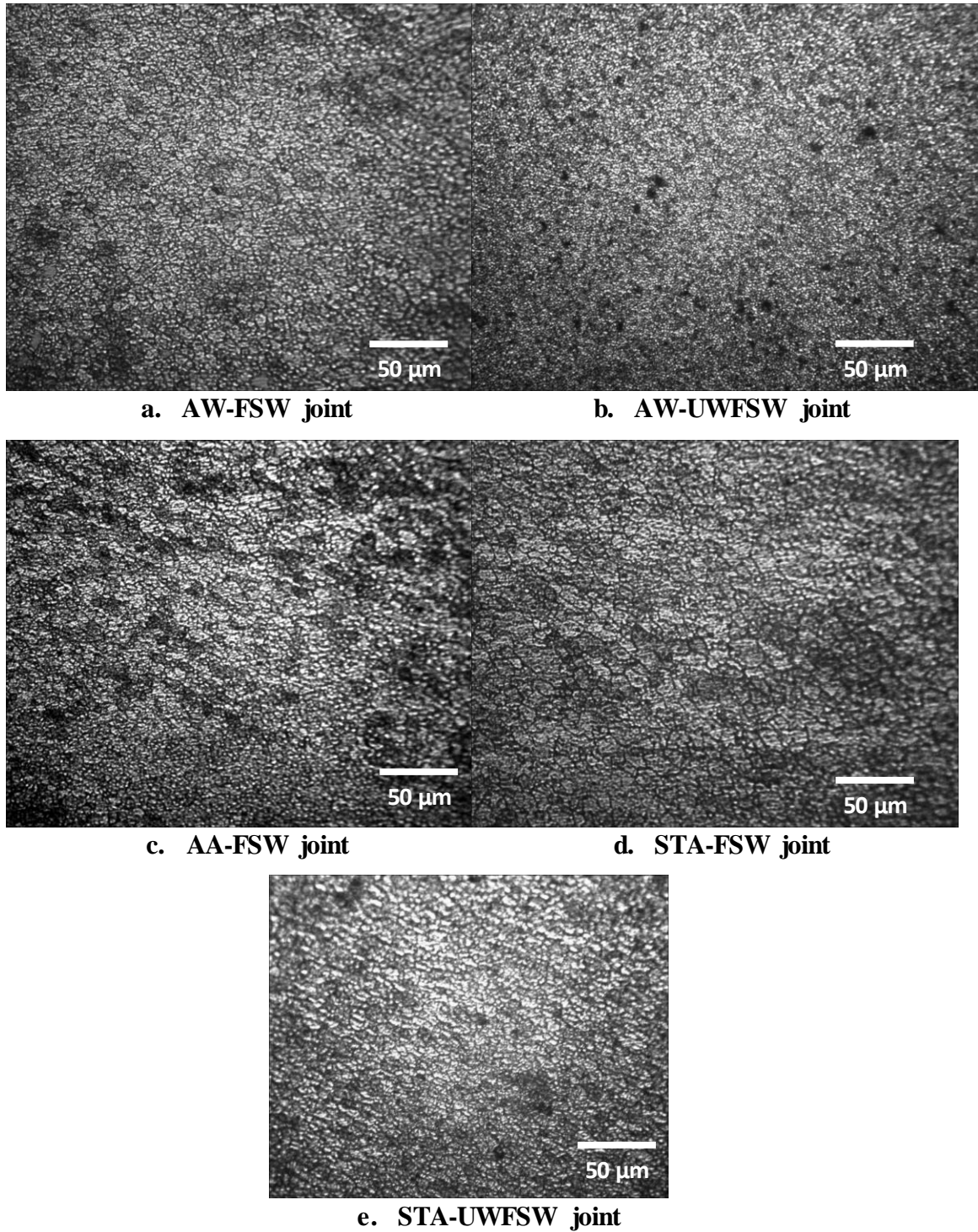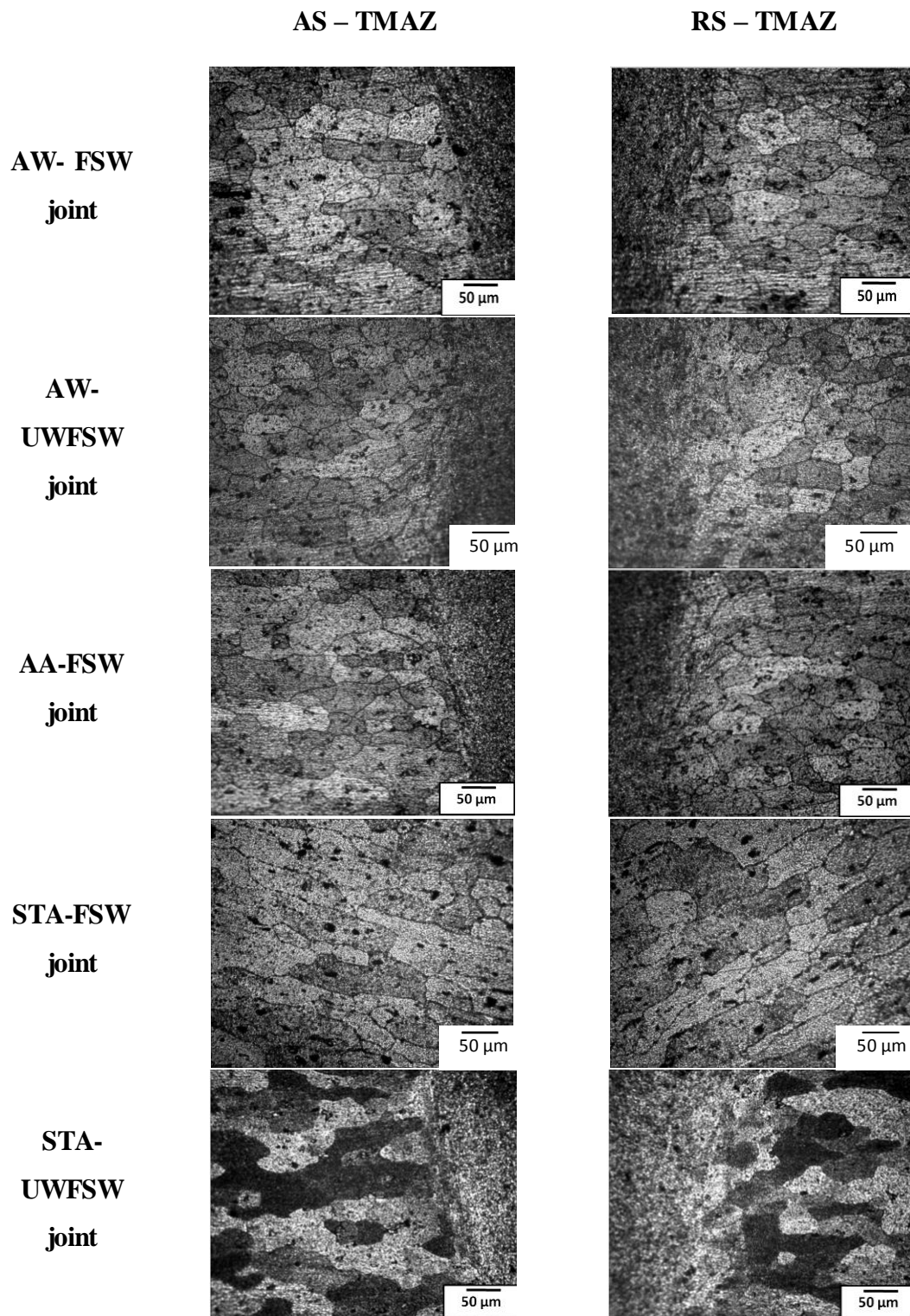
Fig. 9.5 Optical micrographs of interface regions of welded joints

174
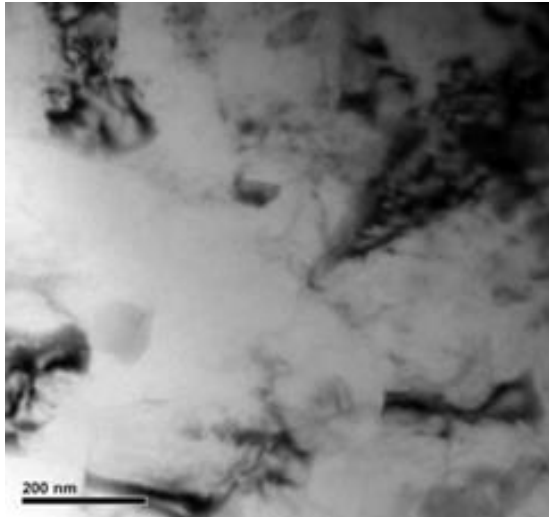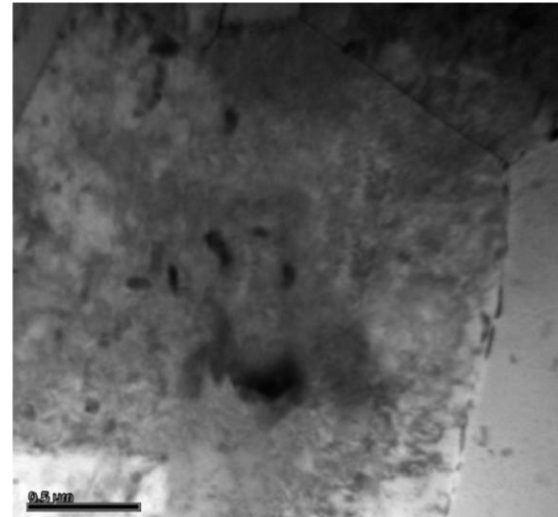
a. AW-FSW joint
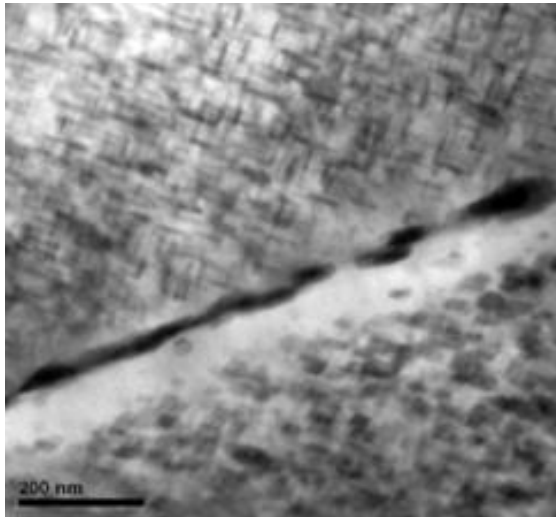
b. AW-UWFSW joint
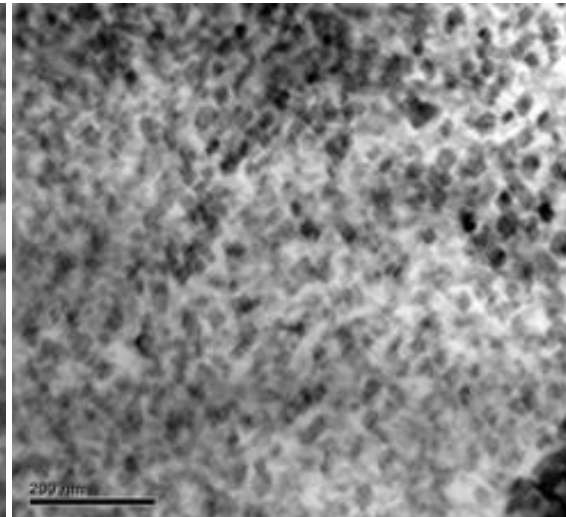
c. AA- FSW joint

d. STA-FSW joint
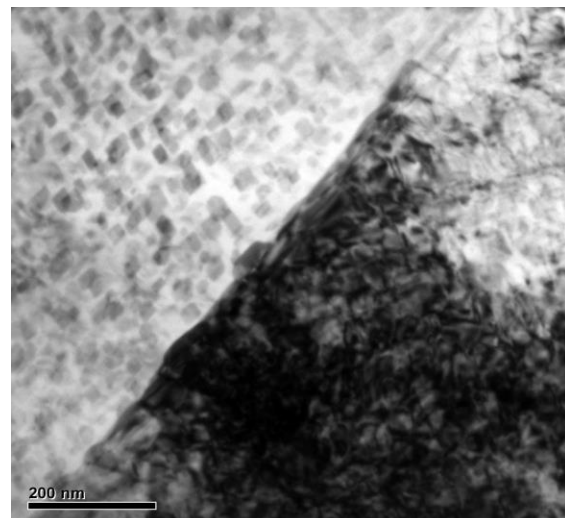
e. STA-UWFSW joints

Fig. 9.6 TEM micrograph of the stir zone

Table 9.3 Image analysis results of TEM and OM images

Joint	Area fraction (%)		Average precipitate size (nm)		Approximate particle spacing (nm)	Average grain size (µm)
PM	Matrix	- 75	Diameter	- 43	48	49
	θ'	- 22	Thickness	− 3		
	θ	- 0				
AW-FSW	Matrix	- 92	Diameter	- 93	482	3.95
	θ'	- 1	Thickness	− 36		
	θ	- 6				
AW-UWFSW	Matrix	- 90	Diameter	- 93	431	4
	θ'	- 0	Thickness	− 36		
	θ	- 10				
AA-FSW	Matrix	- 62	Diameter	- 62	28	4.2
	θ'	- 32	Thickness	− 17		
	θ	- 2				
STA-FSW	Matrix	- 53	Diameter	- 41	18	4
	θ'	- 42	Thickness	− 21		
	θ	- 3				
STA-UWFSW	Matrix	- 57	Diameter	- 41	22	3
	θ'	- 40	Thickness	− 21		
	θ	- 3				

Table 9.3 presented the image analysis results of TEM image of stir zone. The area fraction, average precipitate size, approximate particle spacing and grain size of stir zone microstructure were analyzed and estimated. Parent material shows a dense distribution of θ' precipitate of 22 % and no stable θ precipitate is noted. The size of the precipitate is 43 nm in diameter and 3 nm in thickness. The precipitates are dense and evenly distributed and thus it results in lower particle spacing of 48 nm. In AW-FSW joint, stir zone microstructure reveals the minimum amount of θ' precipitate of

1 % and θ precipitate of 6 %. The precipitates are coarse and have a diameter of 93 nm and thickness of 36 nm. The AA-FSW joint shows 32 % of θ' precipitate and 2 % of θ precipitate. The diameter and the thickness of the precipitates are 62 nm and 17 nm respectively. The dense precipitate distribution of AA-FSW joint shows particle spacing of 28 nm. In STA-FSW joint, the θ' precipitate contributes 42 %, which is higher than the other joints. The average precipitate diameter is 41 nm and thickness is 21 nm. The inter particle spacing between the precipitate is 18 nm in distance.

AW-UWFSW joint exhibit 1 % and STA-UWFSW joint exhibit 40 % of θ' precipitate. By STA treatment, the thickness of precipitate is reduced from 36 nm to 21 nm. The average grain size is measured using the line intercept method. The grain size of the parent metal was measured and compared with the grain size of stir zone of AW, AA and STA joints. The average grain diameter of parent metal is 49 μm. The grain diameter is greatly reduced to 3.95 μm, 4 μm, 4.2 μm, 4 μm and 3 μm in the stir zone of AW-FSW, AW-UWFSW, AA-FSW, STA-FSW and STA-UWFSW joints respectively.

9.5 DISCUSSION

9.5.1 Influences of PWHT on mechanical properties

The strength or hardness of the aluminium alloys is mainly dependent on the interaction between the dislocation motions and its hindrance (Russell and Lee 2005). In an age hardenable aluminium alloy, the hindrance of dislocations is mainly achieved by the grain boundary and the precipitate availability. By Hall Petch relation, it was found that grain size is inversely proportional to the hardness (Sato *et*

al. 2003; Jiahu *et al.* 2006). Finer grain size results higher hardness or strength due to the higher grain boundary energy. However, stir zone of AW and AA joints results lower hardness values despite of the finer grain size. It can be inferred that, for heat treatable aluminium material, the effect of grain boundary on hardness is less significant.

During indentation, the precipitates act as the obstacles for the dislocation motion. The plastic deformation was resisted by the precipitates which in turn increase the hardness or strength. In the AW condition, the area fraction of θ' precipitates is too low to resist the indentation (Table 9.2). The hardness value in the stir zone is higher than the TMAZ. This is because, the PFZ identified by TEM analysis cannot show the tiny cluster of solute particle called GP zone which is few angstroms in size. The presence of this GP zone increases the hardness or strength of the stir zone. Similar strengthening by GP zone is observed by Fonda and Bingert (2004).

Few researchers studied the mechanical properties of FSW joints of AA2519 alloy. Xiao *et al.* (2012) found that TMAZ is the weakest region and similarly Fonda and Bingert (2004) also reported that TMAZ as the softer region in the joint. They attribute the softening of TMAZ to the dissolution of precipitates. During FSW, the precipitates in the stir zone and TMAZ region are dissolved. The stir zone exhibit higher temperature than the TMAZ and thus the lowest cooling rate is observed in the stir zone. The slow cooling in the stir zone enabled the diffusion to form clusters of solute particle (GP zone). But, the higher cooling rate prevails in the TMAZ, restricts the reprecipitation. And so the TMAZ of AW condition exhibited lower

hardness values (Fig. 9.3). In AA condition, the hardness in the stir zone and TMAZ-stir zone boundary region are recovered to a maximum value of 148 HV. This region is regarded as pre-solutionize region created by FSW. Thus, it is able to re-precipitate on aging. The high area fraction of θ' precipitates in the stir zone are the reason for the higher hardness. However, the fluctuating hardness is observed due to the presence of PFZ and precipitate zone.

During FSW, the heat conducted to HAZ has coarsened the precipitates. During aging, the coarsened precipitates grow in size to become stable θ precipitates. Thus the hardness values are lower at TMAZ-HAZ boundary and HAZ. In STA condition, the loss of hardness values at stir zone, TMAZ and HAZ are recovered to a greater extent. The solution treatment followed by aging treatment increase the area fraction of θ' precipitates in the all the zone. This is the only reason for the improvement of hardness in the entire joint (Fig. 9.3) of both air cooled and water cooled joints. However, due to the accelerated nucleation enabled by the dislocations and grain boundaries, few coarsened stable θ precipitates were formed which results in fewer lower hardness values in the stir zone.

In addition to the precipitate availability, the strengthening of material is governed by the interparticle spacing between the precipitates. If the interparticle spacing is high, the hindrance of dislocation movement is prominently reduced. The dislocation movement cut through or bypasses the precipitate during tensile loading. The precipitate required shear energy to break up which determines the strength of the joint. In other hand, the dislocations bypass the precipitates leaving dislocation loops

called Orowan loop. The finer precipitates undergone break ups and on the increase of precipitate above a critical radius, the dislocation is moved by bypassing. Thus the precipitate size has an influence on deciding the mode of dislocation movement. If the particle is fine, closely distributed and dense in number, then the movement of dislocation is hindered greatly. Thus based on these factors, the strength of the joint is decided. Among the PWHT condition, STA joint have dense and closely distributed precipitates. This is the reason for enhancing the tensile strength of STA joint. However due to high dislocation density in the stir zone, the precipitate growth get accelerated to 21 nm thickness which is much higher than the parent material. Therefore irrespective of aging type and cooling type, the precipitation behaviour in the stir zone is almost same. The accelerated precipitation results in coarse precipitates in the stir zone than the PM which result make the stir zone as relatively softer. Thus during tensile loading, the fracture falls in the stir zone which can also be correlate with the softer region of microhardness plot (Table 9.2).

As discussed in the microhardness plot, for the AW condition the fracture falls in the retreating TMAZ which is the softest region among the various regions. Due to less area fraction of θ' precipitates and occurrence of wide PFZ, the AW joint results lower tensile strength. In AA joint, high degree of heterogeneous microstructure was evolved due to the partial precipitation and coarsening of precipitates. Despite the TMAZ is softer, the tensile fracture occured in the weld center. This is because during aging the copper depletion creates nano level PFZ near to the grain boundaries of stir zone. From this investigation, it is found that aging has greater effect on the enhancement of hardness and strength. But the ductility properties are not

180

significantly altered after aging which can be confirmed by the fracture surface analyses. This is because the presence or absences of precipitates does not considerably influence the ductility due to the inherent   Al matrix exhibit high degree of ductility.

9.5.2 Influences of PWHT on microstructure

The microstructure of FSW joint shows variation in the grain size from the stir zone to the parent metal region. The stir zone exhibits recrystallized grains of fine size (3.95 μm). Since aluminium has high stacking fault energy, the grains are expected to be dynamic recrystallized during the plastic deformation at elevated temperatures created by tool stirring. Few researchers Liu and Feng (2013); Hassan *et al.* (2003) made investigation on aging behaviour of AA2219 and AA7010 FSW joint respectively. From these investigations they reported that on aging, the stir zone of AA2219 and AA7010 joints undergone abnormal grain coarsening due to the thermal activation energy supplied. However, on AA and STA, the grain size is very similar to the AW condition (Table 9.3), owing to the precipitation along the grain boundary pins the grain growth further (Safarkhanian *et al.* 2009).

AA2519-T87 aluminium alloyed with copper for the enhancement of strength of the material (Laure *et al.* 2011). The solubility of the Cu element in Al system is varied with respect to the temperature. In addition the Cu induces significant misfit strain in the aluminium. By satisfying the above two conditions, AA2519 T87 aluminium alloy can be substantially strengthened by the precipitation process. In the age hardnenable aluminium alloys, the precipitates searched for the existence of

favorable sites for the nucleation. The sites like grain boundary, dislocations or dislocation loops are the favorable sites which accelerate and assist the precipitate nucleation (Feng et al. 2014; Farshidi *et al.* 2013). The tempering condition T87 stands for solution treated and cold worked followed by artificial aging. During cold working of parent material, dislocations were evenly formed in the entire matrix. Dislocations are the favorable site and so the precipitates nucleate at the dislocations during artificial aging. This is the reason for the evenly distribution of θ' precipitate in the parent metal.

During FSW, the high strain induced plastic deformation results dense dislocations in the weld region. The dislocation favors the precipitation because dislocations can lower the energy barrier and motivate the formation of θ' precipitates Yi *et al.* (2014). The degree of straining is varied from shoulder influenced region to pin influenced region and from weld center to the periphery. Thus heterogeneous formation of dislocation is observed in the stir zone of AW condition (Fig. 9.6). During FSW, the stir zone attains nearly 80 % of melting temperature of the parent material. This heat is sufficient for solutionizing the precipitates in the stir zone region. During cooling cycle, the time and heat is not sufficient in the stir zone to diffuse Cu atoms from the Al matrix. The temperature distribution is varied from shoulder influenced region to pin influenced region and from weld center to the periphery. Thus the weld joint attains further heterogeneity due to the difference in the thermal condition. Because of this reason, both precipitate zone and PFZ are observed in the AW condition (Fig. 9.6).

However, the diverse precipitation can be thermally stabilized to a great extent by the solution treatment. During solution treatment, the precipitates in the entire joint get dissolved and stable microstructure is observed. On quenching, it results in the super-saturated solid solution. During quenching, the time and temperature are insufficient for the system to diffuse Cu atoms from the Al matrix. In STA process, the precipitates nucleate more evenly from the matrix (Fig. 9.6). In AA joints, precipitates of different size and distribution were observed. During FSW, the temperature distribution and cooling rates differ from the shoulder influenced region to pin influenced region and from stir zone to the parent metal region. Thus, in AW condition, the geometry and availability of the precipitates are different. It is composed of PFZ, fine precipitates and coarsened precipitates. On further aging of this heterogeneous structure, varied degree of precipitate nucleation and growth were resulted (Figure 6c).

9.5 SUMMARY

In this investigation, the response of friction stir welded AA 2519-T87 armour grade aluminium alloy joints to post weld heat treatment was investigated in detail and following important observations are derived

   i.   The solution treatment followed by artificially aging (STA) yielded superior tensile properties irrespective of FSW processes. The as welded FSW joint yielded lower tensile strength of 248 MPa and hardness of 116 HV. An enhanced tensile strength of 395 MPa and maximum hardness of 151 HV were achieved due to the STA treatment.

   ii. FSW and UWFSW joints undergone similar precipitation behaviour during

STA treatment and exhibited almost similar properties. During STA treatment, homogenization and reprecipitation occurred in the entire joint unlike AA condition.

iii. The superior mechanical properties are mainly attributed to the presence of fine precipitate with dense distribution in the entire joint. However, finer grain size has no obvious effects on enhancing the hardness and strength value of this heat treatable Al alloy.

iv. The precipitation is highly accelerated by the dislocations and the grain boundaries which brought uneven nucleation and growth of precipitates. This attributes the fluctuation in hardness values.

CHAPTER 10
SUMMARY AND CONCLUSION

10.1 SUMMARY

AA2519-T87 aluminium alloy is widely used in the fabrication of light combat military vehicles, because of the beneficial properties like damage tolerance, high ballistic strength and high strength to weight ratio. However, the wide applications of this alloy are limited because of the poor fusion weldability results in hot cracking, porosity formation and alloy segregation. The solidification problems can be overcome by employing FSW process which does not involve in melting of the material. However, the thermal cycles involved in FSW process coarsen or dissolute the precipitates and also results in wider LHDR. To overcome such shortcomings, UWFSW process can be adopted. Tool tilt angle is one of the significant parameters of FSW process which governs the heat generation and material flow. The impact of this parameter in conventional FSW is known, but its influence in UWFSW is not yet fully revealed. Hence, this investigation aims a comparative study on the effect of process parameters and aging behaviour of the FSW and UWFSW joints. The results showed that the water cooling have significant effect on improving the tensile strength of up to 20 % than the FSW joints. This is attributed to the attainment of adequate heat generation, proper material flow, narrowed LHDR, higher grain boundary strengthening, lower dissolution of precipitates and restricted precipitate coarsening. All the above, the STA treatment resulted maximum tensile strength of 395 MPa which is only 12 % parent metal strength.

10.2 CONCLUSION

In this investigation an attempt was made to study the effect of process parameters and ageing behaviour of friction stir welded (FSW) and underwater friction stir welded (UWFSW) AA2519-T87 aluminium alloy joints and the effort was very successful. The conclusions from the investigations are as follows:

i.   Of the four tool pin profiles used in this investigation, straight threaded cylindrical pin profile (THC) and taper threaded cylindrical pin profile (TTC) yielded defect free joints.

ii. The joint fabricated using taper threaded pin profile with water cooling exhibited tensile strength of 345 MPa and joint efficiency of 76 % is 29 % higher than FSW-THC joint and 22 % higher than FSW-TTC joint. It is attributed to the attainment of optimum level of heat generation and proper material flow during stirring.

iii. Of the five tool rotational speed, UWFSW joint fabricated using tool rotation speed of 1200 rpm exhibited maximum tensile strength of 372 MPa and joint efficiency of 82 %, whereas maximum tensile strength of 282 MPa is resulted in the conventional FSW joints. UWFSW joint showed 20 % enhancement in joint efficiency compared to FSW joints.

iv. The superior performance of UWFSW joints over FSW joints is attributed to the presence of relatively finer grains in the stir zone, marginally higher hardness of stir zone, high volume fraction of precipitates in lower hardness distributed region (LHDR), and appreciably lower width of LHDR.

v.   Of the five tool traverse speed, the UWFSW joint fabricated using tool traverse speed of 30 mm/min exhibited maximum tensile strength of 345 MPa with a joint efficiency of 76 %. On the other hand, tool traverse speed

of 40 mm/min yielded maximum tensile strength of 278 MPa in air cooled FSW joint. UWFSW joints showed 25 % enhancement in joint efficiency compared to FSW joints.

vi. Lower heat input and appreciably narrow lower hardness region are the main reasons for the superior performance of the UWFSW joint fabricated using tool traverse speed of 30 mm/min than other joints.

vii. Of the various tool tilt angles (0° to 4°) used, the joint fabricated using tool tilt angles of 2° to 4° resulted in defect free joints. The UWFSW joint fabricated using tool tilt angle of 2° exhibited maximum tensile strength of 345 MPa and joint efficiency of 76 %. Whereas, tool tilt angle of 2° yielded maximum tensile strength of 278 MPa in conventional FSW joints. UWFSW joints showed 25 % enhancement in joint efficiency compared to FSW joints.

viii. The attainment of adequate heat generation and proper material flow with the aid of sufficient forging force is the reasons for the superior tensile properties.

ix. From the finite element analysis, it was found that the UWFSW joint resulted in higher cooling rate and higher temperature gradient than FSW joint which is due to the severe and even heat absorption capacity of the water cooling system. The controlling of thermal histories, low heat input and its subsequent effect on precipitation behaviour are found to be the main reasons for the enhancement in the strength of UWFSW joints.

x. Solution treated and aged (STA) joints under air cooling and water cooling exhibited higher joint efficiency of 85%; artificially aged (AA) FSW joints showed joint efficiency of 72%; as welded (AW) FSW joints recorded joint

efficiency of 75% and as welded (AW) joints yielded joint efficiency of 55%.

xi. The combined effect of fine and uniformly distributed precipitates in the stir zone and higher hardness in entire regions are responsible for superior tensile properties of STA joints under air and water cooling conditions.

10.3 SUGGESTION FOR FURTHER RESEARCH

The present investigation on FSW and UWFSW of age hardenable aluminium alloy AA2519-T87 has given important information on the effect of cooling medium and effect of post weld heat treatment on mechanical properties and evolution of microstructure of the joints. However, there are few other aspects need to be investigated to explore the process effectively. In this regard, following suggestions are to be considered for further research on this topic.

i. The research works on the fatigue, fracture toughness and fatigue crack growth behaviour of the FSW and UWFSW of AA2519-T87 aluminium alloy joints are limited. Hence, it would be more appropriate to study the fatigue and fracture behaviour of FSW and UWFSW joints.

ii. Similarly, the research works on the ballistic behaviour of FSW and UWFSW of AA2519-T87 aluminium alloy joints are not attempted any researchers. It is an armour grade aluminium alloy and so, it is appropriate to estimate the ballistic strength and residual velocity of the joints.

REFERENCES

1. Adeosun, S.O., Balogun, S.A., Sekunowo, O.I., and Usman, M. A., (2010), Effects of Heat Treatment on Strength and Ductility of Rolled and Forged Aluminum 6063 Alloy, *Materials Characterization*, Vol.9(8), pp.763–773.

2. Arun Prasath, A., and Ramachandran, K., (2015), Investigation of mechanical and metallurgical properties of friction stir welded magnesium alloy, *Journal of Manufacturing Engineering*, Vol.10, pp.81–85.

3. Asadi, P., Akbari, M., Besharati Givi, M.K., and Shariat Panahi, M., (2016), Optimization of AZ91 friction stir welding parameters using Taguchi method, *Proceedings of the Institution of Mechanical Engineers, Part L: Journal of Materials: Design and Applications*, Vol.230(1), pp.291–302.

4. Attallah, M.M., and Salem, H.G., (2005), Friction stir welding parameters: A tool for controlling abnormal grain growth during subsequent heat treatment, *Materials Science and Engineering A*, Vol.391(1-2), pp.51–59.

5. ASTM E112-10. Standard Test Methods for Determining Average Grain Size.

6. ASTM E8M-15 Standard Test Methods for Tension Testing of Metallic Materials

7. ASTM E-384-05 Standard Test Method for Micro indentation Hardness of Materials

8. Avner., *Introduction to physical metallurgy*, McGraw-Hill, 1997.

9. Aydin, H., Bayram, A., and Durgun, I., (2010), The effect of post-weld heat treatment on the mechanical properties of 2024-T4 friction stir-welded joints, *Materials and Design*, Vol.31(5), pp.2568–2577.

10. Aydın, H., Bayram, A., Uğuz, A., and Akay, K.S., (2009), Tensile properties of friction stir welded joints of 2024 aluminum alloys in different heat-treated-state, *Materials and Design*, Vol.30(6), pp.2211–2221.

11. Borvik, T., Olovsson, L., Dey, S., and Langseth, M., (2011), Normal and oblique impact of small arms bullets on AA6082-T4 aluminium protective plates, *International Journal of Impact Engineering*, Vol.38(7), pp.577–589.

12. Babu, N., Karunakaran, N., and Balasubramanian, V., (2014), Comparative evaluation of temperature distribution in GTAW and FSW joints of AA 5059 aluminium alloy, *Journal of Manufacturing Engineering*, Vol.9(2), pp.71–76.

13. Bahram, A., and Borhani, E., (2016), A study on the effect of nano-precipitates on fracture behavior of nano-structured Al-2wt%Cu alloy fabricated by accumulative roll bonding (ARB) process, *Journal of Mining and Metallurgy B: Metallurgy*, Vol.52, pp.93–98.

14. Balasubramanian, V., Jayabalan, V., and Balasubramanian, M., (2008), Effect of current pulsing on tensile properties of titanium alloy, *Materials and Design*, Vol.29(7), pp.1459–1466.

15. Barcellona, A., Buffa, G., Fratini, L., and Palmeri, D., (2006), On microstructural phenomena occurring in friction stir welding of aluminium alloys, *Journal of Materials Processing Technology*, Vol.177(1-3), pp.340–343.

16. Bayazid, S., Farhangi, H., Asgharzadeh, H., Radan, L., Ghahramani, A., and Mirhaji, A., (2016), Effect of cyclic solution treatment on microstructure and mechanical properties of friction stir welded 7075 Al alloy, *Materials Science and Engineering: A*, Vol.649(1), pp.293–300.

17. Benavides, S., Li, Y., Murr, L.E., Brown, D., and McClure, J.C., (1999), Low-temperature friction-stir welding of 2024 aluminum, *Scripta Materialia*, Vol.41(8), pp.809–815.

18. Berbon, P.B., Bingel, W.H., Mishra, R.S., Bampton, C.C., and Mahoney, M.W., (2001), Friction stir processing: A tool to homogenize nanocomposite aluminum alloys, *Scripta Materialia*, Vol.44(1), pp.61–66.

19. Birol, Y., and Kasman, S., (2013), Effect of welding parameters on the microstructure and strength of friction stir weld joints in twin roll cast en AW Al-Mn1Cu plates, *Journal of Materials Engineering and Performance*, Vol.22(10), pp.3024–3033.

20. Bourgeois, L., Dwyer, C., Weyland, M., Nie, J.F., and Muddle, B.C., (2011), Structure and energetics of the coherent interface between the θ' precipitate phase and aluminium in Al-Cu, *Acta Materialia*, Vol.59(18), pp.7043–7050.

21. Buffa, G., Fratini, L., Hua, J., and Shivpuri, R., (2006), Friction stir welding of tailored blanks: Investigation on process feasibility, *CIRP Annals - Manufacturing Technology*, Vol.55(1), pp.279–282.

22. Carroll, M.C., Gouma, P.I., Mills, M.J., Daehn, G.S., and Dunbar, B.R., (2000), Effects of Zn additions on the grain boundary precipitation and corrosion of Al-5083, *Scripta Materialia*, Vol.42(4), pp.335–340.

23. Cavaliere,P., De Santis,A., Panella,F., and Squillace,A., (2009), Effect of welding

parameters on mechanical and microstructural properties of dissimilar AA6082-AA2024 joints produced by friction stir weldin, *Materials and Design*, Vol.*30*(3), pp.609–616.

24. Cheeseman,A., Gooch,W., and Burkins,M., (2008), Ballistic evaluation of aluminum 2139-T8. In B. SJ and W. JW (eds.), *Proceedings of the 24th international symposium on ballistics*, New Orleans, USA, 651.

25. Chen, G., Shi, Q., Li, Y., Sun, Y., Dai, Q., Jia, J., Zhu, Y., and Wu, J., (2013), Computational fluid dynamics studies on heat generation during friction stir welding of aluminum alloy, *Computational Materials Science*, Vol.79, pp.540–546.

26. Chen, Y.C., Feng, J.C., and Liu, H.J., (2009), Precipitate evolution in friction stir welding of 2219-T6 aluminum alloys, *Materials Characterization*, Vol.60(6), pp. 476–481.

27. Cho, A., and Bès, B., (2006), Damage Tolerance Capability of an Al-Cu-Mg-Ag Alloy (2139), *Materials Science Forum*, Vol.519, pp.603–608.

28. Chowdhury, S.M., Chen, D.L., Bhole, S.D., and Cao, X., (2010), Effect of pin tool thread orientation on fatigue strength of friction stir welded AZ31B-H24 Mg butt joints, In *Procedia Engineering*, Vol.2, pp. 825–833.

29. Colegrove, P.A., and Shercliff, H.R., (2005), 3-Dimensional CFD modelling of flow round a threaded friction stir welding tool profile, *Journal of Materials Processing Technology*, Vol.169(2), pp.320–327.

30. Colligan, K., (1999), Material Flow Behavior during Friction Stir Welding of Aluminum, *Welding Journal*, Vol.78, pp.229–237.

31. Crawford, R., Cook, G.E., Strauss, A.M., Hartman, D.A., and Stremler, M.A. (2006), Experimental defect analysis and force prediction simulation of high weld pitch friction stir welding, *Science and Technology of Welding and Joining*, Vol.11(6), pp.657-665.

32. Davis, J., *Aluminum and Aluminum Alloys*. (J. R. Davis, Ed.). Ohio: American Society for Metals (ASM), 1993

33. Dehghani, M., Amadeh, A., and Akbari Mousavi, S.A.A., (2013), Investigations on the effects of friction stir welding parameters on intermetallic and defect formation in joining aluminum alloy to mild steel, *Materials and Design*, Vol.49*(4)* , pp.33–441.

34. Dieter, G., and Bacon, D., *Mechanical Metallurgy*. SI Metric Edition, McGrawHill Shoppenhangers Road Maidenhead Berkshire SL2 2QL UK, 1988.

35. Elangovan, K., and Balasubramanian, V., (2007), Influences of pin profile and rotational speed of the tool on the formation of friction stir processing zone in AA2219 aluminium alloy, *Materials Science and Engineering A*, Vol.459(1-2), pp.7–18.

36. Elangovan, K., Balasubramanian, V., and Valliappan, M. (2008a), Effect of Tool Pin Profile and Tool Rotational Speed on Mechanical Properties of Friction Stir Welded AA6061 Aluminium Alloy, *Materials and Manufacturing Processes*, Vol.*23*(3), pp.251–260.

37. Elangovan,K., Balasubramanian,V., and Valliappan,M., (2008b), Influences of tool pin profile and axial force on the formation of friction stir processing zone in AA6061 aluminium alloy, *International Journal of Advanced Manufacturing Technology*, Vol.38(3-4), pp.285–295.

38. El-Nasr, and Abo, A.B.A., (2010), Mechanical Properties and Fracture Behavior of Friction Stir Welded 7075-T6 Al Alloy, *Journal of Engineering and Computer Sciences*, Vol.3(2), pp.147–161.

39. Ericsson, M., and Sandström, R., (2003), Influence of welding speed on the fatigue of friction stir welds, and comparison with MIG and TIG, *International Journal of Fatigue*, Vol.25(12), pp.1379–1387.

40. Eskin, D., Du, Q., Ruvalcaba, D., and Katgerman, L., (2005), Experimental study of structure formation in binary Al-Cu alloys at different cooling rates, *Materials Science and Engineering A*, Vol.405(1-2), pp.1–10.

41. Etter, A.L., Baudin, T., Fredj, N., and Penelle, R., (2007), Recrystallization mechanisms in 5251 H14 and 5251 O aluminum friction stir welds, *Materials Science and Engineering A*, Vol.445, pp.94–99.

42. Farshidi, M.H., Kazeminezhad, M., and Miyamoto, H., (2013), On the natural aging behavior of Aluminum 6061 alloy after severe plastic deformation, *Materials Science and Engineering A*, Vol.580, pp.202–208.

43. Feng, D., Zhang, X.M., Liu, S.D., Wang, T., Wu, Z.Z., and Guo, Y.W., (2013), The effect of pre-ageing temperature and retrogression heating rate on the microstructure and properties of AA7055. *Materials Science and Engineering A*, Vol.588, pp.34–42.

44. Feng, X., Liu, H., and Lippold, J.C., (2013), Microstructure characterization of the stir zone of submerged friction stir processed aluminum alloy 2219, *Materials Characterization*, Vol.82, pp.97–102.

45. Fisher James, J., Lawrence, S.K., and Joseph, R., (2002), Aluminum alloy 2519 in military vehicles, *Advanced Materials Process*, Vol.160, pp.43–46.

46. Fonda, R.W., and Bingert, J.F., (2004), Microstructural evolution in the heat-affected zone of a friction stir weld, *Metallurgical and Materials Transactions A*, Vol.35(5), pp.1487–1499.

47. Fonda, R.W., and Bingert, J.F., (2006), Precipitation and grain refinement in a 2195 Al friction stir weld, *Metallurgical and Materials Transactions A: Physical Metallurgy and Materials Science*, Vol.37(12), pp.3593–3604.

48. Fratini, L., Buffa, G., and Shivpuri, R., (2010), Mechanical and metallurgical effects of in process cooling during friction stir welding of AA7075-T6 butt joints, *Acta Materialia*, Vol.58(6), pp.2056–2067.

49. Frigaard, Ø., Grong, Ø., and Midling, O.T., (2001), A process model for friction stir welding of age hardening aluminum alloys, *Metallurgical and Materials Transactions A*, Vol.32, pp.1189–1200.

50. Fu, R., Zhang, J., Li, Y., Kang, J., Liu, H., and Zhang, F., (2013), Effect of welding heat input and post-welding natural aging on hardness of stir zone for friction stir-welded 2024-T3 aluminum alloy thin-sheet, *Materials Science and Engineering: A*, Vol.559, pp.319–324.

51. Fuller, C.B., Mahoney, M.W., Calabrese, M., and Micona, L., (2010), Evolution of microstructure and mechanical properties in naturally aged 7050 and 7075 Al friction stir welds, *Materials Science and Engineering A*, Vol.527(9), pp.2233–2240.

52. Gachi, S., Boubenider, F., and Belahcene, F., (2011), Residual stress, microstructure and microhardness measurements in AA7075-T6 FSW welded sheets, *Nondestructive Testing and Evaluation*, Vol.26(1), pp.1–11.

53. Genevois, C., Deschamps, A., Denquin, A., and Doisneau-Cottignies, B., (2005), Quantitative investigation of precipitation and mechanical behaviour for AA2024 friction stir welds, *Acta Materialia*, Vol.53(8), pp.2447–2458.

54. Grujicic, M., Arakere, G., Pandurangan, B., Ochterbeck, J.M., Yen, C.F., Cheeseman, B.A., Reynolds, A.P., and Sutton, M.A., (2012), Computational analysis of material flow during friction stir welding of AA5059 aluminum alloys, *Journal of Materials Engineering and Performance*, Vol.21(9), pp.1824–1840.

55. Hassan., (2002), The Effect of welding condition on the nugget zone in friction stir welds AA 7010 alloy, In *6th International trends in Welding Research Conference Proceedings*, 287–292.

56. Hassan, K.A.A., Norman, A.F., Price, D.A., and Prangnell, P.B., (2003), Stability of nugget zone grain structures in high strength Al-alloy friction stir welds during solution treatment, *Acta Materialia*, Vol.51(7), pp.1923–1936.

57. Hassan, K.A.A., Prangnell, P.B., Norman, A.F., Price, D.A., and Williams, S.W., (2003), Effect of welding parameters on nugget zone microstructure and properties in high strength

aluminium alloy friction stir welds, *Science and Technology of Welding and Joining*, Vol.8(4), pp.257–268.

58. Hatch, J.E., *Aluminum Properties and Physical Metallurgy*. ASM ,Ohio, US, 1984.

59. Hirosawa, S., Hamaoka, T., Horita, Z., Lee, S., Matsuda, K., and Terada, D., (2013), Methods for designing concurrently strengthened severely deformed age-hardenable aluminum alloys by ultrafine-grained and precipitation hardenings, *Metallurgical and Materials Transactions A: Physical Metallurgy and Materials Science*, Vol.44(8), pp.3921–3933.

60. Hosseini, M., and Danesh Manesh, H., (2010a), Immersed friction stir welding of ultrafine grained accumulative roll-bonded Al alloy, *Materials and Design*, Vol.31(10), pp.4786–4791.

61. Hosseini, M., and Danesh Manesh, H., (2010b), Immersed friction stir welding of ultrafine grained accumulative roll-bonded Al alloy, *Materials and Design*, Vol.31(10), pp.4786–4791.

62. Hou, K.., and Baeslack, W., (1996), Characterization of the heat-affected zone in gas tungsten arc welded aluminium alloy 2195-T8, *Journal of Materials Science Letters*, Vol.15(3), pp.239–244.

63. Hu, Z., Yuan, S., Wang, X., Liu, G., and Huang, Y., (2011), Effect of post-weld heat treatment on the microstructure and plastic deformation behavior of friction stir welded 2024, *Materials and Design*, Vol.32(10), pp.5055–5060.

64. İpekoğlu, G., and Çam, G., (2014), Effects of Initial Temper Condition and Postweld Heat Treatment on the Properties of Dissimilar Friction-Stir-Welded Joints between AA7075 and AA6061 Aluminum Alloys, *Metallurgical and Materials Transactions A*, Vol.45, pp.864–877.

65. Ipekoğlu, G., Erim, S., and Çam, G., (2014), Effects of temper condition and post weld heat treatment on the microstructure and mechanical properties of friction stir butt-welded AA7075 Al alloy plates, *International Journal of Advanced Manufacturing Technology*, Vol.70(1-4), pp.201–213.

66. Jonathan, E.S., and Montgomery, S., (2004), Next Generation of Metallic Armor Leads the Way, *Amcptiac Q*, Vol.8, pp.4.

67. Fisher Jr, J.J., Kramer, L.S., and Pickens, J.R., (2002), Aluminum alloy 2519 in military vehicles. *Advanced Materials Process*, Vol.160, pp.43–46.

68. Kalemba, I., Hamilton, C., and Dymek,S., (2014), Natural aging in friction stir welded 7136-T76 aluminum alloy, *Materials and Design*, Vol.60, pp.295–301.

69. Babu, N., Karunakaran, N., and Balasubramanian,V., (2014), Comparative evaluation of temperature distribution in GTAW and FSW joints of AA 5059 aluminium alloy. *Journal of Manufacturing Engineering*, Vol.9(2), pp.71–76.

70. Katsas, S., Nikolaou, J., and Papadimitriou, G., (2006a), Microstructural changes accompanying repair welding in 5xxx aluminium alloys and their effect on the mechanical properties, *Materials and Design*, Vol.27(10), pp.968–975.

71. Katsas, S., Nikolaou, J., and Papadimitriou, G. (2006b), Microstructural changes accompanying repair welding in 5xxx aluminium alloys and their effect on the mechanical properties, *Materials and Design*, Vol.27(10), pp.968–975.

72. Koteswara Rao, S.R., Madhusudhan Reddy, G., Srinivasa Rao, K., Kamaraj, M., and Prasad Rao, K., (2005), Reasons for superior mechanical and corrosion properties of 2219 aluminum alloy electron beam welds, *Materials Characterization*, Vol.55(4-5), pp.345–354.

73. Krishna, G.G., Reddy, P.R., and Hussain, M.M., (2014), Effect of Tool Tilt Angle on Aluminum 2014 Friction Stir Welds, *Global Journal of Researches in Engineering*, Vol.14(7), pp.1-14.

74. Kumar, K., and Kailas, S.V., (2008a), The role of friction stir welding tool on material flow and weld formation, *Materials Science and Engineering A*, Vol.485(1-2), pp.367–374.

75. Kumar, K., Kailas, S.V., and Srivatsan,T.S., (2008b), Influence of Tool Geometry in Friction Stir Welding, *Materials and Manufacturing Processes*, Vol.23(2), pp.188–194.

76. Kumar, K., Kailas, S.V., and Srivatsan, T.S., (2011), The Role of Tool Design in Influencing the Mechanism for the Formation of Friction Stir Welds in Aluminum Alloy 7020, *Materials and Manufacturing Processes*, Vol.26, pp.915–921.

77. Kumar, K., and Kailas, S.V., (2008c), On the role of axial load and the effect of interface position on the tensile strength of a friction stir welded aluminium alloy, *Materials and Design*, Vol.29(4), pp.791–797.

78. Kumbhar, N.T., and Bhanumurthy, K., (2008a), Friction Stir Welding of Al 6061 Alloy, *Asian Journal of Experimental Science*, Vol.22(2), pp.63–74.

79. Kwon, Y.J., Shigematsu, I., and Saito, N., (2004), Mechanical Property Improvements in Aluminum Alloy through Grain Refinement using Friction Stir Process, *Materials Transactions*, Vol.45(7), pp.2304–2311.

80. Quintino, L., (2011), Laser Welding of Structural Aluminium, *Advance Structural Materials*, Vol.8, pp.33–57.

81. Lakshmana Rao, M., Shyam, P., Kodali Suresh Babu, P., Rammohan, T., and Seenaiah, Y., (2014), Experimental investigations on friction stir welding of Al2219, *Journal of Manufacturing Engineering*, Vol.*9*(1), pp.45–48.

82. Lakshminarayanan, A.K., and Balasubramanian, V., (2008), Process parameters optimization for friction stir welding of RDE-40 aluminium alloy using Taguchi technique, *Transactions of Nonferrous Metals Society of China*, Vol.18(3), pp.548–554.

83. Lakshminarayanan, A.K., Balasubramanian, V., and Elangovan, K., (2009), Effect of welding processes on tensile properties of AA6061 aluminium alloy joints, *International Journal of Advanced Manufacturing Technology*, Vol.40(3-4), pp.286–296.

84. Lee, W.B., Yeon, Y.M., and Jung, S.B., (2003)., The improvement of mechanical properties of friction-stir-welded A356 Al alloy, *Materials Science and Engineering A*, Vol.355(1-2), pp.154–159.

85. Lee, W.B., Yeon, Y.M., and Jung, S.B., (2004), Mechanical Properties Related to Microstructural Variation of 6061 Al Alloy Joints by Friction Stir Welding, *Materials Transactions*, Vol.45(5), pp.1700–1705.

86. Li, Y., Murr, L.E., and McClure, J.C., (1999), Flow visualization and residual microstructures associated with the friction-stir welding of 2024 aluminum to 6061 aluminum, *Materials Science and Engineering A*, Vol.271(1-2), pp.213–223.

87. Liang, X., Li, H., Li, Z., Hong, T., Ma, B., Liu, S., and Liu, Y., (2012), Study on the microstructure in a friction stir welded 2519-T87 Al alloy, *Materials and Design*, Vol.35, pp.603–608.

88. Liu, G., Zhang, G.J., Ding, X.D., Sun, J., and Chen, K.H., (2004), The influences of multiscale-sized second-phase particles on ductility of aged aluminum alloys, *Metallurgical and Materials Transactions A*, Vol.35(6), pp.1725–1734.

89. Liu, H., and Feng, X.L., (2013), Effect of post-processing heat treatment on microstructure and microhardness of water-submerged friction stir processed 2219-T6 aluminum alloy, *Materials and Design*, Vol.47, pp.101–105.

90. Liu, H., Fujii, H., Maeda, M., and Nogi, K., (2003a), Heterogeneity of mechanical properties of friction stir welded joints of 1050-H24 aluminum alloy, *Journal of Materials Science Letters*, Vol.22(6), pp.441–444.

91. Liu, H.J., Fujii, H., Maeda, M., and Nogi, K., (2003b), Tensile properties and fracture locations of friction-stir-welded joints of 2017-T351 aluminum alloy, *Journal of Materials Processing Technology*, Vol.142(3), pp.692–696.

92. Liu, H.J., Zhang, H.J., Huang, Y.X., and Yu, L., (2010), Mechanical properties of underwater friction stir welded 2219 aluminum alloy, *Transactions of Nonferrous Metals Society of China (English Edition)*, Vol.20(8), pp.1387–1391.

93. Liu, H.J., Zhang, H.J., and Yu, L., (2011), Effect of welding speed on microstructures and mechanical properties of underwater friction stir welded 2219 aluminum alloy, *Materials and Design*, Vol.32(3), pp.1548–1553.

94. Liu, H.J., Zhang, H.J., and Yu, L., (2011), Homogeneity of Mechanical Properties of Underwater Friction Stir Welded 2219-T6 Aluminum Alloy, *Journal of Materials Engineering and Performance*, Vol.20(8), pp.1419–1422.

95. Lombard, H., (2007), *Optimized fatigue and fracture performance of friction stir welded aluminium plate: A study of the inter-relationship between process parameters, TMAZ, microstructure, defect population and performance*. University of Plymouth, England.

96. Lorrain, O., Favier, V., Zahrouni, H., and Lawrjaniec, D., (2010), Understanding the material flow path of friction stir welding process using unthreaded tools, *Journal of Materials Processing Technology*, Vol.210(4), pp.603–609.

97. Mahoney, M.W., Rhodes, C.G., Flintoff, J.G., Bingel, W.H., and Spurling, R.A., (1998), Properties of friction-stir-welded 7075 T651 aluminum, *Metallurgical and Materials Transactions A*, Vol.29(7), pp.1955–1964.

98. Malarvizhi, S., Raghukandan, K., and Viswanathan, N., (2008), Effect of post weld aging treatment on tensile properties of electron beam welded AA2219 aluminum alloy, *International Journal of Advanced Manufacturing Technology*, Vol.37(3-4), pp.294–301.

99. Manickam, S., and Balasubramanian, V., (2015a), Developing empirical relationships to predict the strength of friction stir spot welded AA6061-T6 aluminum alloy and copper alloy dissimilar joints, *Journal of Manufacturing Engineering*, Vol.10, pp.207–214.

100. Marceau, R.K.W., Sha, G., Ferragut, R., Dupasquier, A., and Ringer, S.P., (2010), Solute clustering in Al-Cu-Mg alloys during the early stages of elevated temperature ageing, *Acta Materialia*, Vol.58(15), pp.4923–4939.

101. Mehta, K.P., and Badheka, V.J., (2016), Effects of tilt angle on the properties of dissimilar friction stir welding copper to aluminum, *Materials and Manufacturing Processes*, Vol.31(3), pp.255–263.

102. Mishra, R.S., and Ma, Z.Y., (2005), Friction stir welding and processing, *Materials Science and Engineering R: Reports*, Vol.50(1-2), pp.1-78

103. Mitra, T.K., (2001), Welding of Aluminium alloys, *Welding Research Institute Journal*, Vol.22(1), pp.24–30.

104. Mohamadreza Nourani, Abbas, S., Milani, S., Yannacopoulos., and Taguchi., (2011), Optimization of Process Parameters in Friction Stir Welding of 6061 Aluminum Alloy, *A Review and Case Study, Engineering*, Vol.3, pp.144–155.

105. Mondolfo, L.F., *Aluminum Alloys: Structure and Properties*. London: Butterworth, 1976.

106. Muthu, M.F.X., and Jayabalan, V., (2015), Tool travel speed effects on the microstructure of friction stir welded aluminum-copper joints, *Journal of Materials Processing Technology*, Vol. 217, pp.105–113.

107. Muthukumaran, S., and Mukherjee, S.K., (2008), Multi-layered metal flow and formation of onion rings in friction stir welds, *International Journal of Advanced Manufacturing Technology*, Vol.38(1-2), pp.68–73.

108. Ouyang, J., Yarrapareddy, E., and Kovacevic, R., (2006), Microstructural evolution in the friction stir welded 6061 aluminum alloy (T6-temper condition) to copper, *Journal of Materials Processing Technology*, Vol.172(1), pp.110-122

109. Palanivel, R., and Koshy Mathews, P., (2012), Prediction and optimization of process parameter of friction stir welded AA5083-H111 aluminum alloy using response surface methodology, *Journal of Central South University*, Vol.19(1), pp.1–8.

110. Palanivel, R., Koshy Mathews, P., Murugan, N., and Dinaharan, I., (2012), Effect of tool rotational speed and pin profile on microstructure and tensile strength of dissimilar friction stir welded AA5083-H111 and AA6351-T6 aluminum alloys, *Materials and Design*, Vol.40, pp.7–16.

111. Pang, J.J., Liu, F.C., Liu, J., Tan, M.J., and Blackwood, D.J., (2016), Friction stir processing of aluminium alloy AA7075: Microstructure, surface chemistry and corrosion resistance, *Corrosion Science*, Vol.106, pp.217–228.

112. Papahn, H., Bahemmat, P., Haghpanahi, M., and Sommitsch, C., (2015), Study on governing parameters of thermal history during underwater friction stir welding, *International Journal of Advanced Manufacturing Technology*, Vol.78(5-8), pp.1101–1111.

113. Paston, M., Zhao, H., Martukannitz, R.P., and Debroy,T.. Porosity, Underfill and Magnesium loss during continuous wave Wd: YAG Laser welding of thin plates of Aluminium alloy 5182 and 5754. *Welding Journal*, pp.207–216.

114. Pérez-Bergquist,S.J., Gray,G.T.R., Cerreta,E.K., Trujillo,C.P., and Pérez-Bergquist,A., (2011), The dynamic and quasi-static mechanical response of three aluminum armor alloys: 5059, 5083 and 7039, *Materials Science and Engineering A*, Vol.528(29-30), pp.8733–8741.

115. Polmear, I. J. (1995). *Light Alloys: Metallurgy of the Light Metals*. Wiley.

116. Rajakumar, S., Muralidharan, C., and Balasubramanian, V., (2011), Statistical analysis to predict grain size and hardness of the weld nugget of friction-stir-welded AA6061-T6 aluminium alloy joints, *The International Journal of Advanced Manufacturing Technology*, Vol.57(1-4), pp.151–165.

117. Ravindra Thube, S., and Surjya Pal, K., (2014), Effect of Tool Pin Profile and Welding Parameters on Friction Stir Processing Zone, Tensile Properties and Micro-hardness of AA5083 Joints Produced by Friction Stir Welding, *International Journal of Innovative Research in Advanced Engineering*, Vol.1(4), pp.1–8.

118. Reddy, G.M., Mastanaiah, P., Prasad, K.S., and Mohandas, T., (2009), Microstructure and mechanical property correlations in AA 6061 aluminium alloy friction stir welds, *Transactions of the Indian Institute of Metals*, Vol.62(1), pp.49–58.

119. Rhodes, C.G., Mahoney, M.W., Bingel, W.H., Spurling,R.A., and Bampton, C.C., (1997), Effects of friction stir welding on microstructure of 7075 aluminum, *Scripta Materialia*, Vol.36(1), pp.69–75.

120. Rodriguez, R.I., Jordon, J.B., Allison, P.G., Rushing, T., and Garcia, L., (2015), Microstructure and mechanical properties of dissimilar friction stir welding of 6061-to-7050 aluminum alloys, *Materials and Design*, Vol.83, pp.60–65.

121. Roth, R., Clark, J., and Kelkar, A., (2001), Automobile bodies: Can aluminum be an economical alternative to steel, *Jom*, Vol.53(8), pp.28–32.

122. Rui-dong, F., Zeng-qiang, S., Rui-cheng, S., Ying,L., Hui-jie, L., and Lei, L., (2011), Improvement of weld temperature distribution and mechanical properties of 7050 aluminum alloy butt joints by submerged friction stir welding, *Materials and Design*, Vol.32(10), pp.4825–4831.

123. Russell, A.M., and Lee, K.L., Structure-Property Relations in Nonferrous Metals. Structure-Property Relations in Nonferrous Metals, John Wiley & Sons Technology & Engineering, 2005.

124. Sabari, S.S., Balasubramanian, V., Malarvizhi, S., and Reddy, G.M., (2015), Influences of post weld heat treatment on tensile properties of friction stir welded AA2519-T87 aluminium alloy joints, *Journal of the Mechanical Behavior of Materials*, Vol.24(5-6), 195-205.

125. Saeid, T., Abdollah-zadeh, A., Assadi, H., and Malek Ghaini, F., (2008), Effect of friction stir welding speed on the microstructure and mechanical properties of a duplex stainless steel, *Materials Science and Engineering A*, Vol.496(1-2), pp.262–268.

126. Safarkhanian, M.A., Goodarzi, M., and Boutorabi, S.M.A., (2009), Effect of abnormal grain growth on tensile strength of Al-Cu-Mg alloy friction stir welded joints, *Journal of Materials Science*, Vol.44(20), pp.5452–5458.

127. Sato, Y.S., Kokawa, H., Enomoto, M., Jogan, S., and Hashimoto, T., (1999), Precipitation sequence in friction stir weld of 6063 aluminum during aging, *Metallurgical and Materials Transactions A*, Vol.30, pp.3125–3130.

128. Sato, Y.S., Onuma, T., Ikeda, K., and Kokawa, H., (2016), Experimental verification of heat input during friction stir welding of Al alloy 5083, *Science and Technology of Welding and Joining*, Vol.21(4), pp.325–330.

129. Sato, Y.S., Park, S.H.C., Michiuchi, M., and Kokawa, H., (2004), Constitutional liquation during dissimilar friction stir welding of Al and Mg alloys, *Scripta Materialia*, Vol.50(9), pp.1233–1236.

130. Sato, Y.S., Urata, M., and Kokawa, H., (2002), Parameters controlling microstructure and hardness during friction-stir welding of precipitation-hardenable aluminum alloy 6063, *Metallurgical and Materials Transactions A*, Vol.33(3), pp.625–635.

131. Sato, Y.S., Urata, M., Kokawa, H., and Ikeda, K., (2002), Reproduction of Ultra-Fine Grains in Equal Channel Angular Pressed Al Alloy 5083 by Friction Stir Process, In *ASM Proceedings of the International Conference: Trends in Welding Research* , 262–266.

132. Sato, Y.S., Urata, M., Kokawa, H., and Ikeda, K., (2003), Hall-Petch relationship in friction stir welds of equal channel angular-pressed aluminium alloys, *Materials Science and Engineering A*, Vol.354(1-2), pp.298–305.

133. Schneider, J.A., and Nunes, A.C., (2004), Characterization of plastic flow and resulting microtextures in a friction stir weld, *Metallurgical and Materials Transactions B*, Vol.35(8), pp.777–783.

134. Schneider, J., Brooke, S., and Arthur Nunes Jr, C., (2016), Material Flow Modification in a FSW Through Introduction of Flats, *Metallurgical and Materials Transactions B*, Vol.47(1), pp.720–730.

135. Seighalani, K.R., Givi, M.K.B., Nasiri, A.M., and Bahemmat, P., (2010), Investigations on the effects of the tool material, geometry, and tilt angle on friction stir welding of pure titanium, *Journal of Materials Engineering and Performance*, Vol.19(7), pp.955–962.

136. Senthil Kumar, T., Balasubramanian, V., and Sanavullah, M.Y., (2007), Influences of pulsed current tungsten inert gas welding parameters on the tensile properties of AA 6061 aluminium alloy, *Materials and Design*, Vol.28(7), pp.2080–2092.

137. Sharma, C., Dwivedi, D.K., and Kumar, P., (2012), Influence of in-process cooling on tensile behaviour of friction stir welded joints of AA7039, *Materials Science and Engineering A*, Vol.556, pp.479–487.

138. Sharma, C., Dwivedi, D.K., and Kumar, P., (2013), Effect of post weld heat treatments on microstructure and mechanical properties of friction stir welded joints of Al-Zn-Mg alloy AA7039, *Materials and Design*, Vol.43, pp.134–143.

139. Shen, J.J., Liu, H., and Cui, W., (2010), Effect of welding speed on microstructure and mechanical properties of friction stir welded copper, *Materials and Design*, Vol.31(8), pp.3937–3942.

140. Shercliff, H.R., Russell, M.J., Taylor, A., and Dickerson, T.L., (2005), Microstructural modelling in friction stir welding of 2000 series aluminium alloys, *Mécanique and Industries*, Vol.6(1), pp.25–35.

141. Shukla, A.K., and Baeslack, W.A., (2007), Study of microstructural evolution in friction-stir welded thin-sheet Al–Cu–Li alloy using transmission-electron microscopy, *Scripta Materialia*, Vol.56(6), pp.513–516.

142. Singh, R.K.R., Sharma, C., Dwivedi, D.K., Mehta, N.K., and Kumar, P., (2011), The microstructure and mechanical properties of friction stir welded Al-Zn-Mg alloy in as welded and heat treated conditions, *Materials and Design*, Vol.32(2), pp.682–687.

143. Sivaraj, P.,Kanagarajan, D., and Balasubramanian, V., (2014a), Effect of post weld heat treatment on fracture toughness properties of friction stir welded AA7075-T651 aluminium alloy joints, *Journal of Manufacturing Engineering*, Vol.9(2), pp.110–115.

144. Sivaraj, P., Kanagarajan, D., and Balasubramanian,V., (2014b), Effect of post weld heat treatment on tensile properties and microstructure characteristics of friction stir welded armour grade AA7075-T651 aluminium alloy, *Defence Technology*, Vol.*10*(1), pp.1–8.

145. Smith, G.W., Baxter, W.J., and Mishra, R.K., (2000), Precipitation in 339 and 2124 aluminum: a caveat for calorimetry. *Journal of Materials Science*, Vol.35(15), pp.3871–3880.

146. Smith,W.F., (1996), *Principles of Materials Science and Engineering,* Third edition, New York: McGraw-Hill.

147. Sonne, M.R., Tutum, C.C., Hattel, J.H., Simar, A., and de Meester, B., (2013), The effect of hardening laws and thermal softening on modeling residual stresses in FSW of aluminum alloy 2024-T3, *Journal of Materials Processing Technology*, Vol.213(3), pp.477–486.

148. Suresha, C.N., Rajaprakash, B.M., and Upadhya, S., (2011), A Study of the Effect of Tool

Pin Profiles on Tensile Strength of Welded Joints Produced Using Friction Stir Welding Process, *Materials and Manufacturing Processes*, Vol.26(9), pp.1111–1116.

149. Tan, E., and Ogel, B., (2007), Influence of Heat Treatment on the Mechanical Properties of AA6066 Alloy, *Turkish Journal of Engineering Environmental Science*, Vol.31, pp.53–60.

150. Tang, J., and Shen, Y., (2016), Numerical simulation and experimental investigation of friction stir lap welding between aluminum alloys AA2024 and AA7075, *Journal of Alloys and Compounds*, Vol.666, pp.493–500.

151. Thomas, S.A., and Wolfe, D., (1987), *Weldability of 2219-T851 and 2519-T87 Aluminum armor alloys for use in army vehicle systems*, U.S. Army Materials Technology Laboratory, Report No. MTL TR 87-28.

152. Totten, G.E., and MacKenzie, D.S., (2003), *Handbook of Aluminium, Volume 1: Physical Metallurgy and Processes*. Volume 7, CRC Press, New York, Taylor and Francis.

153. Upadhyay, P., and Reynolds, A.P., (2015), Thermal Management in Friction-Stir Welding of Precipitation-Hardened Aluminum Alloys, *Jom*, Vol.67(5), pp.1022–1031.

154. Venkatesan, S., Rajamani, G., Balasubramanian, V., and Rajakumar, S., (2015), S-N behaviour of friction stir welded AZ31B magnesium alloy joints, *Journal of Manufacturing Engineering*, Vol.10, pp.10–16.

155. Vijay, S.J., and Murugan, N., (2010), Influence of tool pin profile on the metallurgical and mechanical properties of friction stir welded Al-10wt.% TiB2 metal matrix composite, *Materials and Design*, Vol.31(7), pp.3585–3589.

156. Wang, K., Wu, J., Wang, W., Zhou, L., Lin, Z., and Kong, L., (2012a), Underwater friction stir welding of ultrafine grained 2017 aluminum alloy, *Journal of Central South University*, Vol.19(8), pp.2081–2085.

157. Wang, S.C., and Starink, M.J., (2005), Precipitates and intermetallic phases in precipitation hardening Al–Cu–Mg–(Li) based alloys. *International Materials Reviews*, Vol.50(4), pp.193–215.

158. Wang, S.C., Starink, M.J., and Gao, N., (2006), Precipitation hardening in Al-Cu-Mg alloys revisited. *Scripta Materialia*, Vol.54(2), pp.287–291.

159. Watanabe, T., Takayama, H., and Yanagisawa, A., (2006), Joining of aluminum alloy to steel by friction stir welding, *Journal of Materials Processing Technology*, Vol.178(1-3), pp.342–349.

160. Woo, W., Choo, H., Brown, D.W., and Feng, Z., (2007), Influence of the Tool Pin and Shoulder on Microstructure and Natural Aging Kinetics in a Friction-Stir-Processed 6061–

T6 Aluminum Alloy, *Metallurgical and Materials Transactions A*, Vol.38(1), pp.69–76.

161. WU, Y., YE, L., JIA, Y., LIU, L., and Zhang, X., (2014), Precipitation kinetics of 2519A aluminum alloy based on aging curves and DSC analysis, *Transactions of Nonferrous Metals Society of China*, Vol.24(10), pp.3076–3083.

162. Xu, W.F., Liu, J.H., Chen, D.L., Luan, G.H., and Yao, J.S., (2012), Improvements of strength and ductility in aluminum alloy joints via rapid cooling during friction stir welding, *Materials Science and Engineering A*, Vol.548, pp.89–98.

163. Yoon, S., Ueji, R., and Fujii, H., (2015a), Effect of rotation rate on microstructure and texture evolution during friction stir welding of Ti-6Al-4V plates, *Materials Characterization*, Vol.*106*, pp.352–358.

164. Zhang, H.J., Liu, H.J., and Yu, L., (2011), Microstructure and mechanical properties as a function of rotation speed in underwater friction stir welded aluminum alloy joints, *Materials and Design*, Vol.32(8-9), pp.4402–4407.

165. Zhang, H.J., Liu, H.J., and Yu, L., (2012a), Effect of water cooling on the performances of friction stir welding heat-affected zone, *Journal of Materials Engineering and Performance*, Vol.*21*(7), pp.1182–1187.

166. Zhang, H.J., Liu, H.J., and Yu, L., (2012b), Effect of Water Cooling on the Performances of Friction Stir Welding Heat-Affected Zone, *Journal of Materials Engineering and Performance*, Vol.21(7), pp.1182–1187.

167. Zhang, H.J., Liu, H.J., and Yu, L., (2013), Thermal modeling of underwater friction stir welding of high strength aluminum allo, *Transactions of Nonferrous Metals Society of China*, Vol.23(4), pp.1114–1122.

168. Zhang, H., and Liu, H., (2012), Characteristics and Formation Mechanisms of Welding Defects in Underwater Friction Stir Welded Aluminum Alloy, *Metallographic, Microstructure and Analysis*, Vol.1, pp.269–281.

169. Zhang, H., and Liu, H., (2013), Mathematical model and optimization for underwater friction stir welding of a heat-treatable aluminum alloy, *Materials and Design*, Vol.45, pp.206–211.

170. Zhang, X., Deng, C., Wang, D., Wang, Z., Teng, J., Cao, J., Yang, F., (2016), Improving bonding quality of underwater friction stitch welds by selecting appropriate plug material and welding parameters and optimizing joint design, *Materials and Design*, Vol.91, pp.398–410.

171. Zhang, X., Li, H., Gao, H., Gao, Z., Liu, Y., and Liu, B., (2008), Dynamic property evaluation of aluminum alloy 2519A by split Hopkinson pressure bar, *Transactions of*

Nonferrous Metals Society of China, Vol.18(1), pp.1–5.

172. Zhang, X.X., Xiao, B.L., and Ma, Z.Y., (2011), A transient thermal model for friction stir weld. Part I: The model, *Metallurgical and Materials Transactions A: Physical Metallurgy and Materials Science*, Vol.42(10), pp.3218–3228.

173. Zhang, Z., Xiao, B.L., and Ma, Z.Y., (2014), Influence of water cooling on microstructure and mechanical properties of friction stir welded 2014Al-T6 joints, *Materials Science and Engineering: A*, Vol.614, pp.6–15.

174. Zhang, Z., Xiao, B.L., and Ma, Z.Y., (2015), Enhancing mechanical properties of friction stir welded 2219Al-T6 joints at high welding speed through water cooling and post-welding artificial ageing, *Materials Characterization*, Vol.106, pp.255–265.

175. Zhang, Z., Xiao, B.L., Wang, D., and Ma, Z.Y., (2011), Effect of alclad layer on material flow and defect formation in friction-stir-welded 2024 aluminum alloy, In *Metallurgical and Materials Transactions A: Physical Metallurgy and Materials Science*, Vol.42, pp. 1717–1726.

176. Zhao, Y.H., Lin, S.B., Wu, L., and Qu, F.X., (2005), The influence of pin geometry on bonding and mechanical properties in friction stir weld 2014 Al alloy, *Materials Letters*, Vol.*59*(23), pp.2948–2952.

177. Zhao,Y., Wang,Q., Chen,H., and Yan,K., (2014), Microstructure and mechanical properties of spray formed 7055 aluminum alloy by underwater friction stir welding, *Materials and Design*, Vol.56, pp.725–730.

LIST OF PAPERS SUBMITTED BASED ON THIS THESIS

PAPERS PUBLISHED IN NATIONAL JOURNALS

1. Sree Sabari, S., Balasubramanian, V., and Malarvizhi, S. (2015), Effect of tool pin profiles on joint characteristics of under water friction stir welded AA2519-T87 aluminium alloy, *Manufacturing Technology Today*, Vol. 14 (11), 21-28.

2. Sree Sabari, S., Malarvizhi, S., and Balasubramanian, V. (2016), Influences of tool travel speed on tensile properties of underwater friction stir welded high strength armour grade aluminium alloy joints, Journal of Manufacturing Engineering, Vol. 11(2), 94-100.

PAPERS PUBLISHED IN INTERNATIONAL JOURNALS

1. Sree Sabari, S., Malarvizhi, S., Balasubramanian, V., and Madusudhan Reddy, G. (2015), Influence of post weld heat treatment on tensile properties of friction stir welded AA2519-T87 aluminium alloy joints, *Journal of the Mechanical Behavior of Materials*, Vol. 24(5-6), pp. 195-205 (De Gruyter Publishers).

2. Sree Sabari, S., Malarvizhi, S., and Balasubramanian, V. (2016a), Influences of tool travel speed on tensile properties of air cooled and water cooled friction stir welded AA2519-T87 aluminium alloy joints, *Journal of Material Processing Technology*, Vol. 237, pp. 286-300 (Elsevier Publishers).

3. Sree Sabari, S., Malarvizhi, S., Balasubramanian, V., and Madusudhan Reddy, G. (2016b), Experimental and numerical investigation on under water friction stir welding of armour grade AA2519-T87 aluminium alloy, *Defence Technology*, Vol. 12(4), pp. 324-333 (Elsevier Publishers).

4. Sree Sabari, S., Malarvizhi, S., and Balasubramanian, V. (2016c), Characteristics of FSW and UWFSW joints of AA2519-T87 aluminium alloy: Effect of tool rotation speed, *Journal of Manufacturing Processes*, Vol. 22, pp. 278-289 (Elsevier Publishers).

5. Sree Sabari, S., Malarvizhi, S., and Balasubramanian, V. (2016d), Effect of pin profiles on the microstructure and mechanical properties of under water friction stir

welded AA2519 T87 aluminium alloy, *International Journal of Mechanical and Materials Engineering*, Vol. 11 (5), pp. 1-14 (Springer Publishers).

6. Sree Sabari, S., Malarvizhi, S., and Balasubramanian, V. (2016), Effect of tool rotation speed on joint characteristics of under water friction stir welded AA2519-T87 aluminium alloy, *Journal of Applied Research and Technology*, (Elsevier Publishers) (Revision submitted).

7. Sree Sabari, S., Malarvizhi, S., and Balasubramanian, V. (2016), Effect of tool tilt angle on the joint characteristics of friction stir welded (Air cooled & water cooled) AA2519-T87 aluminium alloy, *Materials and Design*, (Elsevier Publishers) (Under Review).

8. Sree Sabari, S., Malarvizhi, S., and Balasubramanian, V. (2016), Effect of tool tilt angle on joint characteristics of under water friction stir welded AA2519-T87 aluminium alloy, *Materials and Manufacturing Processes*, Taylor and Francis Publishers (Under Review).

PAPER PRESENTED IN CONFERENCES

1. **Sree Sabari, S., Malarvizhi, S., and Balasubramanian, V (2012),** Modeling of friction stir welding process and prediction of thermal history of aluminum alloy AA2519-T87 using finite element method, *International Welding Symposium (IWS-2k12)*, Mumbai, October, 453-463.

2. **Sree Sabari, S., Malarvizhi, S., and Balasubramanian, V (2014),** Evaluation of mechanical properties of friction stir welded AA2219 T87 and AA2519 T87 aluminium alloys, *National Conference on Recent Advances in Welding and Surface Engineering (RAWSE' 14),* Annamalai University, Annamalai Nagar, March, 38.

3. **Sree Sabari, S., Malarvizhi, S., and Balasubramanian, V (2014),** Effect of post weld heat treatment and mechanical properties of friction stir welded AA2519 T87 armour grade aluminium alloy, *International welding congress (IC2014)*, International Institute of Welding, New Delhi, April, 124. **Received "D & H Secheron Award" and Rupees Ten Thousand cash prize for the best paper presentation**.

4. **Sree Sabari, S., Malarvizhi, S., and Balasubramanian, V (2014),** Finite element modeling of underwater friction stir welded AA 2519-T87 aluminium alloy joints" *National Weld Meet (NWM-2014),* International Institute of Welding and Mohamed Sathak Engineering College, Kilakarai, April, 34.

206

5. **Sree Sabari, S., Malarvizhi, S., and Balasubramanian, V (2014),** Effect of post weld heat treatment on microstructural characteristics and mechanical properties of friction stir welded AA2519 T87 aluminium alloy joints, *International Conference on Friction Based Processes (ICFP-2014)*, International Institute of Science (IISc), Bangalore, September, 30.

6. **Sree Sabari, S., Malarvizhi, S., and Balasubramanian, V (2015),** Effect of underwater friction stir welding on mechanical properties and microstructural characteristics of AA2519 aluminium alloy joints, *National Welding Seminar (NWS 14-15),* Tata Steel, Jamshedpur, January, 46.

7. **Sree Sabari, S., Malarvizhi, S., and Balasubramanian, V (2015),** Evolution of microstructure of friction stir welded AA2519-T87 aluminium alloy, *National Technical Conference (NCTME15),* M.Kumarasamy College of Engineering, Karur, March.

8. **Sree Sabari, S., Malarvizhi, S., and Balasubramanian, V (2015),** Texture analysis of friction stir welded AA2519-T87 aluminium alloy joint, *International conference on Cutting, Welding and Surfacing (CWS 2015),* Coimbatore institute of technology (CIT), Coimbatore, August, 494-503.

9. **Sree Sabari, S., Malarvizhi, S., and Balasubramanian, V** (2015), Effect of pin profiles on material flow behaviour of underwater friction stir welded AA2519 T87 aluminium alloy joints, *National Welding Seminar (NWS 2015),* Indian Institute of Welding, Mumbai, December.

10. **Sree Sabari, S., Malarvizhi, S., and Balasubramanian, V** (2016), Influences of tool travel speed on tensile properties of underwater friction stir welded high strength armour grade aluminium alloy joints, *International conference on Futuristic Innovations in Mechanical Engineering and Manufacturing Management (ICFIMEMM 2016)*, M.Kumarasamy college of engineering Karur, March.

11. **Sree Sabari, S., Malarvizhi, S., and Balasubramanian, V** (2016), Characteristics of FSW and UWFSW joints OF AA2519-T87 aluminium alloy: effect of tool rotation speed, *One day symposium on Recent Investigation on Welding Research (RIWER)*, Indian Institute of Welding, Indian Welding Society and Annamalai University, Chidambaram, July.